Sismicité, couplages sismique-asismiques et processus transitoires de déformation dans un système de failles actives : le rift de Corinthe, Grèce

Clara Duverger

UNIVERSITÉ SORBONNE PARIS CITÉ

Thèse préparée à l'Université Paris Diderot
École Doctorale STEP'UP – ED 560
Institut de Physique du Globe de Paris – Equipe de sismologie

---

Sismicité, couplages sismique-asismiques et processus transitoires de déformation dans un système de failles actives : le rift de Corinthe, Grèce

---

présentée par

Clara DUVERGER

THÈSE de DOCTORAT de Sciences de la Terre et de l'environnement

Spécialité Géophysique

dirigée par Pascal BERNARD *et* Hélène LYON-CAEN

Soutenue publiquement à l'IPGP le 29 novembre 2017 *devant le jury composé de :*

Françoise COURBOULEX	Directrice de recherche (Géoazur, Nice)	Rapporteure
David MARSAN	Professeur (ISTerre, Grenoble)	Rapporteur
Mary FORD	Professeure (ENSG, Nancy)	Présidente du jury - Examinatrice
Alexandre SCHUBNEL	Chargé de recherche (ENS, Paris)	Examinateur
Pascal BERNARD	Physicien (IPGP, Paris)	Directeur de thèse
Hélène LYON-CAEN	Directrice de recherche (ENS, Paris)	Co-directrice de thèse

UNIVERSITÉ SORBONNE PARIS CITÉ

Thèse préparée à l'Université Paris Diderot
École Doctorale STEP'UP – ED 560
Institut de Physique du Globe de Paris – Equipe de sismologie

Sismicité, couplages sismique-asismiques et processus transitoires de déformation dans un système de failles actives : le rift de Corinthe, Grèce

présentée par

Clara DUVERGER

THÈSE de DOCTORAT de Sciences de la Terre et de l'environnement

Spécialité Géophysique

dirigée par Pascal BERNARD *et* Hélène LYON-CAEN

Soutenue publiquement à l'IPGP le 29 novembre 2017 *devant le jury composé de :*

Françoise COURBOULEX	Directrice de recherche (Géoazur, Nice)	Rapporteure
David MARSAN	Professeur (ISTerre, Grenoble)	Rapporteur
Mary FORD	Professeure (ENSG, Nancy)	Présidente du jury - Examinatrice
Alexandre SCHUBNEL	Chargé de recherche (ENS, Paris)	Examinateur
Pascal BERNARD	Physicien (IPGP, Paris)	Directeur de thèse
Hélène LYON-CAEN	Directrice de recherche (ENS, Paris)	Co-directrice de thèse

Résumé

La partie ouest du rift de Corinthe, en Grèce, s'ouvre à une vitesse d'environ 15 mm par an générant un taux de déformation parmi les plus élevés au monde, quelques séismes destructeurs de magnitude M > 6 par décennie, et une forte activité microsismique irrégulière spatialement et temporellement. Afin de mieux comprendre les mécanismes liés à cette déformation crustale et de préciser les structures majeures actives, ce travail de recherche exploite la base de données sismologiques du *Corinth Rift Laboratory* de 2000 à 2015 en analysant finement les microséismes et leur évolution spatio-temporelle. La relocalisation globale des sources sismiques ainsi que leur classification en multiplets ont permis de préciser la géométrie des failles et d'identifier des comportements mécaniques différents. La zone ouest, au milieu du golfe, est affectée par des variations de pressions de fluides dans une couche géologique, entraînant des migrations des essaims de microséismes à des vitesses d'environ 50 m par jour. Les multiplets profonds de la partie centrale, près de la côte nord, sont persistants et semblent déclenchés par des épisodes de glissements lents asismiques sur un détachement immature pouvant atteindre la croûte ductile. Le faible pourcentage de déclenchement dynamique par les ondes sismiques suggère que l'état global du système de failles n'est pas au seuil critique de rupture. La magnitude des séismes est corrélée à l'impulsivité initiale de la rupture. Ces résultats précisent la dynamique de déformation du rift, les interactions sismique-asismiques, et permettront d'améliorer les modèles d'aléas sismiques de la région.

Mots clés : failles actives, essaims sismiques, multiplet, déformation transitoire, pression de pore, glissement lent, migration sismique, déclenchement dynamique, initiation de la rupture, rift de Corinthe.

Abstract

The western part of the Corinth Rift in Greece is opening at about 15 mm per year, generating one of the highest deformation rates in the world, some destructive earthquakes of magnitude M > 6 per decade, and high microseismic activity irregular in space and time. In order to better understand the mechanisms related to this crustal deformation and to specify the major active structures, this research work makes use of the seismological database of the *Corinth Rift Laboratory* from 2000 to 2015 by finely analyzing microearthquakes and their spatio-temporal evolution. The global relocation of the seismic sources and their classification into multiplets enable to refine the geometry of the faults and to identify different mechanical behaviors. The western zone, in the middle of the gulf, is affected by fluctuations of fluid pore pressures in a geological layer, resulting in microseismic swarm migrations at a velocity of about 50 m per day. The deep multiplets of the central part, near the northern coast, are persistent and appear to be triggered by episodes of slow aseismic slip along an immature detachment, which can reach the ductile crust. The low percentage of dynamic triggering by passing seismic waves suggests that the overall state of the fault system is not at the critical breaking point. The magnitude of earthquakes is correlated with the initial impulsiveness of the rupture. These results specify the dynamics of the rift deformation, the seismic-aseismic interactions, and will make possible the improvement of the seismic hazard models of the region.

Key words: active faults, seismic swarm, multiplet, transient deformation, pore pressure, slow slip, seismic migration, dynamic triggering, rupture initiation, Corinth rift.

Remerciements

“ *Le meilleur ami de* merci *est* beaucoup. ”

Michel Bouthot

Voici le temps des remerciements après trois années passées dans le domaine de la recherche académique. J'aimerais remercier en premier lieu les membres du jury, Françoise COURBOULEX, Mary FORD, David MARSAN, et Alexandre SCHUBNEL, qui ont accepté de lire et évaluer ce travail, tout en apportant des commentaires enrichissants et des suggestions pour l'avenir.

Je tiens à remercier très chaleureusement mes directeurs de thèse, Pascal BERNARD et Hélène LYON-CAEN, pour l'ensemble des riches discussions apportées, pour votre patience à toute épreuve, votre soutien constant et votre bienveillance.

Pascal, merci d'avoir partagé une partie (sûrement minime) de ta culture scientifique avec moi, de m'avoir donné envie de poursuivre sur le chantier de Corinthe qui existe depuis plus de 20 ans maintenant mais semble toujours plus attrayant. Merci d'avoir pris le temps de me réexpliquer certains concepts fondamentaux avec tes gribouillis, que je garderais d'ailleurs à mes côtés grâce à ton livre. Merci d'avoir toujours cru en moi, d'être toujours à l'écoute et parfois même d'avoir consacrer tes journées et soirées entières à répondre à nos multiples et intempestives sollicitations de jeunes padawans.

Hélène, merci pour tes précieux conseils et ta disponibilité, surtout lors des récurrentes excursions de Pascal. Merci aussi d'avoir été un frein à ses idées, certes lumineuses, mais toujours plus nombreuses et énergivores, au moment oppurtun. Merci pour tes remarques toujours positives sur mon travail qui permettaient de me redonner confiance en moi.

Je souhaiterais également fortement remercier Maxime GODANO et Sophie LAMBOTTE avec qui j'ai pu colaborer de manière régulière et qui m'ont offert leur connaissance scientifique et leur soutien. Merci pour vos développements méthodologiques et vos discussions enrichissantes. Je remercie vivement Harsha BHAT, Alexandre SCHUBNEL, Alexis RIGO et Claudio SATRIANO pour m'avoir conseillé chaque année en me suggérant de nombreuses pistes intéressantes pour la poursuite de la thèse, tout en ne me faisant pas oublier les objectifs premiers. Merci pour toutes vos remarques, reflexions, et partages d'expérience.

J'aimerais remercier Pierre BRIOLE et le laboratoire de Géosciences de l'ENS pour m'avoir permis de participer à une mission de terrain dans le golfe de Corinthe. Un grand merci à Anne DESCHAMPS, ma principale partenaire de route, pour m'avoir fait faire le tour des stations sismiques du réseau CRL, pour toutes les explications techniques et les discussions diverses et variées pendant les trajets parfois cahotiques. Merci à Panaiotis ELIAS pour son entrain, sa bonne humeur inaltérable et les présentations grecques aux locaux; Maurin VIDAL pour son énergie débordante et ses démonstrations de travail très ordonné sur les cablages électriques. Dimitar DIMITROV pour son partage d'expériences sur les GPS, ses conseils avisés et sa patience. Michel CAPDEROU pour sa prise de notes exemplaire dans ses cahiers de terrain qui deviennent emblématiques. Carlo LAJ pour les discussions multiples très enrichissantes ainsi que les photos souvenirs.

Merci à l'équipe de sismologie pour son dynamisme et sa jovialité, la plus grande des familles de l'IPGP. Pensée particulière à Sophie, Marie-Christine et Sylvie pour avoir gérer l'organisation des différentes missions. Je remercie Michel pour les installations de matériel informatique toujours plus performant et sa capacité à solutioner tous les petits problèmes sur les réseaux de l'IPGP, ainsi que Geneviève, grande manitou des clusters de calculs en parallèle et experte en LaTeX à ses heures perdues, pour ses directives et conseils en tout genre.

Merci à l'équipe de tectoniciens qui m'a laissée m'infiltrer à de nombreuses reprises pour prendre un café, parfois accompagné de quelques parts de gâteaux offertes, dans les confortables fauteuils du 2e étage.

Comment évoquer ces trois dernières années sans avoir une pensée toute particulière envers mes chers co-bureaux : Léonard, Florent, Kevin, Mathurin, et John-Robert. Merci à cette équipe masculine pour m'avoir soutenue et supportée durant ces longues journées passées devant nos écrans. Merci pour toutes les distractions apportées à des moments 'bienvenus' (je pense particulièrement aux interminables parties de petit baccalauréat et aux cache-caches du père Noël) et surtout pour les très nombreux conseils délivrés, partage de problèmes et solutions scientifiques et votre temps accordé. L'entraide fait la force dans le bureau (312)!

Merci aux organisateurs des séances sportives hebdomadaires : Vincent, Aurélie, Manon, Pierre C., Julien, Chloé, Marine, les quelques collègues du Langevin et ceux déjà cités pour les parties de squash en folie; Pierre R., Gino et Martha, pour les sorties natation et les entrainements de course à pied dans le Jardin des Plantes. À Delphine, capitaine de mon équipe de basket, pour nos victoires et notre magnifique montée au meilleur niveau universitaire. Tous ces moments défouloirs m'ont permis de recharger les batteries et de me sentir en forme pour l'ascension du mont Thèse et ses multiples lacets! Merci à l'Hekla pour l'organisation des activités sportives (notamment les Géolympiques), des activités artistiques, cinématographiques, culinaires et arrosées. Merci à l'orchestre PhiloGaia pour ses mélodies rythmées parfois innovantes voire expérimentales qui apportent toujours de la bonne humeur. Merci aux organisateurs des beer party et aux annonces illustrées bien amusantes du vendredi soir, ;-) Marina.

De manière générale, un grand merci à toutes les personnes cotoyées, certains même déjà avant la thèse : Marthe, Tom, Sophie, Anaïs, Seb, Raphaël, Océane, Chloé avec nos déjeuners-narratifs et nos soirées régulières. Merci aux thésards et post-doctorants, ingénieurs et chercheurs des laboratoires de l'IPGP et de l'ENS à la fois pour le sérieux des réflexions scientifiques et les diverses occasions données d'aller grignoter ou prendre un verre après de longues journées. Merci aux copains pour les quelques découvertes gastronomiques et œnologiques dans le quartier.

Merci à ma famille, pour m'avoir encouragée dans cette voie et toujours soutenue moralement, voire même alimentairement pour ne pas perdre les saveurs des bons produits tourangeaux, et des délicieuses recettes que seules nos mères et nos grand-mères savent préparer à la perfection. Merci au rapporteur haute-technologie de ma petite soeur qui m'a bien dépanné pour mesurer tous ces azimuths et pendages de faille :-).

Enfin, le meilleur pour la fin, mille mercis à mon Rémimi dont la présence (même à distance) et le soutien inébranlable m'ont été indispensables. Merci de m'avoir poussée, presque chaque jour de fin de thèse, à ne pas m'éterniser au bureau pour continuer à profiter des autres aventures personelles. Merci pour avoir su me raisonner, me conseiller, me relaxer, me guider, tout simplement d'avoir été mon pilier.

Table des matières

Liste des figures

Liste des tableaux

Introduction générale

« *La vie est un mystère qu'il faut vivre, et non un problème à résoudre.* »

Gandhi

La croûte terrestre, ou lithosphère de son nom d'origine, est en mouvement perpétuel depuis sa naissance il y a des milliards d'années et aime à rappeler à ses habitants qu'elle est toujours en activité. Les tremblements de terre en sont sa démonstration la plus éloquente, affolant les populations autant qu'ils suscitent la curiosité. Cette croûte rigide est la couche la plus superficielle et la plus complexe de la Terre. Elle est morcelée en plaques tectoniques qui se déplacent continuellement grâce aux courants de convection mantelliques qui permettent d'évacuer la chaleur interne de la Terre. Les périodes de quiescence en surface ne sont qu'un leurre, les plaques ne dorment jamais et forment un véritable ballet. Elles fluent, se distordent, craquent, et interagissent les unes avec les autres générant des déformations crustales importantes parfois silencieuses.

Ces déformations se localisent majoritairement aux frontières des plaques, dans les zones de subduction comme au Japon ou le long de la Cordillère des Andes, de collision comme en Himalaya, en décrochement comme par exemple le long de la faille de San Andreas aux États-Unis, ou en extension comme au niveau des dorsales océaniques ou des zones de rift continentales. Ces zones sont ainsi le siège de systèmes de failles qui accommodent la déformation fragile par du glissement le long des plans de failles. Les séismes sont certainement l'observable le plus démonstratif de cette déformation fragile, le plus accessible et le plus abondant. Lors d'un séisme, l'accommodation de la déformation se fait de manière intermittente, la faille reste bloquée jusqu'à un certain seuil de contraintes dépendant de ses caractéristiques physiques, puis glisse brutalement en libérant l'énergie accumulée en seulement quelques secondes et générant des ondes sismiques qui sont parfois dévastatrices. Dans d'autres cas, la situation n'est pas aussi dangereuse, et le glissement le long du plan de faille s'effectue de manière stable, en fluage régulier asismique, la déformation s'accommodant en continu sans manifestation catastrophique. L'imbrication de ces deux phénomènes est parfois nécessaire afin d'expliquer la mécanique d'un système de failles voire d'une seule et même faille, bien qu'ils fonctionnement de manière relativement différente.

Cependant, cette mécanique ne se limite pas à un modèle idéal de cycle sismique avec une phase de chargement tectonique lent suivi par une relaxation sismique rapide, ou de fluage constant. De nombreuses instabilités et processus transitoires, tels que des essaims de microséismes, des séismes lents, des cascades de grands séismes, etc. sont également observés dans les régions actives dans des gammes spatio-temporelles très larges. Elles révèlent l'existence de couplages entre déformations lentes et rapides et suggèrent un rôle important des pressions de fluides aux profondeurs crustales.

L'objectif est alors de déceler et analyser les différents types de déformations, qu'elles soient continues ou transitoires, sismiques ou asismiques, et de quantifier leur proportion respective afin de mieux comprendre la dynamique des systèmes de failles et mieux anticiper la possible naissance d'une forte secousse sismique. Les phases de nucléation des séismes et d'interactions à la fois

entre eux et avec les différents forçages externes sont des notions clés de la compréhension des mécanismes qui les gouvernent. Dans cette thèse, il s'agira en particulier, à l'aide des données sismologiques, de caractériser finement les zones sismiques et asismiques du système étudié et de cerner le rôle éventuel des fortes pressions de fluide dans les zones de failles profondes. Ces éléments permettront de mieux préciser le couplage mécanique avec les différents phénomènes transitoires associés et cachés, et de déterminer leur potentiel sismogène en matière de séismes destructeurs.

Pour cela, l'étude se place dans un lieu et contexte tectonique privilégié pour le suivi en continu de la sismicité et des déformations associées depuis plus de 15 ans. Notre zone de recherche est le Golfe de Corinthe, en Grèce, jeune rift continental séparant la Grèce continentale du Péloponnèse et montrant une extension parmi les plus élevées au monde. Son taux de déformation très important (10^{-6} par an), sa forte activité microsismique (environ 10 000 par an) ainsi que l'occurrence de plusieurs séismes de magnitude supérieure à M_W6 au cours des dernières décennies, en font un cadre idéal pour mener des études pluridisciplinaires, en plus de pouvoir apporter des données supplémentaires aux calculs d'aléa sismique pour la protection des populations. Cette zone de rift est caractérisée par un système de failles normales antithétiques actives, générant une microsismicité très irrégulière sous forme d'essaims durant plusieurs jours à plusieurs mois, concentrés dans l'espace sur quelques kilomètres à quelques dizaines de kilomètres et montrant parfois des migrations. L'analyse de cette activité microsismique sous différents angles, en termes de statistiques d'Omori, de Gutemberg-Richter, de corrélation de forme d'ondes, de clusterisation spatio-temporelle, de magnitude de moment, de dimension de sources, etc. permet une meilleure compréhension de la mécanique sous-jacente de forçage.

Dans le premier chapitre, nous présenterons tout d'abord brièvement les déformations majeures internes et externes que subit notre Terre, avant d'introduire les différents témoins naturels de ces forçages, pour certains découverts durant ces dernières décennies grâce au développement des instruments sismologiques et géodésiques. Nous aborderons les notions d'interactions entre les évènements sismiques et asismiques. Cette étude bibliographique nous permettra de bien comprendre les concepts de déclenchement des séismes, les lois d'occurrence et les modèles de sources classiquement utilisés en sismologie, pour enfin définir les grandes questions mécaniques et théoriques qui seront abordées.

Le deuxième chapitre est consacré au rift de Corinthe, en présentant son contexte géodynamique, géologique et tectonique. Nous détaillerons les caractéristiques sismogènes de la région à travers les résultats des dernières études sismologiques majeures. Nous développerons également la diversité et l'évolution des réseaux d'instruments qui sont installés au sein du rift, ainsi que l'organisation de la base de données sismologiques mise à disposition. Les motivations nous ayant conduits à étudier cette région seront discutées, et nous définirons les problématiques propres aux conditions tectoniques et à la forte activité sismique de ce lieu d'observation.

Dans le troisième chapitre, nous présenterons un premier exemple permettant d'identifier les liens d'interaction entre les fluides et la microsismicité. Il traitera d'une crise sismique particulière ayant eu lieu en 2003–2004, suspectée être occasionnée par des migrations de pression de pore dans la croûte. Cette étude permettra de mieux comprendre l'évolution spatio-temporelle de l'activité microsismique au milieu du Golfe de Corinthe ainsi que de mettre en lumière les mécanismes moteurs cachés.

Le quatrième chapitre portera sur le développement d'une méthode de calcul de corrélation des formes d'ondes de la base de données du *Corinth Rift Laboratory* (2000–2015) et la présentation des résultats à échelle locale qui en découlent. Nous détaillerons la géométrie et l'activité des structures tectoniques mises en évidence à l'aide d'une relocalisation globale des microséismes détectés. Nous présenterons également certaines caractéristiques spatio-temporelles des familles

d'évènements sismiques fortement corrélés et leur implication quant à la compréhension de la dynamique de fonctionnement du rift. Cette étude donnera également des éléments clés qui pourront permettre d'améliorer les modèles de quantification de l'aléa sismique dans la région.

La réactivité de la microsismicité locale aux passages des ondes sismiques d'évènements forst et lointains est regardée dans le cinquième chapitre. Nous y présentons les résultats de cette analyse de déclenchement dynamique à plusieurs échelles : mondiale, régionale et locale, qui permet de révéler l'état de contraintes des différentes failles du système au cours du temps, de mieux comprendre l'occurrence de certains essaims de microséismes locaux et de comparer la sensibilité respective de certaines zones à une excitation oscillatoire extérieure.

Dans le sixième chapitre, nous nous focaliserons sur l'initiation de la rupture sismique. Nous essayerons de comparer les signaux sismiques au démarrage de la rupture en fonction de la magnitude finale des évènements enregistrés. Ceci nourrira les discussions autour de la possibilité de prédiction de la taille finale des séismes avant la fin de la propagation de la rupture sur le plan et de potentiellement aider à l'établissement de système d'alerte précoce. L'initiation de la rupture est également analysée en fonction de la nature du forçage générant les évènements sismiques. En effet, il est possible que des caractéristiques intrinsèques au forçage puissent être identifiables lors de la nucléation du séisme, permettant de définir si l'origine du séisme est tectonique liée à des interactions mécaniques entre les petites failles, liée aux circulations de fluides, ou liée à un glissement asismique environnant.

Finalement, nous conclurons en rappelant les principaux résultats apportés par ce travail et leurs implications. Nous discuterons également des développements futurs qui restent à accomplir, notamment en ce qui concerne l'automatisation de la méthodologie de classification des évènements par familles, de la confrontation des résultats sismologiques aux mesures géodésiques et extensométriques et de l'exploration de la réponse du rift aux déformations liées à la marée terrestre et océanique.

Chapitre 1

Les interactions sismique–asismiques

Sommaire

1.1 Introduction

Ce premier chapitre est consacré à la présentation des différents types de déformations de notre globe terrestre. Les déformations dites séculaires, c'est-à-dire suffisamment lentes pour être considérées comme linéaires et apériodiques, se différencient des déformations transitoires, qui sont non-linéaires. Ce chapitre développe brièvement les déformations séculaires en introduisant par la même occasion les notions de tectonique des plaques, de cycle sismique, avant de se focaliser sur les déformations transitoires qui peuvent être périodiques voire saisonnières, comme épisodiques avec des durées et extensions spatiales très variables. L'éventuelle dépendance entre ces dernières et l'activation des failles sismogènes est un sujet complexe à prendre en compte pour améliorer l'évaluation de l'aléa sismique dans les régions tectoniquement actives. L'objectif est d'exposer la diversité des interactions possibles entre les phénomènes sismiques et asismiques, en développant les possibles causes et les témoins des déformations transitoires, ainsi que les changements de contraintes liés aux séismes. Ce chapitre conclut sur la formulation des problématiques mécaniques génériques qui seront abordées dans ce manuscrit.

1.2 La Terre se déforme

Les déformations de la Terre sont très variées et de diverses natures. Dans cette partie, nous présentons brièvement les acteurs majeurs externes ou internes. En guise de premier aperçu, voici les ordres de grandeur des déformations verticales et horizontales les plus importantes (Tableau 1.1), qui seront évoquées dans cette partie.

TABLEAU 1.1 – Ordres de grandeur des déformations terrestres.

Déformation	verticale	horizontale
Marée terrestre	30 cm	10 cm
Marée océanique	10 cm	2 cm
Charge hydrologique	5 cm	1 cm
Charge atmosphérique	1 cm	2 mm
Rebond post-glaciaire	1 cm.an^{-1}	2 mm.an^{-1}
Tectonique	1 cm	1–10 cm

1.2.1 Les déformations liées aux forces de marées

Dans un premier temps, la planète bleue se déforme à cause de sa rotation autour d'elle-même et des champs de gravité des astres du système solaire. La conséquence la plus évidente qui témoigne de l'existence de ces forces est la marée océanique. Les mers et les océans se déplacent et se déforment par les forces d'attraction–répulsion principalement de la Lune et du Soleil, donnant naissance aux fluctuations périodiques du niveau de l'eau, les marées hautes et marées basses (Figure 1.1.b). Toute personne habitant sur le littoral observe ce phénomène quotidiennement. Cependant, ce qu'elle ne voit pas, c'est que la Terre solide elle-même subit des marées. La marée dite terrestre correspond à la déformation élastique de la partie solide du globe. Elle est de plus grande ampleur que celle de la marée océanique, et donne à notre planète une forme ovoïde (Figure 1.1.a).

De plus, l'enveloppe océanique par son poids et sa marée participe à la déformation des couches superficielles, en accentuant ou en diminuant les effets de la marée terrestre suivant leur orientation. Pour information, il existe également des marées atmosphériques qui se manifestent par des variations de la pression de l'air, mais qui ne participent que dans une plus faible mesure aux déformations de la surface du géoïde.

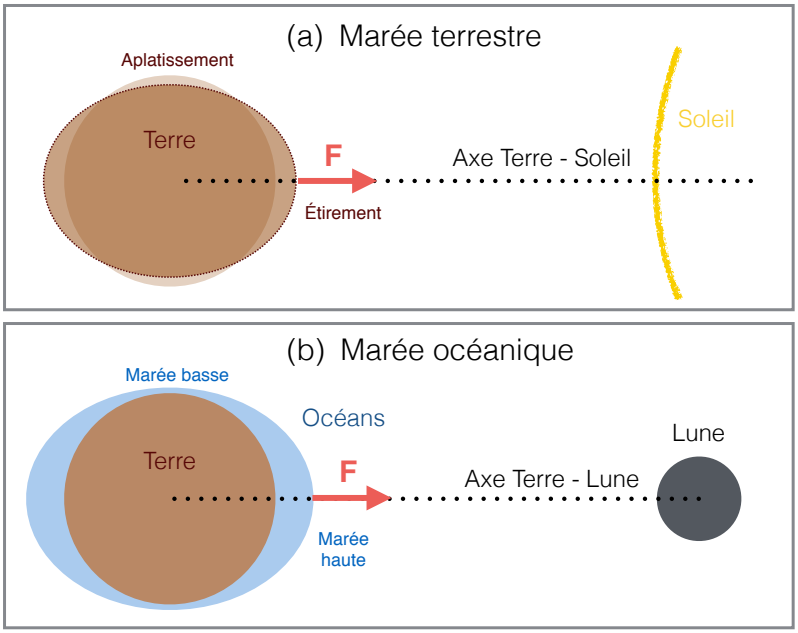

FIGURE 1.1 – Schémas simplifiés des déformations liées aux marées terrestre et océanique. (a) Marée terrestre : les masses solides de la Terre sont attirées par les astres de notre système solaire, principalement le Soleil, déformant le géoïde. (b) Marée océanique : l'enveloppe fluide de la Terre est attirée par les astres du système solaire, majoritairement la Lune, générant un bourrelet liquide le long de l'axe Terre-Lune.

Ces déformations liées aux forces de marées, même si elles ne seront pas directement analysées dans ce manuscrit sont à garder à l'esprit, car de plus en plus d'études montrent des corrélations positives entre les phases des marées (océaniques et/ou terrestres) et l'occurrence de séismes [Cochran et al., 2004; Tanaka et al., 2002], dans des régions spécifiques du globe [e.g. Wilcock, 2001], pour certains types de mécanismes de faille [e.g. Tsuruoka et al., 1995], ou encore certaines gammes de magnitudes [e.g. Chen et al., 2012a]. D'après Métivier et al. [2009], les déclenchements d'évènements sismiques par les marées semblent plus nombreux dans les régions dominées par de l'extension et/ou du décrochement, et les corrélations sont plus grandes avec les petits évènements superficiels.

1.2.2 Les déformations isostatiques

La Terre solide est composée de trois grandes couches principales (Figure 1.2) :

1. la croûte terrestre, qui regroupe la croûte océanique et la croûte continentale ;
2. le manteau, qui est souvent dissocié en un manteau supérieur plus ductile (moins visqueux) et un manteau inférieur, dans lesquels siègent les courants de convection ;
3. le noyau, qui est composé d'une graine solide (noyau interne) et d'une enveloppe liquide (noyau externe).

Les géologues ou tectoniciens, qui s'intéressent aux parties superficielles de la Terre, préfèrent utiliser les termes de :

— lithosphère (du grec "lithos" : pierre) qui est l'enveloppe rigide de la surface de la Terre. Elle comprend la croûte terrestre et la partie plus cassante du manteau supérieur ;

— asthénosphère (du grec "asthenos" : sans résistance) qui correspond à la partie ductile du manteau supérieur jusqu'au manteau inférieur.

Ces termes sont apparus avec l'émergence de la théorie de la tectonique des plaques, au début des années 1960 (voir Section 1.2.3). Ces couches se distinguent en fonction de leurs propriétés mécaniques et physiques plutôt qu'à l'aide des discontinuités rendues visibles par la sismologie.

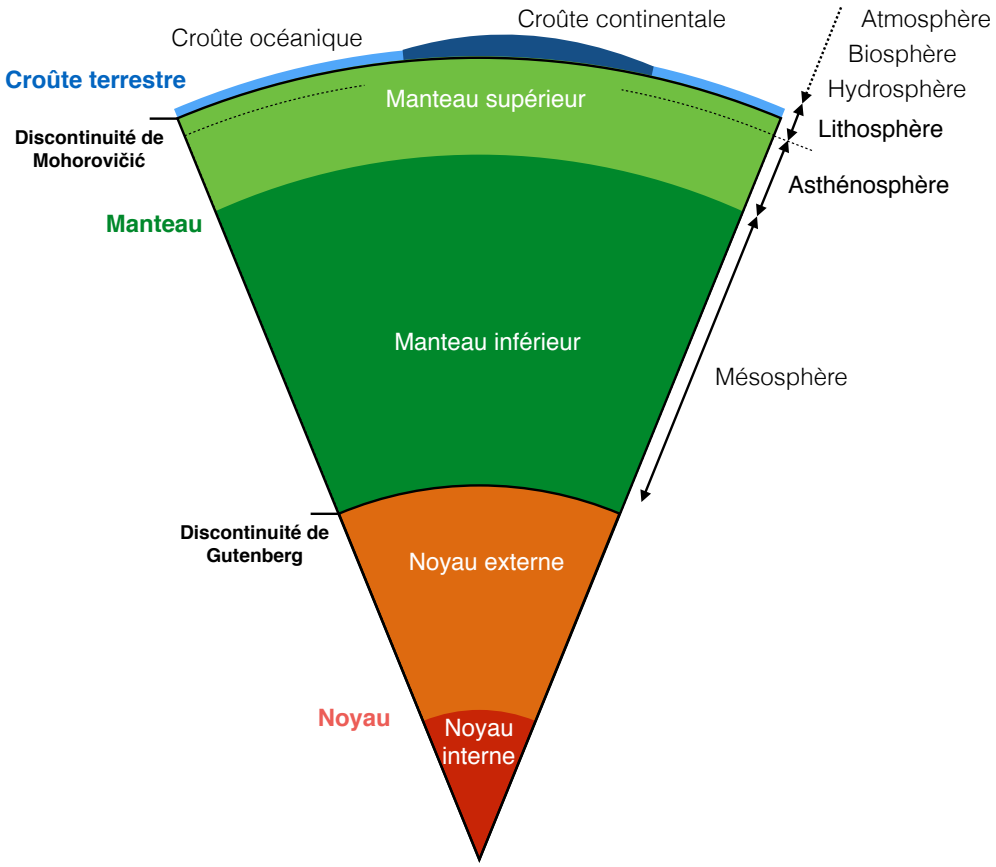

FIGURE 1.2 – Schéma simplifié de la structure interne de la Terre. On distingue la terminologie des enveloppes principales basée sur les discontinuités mises en évidence par la sismologie, de la terminologie des enveloppes secondaires (à droite) issue de la tectonique des plaques et basée sur les propriétés mécaniques et physiques des couches.

La lithosphère constitue donc la couche cassante à la surface de la planète. Elle est subdivisée en une douzaine de plaques tectoniques ou lithosphériques mobiles les unes par rapport aux autres, et en équilibre sur l'asthénosphère ductile selon le principe d'isostasie. Lors de la collision de deux plaques continentales, des chaînes de montagnes se forment, donnant lieu à des reliefs majeurs. L'épaississement de la lithosphère, qui se produit par plissements et chevauchements, implique une augmentation de sa masse. Cet excès de masse en surface est alors compensé par un déficit de masse en profondeur, par ré-équilibrage isostatique (Figure 1.3). En simplifiant très fortement, ce concept peut être illustré avec la poussée d'Archimède. La lithosphère aux propriétés élastiques s'enfonce légèrement dans l'asthénosphère plus visqueuse (comme un bateau que l'on charge), mais remonte par la suite lorsqu'elle est allégée grâce à l'érosion des reliefs.

Outre la formation et l'érosion des chaînes de montagnes qui se produisent sur des échelles de temps non visibles à l'échelle humaine, les déformations isostatiques sont essentiellement liées aux avancées et reculs des calottes glaciaires. Dans ce cas, on parle de rebond post-glaciaire, ou réajustement glacio-isostatique. Il se définit comme le soulèvement de masses terrestres consécutif à la déglaciation des calottes polaires ou à la fonte des glaciers (Figure 1.3). Cette fonte est parfois, à certains endroits du globe, très rapide et peut donc induire de forts déséquilibres qui génèrent des déformations visibles à l'échelle humaine.

Ces déformations sont introduites ici seulement dans le but de les présenter brièvement au lecteur, car elles peuvent jouer un rôle majeur dans certaines parties du globe, mais sont absentes dans la zone qui sera étudiée dans ce manuscrit.

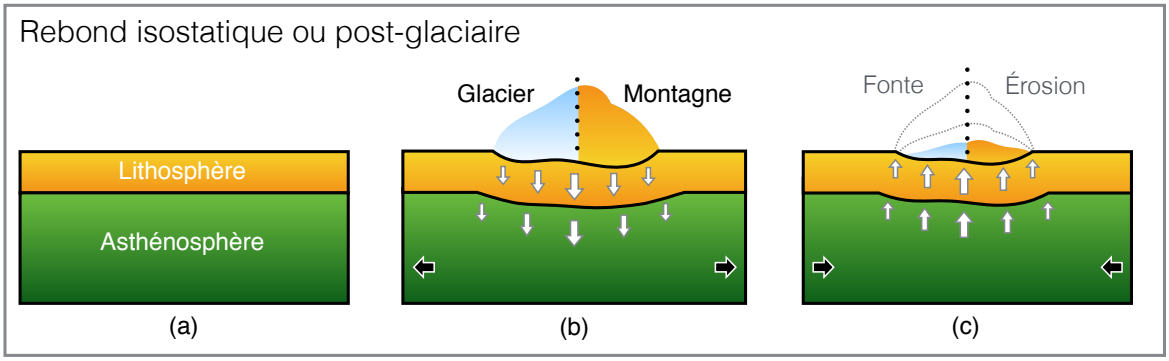

FIGURE 1.3 – Schémas simplifiés des déformations dues au rebond isostatique. Les cas de l'érosion d'un massif montagneux ou de la fonte glaciaire sont équivalents. (a) Isostasie : la lithosphère repose sur l'asthénosphère en équilibre. (b) Déséquilibre isostatique dû à la surcharge rocheuse ou glaciaire, qui induit l'enfoncement de la lithosphère jusqu'à obtention d'un nouvel équilibre. (c) Rebond isostatique : nouveau déséquilibre lié à la disparition de la surcharge. La lithosphère remonte lentement pour retrouver un état d'équilibre.

1.2.3 Les déformations tectoniques

La tectonique des plaques

La théorie de la *tectonique des plaques* à proprement parler est apparue au début des années 1960 grâce à la contribution du professeur de géologie Henri Hess. Cette théorie propose que la couche la plus superficielle de la Terre est fragmentée en grandes unités rigides de roches solides, appelées plaques, qui se déplacent les unes par rapport aux autres et reposent sur un matériel plus chaud et plus mobile.

Avant la tectonique des plaques, l'idée que les continents actuels étaient des fragments d'une plus grande masse continentale ('super-continent') était déjà présente. Dès le 16e siècle, avec la confection des cartes mondiales, les géographes pensaient que les continents n'avaient pas toujours été fixés dans leur position actuelle. Mais ce n'est qu'en 1912 que l'idée de continents en mouvement a été sérieusement considérée par la communauté scientifique, avec la publication de deux articles du météorologue Alfred Wegener qui y introduit la théorie de la *dérive des continents*. Wegener apporte des éléments géologiques aux observations géographiques, tels que la continuité de grandes chaînes de montagne ou de cratons, l'existence de fossiles communs ainsi que des traces de glaciations sur des continents très éloignés actuellement (Figure 1.4). Cette théorie a été longuement et vivement débattue avant de finalement être largement discréditée.

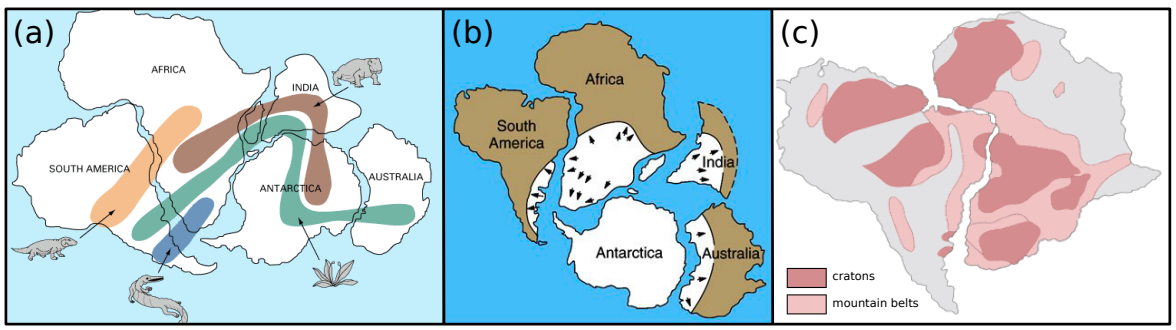

FIGURE 1.4 – Schémas simplifiés des différents arguments de Wegener appuyant la théorie de la dérive des continents. (a) Présence de fossiles communs sur différents continents. (b) Traces de glaciation. (c) Continuité de cratons ou grandes chaînes de montagnes. Modifié d'après Kious and Tilling [1996].

Certains physiciens s'y intéressent tout de même, comme Arthus Holmes, qui propose un lien entre le mouvement des continents et l'évacuation de la chaleur interne de la Terre dès les années

30 (Figure 1.5). Mais il faut attendre le début des années 50, avec l'arrivée de nouvelles preuves scientifiques, pour relancer le débat dans la communauté scientifique.

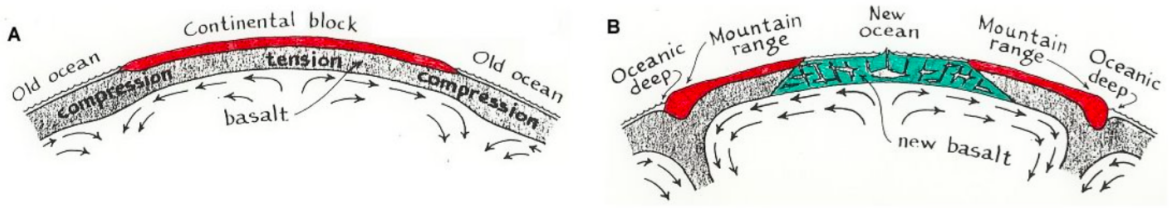

FIGURE 1.5 – Le modèle d'Holmes. Les mouvements des continents sont liés à l'évacuation de la chaleur interne de la Terre par convection. Du magma remonte du manteau vers la surface et forme le fond des océans en se refroidissant. Modifié d'après Holmes [1948].

Quatre avancées scientifiques majeures, grâce à l'exploration des océans, ont en particulier incité la formulation de la théorie des plaques tectoniques [Kious and Tilling, 1996] :

1. les forts reliefs accidentés et l'âge relativement jeune du plancher océanique ;
2. l'émergence de l'hypothèse d'un tapis roulant du plancher océanique, associé au recyclage de la croûte océanique ;
3. la mise en évidence d'inversions répétées du champ magnétique terrestre dans le passé ;
4. la concentration des séismes mondiaux et des activités volcaniques le long des fosses océaniques et des chaînes de montagnes submergées.

Hess croyait en beaucoup des observations faites par Wegener et défendait sa théorie de dérive des continents. Avec l'apparition de ces éléments scientifiques nouveaux, il publie un article intitulé 'The History of Ocean Basins' en 1962 [Hess, 1962] dans lequel il développe le fonctionnement du plancher océanique. Selon lui, des roches en fusion (magma) remontent de l'intérieur de la Terre au niveau des rides océaniques et s'écoulent en surface, donnant naissance à du nouveau plancher océanique qui s'étale et pousse le plancher existant loin des crêtes actives, pour finalement éventuellement sombrer dans les fosses profondes.

Aujourd'hui, nous savons que les plaques lithosphériques se déplacent de quelques centimètres par an dans des directions différentes, et ce grâce premièrement aux mesures d'anomalies magnétiques, puis aux mesures plus précises des GPS et satellites. Cette dynamique provient des mouvements de convection mantellique, mécanisme permettant à la Terre de dissiper sa chaleur interne vers la surface. Les mouvements relatifs des plaques entre elles entraînent la formation de zones de convergence, de divergence ou de coulissage (Figure 1.6). Ce sont au niveau de ces frontières de plaques que se produisent la très grande majorité des séismes mondiaux (Figure 1.7).

Ces séismes se produisent le long de plans de failles qui sont regroupées en trois types : les failles inverses, les failles normales et les failles décrochantes ou transformantes (Figure 1.8).

Le cycle sismique

Les propriétés frictionnelles au niveau des interfaces de plaques, ou à plus petite échelle au niveau d'une faille, entraînent un comportement cyclique des ruptures sismiques, sans forcément de périodicité identifiable. C'est ce que l'on appelle le cycle sismique. Les principales phases de ce cycle (Figure 1.9) sont :

— un état initial de référence,

— un chargement intersismique,

— une phase co-sismique.

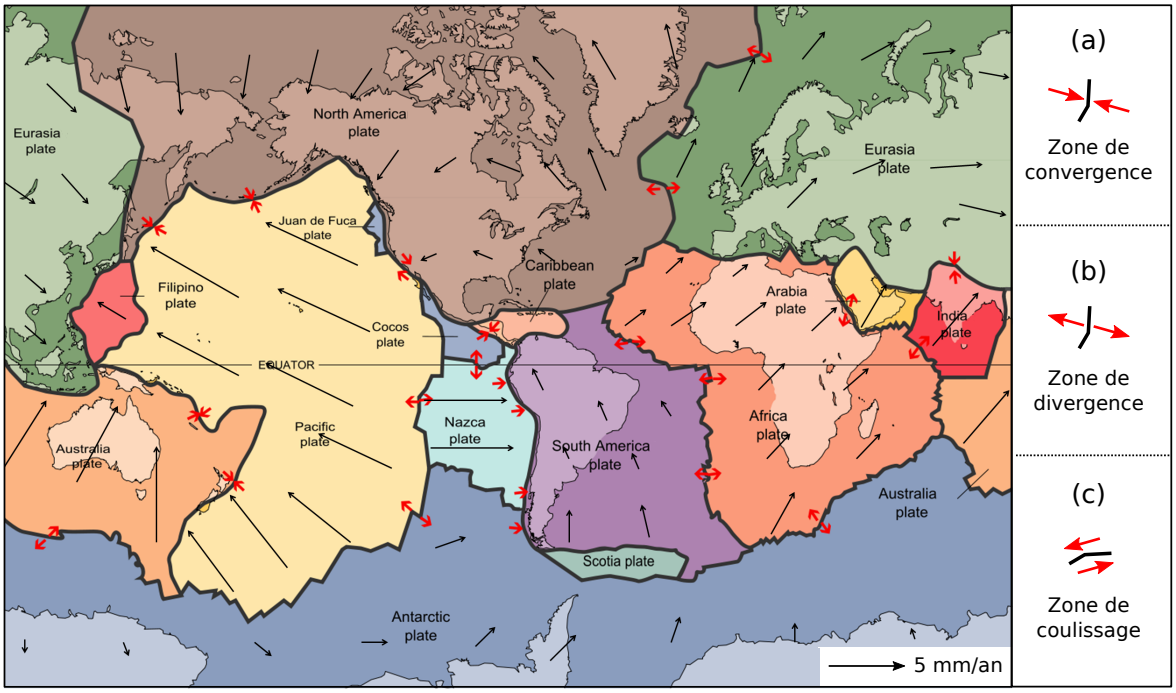

FIGURE 1.6 – Schéma simplifié des différentes frontières de plaques tectoniques et leurs mouvements respectifs. (a) Zone de convergence : les deux plaques se rapprochent l'une de l'autre et s'affrontent. (b) Zone de divergence : les deux plaques s'éloignent l'une de l'autre. (c) Zone de coulissage : les deux plaques coulissent l'une par rapport à l'autre. Carte des plaques tectoniques d'après un document de l'USGS (United States Geological Survey), 2001.

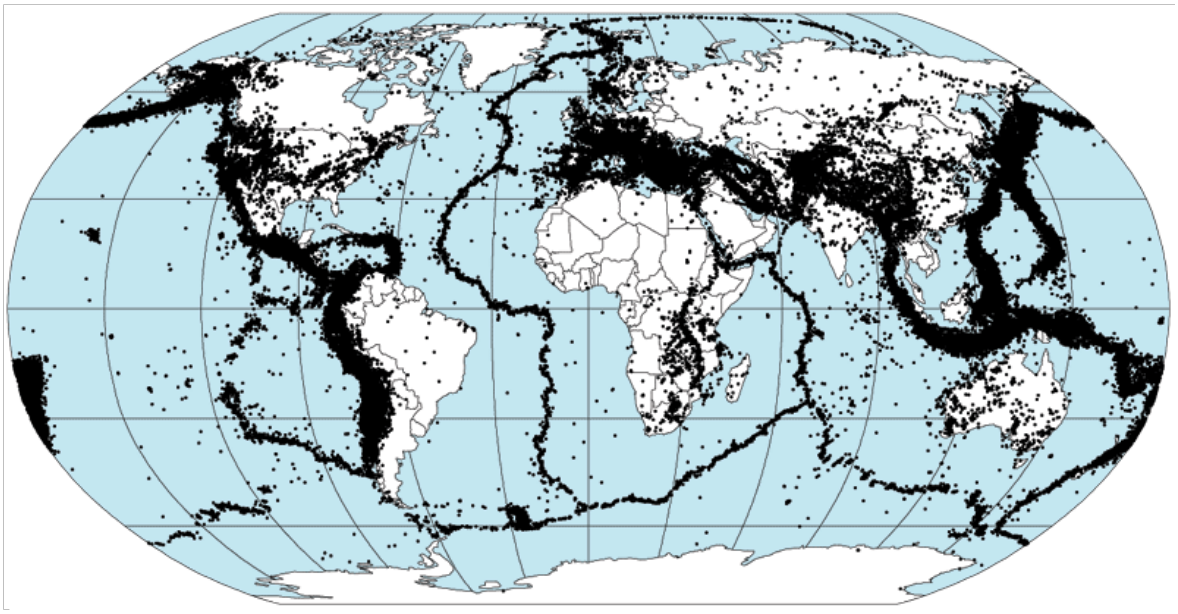

FIGURE 1.7 – Répartition mondiale des séismes. Les points noirs correspondent aux épicentres de plus de 350 000 séismes de magnitude M > 3.5 enregistrés entre 1963 et 1998. Les principales zones de sismicité décrivent les frontières de plaques. Document de la NASA réalisé à partir des catalogues de sismicité régionale et mondiale du NOAA's National Geophysical Data Center et USGS's National Earthquake Information Center.

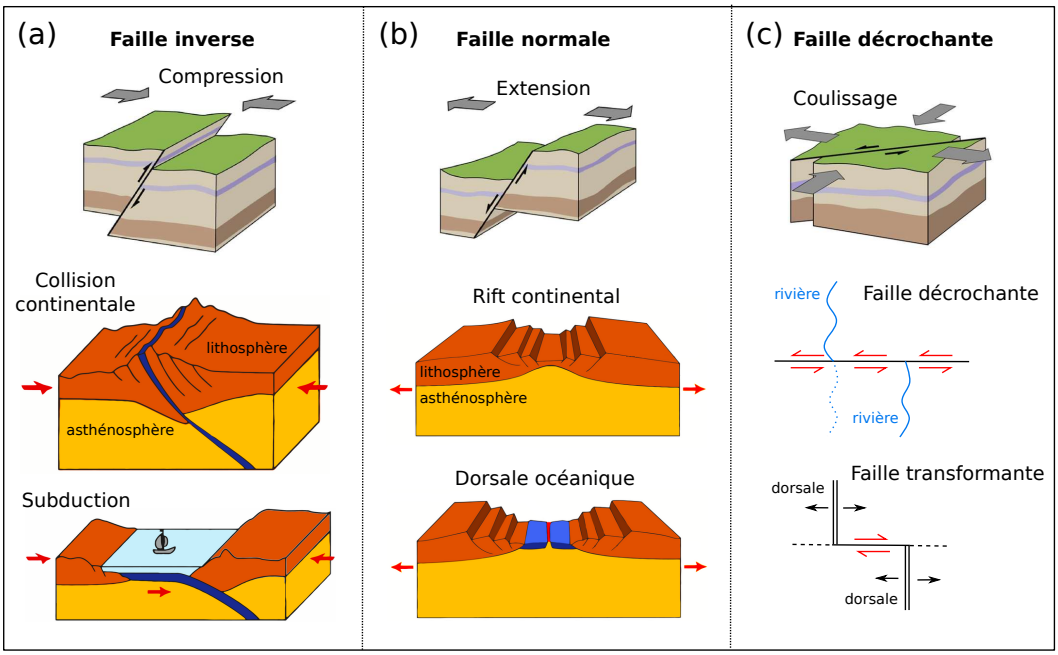

FIGURE 1.8 – Schémas simplifiés des différents types de failles et de leur contexte tectonique. (a) Les failles inverses s'observent en régime compressif, dans des contextes de collision continentale (deux plaques continentales s'affrontent) ou de subduction (une plaque océanique s'enfonce sous une autre plaque continentale ou océanique). (b) Les failles normales se développent en régime extensif, dans des contextes de rift continental ou de dorsale océanique. (c) Les failles décrochantes sont présentes à la frontière de plaques qui coulissent l'une par rapport à l'autre, comme la célèbre faille de San Andreas en Californie, ou dans le cas des failles dites transformantes, au niveau des dorsales océaniques.

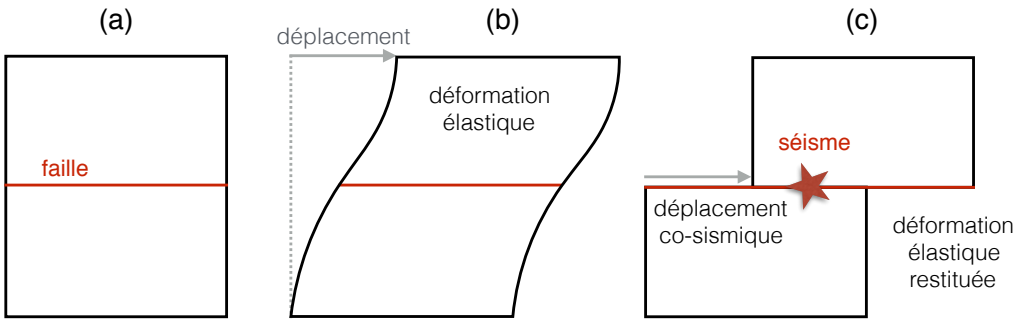

FIGURE 1.9 – Les phases du cycle sismique. (a) Stade initial. (b) Chargement intersismique. (c) Glissement co-sismique.

Pendant la phase intersismique, les contraintes s'accumulent le long du plan de faille. Cette accumulation peut durer de quelques dizaines à des centaines d'années. Elle entraîne une déformation élastique des blocs rocheux de part et d'autre de la faille.

Quand les contraintes accumulées deviennent trop grandes et dépassent le seuil de rupture des roches, une instabilité est créée et le séisme déclenché. Cette instabilité est précédée par une phase de nucléation ou d'initiation du séisme qui reste encore assez mal comprise aujourd'hui. La phase co-sismique est très courte à l'échelle du cycle sismique car elle ne dure que de quelques secondes à quelques minutes. C'est pendant cette phase que les contraintes sont relâchées et que le déficit de glissement accumulé est rattrapé.

Dans le modèle de cycle sismique, l'accumulation des déformations est supposée se faire de manière constante. Par conséquent, connaissant le taux de chargement et le seuil de rupture de la faille étudiée, il serait possible de prévoir le prochain séisme. Plusieurs types de modèles prédictifs sont présentés dans la Figure 1.10. Ces modèles sont des outils intéressants pour la prévision des séismes et sont donc utiles pour implémenter des modèles d'aléa sismique dans une zone donnée. Cependant, les observations récentes, notamment depuis l'existence des GPS continus, montrent que le comportement des failles est en réalité bien plus complexe que ces simples modèles.

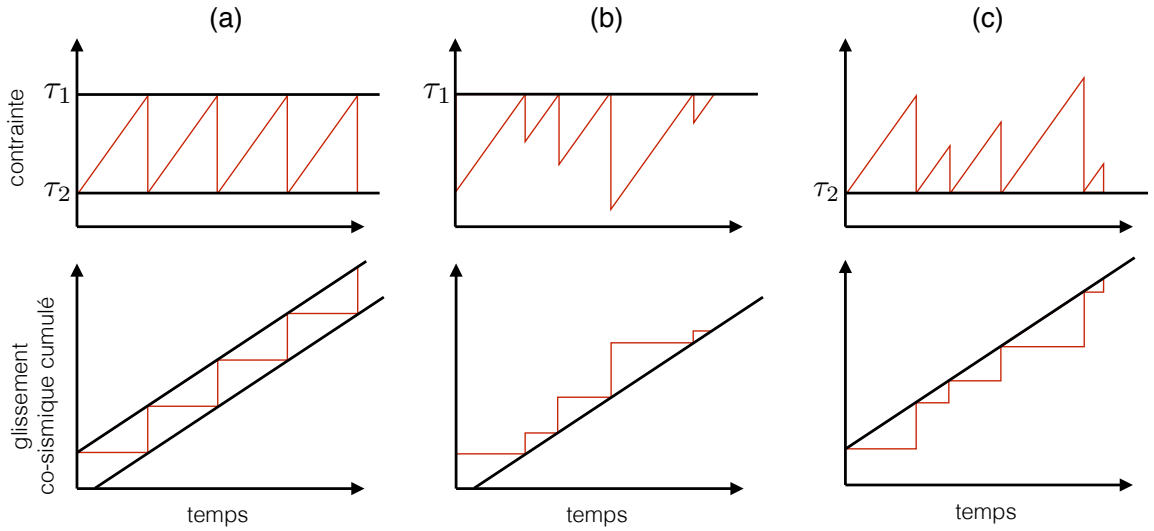

FIGURE 1.10 – Différents modèles de cycles sismiques : évolution temporelle des déplacements et des contraintes au cours du cycle sismique. (a) Modèle périodique. La contrainte seuil (τ_1) et la chute de contrainte ($\tau_1 - \tau_2$) sont constantes (la faille relâche systématiquement la même quantité d'énergie. Dans ce cas, la date et la magnitude du prochain séisme sont prédictibles. (b) Modèle de temps prédictible. La contrainte seuil est constante mais la chute de contrainte est variable. Dans ce cas, la date du prochain séisme est prédictible mais pas sa magnitude qui dépend de la chute de contrainte. (c) Modèle de glissement prédictible. La contrainte seuil est variable, mais la contrainte minimale (τ_2) est constante. Dans ce cas, la date du prochain séisme n'est pas prédictible car on ne connaît pas la contrainte maximale à partir de laquelle la faille va rompre, mais la magnitude est prévisible en fonction de la date hypothétique du séisme. Plus le séisme se déclenchera tardivement, plus la chute de contrainte sera grande et plus sa magnitude sera élevée. Modifié d'après Shimazaki and Nakata [1980].

1.3 Les témoins des forçages transitoires

Depuis une quinzaine d'années, il apparaît de plus en plus clairement que la mécanique des failles sismogènes ne se limite pas à un cycle sismique idéal avec une phase de chargement tectonique régulier et lent suivi par une relaxation sismique quasi-instantanée. De nombreuses instabilités sont observées dans les régions tectoniquement actives :

— des séismes lents,

— des trémors tectoniques,

— des essaims de microséismes,

— des cascades de séismes.

Ces évènements sont en réalité les témoins de processus transitoires cachés et révèlent l'existence de couplages entre les déformations lentes et rapides.

1.3.1 Les *Slow Slip Events*

Les évènements sismiques lents ou *Slow Slip Events* (SSEs) correspondent à des glissements se faisant à des vitesses de déformation intermédiaires entre le chargement tectonique et la rupture sismique. Les séismes génèrent des ondes sismiques par le glissement rapide de deux blocs rocheux l'un contre l'autre. Or parfois, certains glissement ne se produisent pas de manière rapide comme pour un séisme, mais de manière lente, avec ou sans génération d'ondes sismiques détectables par les instruments de mesure. On distingue donc ici :

— les séismes lents (à vitesses de rupture lentes),

— les glissements asismiques.

Les séismes lents ou *slow earthquakes*

Les séismes lents ou plutôt le terme anglais *slow earthquakes* fait référence aux séismes à vitesses de rupture lentes (quelques dizaines de mètres par seconde) et qui émettent des ondes sismiques détectables. Le séisme tsunamigène du Nicaragua 1992 [Kanamori and Kikuchi, 1993] et les séismes suivant le séisme majeur de Izu-Oshima au Japon [Sacks et al., 1982] en sont des exemples.

Ces évènements ne doivent pas être confondus avec les *silent earthquakes*, qui eux durent beaucoup plus longtemps, de quelques jours à quelques années, et ne libèrent pas d'énergie sous forme de radiation sismique détectable. Dans ce manuscrit, nous nous intéresserons uniquement à ce dernier type d'évènements que nous appelons glissements asismiques, mais qui sont également couramment dénommés séismes lents dans la littérature, ou en anglais *slow slip events, SSEs* ou encore *creep events*, même si une ambiguïté est présente. C'est pourquoi, dans la suite du manuscrit, les termes de glissement asismique, glissement lent ou séisme lent désigneront systématiquement des évènements sans émissions d'ondes sismiques détectables.

Les glissements asismiques ou *silent earthquakes*

Les glissements asismiques sont des glissements ne produisant pas d'ondes sismiques détectables mais générant des déformations parfois très importantes étalées sur des périodes de temps de plusieurs jours à plusieurs mois. Il a été mis en évidence par l'observation du déficit de glissement accumulé, généré par les séismes au cours du temps en comparaison avec le taux de glissement moyen des plaques ou blocs tectoniques mesuré à l'aide de GPS. De la même manière, les mesures

géodésiques de déformation réalisées après un grand séisme montrent des valeurs de glissement bien supérieures aux glissements sismiques générés par les répliques ou *aftershocks*. Afin de compléter le bilan du glissement total sur la faille, il est nécessaire d'ajouter ce glissement lent dit asismique qui n'est pas observé via les capteurs sismiques.

Des glissements lents ont été observés majoritairement dans les zones de subduction, après l'occurrence du séisme majeur. On parle alors de glissements post-sismiques, qui ont été mis en évidence à la fois sous la zone de rupture co-sismique [e.g. Heki et al., 1997; Melbourne et al., 2002; Yagi et al., 2003] dans la zone de transition, mais également à des profondeurs comparables à celle de la zone sismogène [e.g. Chlieh et al., 2007; Hsu et al., 2006; Perfettini et al., 2010]. Les zones de glissement co-sismique et post-sismique sont souvent adjacentes et complémentaires [e.g. Miyazaki et al., 2004; Perfettini et al., 2010].

Les séries temporelles obtenues par les GPS permanents, ainsi que le développement des outils de mesures tels que l'interférométrie radar, ou l'installation de nouveaux capteurs de déplacements (*creepmeters*, *strainmeters*, *tiltmeters*, etc.) ont permis de mettre en évidence des glissements asismiques transitoires, qui se produisent à priori indépendamment des ruptures sismiques. Les premières observations de ces glissements transitoires, sans relation apparente avec des séismes, ont été réalisées sur la faille de San Andreas en Californie [Linde et al., 1996] grâce à des *strainmeters*. Ces instruments sont généralement installés dans des forages pour diminuer les bruits de surface et sont extrêmement sensibles. Ils permettent de surveiller en continu les modifications de contraintes crustales proches de failles actives ou de volcans. Les évènements lents détectés étaient superficiels, à moins de 8 km de profondeur, et avaient une magnitude de moment cumulée de $M_W = 4.8$.

Avec le développement des réseaux de GPS continus, des glissements lents transitoires ont aussi été observés dans la majorité des zones de subduction. Hirose et al. [1999] a notamment découvert des anomalies dans les séries GPS dans la région de Bungo Channel, au Japon et a modélisé ces données le long de l'interface de subduction comme un SSE d'une durée de 300 jours et de $M_W = 6.6$. Des observations ont été rapportées dans la zone de subduction de Nankai, au Japon [Ozawa et al., 2001], dans la région des Cascades, au nord des États-Unis [Dragert et al., 2001], dans la zone de subduction de Guerrero, au sud du Mexique [Kostoglodov et al., 2003], en Alaska [Ohta et al., 2006], en Nouvelle-Zélande [Douglas et al., 2005] et au Costa Rica [Protti et al., 2004].

Récemment, des observations de glissements transitoires de plus faible intensité ont également été effectuées dans des régions continentales. C'est notamment le cas dans le rift de Corinthe où un signal anormal durant une heure a été détecté grâce à des inclinomètres et dilatomètres en 2002 [Bernard et al., 2004]. Le maximum de cette anomalie apparaît, à quelques secondes près, en même temps qu'un séisme de magnitude $M = 3.7$ (le plus fort dans la région dans la période observée) et suggère l'occurrence d'un glissement lent de magnitude de moment $M_W = 5$ équivalente.

1.3.2 Les trémors tectoniques

Les trémors sont des évènements sismiques de faible amplitude, de longue durée (de quelques minutes à quelques heures) dont les ondes de volumes ne montrent pas de phase impulsive. Leur contenu fréquentiel se situe principalement entre 1 et 10 Hz. Ils ont été identifiés et découverts en premier lieu dans les régions volcaniques comme étant engendrés par la remontée du magma dans les conduits du volcan, lors d'une éruption. Obara [2002] a cependant découvert des trémors dans des régions non volcaniques et Rogers and Dragert [2003] ont montré que ces trémors tectoniques sont associés à des glissements lents (Figure 1.11). D'après Ide et al. [2007], les trémors non volcaniques peuvent être considérés comme faisant partie de la famille des SSEs.

Actuellement, ces trémors ont été détectés dans la plupart des zones de subduction et leur association avec des glissements lents est plus ou moins claire suivant les régions. Les plus beaux

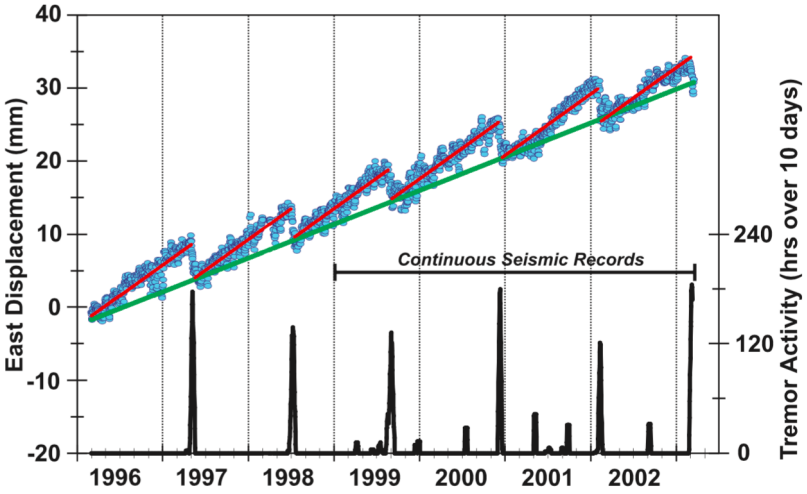

FIGURE 1.11 – Glissements lents et trémors dans la zone de subduction des Cascades, aux USA. Les cercles bleus représentent la variation journalière du déplacement du GPS du site ALBH (Victoria) par rapport au GPS du site de Penticton, supposé fixe par rapport à la plaque américaine. La ligne verte indique le déplacement à long terme (phase intersismique). Les lignes rouges indiquent les déplacements entre deux évènements de glissement lent, qui sont marqués par une inversion du glissement tous les 13 à 16 mois. Les périodes d'activité des trémors sont représentées par la courbe noire. Ils durent une dizaine de jours et correspondent aux durées et à l'occurrence des glissements lents. D'après Rogers and Dragert [2003].

exemples de corrélations spatiale et temporelle entre les zones de glissement lent et les zones de trémors tectoniques sont au Japon (Nankai) et dans les Cascades, mais cette corrélation est absente au Mexique et au Costa Rica [Beroza and Ide, 2011]. Les connaissances actuelles ne permettent pas de savoir si ces variations apparentes reflètent des disparités de fonctionnement entre ces zones de subduction, ou si des différences dans les outils de détection et les techniques de localisation de ces trémors sont à incriminer.

1.3.3 Les essaims de microséismes

Les essaims de séismes sont des séquences prolongées d'activité sismique dont l'évènement de plus forte magnitude n'apparaît pas forcément au début de la séquence. Les essaims ne suivent pas une organisation typique 'choc principal - secousses secondaires' (ou séquence *mainshock-aftershocks*) avec une décroissance en loi d'Omori [e.g. Omori, 1894; Utsu et al., 1995], qui est classique dans les régions tectoniquement actives. Ils s'organisent de manière plus aléatoire et souvent aucun pattern en temps-magnitude n'est identifiable (Figure 1.12).

Les essaims de microséismes sont des activités transitoires communes, déclenchés soit (1) par des interactions mécaniques directes entre les évènements de par les changements de contrainte statique et/ou dynamique (voir Section 1.4), soit (2) par des forçages qui accroissent les contraintes et/ou réduisent les forces de frottements le long de failles sismogéniques [e.g. Vidale and Shearer, 2006]. Ces derniers processus peuvent être des glissements lents asismiques, des intrusions magmatiques, et/ou des variations de pression de pore.

Les déformations transitoires sont mesurables et souvent analysées via la géodésie. Cependant, la résolution obtenue par inversion de données GPS est limitée, et la méconnaissance des structures en profondeur complique encore plus la situation. Une alternative est alors d'analyser les occurrences de petits séismes résiduels ou microséismes liés à ces processus transitoires externes. Effectivement, les microséismes sont une donnée abondante dans un très grand nombre de sites d'étude différents. Dans ce cas, les chercheurs analysent souvent les évolutions spatio-temporelles des essaims, ainsi que les caractéristiques propres aux sources des microséismes. Ces tout petits

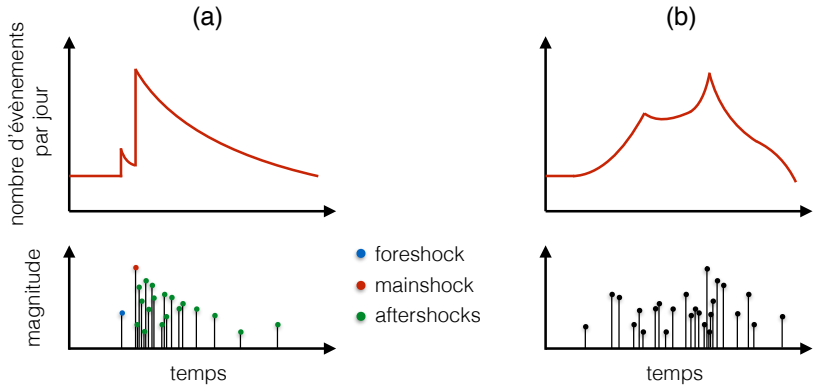

FIGURE 1.12 – Différentes séquences temporelles de séismes. (a) Séquence typique 'séisme principal (mainshock) - secousses secondaires (aftershocks)', avec ou non présence d'évènements précurseurs (foreshocks). (b) Organisation d'un essaim de microséismes. Aucun pattern particulier n'est identifiable. Les évènements de forte magnitude sont placés aléatoirement au sein de la séquence.

séismes étant plus difficilement identifiables et localisables que les gros, du fait de leur faible rapport signal sur bruit dans les données, la ressemblance des formes d'ondes des microséismes est souvent utilisée afin de les détecter, déterminer leur position relative précise, et les regrouper en familles pour mieux quantifier leurs propriétés et connaître leur relation avec les structures actives.

Les multiplets

Les multiplets désignent des familles d'évènements sismiques proches spatialement, qui se développent sur des plans de failles parallèles, coplanaires ou non, et montrent des mécanismes au foyer identiques. Du fait de la proximité des sources et du même mécanisme de rupture, les ondes générées par ces évènements à la source sont semblables et traversent quasiment les mêmes milieux jusqu'aux différentes stations. Ces groupes de séismes présentent alors des formes d'ondes similaires (Figure 1.13.a) enregistrées à chaque capteur sismique, qui sont facilement reconnaissables dans les séries temporelles [Poupinet et al., 1984]. Cependant, elles peuvent parfois présenter quelques différences à plus hautes fréquences et correspondre à des évènements de magnitude assez différente donnant des rapports signal-sur-bruit variables. Parmi les évènements des multiplets, certains présentent au contraire des formes d'ondes quasiment strictement identiques, quantifiés en corrélation. Dans ce cas, on parle de repeaters (Figure 1.13.b).

Les repeaters

Les repeaters sont une famille de microséismes plus restreints que les multiplets. Ils ont la particularité supplémentaire d'être composés d'évènements sismiques qui cassent la même aspérité ou des aspérités qui se chevauchent [Nadeau and McEvilly, 1999]. Leur nom provient de leur caractère répétitif avec des intervalles de temps plus ou moins réguliers selon les cas [Chen et al., 2007; Vidale et al., 1994].

Intérêt des multiplets et repeaters

Ces évènements similaires sont de véritables indices pour une meilleure compréhension des mécanismes de déformation environnants. Leur analyse permet d'imager finement les structures actives, en révélant parfois des déformations transitoires cachées, qui n'ont pu être mesurées directement par des capteurs de déformation, soit par absence d'instruments sur le site, soit par invisibilité du phénomène dans les données géodésiques.

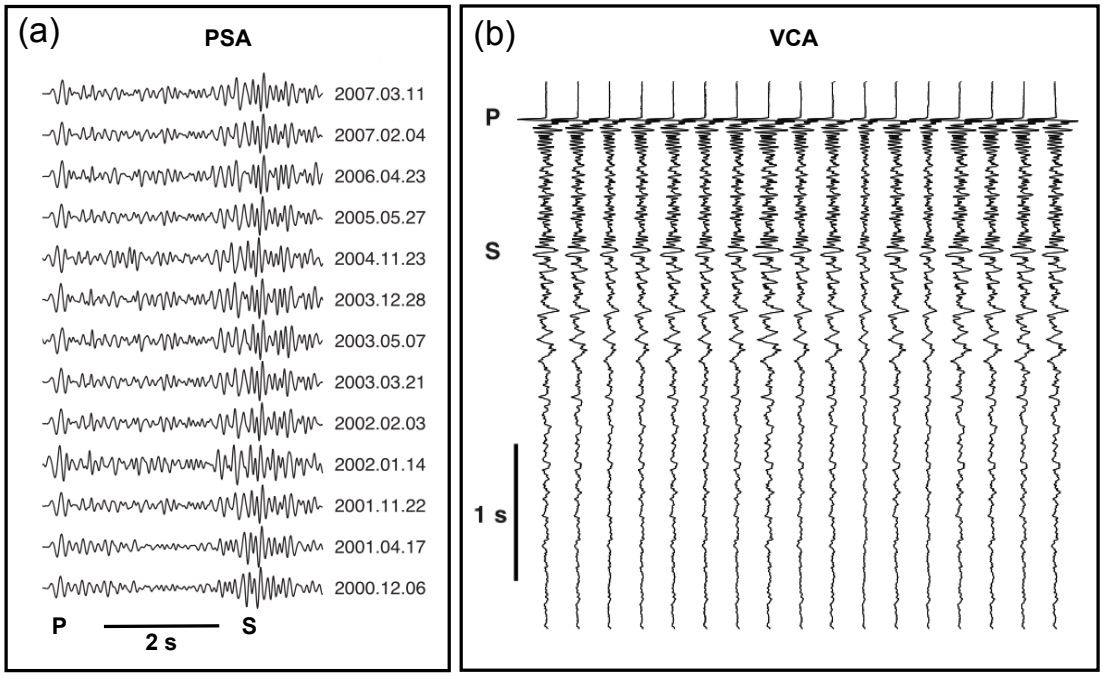

FIGURE 1.13 – Un exemple de multiplet (a) et de repeater (b). (a) Les formes d'ondes des évènements du multiplet ont été enregistrées dans le rift de Corinthe, à la station PSA, sur la composante verticale et filtrées entre 3 et 20 Hz. Les coefficients de corrélation des formes d'ondes sont supérieurs à 0.85. Modifié d'après Lambotte et al. [2014]. (b) Les formes d'ondes des évènements du repeater ont été enregistrées sur le segment de Parkfield de la faille de San Andreas, en Californie, à la station VCA, sur la composante verticale. Les coefficients de corrélation des formes d'ondes sont supérieurs à 0.98. Modifié d'après Nadeau and McEvilly [1999].

Sur le segment de Parkfield de la faille de San Andreas, par exemple, Niu et al. [2003] ont analysé la variabilité temporelle de sismogrammes de repeaters, pour mettre en évidence un changement structural qui coïncide avec un glissement transitoire asismique bien documenté de la région. Dans ce cas, l'activité microsismique, en plus de permettre l'analyse précise du glissement asismique sous-jacent, peut révéler des modifications structurales de la croûte telles que ses propriétés de fracturation ou son organisation des fractures.

L'identification et l'analyse de multiplets au site géothermal de Soultz réalisées par Bourouis and Bernard [2007] ont fourni des images précises de la géométrie et de la cinématique des patchs de glissement asismique, et indirectement, des changements de pression de pore liés aux injections d'eau. Ces observations contribuent à une meilleure connaissance des couplages entre circulation de fluides, glissement lent transitoire et activité microsismique dans les régions sismogéniques.

La microsismicité induite par des injections de fluide ou activités de production de ressources énergétiques, telles que la fracturation hydraulique, la réinjection de fluides usagés de forage ou les activités géothermales, est devenue un sujet phare des discussions politiques et scientifiques ces dernières années. En effet, plusieurs séismes parmi les plus forts recensés à l'intérieur du continent nord-américain semblent associés à l'activité des puits [e.g. Keranen et al., 2013; McGarr et al., 2015]. Le plus fort de ces évènements, un séisme de magnitude M = 5.6, s'est produit en Oklahoma, causant de nombreux dégâts matériels et blessant 2 personnes [Ellsworth, 2013]. Nous revenons sur cet aspect de déclenchement par les fluides dans la Section 1.4.3.

1.4 Les contraintes et déclenchements de séismes

1.4.1 Les contraintes sismiques

Une contrainte est une force par unité de surface. En sismologie, la surface sur laquelle s'applique une contrainte est la surface de la faille ou du plan de rupture. On distingue habituellement la contrainte normale au plan de faille σ_n de la contrainte cisaillante τ qui est la contrainte tangentielle au plan de faille.

Un séisme étant un glissement sur un plan de faille, il provoque un changement des contraintes dans le milieu avoisinant, qui est particulièrement complexe et intense aux extrémités du plan de glissement [Chinnery, 1963]. Ces changements de contraintes peuvent jouer un rôle très important dans la propagation de la rupture [e.g. Atkinson, 1965; Chinnery, 1963] ou dans l'occurrence de séismes naturels secondaires [Rybicki, 1973; Smith and Van de Lindt, 1969], également appelés répliques. Vers la fin des années 1970, plusieurs études comme celles de Das and Scholz [1981]; Stein and Lisowski [1983]; Yamashina [1978] ont montré que des répliques étaient localisées dans des zones où les contraintes ont augmenté après une rupture principale. Les premières interactions séisme-séisme avec un choc principal suivi par des répliques (séquence appelée *mainshock–aftershocks*, Figure 1.12.a) ont été mises en évidence dès la fin du 19^{e} siècle par Omori [1894]. Ces mécanismes d'interactions expliquent de mieux en mieux la localisation et le temps d'occurrence des séismes observés dans certaines régions du monde, alors que la distribution spatio-temporelle des séismes était auparavant comparée à un comportement poissonien (répartition aléatoire) [Knopoff, 1964] ou contrôlée par le cycle sismique [Shimazaki and Nakata, 1980]. L'ensemble de ces études et des modèles proposés pour expliquer l'occurrence de séismes sont autant d'outils permettant d'améliorer les estimations d'aléa sismique dans une région donnée.

Les contraintes générées par un séisme sont généralement classées en deux catégories :

— les contraintes statiques,

— les contraintes dynamiques.

Contraintes statiques

Les contraintes statiques représentent l'état de contrainte permanent d'une zone donnée. Un changement de contraintes statiques est une modification permanente de cet état qui dépend uniquement du déplacement co-sismique de la faille. Lors d'un séisme, les contraintes sont relâchées le long du plan de faille, et transférées en dehors de la zone de rupture [Chinnery, 1963; Das and Scholz, 1981], principalement aux extrémités de la fracture. Les variations spatiales de contraintes statiques décroissent très rapidement en Δ^{-3} avec Δ la distance épicentrale [Hill and Prejean, 2015]. Par conséquent, le potentiel de déclenchement statique est concentré en champ proche, typiquement à quelques longueurs de faille, rayon où se localisent les répliques.

Plusieurs études de séquences de tremblements de terre ayant lieu sur un même système de failles ont montré que l'occurrence d'un séisme est souvent contrôlé par les changements de contraintes provoqués par un évènement antérieur. C'est par exemple le cas sur la Faille Nord Anatolienne, en Turquie, où une migration de la sismicité par transfert de contraintes statiques a été observée suite au séisme d'Izmit de 1999 [Stein et al., 1997]. L'augmentation des contraintes statiques proches d'un plan de faille va avancer le temps d'occurrence de la rupture. Afin d'évaluer si le temps d'occurrence d'un séisme s'est avancé ou au contraire éloigné par rapport au temps prédit par les modèles, les sismologues analysent généralement les variations de la contrainte de Coulomb.

Critère de Coulomb

Le critère de Coulomb est une représentation permettant de quantifier la capacité d'une faille à rompre lors d'une perturbation des contraintes. La valeur initiale du champ de contrainte dans la croûte est une valeur difficile à mesurer voire à estimer. C'est pourquoi les sismologues utilisent plutôt la variation de contrainte induite par l'occurrence d'un séisme comme mesure. La variation de la contrainte de Coulomb σ_c qui intègre les variations de contraintes parallèles et perpendiculaires au plan de faille, est un indicateur de l'évolution du comportement de la faille vers une rupture ou vers un état stable. Elle s'écrit :

$$\Delta\sigma_c = \Delta\tau - \mu(\Delta\sigma_n - \Delta p) \tag{1.1}$$

où τ est la contrainte cisaillante, σ_n est la contrainte normale (nous utilisons la convention $\Delta\sigma_n > 0$ pour une compression), μ est le coefficient de friction de la faille et p est la pression de pore. En intégrant la pression de pore dans l'équation, l'effet des fluides environnants sur la rupture est pris en compte. Une augmentation de la contrainte de Coulomb (i.e. $\Delta\sigma_c > 0$) signifie que le potentiel de rupture de la faille considérée est augmenté. A l'inverse, une diminution de la contrainte de Coulomb (i.e. $\Delta\sigma_c < 0$) indique la faille s'éloigne de la rupture.

Contraintes dynamiques

Certaines études ont montré une augmentation brutale du taux de sismicité à des distances de plus de 1000 km à la suite du séisme de Landers en 1992 [e.g. Anderson et al., 1994; Hill et al., 1993]. À ces distances télésismiques, les variations des contraintes de Coulomb statiques sont trop faibles pour avoir déclenché ces évènements. Par conséquent, les sismologues se sont tournés vers l'analyse des contraintes dynamiques pour expliquer ces activations [Kilb et al., 2000].

Les contraintes dynamiques sont liées à la propagation des ondes sismiques générées par un tremblement de terre. Elles sont donc transitoires, passagères, et n'induisent aucune modification permanente de l'état de contrainte de la région traversée. De plus, leur amplitude décroit relativement lentement avec la distance, en $\sim \Delta^{-2}$ pour les ondes de volumes et en $\sim \Delta^{-3/2}$ pour les ondes de surface [Hill and Prejean, 2015].

1.4.2 Le déclenchement dynamique

Nous employons l'expression de déclenchement dynamique lorsqu'un lien de causalité existe entre l'apparition d'une réponse locale au passage d'ondes sismiques générées par un évènement éloigné [Hill and Prejean, 2015]. Cette réponse devrait être immédiate, du fait du caractère non permanent de la déformation, mais des délais d'activation sont parfois observés, variant généralement de quelques secondes à plusieurs heures [e.g. Brodsky et al., 2000; Gomberg et al., 2001]. Toute la difficulté ici réside dans la démonstration que les activités locales sont bel et bien provoquées par un séisme lointain et ne sont pas une coïncidence. Pour obtenir plus de la crédibilité, des tests de signification statistique du déclenchement dynamique ont été développés, dont le plus commun est la β–statistique de Matthews and Reasenberg [1988]. Cette statistique a notamment été intégrée dans le package *ZMAP* de Wiemer [2001] développé sous MATLAB™ et en libre d'accès. Ces tests sont indicatifs mais non suffisants pour prouver la causalité entre le passage d'une contrainte dynamique et l'initiation d'une activité locale [Hill and Prejean, 2015]. Ils permettent en revanche d'affiner la probabilité de la relation de cause à effet, en analysant notamment finement l'évolution spatio-temporelle de la sismicité de la région étudiée.

Les déclenchements dynamiques ont régulièrement été observés dans des zones volcaniques ou hydrothermales. C'est par exemple le cas des séismes de Landers en 1992 [Anderson et al., 1994;

Hill et al., 1993], de Hector Mine en 1999 [Gomberg et al., 2001], de Denali en 2002 [Husen et al., 2004; Prejean et al., 2004] ou encore de Tohoku-Oki en 2011 [Hirose et al., 2011; Miyazawa, 2011] qui ont activé plusieurs caldeira (Long Valley, Yellowstone, Hakone), et ont modifié le comportement de systèmes hydrothermaux/geysers.

Dans la plupart des études, les régions activées par du déclenchement dynamique sont associées à des régimes en extension [Hill and Prejean, 2015], même si les déclenchements dynamiques sont présents dans tous types d'environnements tectoniques [Velasco et al., 2008]. Les zones soumises à une tectonique extensive présentent des propriétés qui peuvent augmenter leur susceptibilité au déclenchement dynamique. Étant donné que les fractures en régime extensif ont tendance à se développer verticalement, les régions en extension facilitent la remontée de fluides crustaux profonds, sous haute pression, vers la surface [Hill and Prejean, 2015]. C'est d'ailleurs pour cette raison que les zones géothermales sont généralement localisées dans des régions en extension. De plus, la contrainte à dépasser pour déclencher une rupture sur une faille en régime extensif est plus faible que dans celle en compression, pour un coefficient de friction uniforme donné [Sibson, 1982]. Finalement, dans la partie superficielle de la croûte (jusqu'à 10 km de profondeur) les failles normales sont plus susceptibles de répondre aux contraintes dynamiques conduites par les ondes de surface (Rayleigh) que les failles inverses [Hill, 2012].

Nous avons vu que l'initiation d'une activité locale était parfois non parfaitement concomitante avec le passage des ondes. De plus, l'activité déclenchée ne s'arrête généralement pas à la fin du passage des ondes, mais peut persister plusieurs jours voire plusieurs semaines [e.g. Freed, 2005]. Des processus secondaires, initiés par les contraintes dynamiques, se produisent donc probablement afin d'expliquer les délais observés ainsi que la durée de l'activité déclenchée. Parmi les coupables potentiels, les fluides arrivent en première position, du fait de leur rôle sur les propriétés de friction au niveau du plan faille.

1.4.3 Les migrations de fluides

La circulation de fluides dans la croûte peut avoir une grande influence sur la naissance ou non de séismes à cause des variations de contraintes que ces fluides induisent (Équation 1.1). Effectivement, en augmentant la pression de pore, ils réduisent les contraintes normales effectives appliquées le long de structures pré-existantes, ce qui tend à empêcher la rupture cassante [Nur and Booker, 1972]. En diminuant la contrainte normale, la résistance au glissement en cisaillement sur le plan de faille est alors réduite, facilitant la rupture sismique ou asismique [Hubbert and Rubey, 1959]. Les fluides ont donc tendance à favoriser l'affaiblissement de la faille et donc le glissement sismique dans ce cas. Cependant, une chute de pression de pore peut au contraire stabiliser la faille et la bloquer, amenant parfois des périodes de quiescence sismique.

Shimojo et al. [2014] a par exemple mis en évidence que les fluides étaient moteur de séquences microsismiques, initialement déclenchées par un changement dynamique des contraintes reliées au passage des ondes de surface du séisme de Tohoku-oki (2001, M = 9.0). D'autres auteurs tels que Hainzl [2004]; Hainzl and Fischer [2002] ont pu observer différentes interactions au sein d'essaims sismiques en quantifiant les transferts de contraintes à partir de la migration de fluides et des déclenchements séisme-séisme. Brown et al. [2005] ont, quant à eux, regardé la corrélation entre des pulses transitoires de fluides et l'activité des trémors sismiques dans la zone de subduction du Costa Rica.

Les environnements les plus susceptibles de générer des séismes par des variations de pression de pore sont les zones en extension et les zones avec failles transformantes [Chen et al., 2012b; Vidale and Shearer, 2006]. Cependant, les milieux tectoniques en compression semblent favoriser les effets de valve ou *fault-valve behaviour* [Sibson, 1992] du fait que les pressions de fluides y sont souvent plus élevées que celles hydrostatiques pendant la déformation crustale. Lorsqu'une faille traverse deux réservoirs séparés par une couche imperméable, dont le premier surfacique est en

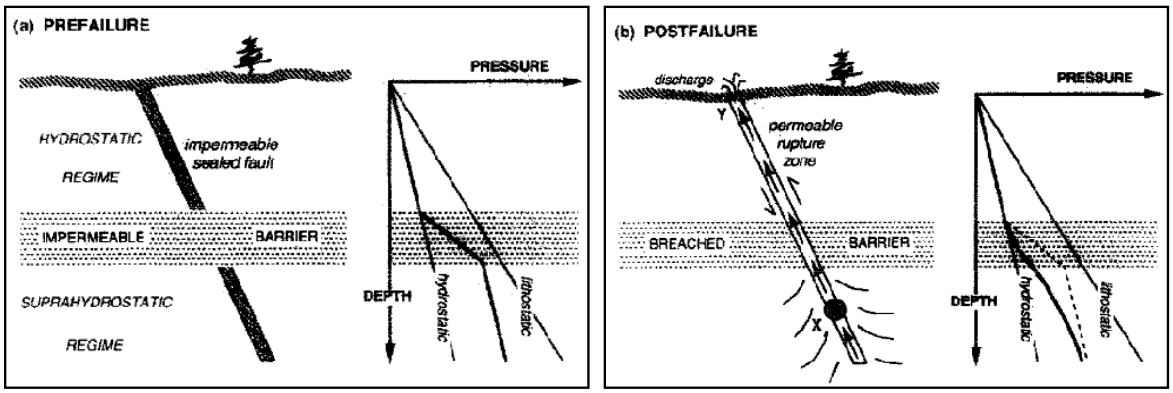

FIGURE 1.14 – Représentation schématique du phénomène d'effet de valve (*fault-valve*). Illustrations des gradients de pressions de fluides (a) pré- et (b) post-rupture, lorsqu'une déstabilisation du système permet de connecter, via le plan de faille, des réservoirs à des pressions différentes. D'après Sibson [1992].

équilibre hydrostatique mais le deuxième plus profond en surpression, une petite déstabilisation du système peut entraîner une rupture sismique, par ouverture du plan de faille originalement scellé et étanche (augmentation soudaine de la porosité) et rééquilibrage des pressions entre les deux réservoirs (Figure 1.14).

La question subsidiaire restante est : d'où proviennent ces fluides ? Plusieurs origines sont possibles :

— volcanique, par remontée du magma profond et chaud (moins dense) vers les réservoirs crustaux.

— tellurique, par infiltration des eaux de pluie dans la croûte.

— mantellique, par déshydratation de la plaque océanique plongeante, qui, avant de subducter, a stocké des quantités de fluides importantes et les libèrent au passage d'isothermes en s'enfouissant dans le manteau.

— anthropique, par extraction des ressources souterraines (eau, pétrole, gaz) ou injections de fluides (géothermie, fluides-déchets).

1.5 Problématiques et enjeux

Cette section rassemble les questions génériques que nous nous sommes posées afin d'aborder le sujet de thèse :

— Les instabilités transitoires ont-elles un rôle majeur dans le mécanisme de rupture des failles ?

— Quels sont les couplages entre les évènements sismiques et asismiques et comment les quantifier ?

— Quelle est la dépendance spatio-temporelle ou la probabilité de déclenchement des évènements sismiques forts par des processus transitoires ?

— Comment améliorer la prise en compte des évènements transitoires dans les modèles d'aléa sismique ?

Pour résumer, nous chercherons à identifier et mieux comprendre les interactions sismique-asismiques possibles (Figure 1.15) en prenant comme lieu d'étude le rift de Corinthe, site privilégié étudié depuis plus de 20 ans.

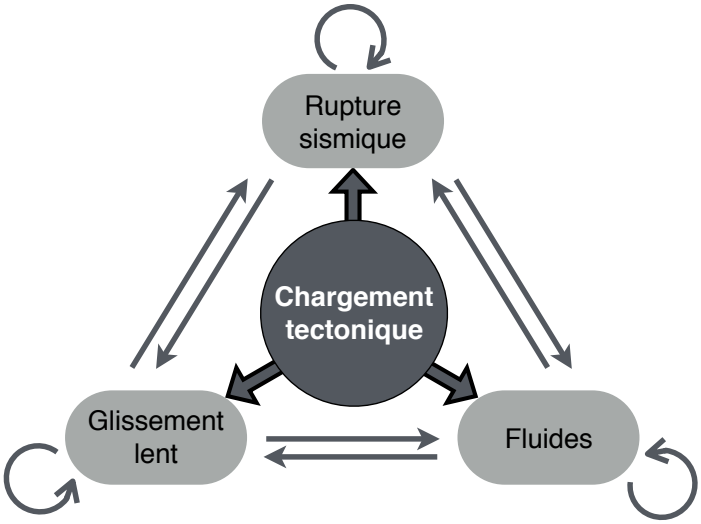

FIGURE 1.15 – Schéma des interactions sismique-asismiques. Les flèches représentent tous les couples possibles d'interactions. Le chargement tectonique est à l'origine des séismes, des glissements asismiques et peut modifier les pressions de pore dans la croûte terrestre. Une rupture sismique peut également déclencher des glissements lents, des migrations de fluide et générer d'autres ruptures sismiques. De la même manière, une circulation de fluide en profondeur peut faciliter la mise en place d'une rupture sismique ou asismique, ou provoquer des modifications de pression de pore dans des environnements voisins, etc.

Chapitre 2

Le rift de Corinthe

Sommaire

2.1 Introduction

Dans ce chapitre, nous présentons la région géographique étudiée, le rift de Corinthe. Nous commençons par expliquer les contextes géodynamique, géologique et tectonique avant de décrire la morphologie actuelle du rift et poursuivre sur les aspects sismiques. Nous présentons ensuite les réseaux (géodésique et sismologique) et les différents instruments qui ont commencé à être installés dans la région depuis plus d'une vingtaine d'années. Nous continuons avec l'organisation des bases de données mises à disposition. Enfin, nous définissons les motivations nous ayant conduits à étudier précisément cette région.

2.2 Contexte géodynamique, géologique et tectonique

2.2.1 Cadre géodynamique régional

Le golfe de Corinthe est un rift continental de la Méditerranée orientale, séparant la Grèce centrale du Péloponnèse. Il fait partie du domaine tectonique égéen, contrôlé par l'interaction de trois plaques principales : l'Eurasie, l'Afrique et l'Arabie, et une micro-plaque, la plaque Anatolienne [McKenzie, 1970]. Les processus majeurs impliqués sont la convergence des plaques Afrique et Arabie vers celle de l'Eurasie [Dercourt et al., 1986] et l'extrusion de la plaque Anatolienne (Figure 2.1). La plaque Afrique converge actuellement vers le domaine égéen à une vitesse atteignant 35 mm.an^{-1} [Nocquet, 2012], via la zone de subduction hellénique. L'initiation de la subduction s'est produite au Mésozoïque, vers 200 Ma et a provoqué la formation de la chaîne de montagnes des Hellénides [Ring et al., 2010]. Le rift de Corinthe est quant à lui l'expression la plus récente de la phase d'extension nord-sud de la Mer Égée qui a débuté il y a environ 15 Ma, au Miocène.

Trois grands mécanismes ont été proposés pour expliquer l'extension en Égée, chacun ayant un rôle plus ou moins important : le retrait de la plaque plongeante africaine vers le sud qui a débuté vers 30 Ma, l'effondrement gravitaire de la chaîne des Hellénides sous son propre poids, l'évolution de la faille nord anatolienne, ou *North Anatolian Fault* (NAF). Selon Armijo et al. [1996], l'affaissement de la chaîne de montagnes a provoqué des instabilités dans le manteau lithosphérique il y a environ 15 Ma, entraînant l'apparition de zones de rifts régulièrement espacées au sein de la mer Égée, d'orientation est-ouest et parallèles à la fosse de subduction (Figure 2.2.a). Vers 5 Ma, les rifts se sont sensiblement ouverts avec des déplacements plus importants au centre que sur les bords occidental et oriental. Ceci a provoqué une courbure du front d'extension ainsi que des rotations anti-horaires observées notamment dans le nord de la Grèce, et horaires au sein de l'Anatolie (Figure 2.2.b). Une accélération de la subduction se produit ensuite, entraînant la propagation de la NAF vers le sud-ouest. Le mouvement latéral de l'Anatolie par rapport à la plaque européenne est partitionnée entre la branche nord et la branche sud de la NAF, accommodant respectivement 60 km et 20 km de glissement total. La progression de sa branche nord qui a lieu vers 2-3 Ma et son jeu dextre augmentent le taux d'extension dans la partie nord-occidentale, donnant lieu à la réactivation des fosses Saros et Nord Égéenne (Figure 2.2.c). La propagation de la branche sud de la NAF dans la mer Égée réactive des structures extensives pré-existantes qui s'expriment en surface par la création des golfes d'Evvia et de Corinthe vers 1 Ma (Figure 2.2.d).

Le rift de Corinthe a été identifié comme un site d'importance majeure à la fois à cause de son intense activité géophysique passée [Papazachos et al., 1997], de son très fort taux de déformation et car il est l'une des régions continentales en ouverture des plus rapides du monde. Sa vitesse d'extension est supérieure à 10 mm.an^{-1} en moyenne [Avallone et al., 2004; Briole et al., 2000] de direction quasiment N-S, depuis les 20 dernières années.

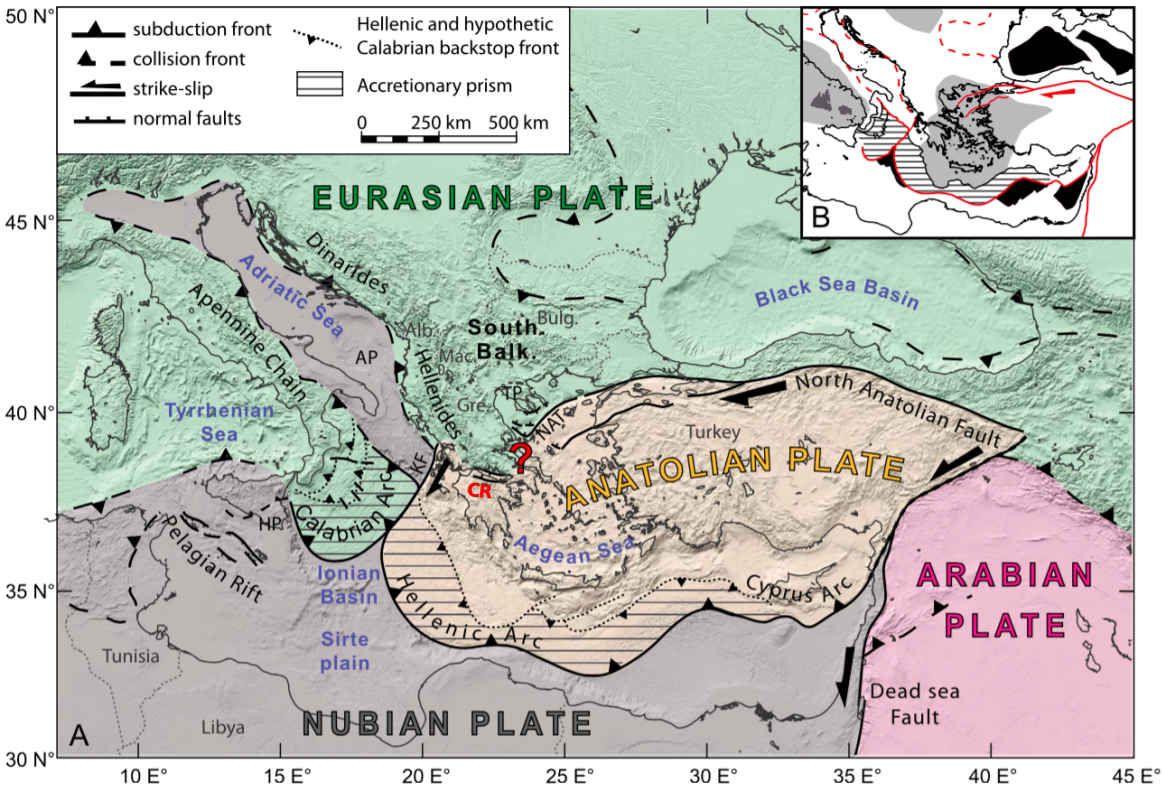

FIGURE 2.1 – Carte simplifiée des plaques tectoniques de la Méditerranée occidentale. (a) Carte modifiée d'après Chamot-Rooke et al. [2005]. South. Balk. : sud des Balkans ; Alb. : Albanie ; Mac. : Macédoine ; Bulg. : Bulgarie ; Gre. : Grèce ; AP : plateforme apulienne ; HP : plateau Hybléen ; KF : faille de Céphalonie ; CR : rift de Corinthe ; TP : péninsule de Thessalonique ; NAT : fosse Nord Égéenne. (b) Encart montrant la nature de la croûte dans la région [Chamot-Rooke et al., 2005; Jolivet et al., 2008]. En noir : relique de la lithosphère océanique Mésozoïque ; en gris foncé : lithosphère océanique Néogène ; en gris clair : fine lithosphère continental Miocène post-orogénique ; en blanc : lithosphère continentale ; lignes en pointillés : prisme d'accrétion. D'après Perouse et al. [2012].

2.2.2 Formations géologiques

La géologie du rift de Corinthe est marquée par deux phases tectoniques majeures : le régime compressif du Miocène et le régime extensif du Quaternaire. La phase de compression, orientée NE-SO, est à l'origine de la chaîne de montagnes des Hellénides (Figure 2.3) qui s'étendent le long de la côte Adriatique. Elle se caractérise également par la formation de nappes chevauchées qui ont migré d'est en ouest jusqu'aux îles Ioniennes.

Cinq nappes principales, ou unités tectoniques majeures, se sont mises en place dans le Golfe de Corinthe durant cette période (Figure 2.4). De la base de l'empilement au sommet, on trouve :

- la nappe des Plattenkalk, composée de calcaires de plateforme ;
- la nappe des Phyllades, ou la série Phyllite-Quartzite, constituée de roches métamorphosées sous des conditions de haute pression et faible température [Latorre et al., 2004] typiques des zones de subduction ou de collision continentale ;
- la nappe de Gavroro-Tripolitsa, composée de calcaires du Trias-Tertiaire, qui affleure dans la zone de Patras ;
- la nappe d'Olonos-Pindos, composée de calcaires formés au Mézosoïque et d'un flysh tertiaire, qui affleure dans la zone d'Aigion ;
- la nappe du Parnasse.

La nappe des Phyllades a une lithologie très différente de celle de Gavroro-Tripolitsa. Elle affleure au sud du Péloponnèse et sa position en profondeur dans la région du rift de Corinthe est encore

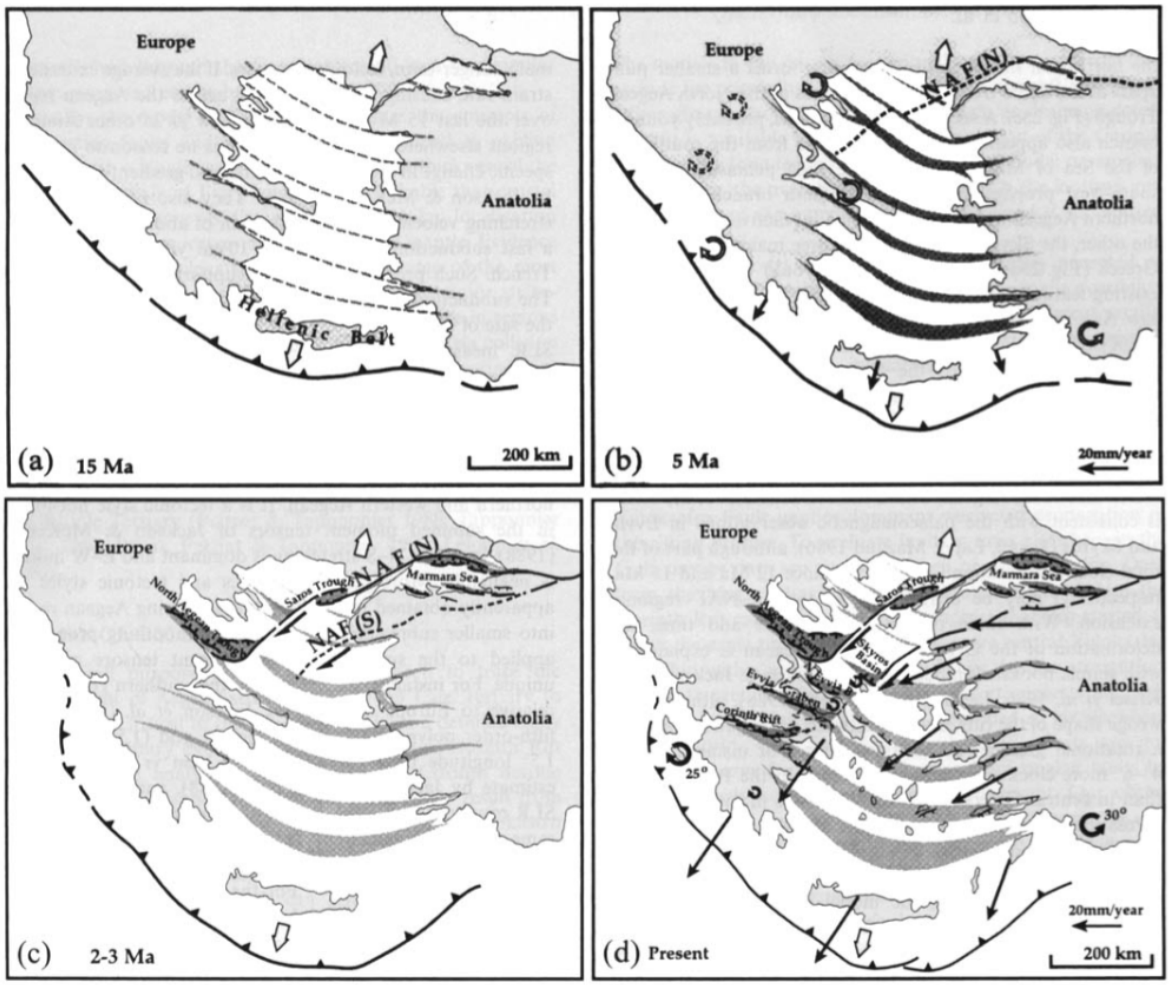

FIGURE 2.2 – Géodynamique de la région égéenne depuis le Miocène. Le rift de Corinthe fait partie du contexte géodynamique égéen. Sa forte vitesse d'extension de direction quasiment N-S est à la fois la conséquence de l'extension arrière-arc de la subduction hellénique (patchs gris clair) et du mouvement décrochant dextre de la faille nord anatolienne, NAF (patchs gris foncé). Les différentes étapes de la formation du rift (a,b,c,d) sont directement décrite dans le corps du texte. D'après Armijo et al. [1996].

très incertaine [Le Pourhiet et al., 2004]. Cependant, le contraste lithologique et probablement rhéologique entre ces deux séries peut avoir des conséquences importantes sur la géodynamique d'ouverture du rift et sur la naissance de ruptures sismiques dans la croûte.

La phase extensive a commencé au Miocène (voir Section 2.2.1) selon un axe N-S et a engendré le rift de Corinthe actuel qui coupe orthogonalement le relief hellénique [Armijo et al., 1996]. Le rift s'est formé en deux étapes distinctes, chacune caractérisée par une sédimentation et une géométrie de bassin différente. Le golfe de la première phase, au Pliocène, appelé proto-golfe, est caractérisé par des dépôts alluviaux et lacustres et une large plaine abyssale [Brooks and Ferentinos, 1984]. Au Pléistocène, le changement du taux d'extension est responsable d'une surrection accélérée et du rétrécissement du rift qui lui a donné sa forme actuelle [Ori, 1989].

2.2.3 Morphologie du rift de Corinthe

Le rift de Corinthe s'étend sur environ 110 km de long, du canal de Corinthe à l'est au golfe de Patras à l'ouest, orienté suivant un axe N110°E (Figure 2.5). Il présente une forme triangulaire avec une distance séparant les côtes nord et sud d'environ 30 km à l'est au niveau de la ville de Xylokastro, contre seulement 3 km à l'ouest près de Nafpaktos. Cette distinction est-ouest est également

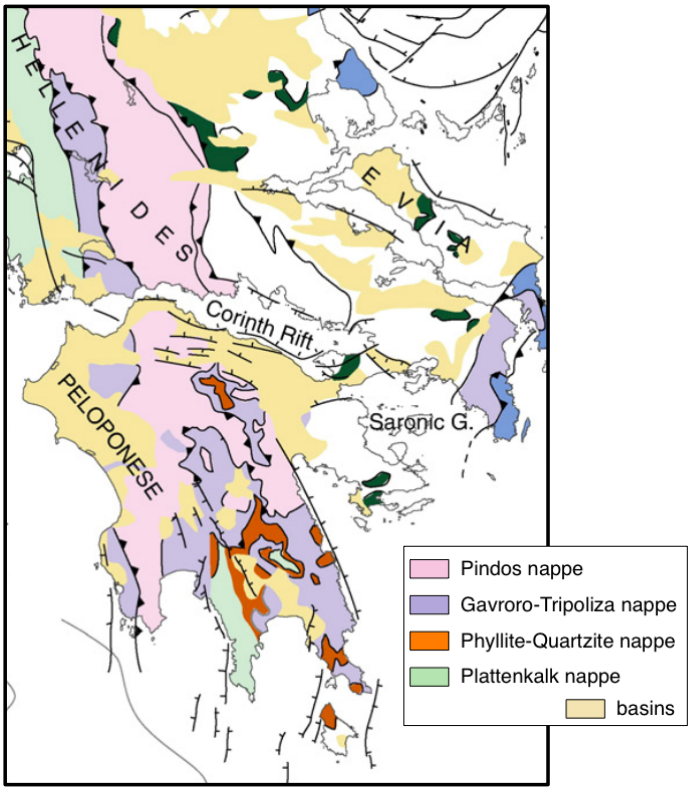

FIGURE 2.3 – Carte structurale des nappes de la chaîne des Hellénides. Modifiée d'après Jolivet et al. [2010].

visible dans la bathymétrie (Figure 2.6) : la plaine abyssale se situe au niveau de Xylokastro à une profondeur de 850 m, tandis que la profondeur du golfe n'atteint qu'environ 60 m au niveau de Nafpaktos [Brooks and Ferentinos, 1984; Nomikou et al., 2011].

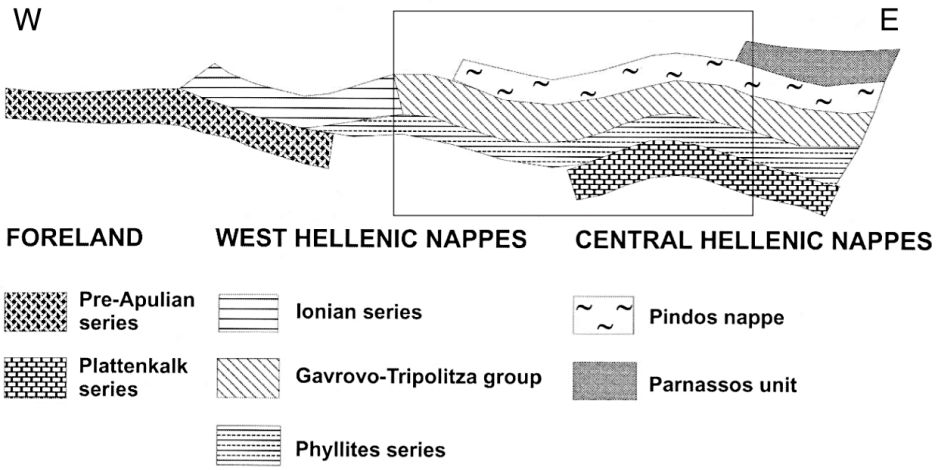

FIGURE 2.4 – Coupe schématique des nappes de la chaîne des Hellénides. La zone dans le cadre correspond à la succession structurale des nappes au sud du rift de Corinthe, selon la reconstruction proposée par Jacobshagen et al. [1978]. D'après Latorre [2004].

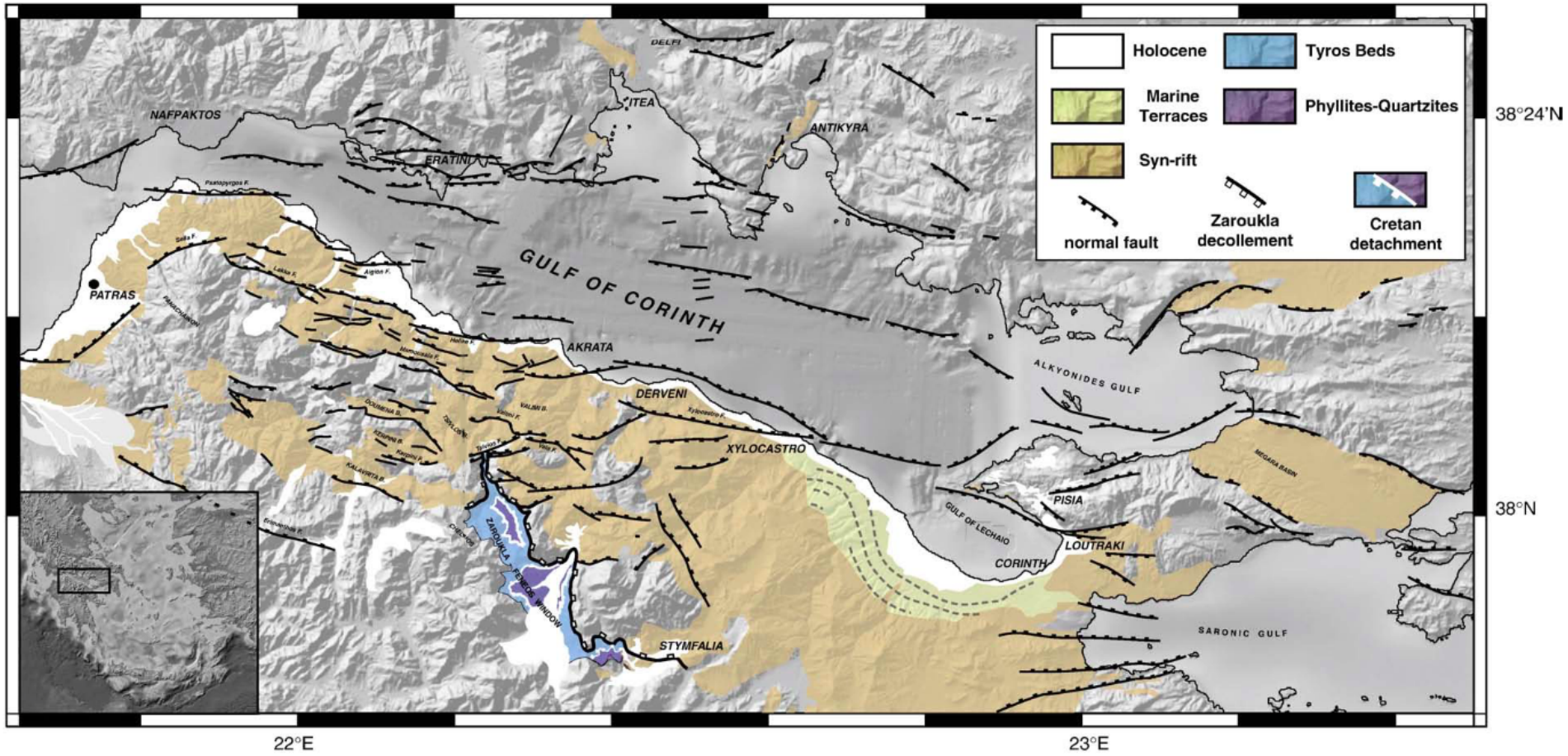

FIGURE 2.5 – Carte tectonique du rift de Corinthe. Cette carte a été compilée grâce à plusieurs publications [Armijo et al., 1996; Bell et al., 2008; Flotté et al., 2005; Ghisetti and Vezzani, 2004; Leeder et al., 2008; McNeill et al., 2005a,b; Palyvos et al., 2005; Rohais, 2007]. D'après Jolivet et al. [2010].

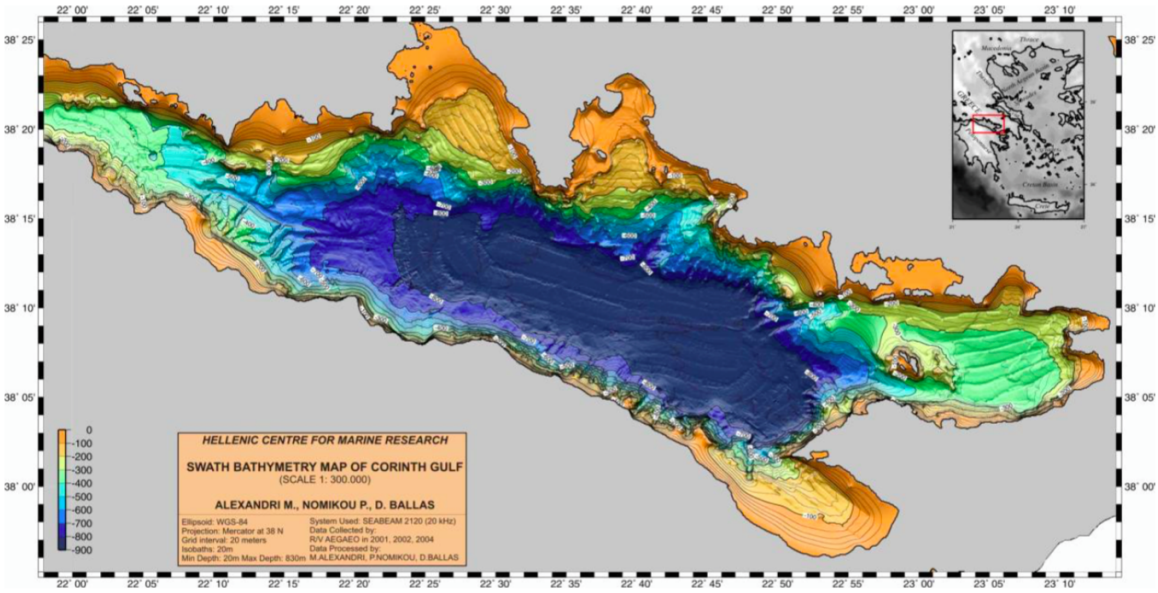

FIGURE 2.6 – Carte bathymétrique du rift de Corinthe. D'après Nomikou et al. [2011].

Les observations bathymétriques, géologiques et de profils sismiques [Sachpazi et al., 2003] montrent que le rift de Corinthe est un demi-graben asymétrique [Armijo et al., 1996] dont la rive sud se soulève de plusieurs millimètres par an [Collier et al., 1992; Martini et al., 2004; Pirazzoli et al., 2004]. Les taux de surrection observés le long de la côte sud du golfe et compilés par Flotté et al. [2005] décroissent d'ouest en est, d'environ 2.5 mm.an^{-1} sur la faille d'Helike à 0.2 mm.an^{-1} sur la faille de Xylokastro. Cette élévation différentielle serait provoquée, d'après Flotté et al. [2005], par l'enfouissement des sédiments du prisme d'accrétion lors de la subduction générant une compensation isostatique localisée à l'ouest du rift.

2.2.4 Failles actives et déformation actuelle

Dans le paysage, les structures actives dévoilent des miroirs et des escarpements de failles principalement sur la côte sud du rift, avec des pendages en surface de l'ordre de 50–60° vers le nord [Armijo et al., 1996; Ford et al., 2013; Palyvos et al., 2005]. Ces failles majeures sont disposées en échelons, orientées ONO-ESE et ont des longueurs qui varient entre 10 et 20 km en moyenne [Armijo et al., 1996]. Des failles antithétiques (à pendage vers le sud) ont été identifiées dans la partie nord du golfe à la fois sur le continent et en milieu sous-marin [Beckers et al., 2015; Bell et al., 2008; Moretti et al., 2003]. Les failles continentales de la côte nord restent de plus petite taille et sont relativement plus isolées que celles du sud.

La zone de rift est actuellement en extension de direction quasiment nord-sud (N5° en moyenne) et est constituée d'un réseau complexe de failles pour la plupart normales, et certaines décrochantes (Figure 2.5). La vitesse d'extension du rift est inhomogène suivant sa longueur. Elle est d'environ 10 mm.an^{-1} dans sa partie orientale et atteint des valeurs de 15 mm.an^{-1} dans sa partie la plus occidentale [Briole et al., 2000], montrant une augmentation du taux d'ouverture d'est en ouest et du taux de déformation. Ceci suggère une différence de vitesse de rotation entre les blocs nord et sud du rift. Un gradient du taux de déformation le long du rift est également établi à l'aide des données GPS [Avallone et al., 2004; Briole et al., 2000], se situant en zone offshore pour la partie ouest du rift et atteignant des valeurs d'environ 16 mm.an^{-1} près de la ville d'Aigion [Avallone et al., 2004]. Une frontière structurale correspondant à des discontinuités dans les systèmes de failles est également remarquable entre les parties orientale et occidentale du rift [Lambotte et al., 2014].

A l'ouest du rift, les failles de la côte sud coupent les sédiments syn-rift (Figure 2.5) et contrôlent leur emplacement en altitude par soulèvement. Effectivement, au cours de l'évolution du rift de Corinthe, les failles actives ont migré vers le nord [Ori, 1989; Sorel, 2000], entraînant l'apparition des plus vieux sédiments, par surrection et érosion, à des altitudes plus grandes et plus au sud. Les failles côtières du système de Kamarai (Lambiri–Selianitika–Fassoulieka), la faille d'Aigion et les failles sous-marines sont les plus jeunes et plus actives du rift. La faille d'Helike un peu plus au sud montre déjà une activité nettement inférieure aux précédentes, car elle est probablement relayée par celles-ci [Bernard et al., 2006]. Le système de failles de Pirgaki-Marmoussia, encore plus au sud, semble inactif depuis plus de 250 ka [Flotté et al., 2005]. Une phase de transition est donc marquée à travers ces différents systèmes et la faille d'Helike pourrait délimiter la zone de déformation [Pacchiani, 2006].

La faille d'Aigion fait partie des structures les plus surveillées et analysées de la région ces dernières années, du fait du risque sismique important qu'elle génère. Effectivement, les sismologues grecques enregistrent une forte activité sismique à sa racine et la ville d'Aigion avec ses plus de 25 000 habitants est littéralement traversée par la faille. Des mesures de pendages ont été réalisées le long de l'escarpement de faille à l'ouest de la ville donnant une valeur de 60° [Pantosti et al., 2004]. Puis le forage AIG10, qui traverse son plan de faille à 720 m de profondeur, a permis de confirmer cette valeur [Cornet et al., 2004].

En ce qui concerne les failles sous-marines, deux d'entre elles semblent particulièrement intéressantes car elles montrent des escarpements de plusieurs centaines de mètres [Moretti et al., 2003] et contribuent certainement à l'accommodation de la déformation [Pacchiani, 2006]. Il s'agit des failles de Trizonia et de Mornos, qui ont été spécifiquement observées par Beckers et al. [2015]; Bell et al. [2009].

En plus des différences structurale, géodésique et morphologique entre la partie orientale et occidentale du rift de Corinthe, une nette différence de sismicité est observée [Lambotte et al., 2014]. La nature de cette frontière n'est pas encore bien connue ou comprise, mais elle a la même orientation que les nappes des Hellénides [Jolivet et al., 2010] héritées de la tectonique de convergence (voir Section 2.2.2), et qui constituent les 5 ou 10 premiers kilomètres de la croûte.

Dans la suite, nous nous concentrons surtout sur la partie ouest du rift, qui montre une activité sismique et un taux de déformation bien plus importante que la partie est.

2.3 Sismicité

2.3.1 Séismes majeurs historiques

Le golfe de Corinthe est l'une des régions les plus sismiques d'Europe. Cependant, la grande majorité des séismes historiques majeurs a eu lieu avant le déploiement de capteurs sismiques, empêchant leur étude quantitative. L'identification des failles associées à ces séismes ainsi que leur localisation, magnitude et mécanisme sont donc assez mal connus. Cependant, les découvertes de textes anciens et des études à partir de l'intensité ressentie des séismes ont tout de même permis des estimations de magnitude et de localisation, voire éventuellement de proposer une faille correspondante.

Plusieurs séismes destructeurs se sont produits ces dernières décennies (Figure 2.7) mais leur magnitude ne dépasse jamais $M_S = 7$ [Ambraseys and Jackson, 1990], ce qui est en accord avec les dimensions limites des systèmes de failles (< 20 km) [Jackson and White, 1989]. La partie orientale a notamment été frappée par une séquence de trois séismes de magnitude 6.2, 6.5 et 6.7 en 1981 [Hubert et al., 1996; Jackson et al., 1982]. Dans la partie ouest, la rupture d'un segment de la faille d'Helike a provoqué un séisme de magnitude estimée à 6.7 en 1861 et le dernier séisme de magnitude supérieure à 6 recensé sur la rive sud-ouest s'est produit en 1888 au niveau de la cité d'Aigion

[Albini et al., 2017; Papazachos et al., 1997]. Un séisme récent, en 1995, de magnitude 6.2 [Bernard et al., 1997], dit d'Aigion car ayant endommagé la ville de ce nom, a rompu une grande surface un peu plus au nord-est (Figure 2.8), sur une faille aveugle de pendage ~30° vers le nord.

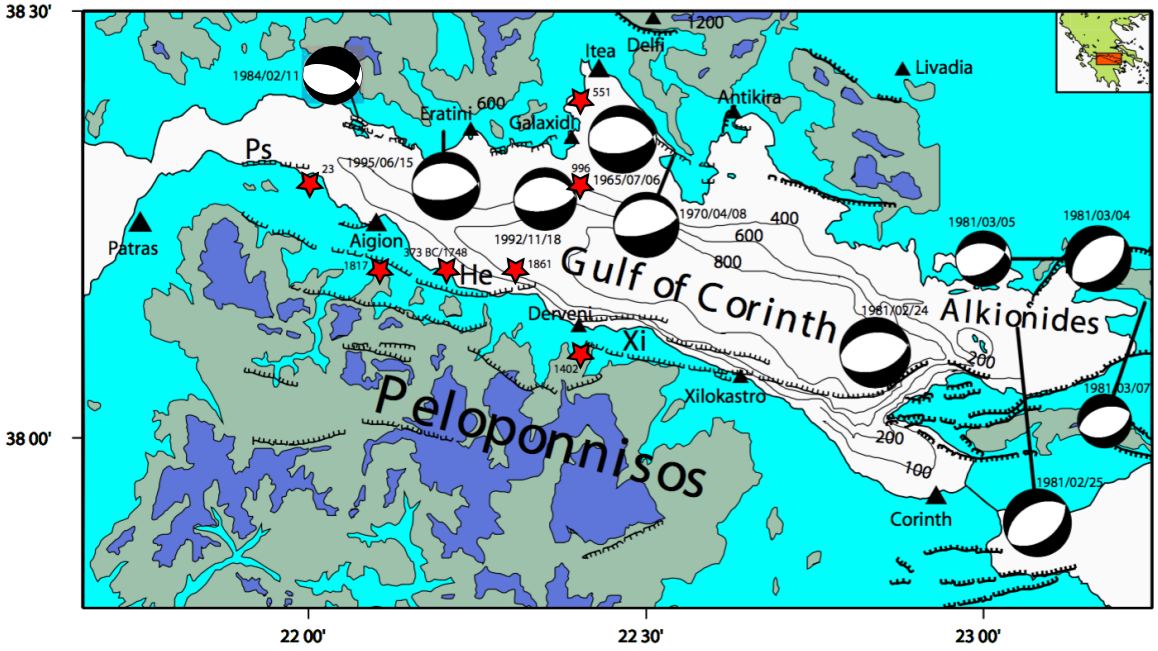

FIGURE 2.7 – Épicentres et mécanismes au foyer des séismes historiques du rift de Corinthe. Les étoiles rouges représentent les épicentres des séismes de magnitude M > 6 qui se sont produits proche de la ville d'Aigion depuis 373 BC [Albini et al., 2017; Papazachos et al., 1997]. Les mécanismes au foyer des séismes de magnitude M_S > 5 depuis 1965 sont résumés dans Briole et al. [2000] et issus des études de Baker et al. [1997]; Bernard et al. [1997]; Rietbrock et al. [1996]; Taymaz et al. [1991] et du catalogue CMT. La topographie provient de DMAAC (1984) et la bathymétrie de Perissoratis et al. [1986] pour la partie est du golfe et de l'UNESCO (1981). Ps : Psathopyrgos fault ; He : Helike fault ; Xi : Xilokastro fault. D'après Pacchiani [2006].

2.3.2 Microsismicité

Le golfe de Corinthe est également le siège d'une forte activité microsismique. Cette activité suit une organisation en essaims avec l'alternance de crises sismiques intenses et de périodes calmes. Dans la partie ouest du rift, la microsismicité apparaît principalement sur une épaisseur de couche de 3-4 km à pendage nord, située principalement entre 5 et 10 km de profondeur [Lyon-Caen et al., 2004; Rigo et al., 1996]. La localisation précise de cette microsismicité apporte de nouvelles informations sur la nature et la structure de la zone active précédemment interprétée comme un détachement [Bernard et al., 2006; Rigo et al., 1996], sur la géométrie des failles en profondeur et sur le processus de rifting [Lambotte et al., 2014]. Récemment, une analyse détaillée de la microsismicité occidentale du rift, finement relocalisée sur la période 2000-2007, a clarifié les structures internes de la couche sismique [Lambotte et al., 2014]. Plusieurs essaims sismiques importants étudiés par Godano et al. [2014] soulignent le pendage nord (et quelques pendages sud) des structures planaires dans la couche sismiquement active, avec des mécanismes de faille normale. Ces structures ont été interprétées comme (1) la base des failles cartées en surface, certaines connues pour avoir déclenché des séismes de forte magnitude (M > 5) et (2) une structure à faible pendage (< 30°) vers le nord sur laquelle les failles viennent se connecter.

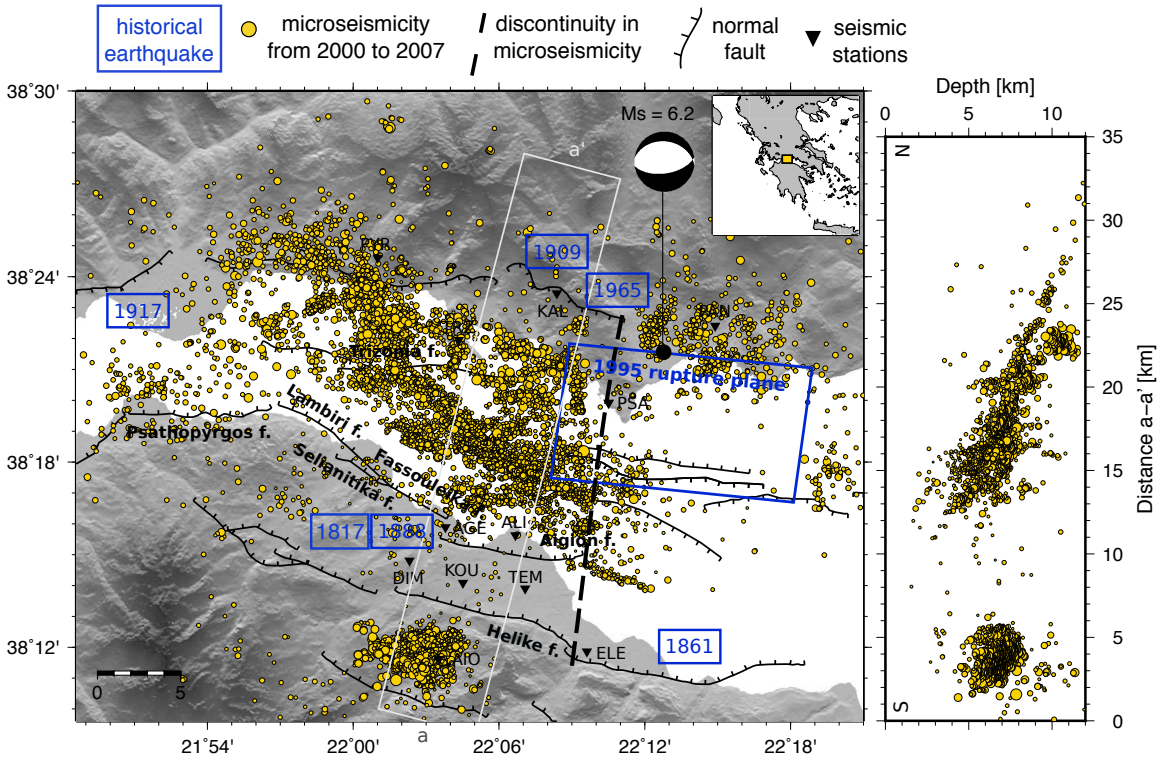

FIGURE 2.8 – Carte des derniers séismes historiques et de la microsismicité de la partie occidentale du rift de Corinthe entre 2000 et 2007. La microsismicité (jaune) a été enregistrée par le réseau CRL, *Corinth Rift Laboratory* (triangles noirs) et relocalisée par Lambotte et al. [2014]. Le mécanisme au foyer de composante normale est associé au séisme de 1995 de magnitude $M_S = 6.2$ Bernard et al. [1997] dont le plan en surface est délimité en bleu. Les séismes historiques [Bernard et al., 1997; Papazachos et al., 1997] sont indiqués par leur date encadrée en bleu. Les failles sont les principales structures présentées dans Moretti et al. [2003], Palyvos et al. [2005] et Ford et al. [2016]. La ligne en pointillé noir marque la discontinuité de sismicité entre la partie est et ouest du rift.

2.4 Les modèles mécaniques proposés

Le plan délimité par la microsismicité de faible pendage vers le nord représente une zone de transition en profondeur, acceptée communément par les différentes composantes scientifiques (tectoniciens, sismologues et géodésiens) mais sa nature et son fonctionnement sont encore inconnus et restent très discutés. Effectivement, l'intégration de ce plan dans des modèles tectoniques soulève des questions sur la mécanique de la déformation au sein du rift.

Le modèle mécanique classiquement retenu, introduit par Rigo et al. [1996], est un enracinement des failles normales à pendage nord le long d'un plan de détachement actif sous le golfe, qui glisse de manière stationnaire jusqu'à des profondeurs mi-crustales, en accord avec la distribution spatiale de la microsismicité et des mécanismes au foyer (Figure 2.9). Le détachement est interprété ici comme la limite inférieure de la zone sismogénique. Des données de terrain [Flotté et al., 2005; Sorel, 2000], des données géodésiques [Bernard et al., 1997; Briole et al., 2000], et des profils sismiques [Taylor et al., 2011] ont ensuite été ajoutés au modèle pour le renforcer.

Dans le modèle de Sorel [2000], le détachement représente la structure principale du rift, celle qui délimite en profondeur la transition fragile–ductile et qui accommode une partie importante de la déformation. Le détachement est peu profond au sud et s'enfonce progressivement vers le nord pour devenir, sous le golfe, le plan illuminé par la microsismicité et celui de rupture des gros séismes du rift, comme celui d'Aigion en 1995 ou de Galaxidi en 1992. Simultanément, pour accommoder la déformation en surface, des failles listriques secondaires se développent successivement du sud vers le nord et s'enracinent sur le détachement [Flotté et al., 2005; Sorel, 2000].

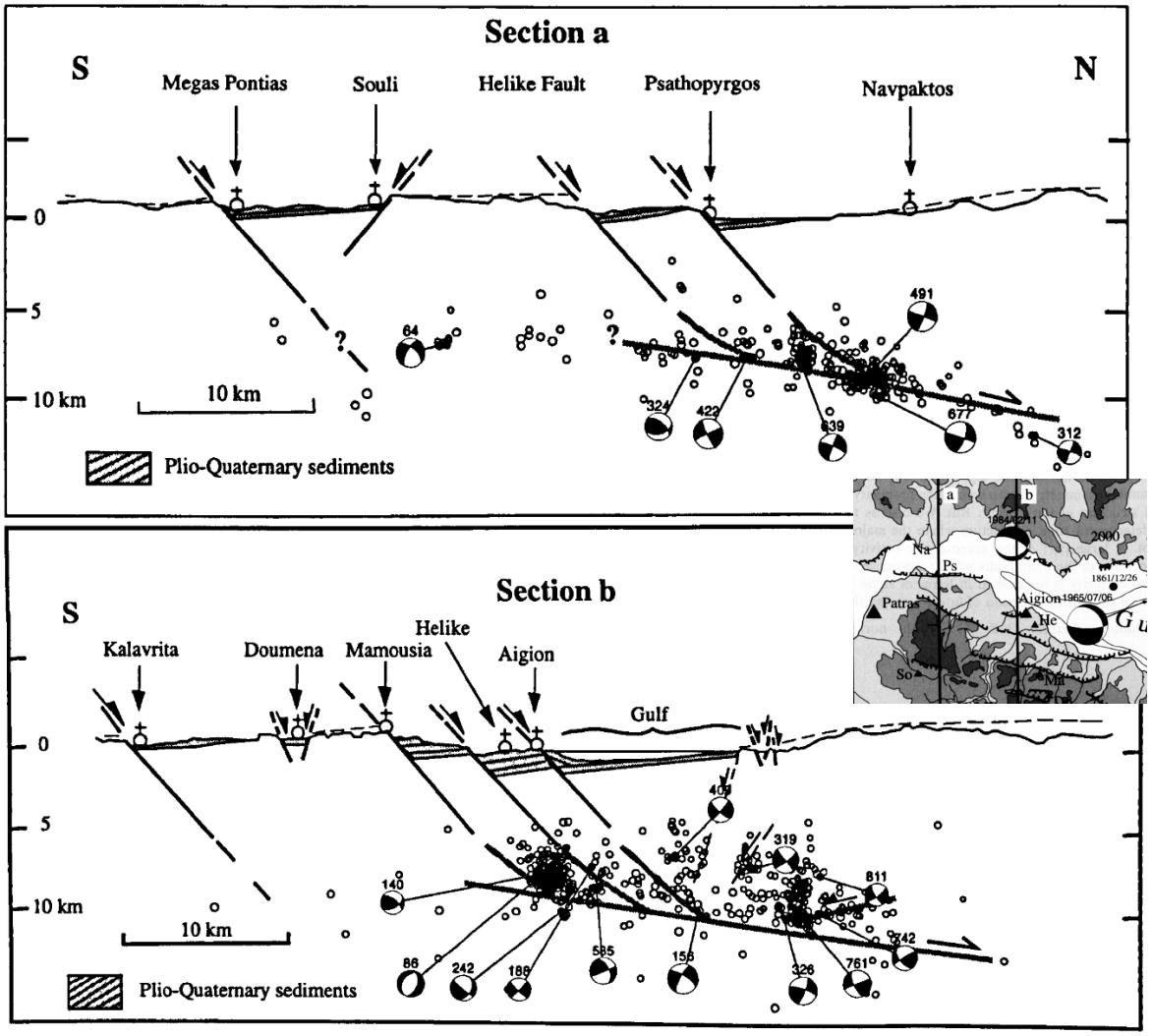

FIGURE 2.9 – Modèles de détachement à faible pendage. (a) Coupe sud-nord au niveau de Psathopyrgos. (b) Coupe sud-nord au niveau d'Aigion. La microsismicité et les mécanismes au foyer sont projetés dans les coupes verticales. Les failles normales actives majeures documentées en surface se connectent au plan de détachement à faible pendage en profondeur. Modifié d'après Rigo et al. [1996].

À partir de la distribution de la microsismcité en profondeur et des données géodésiques de surface, Briole et al. [2000] ont proposé un premier modèle cinématique intégrant un glissement uniforme sur le plan de détachement afin de s'ajuster aux vecteurs vitesse uniformes observés aux stations GPS au niveau de la côte nord du golfe (Figure 2.10.a). Cependant, selon Lambotte et al. [2014], d'un point vue mécanique, un tel modèle impliquerait un coefficient de friction non-stationnaire sur le plan de détachement, qui imposerait une libération des contraintes plus élevées par unité de temps qu'il est possible d'en accumuler par le taux d'ouverture constant dans la partie supérieure du détachement. Dans le cas contraire, les vitesses de glissement sur le plan de détachement devraient augmenter en allant vers le nord, et donc un gradient des vecteurs vitesse GPS devrait être observé en surface au niveau de la côte nord (Figure 2.10.b).

Rejetant ce modèle, Lambotte et al. [2014] propose alors un modèle alternatif : l'ouverture de la partie occidentale du rift serait le résultat d'une ouverture non-élastique hypothétique sous l'axe du rift (Figure 2.10.c). L'étirement du rift résulterait d'une viscosité ou plasticité seuil effective plus faible à 8–10 km de profondeur, possiblement provoquée par la présence de fluides remontant de la plaque plongeante de la subduction (50 km plus profonde). Dans ce modèle, la microsismicité serait le témoin d'une zone de détachement en formation, progressant vers le nord avec un faible pendage et grandissant à chaque séisme majeur dans sa partie profonde.

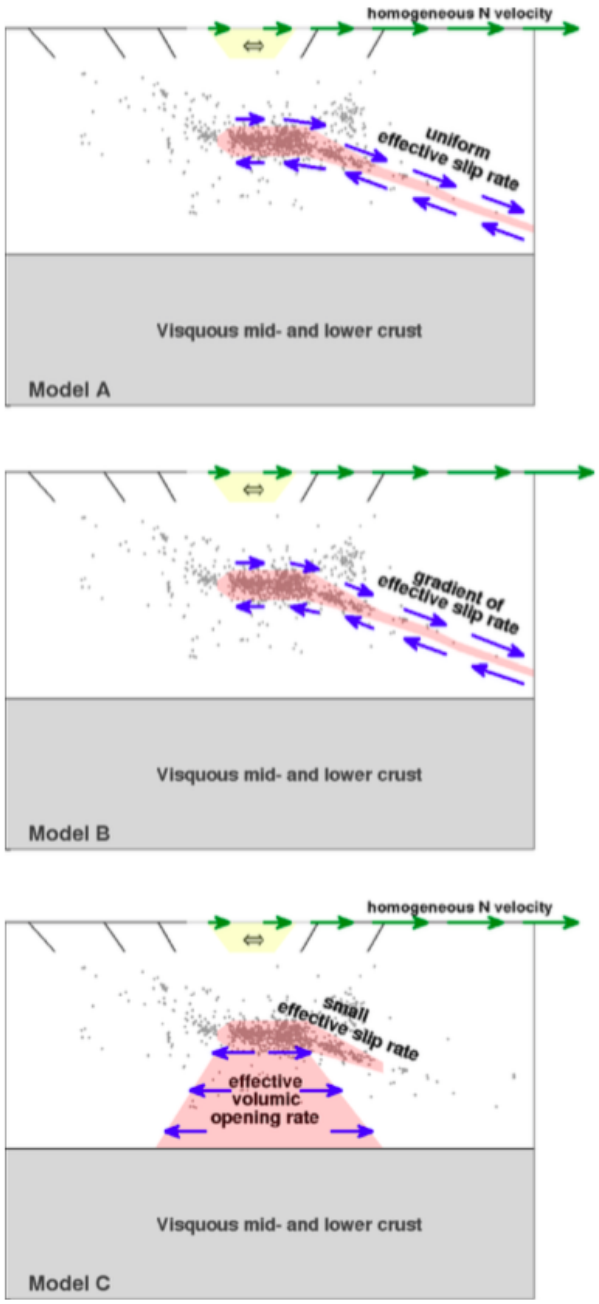

FIGURE 2.10 – Modèles mécaniques proposés pour expliquer les données sismiques et géodésiques. (a) Modèle avec un glissement uniforme sur le plan de détachement. (b) Modèle avec un taux de déplacement stationnaire au niveau des frontières verticales sud et nord et un coefficient de friction statique effectif stationnaire le long du détachement. (c) Modèle avec une ouverture non-élastique localisée sous l'axe du rift. Les flèches vertes sont les vitesses horizontales déduites des données GPS. Les lignes noires correspondent aux principaux plans de failles. D'après Lambotte et al. [2014].

2.5 Le *Corinth Rift Laboratory*

Le laboratoire du Rift de Corinthe (*Corinth Rift Laboratory*, CRL, `http://crlab.eu`) a été initié en 1989 par un projet européen afin d'effectuer des recherches sur la dynamique des failles et des séismes. Son approche multidisciplinaire, impliquant sismologie, géodésie, tectonique, géologie et géochimie, lui a permis de devenir l'un des six observatoire de failles ou *Near Fault Observatory* (NFO), intégrés dans la structure de recherche européenne EPOS (*European Plate Observing System*). Le site du CRL s'étend de la ville de Patras, à l'ouest, à la ville d'Aigion à l'est et couvre une surface de 50 km par 40 km. Depuis 2000, le CRL accueille un nombre croissant de stations permanentes permettant de mesurer les déformations crustales et d'enregistrer l'activité sismique de la région qui sont des données complémentaires.

2.5.1 Le réseau géodésique et les extensomètres

L'observation des déformations de la croûte terrestre demande une grande précision et une stabilité à long-terme. Les stations GPS (*Global Positioning System*) sont les instruments de mesure de la déformation les plus répandus dans le monde et les moins coûteux actuellement. Leur utilisation a connu un essor au début des années 1990 [Segall and Davis, 1997]. Elles permettent de mesurer de manière précise (précision généralement de l'ordre du millimètre) le déplacement tridimensionnel d'un point d'observation au cours du temps grâce aux satellites. La différence de positions à deux instants, à deux points d'observations divisée par la distance séparant ces points nous donne la valeur de déformation de la zone. Le rift de Corinthe est équipé d'une vingtaine de stations GPS permanentes dont 14 sont localisées dans la partie ouest du rift, proche des côtes (Figure 2.11). Ces stations permanentes sont accompagnées d'un grand nombre de stations temporaires qui sont utilisées régulièrement au cours de campagnes de mesures dans des zones spécifiques de la région. La disposition des capteurs GPS permettent à la fois de calculer les gradients de déformation le long des systèmes de failles orientés E-W et de suivre l'évolution de l'extension du golfe N-S.

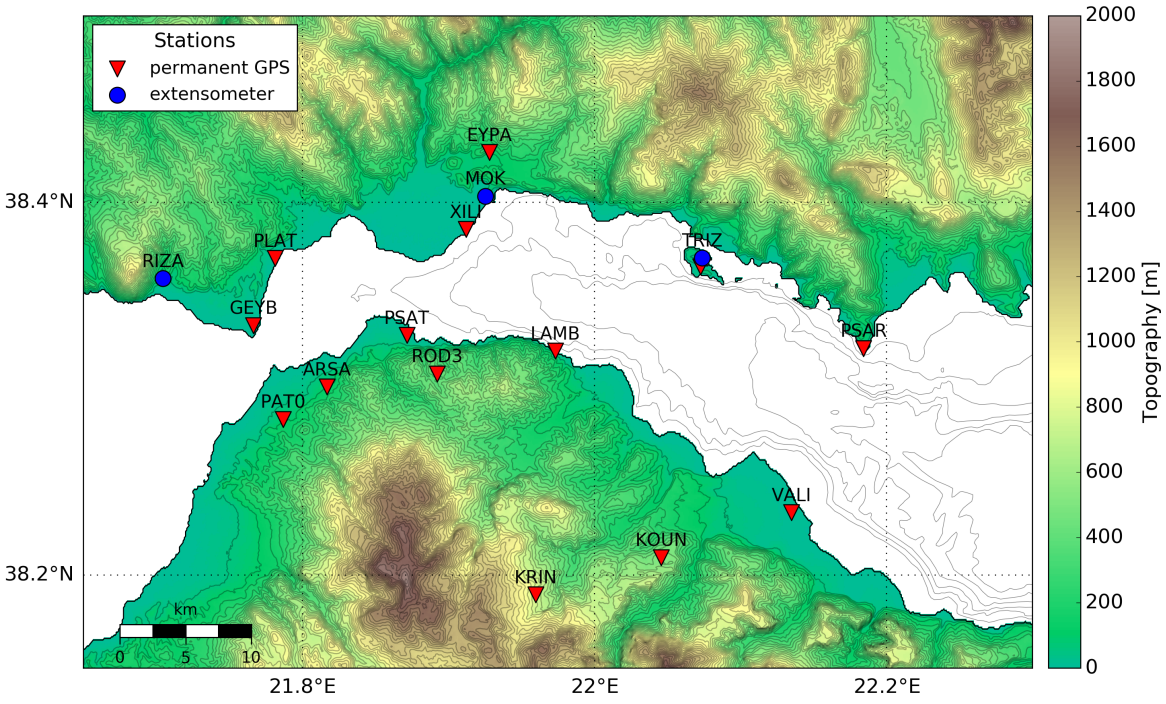

FIGURE 2.11 – Carte des stations géodésiques permanentes et extensomètres du réseau CRL.

Des instruments moins conventionnels, comme les inclinomètres, sont également utilisés pour mesurer des déformations dans la croûte terrestre. Ils permettent d'observer les courbures de la croûte provoquées par exemple par des chargements hydrauliques ou atmosphériques, le chargement tectonique ou encore le poids de la colonne mobile d'un tsunami. Les inclinomètres peuvent mesurer de manière beaucoup plus précise (sensibilité de l'ordre du nanoradian) les déformations volumiques par rapport aux instruments géodésiques habituels (GPS, InSAR). Ils sont particulièrement intéressants pour l'observation des déformations transitoires qui sont très variables en amplitude et en durée selon les sites. Cependant, leur plus grand inconvénient est leur fragilité. Plus on renforce l'appareil, plus celui-ci perd en précision. De plus, ils ne permettent pas de couvrir spatialement de grandes zone d'études et n'ont pas une assez grande stabilité pour des mesures à long-terme (plusieurs années ou décennies).

Enfin, les variations de pression de fluide induisent également des déformations qui sont mesurées par des extensomètres par exemple. Or l'observation de variations du niveau d'eau provoquées par la marée terrestre ou par de la déformation cosismique statique [e.g. Davis et al., 2001;

Gavrilenko et al., 2000] semble montrer que la pression de pore est sensible à la déformation crustale, ce qui complique l'interprétation des signaux. C'est pourquoi les mesures extensométriques sont souvent couplées à des mesures de variation du niveau d'eau afin de pouvoir mieux définir la part des déformations d'origine tectonique ou liées aux pressions de fluide. Les extensomètres sont des outils complémentaires aux mesures GPS de par leur grande sensibilité et leur robustesse à longue période. Ils permettent de mesurer des signaux tectoniques (sismiques ou transitoires) avec une grande précision dans un domaine fréquentiel très large.

Le rift de Corinthe est équipé de 3 extensomètres dont leur localisation est présentée sur la Figure 2.11. Ils ont été installés dans des forages à 150 m de profondeur sur la côte nord, dans le but de déceler d'éventuelles signatures transitoires non détectables avec les GPS. L'installation en forage permet de réduire les variations provenant des effets thermiques, atmosphériques ou encore anthropiques. Ces instruments peuvent mesurer des variations de déformations de l'ordre du nanostrain, après correction des influences majeures extérieures (la marée terrestre et la pression atmosphérique principalement). Ils sont tous les trois accompagnés d'un marégraphe installé à proximité. Des analyses des signaux enregistrés par l'extensomètre de Trizonia (TRIZ) et de Monasteraki (MOK) ont été réalisées par [Canitano et al., 2013, 2014] et ont notamment permis de révéler une augmentation du signal en déformation au passage des ondes générées par des microséismes locaux d'un essaim sismique en 2011, et possiblement du creep sur une petite faille superficielle proche de l'instrument de Trizonia.

2.5.2 Le réseau sismologique

La première station sismique permanente a été installée en 2000. A présent, 35 stations (Figure 2.12) sont télémétrées en temps réel vers l'Université d'Athènes, et rendues accessibles aux partenaires de CRL. Les stations sont majoritairement françaises (CNRS), grecques (Université d'Athènes et de Patras) et tchèques (Université Charles).

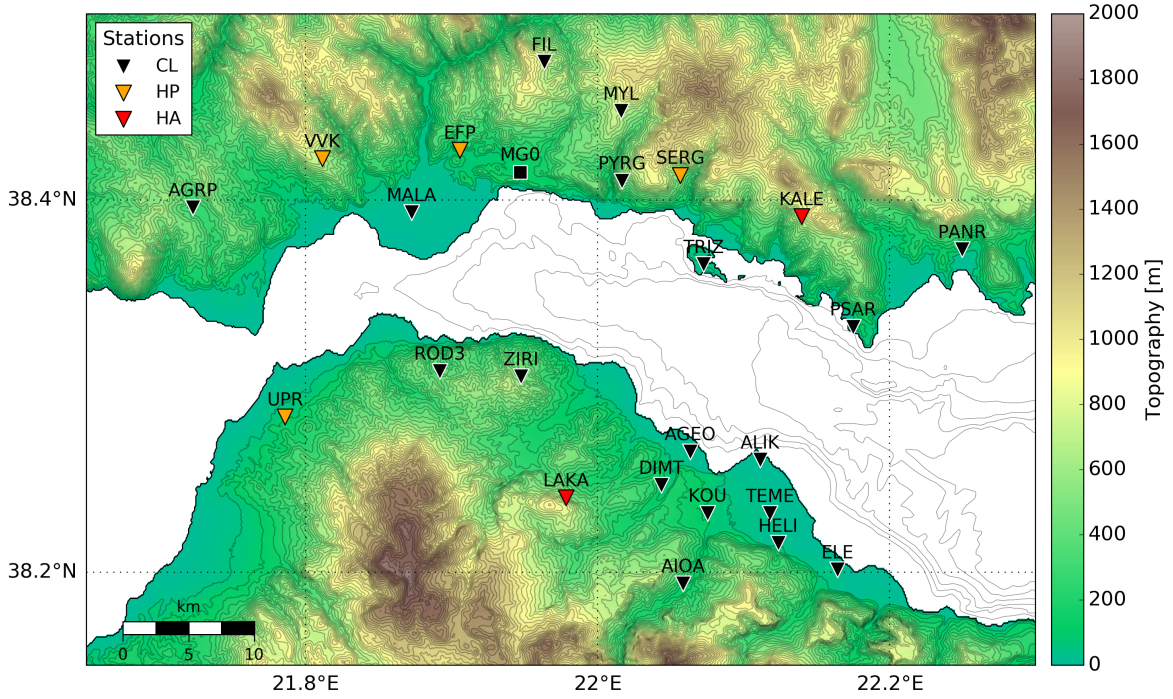

FIGURE 2.12 – Carte des stations sismiques permanentes du réseau CRL. Les couleurs correspondent à l'appartenance des différentes stations : noir = stations du CNRS, orange = stations de l'Université d'Athènes, rouge = stations de l'Université de Patras.

Le CRLNET est actuellement composé de 11 stations équipées avec des sismomètres courte-période

à 2 Hz, 9 stations avec des sismomètres large bande et enregistrant en continu à 100 Hz. De plus, une antenne de 7 sismomètres large bande a également été installée à Magoula sur la côte nord, à partir de 2011. Les sismomètres courte-période sont notamment destinés à l'enregistrement des séismes locaux voire régionaux, tandis que les large bande sont préférentiellement utilisés pour l'observation des évènements télésismiques. Cinq des sismomètres de la côte sud (AGEO, AIOA, ALIK, DIMT, TEME) sont installés dans des forages de 60 à 100 m de profondeur, ainsi que le sismomètre de la station MALA qui se situe dans le delta de Mornos sur la côte nord, à 190 m de profondeur. Cette configuration permet de limiter les perturbations liées aux activités humaines.

L'ensemble de ces stations permanentes permettent de surveiller l'activité sismique du rift en continu et de transmettre les localisations automatiques des séismes en temps réel.

2.5.3 Base de données

Les données sismologiques de CRL sont initialement écrites au format SEED (*Standard for the Exchange of Earthquake Data*), format maintenu par l'IRIS (*Incorporated Research Institutions for Seismology*). Ce format a été développé dans les années 80 afin de faciliter le transfert et les échanges de données parmi les différentes communautés sismologiques. Il est actuellement très répandu, voire mondialement utilisé car extrêmement pratique et facile d'utilisation. Le format SEED combine les séries temporelles sismiques recueillies par les sismomètres (fichiers *mini-SEED*) et les fichiers de métadonnées (fichiers *dataless*). Ces derniers conservent les informations relatives à l'instrument de mesure des vibrations du sol utilisé, notamment la position géographique du capteur, le temps, le type de réponse instrumentale, la fréquence d'échantillonnage, etc. Un *dataless* peut également fournir l'historique complet et exhaustif des métadonnées pour une ou plusieurs stations du réseau. Les données à proprement parler sont les enregistrements directement issus du convertisseur analogique–numérique, en sortie du sismomètre. La conservation séparée des données brutes et des métadonnées garantit une sécurité dans le sens où l'utilisateur reste libre d'effectuer le type de traitement adéquat à son étude.

Le format SEED utilise 4 variables pour identifier de manière unique une donnée (Figure 2.13) :

1. le code réseau, en 2 caractères. Il s'agit de 'CL' pour le réseau CRL.
2. le code station, de 1 à 5 caractères. Les stations de CRL sont quasiment toutes identifiées à l'aide de 4 caractères (ou 3 pour certaines anciennes stations).
3. ID de localisation, en 2 caractères. Dans le cadre de CRL, cette variable est utilisée si la station a été déplacée ou repositionnée.
4. le code du canal d'enregistrement, une combinaison de 3 caractères dont le premier représente le type de bande ou taux d'échantillonnage (E : *Extremely Short Period*, H : *High Broad Band* , B : *Broad Band*), le deuxième, le type d'instrument (H : *High Gain Seismometer*, N : *Accelerometer*) et le troisième, l'orientation du capteur (N : nord, E : est , Z : vertical).

Cependant, ce format n'est pas adapté aux traitements des données que nous souhaitions mener. Nous avons donc converti l'ensemble des formes d'ondes au format *Seismic Analysis Code* (SAC). La méthode STA/LTA (*Short-term average / Long-term average*) [Allen, 1982] était initialement utilisée pour la détection des évènements sismiques jusqu'en 2015. Depuis 2015–2016, le logiciel *SeisComP3* est utilisé à la fois pour la détection et le pointé des séismes. La méthode Kurtosis développée par Baillard et al. [2014] est en phase de test pour Corinthe pour tenter d'amliorer la précision des pointés automatiques. La Figure 2.14 récapitule l'ensemble des étapes de pré-traitement des données afin d'obtenir une base de données de formes d'ondes propres et cohérentes.

Au total, entre 2000 et 2015, la base de données contient environ 225 000 évènements sismiques, ce qui représentent un peu moins de 14 millions de formes d'onde stockées ($\approx$ 1 Tb).

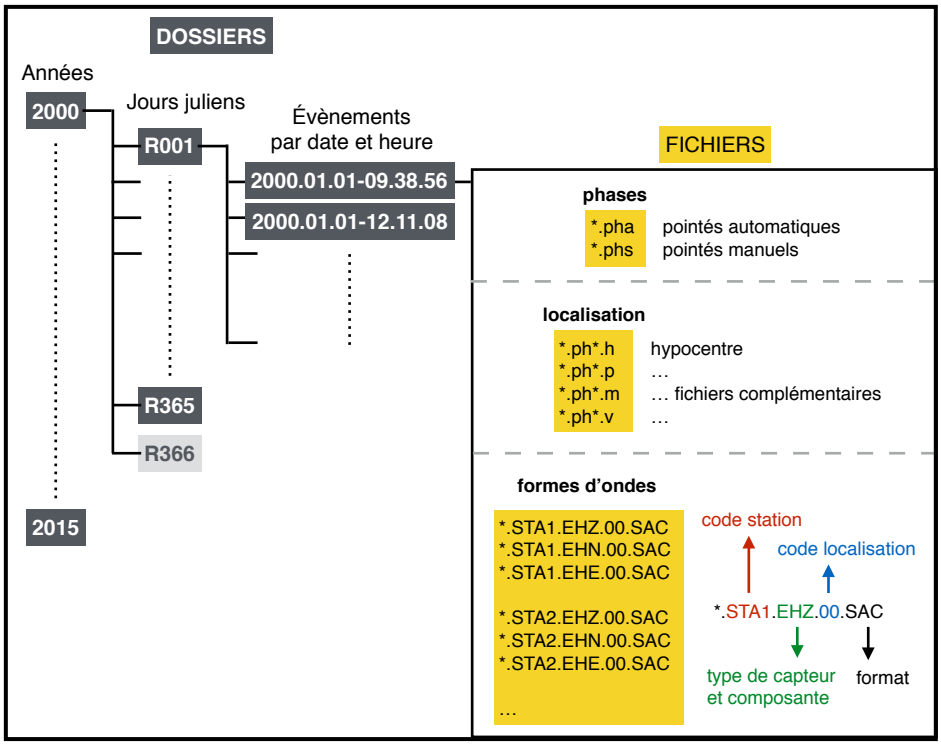

FIGURE 2.13 – Architecture du stockage des données de CRL et nomenclature.

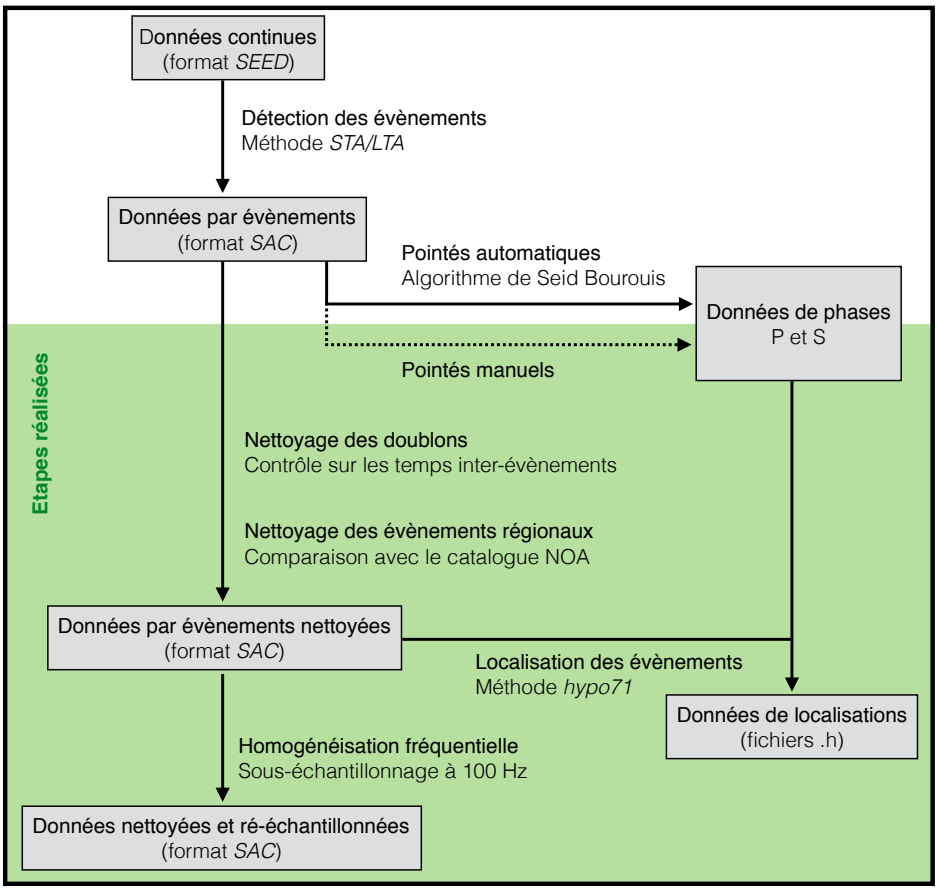

FIGURE 2.14 – Étapes de traitement de la base de données en continu aux évènements sismiques isolés.

2.6 Intérêts et particularités du rift de Corinthe

Cette section rassemble les questions relatives à la zone d'étude :

— Quelles sont les origines ou les causes des crises sismiques du golfe de Corinthe ?

— Quelles sont les barrières géologiques, tectoniques, ou/et sismologiques qui existent au sein du rift ?

— Quelles sont les zones géographiques où l'aléa sismique est le plus fort ?

En reformulant ces questions tout en tenant compte des aspects mécaniques vus dans le premier chapitre, nous pouvons nous demander si les microséismes enregistrés dans le golfe sont des précurseurs de forts séismes ou si, au contraire, ils permettent de décharger les contraintes accumulées sur les plans de failles majeures et empêchent la naissance d'une rupture dévastatrice. De plus, même sans être moteurs ou contributeurs de la préparation de grandes instabilités, les microséismes peuvent témoigner des conditions de frottement ou de contraintes des failles et donc éclairer sur le potentiel sismogène des grands séismes. Leur étude est donc un outils majeur pour une meilleur compréhension de l'initiation et des déclenchements des grandes rutpures.

Chapitre 3

Des indices de migration de pression de pore

Sommaire

Nous avons vu dans le premier chapitre que les essaims de microsismicité étaient régulièrement associés voire déclenchés par des changements de contraintes liés aux fluides. Ce chapitre se focalise sur l'évolution spatio-temporelle de la microsismicité durant la crise sismique de 2003–2004 qui a lieu dans la partie occidentale du rift de Corinthe. L'étude utilise les évènements relocalisés et les multiplets (familles de séismes similaires) définis par Lambotte et al. [2014] dans son analyse de la microsismicité enregistrée par le réseau CRLNET sur la période 2000–2007. Les résultats de notre analyse détaillée, multi-échelle de l'essaim, mettent en évidence un comportement pouvant être expliqué par de la diffusion de fluides en profondeur. Nous proposons au final qu'un processus d'hydro-fracturation, dû à la migration de pression de pore à l'intersection des plans de failles majeures (Aigion et Fassouleika) avec une couche géologique cassante héritée des nappes des Hellénides, a déclenché la séquence de séismes.

Les différentes parties de ce chapitre sont issues de l'article Duverger et al. [2015], publié dans le journal *Geophysical Research Letter*. Le texte principal de l'article est repris dans son intégralité en incluant l'annexe méthodologique dans le corps du texte, en anglais, langue de publication. Il est présenté dans sa version originale avec ses figures additionnelles et les légendes des documents numériques en Annexe A, à la fin du manuscrit.

3.1 Introduction

The characterization of the structure of active fault zones is essential for understanding earthquake nucleation, dynamic rupture and fault evolution, and can thus contribute to quantify the probability of major earthquake triggering. Our knowledge of fault zone structure and properties is mostly provided by geological and geomorphological studies based on direct observations of exhumed faults [e.g., Allen, 2005] and drilling projects that intersect active faults at depths [e.g., Cornet et al., 2004; Janssen et al., 2014]. Other inferences are obtained through indirect observations based on geophysical studies such as seismic reflection profiles [e.g., Bell et al., 2008; Long and Imber, 2012] and tomographic investigations [e.g., Allam and Ben-Zion, 2012; Latorre et al., 2004]. In particular, in the last decade, hypocentral locations of clustered events with double-difference techniques described the complex geometry of faults at depth, with a high-resolution [e.g., Lambotte et al., 2014; Valoroso et al., 2014; Waldhauser et al., 2004]. Adding the temporal information to the spatial distribution allows to study the mechanical processes at work within fault systems during the migration of seismic swarms. In numerous cases, such migrations are associated with aseismic creep [e.g., Lohman and McGuire, 2007]. In other cases, fluid circulations at depth are invoked to explain spatio-temporal variations of the seismicity, as for induced earthquakes due to man-made pore pressure perturbations [Hainzl, 2004; Shapiro et al., 1997]. Whether the controlling factor of a given seismic swarm is transient creep or pore pressure, their mutual cross-triggering and coupling with microseismicity is expected to produce complex mechanical processes [e.g., Bourouis and Bernard, 2007]. As these phenomena are controlled by the geometry, permeability and frictional properties of the faults, often poorly known, a better understanding of the role of the fault zone structure on seismic and aseismic activities is a challenging issue.

These questions are addressed here with the detailed analysis of the 2003–2004 microseismic sequence that occurred in the western Corinth rift, Greece. We assume that the pore pressure mainly controls the observed swarm activity, as proposed by Pacchiani and Lyon-Caen [2010] for the nearby 2001–swarm. In this study, we first present the tectonic context and the data along with the tools used for characterizing the geometry of the multiplets and the seismicity diffusion process. We then present the global activated structures, in relationship with major faults, followed by our interpretation of the multiscale space-time evolution of the activity in terms of pore pressure migration. We finally discuss the inferred permeable channels and the pore pressure source.

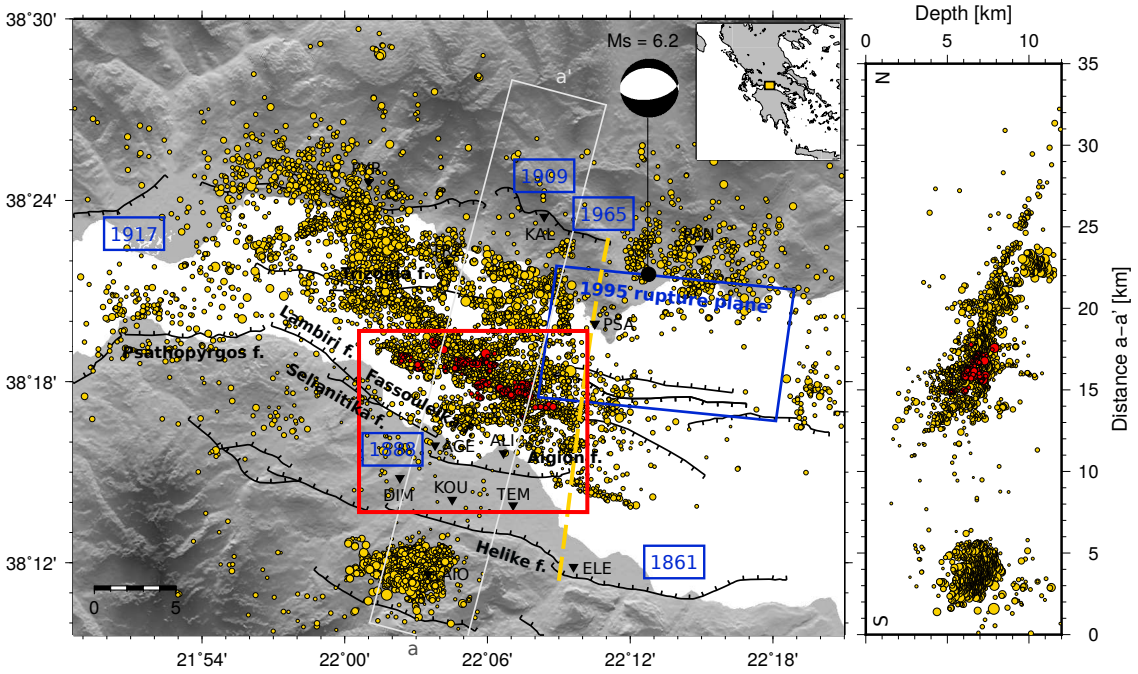

Figure 3.1 – Map and vertical section of historical earthquakes and microseismicity between 2000 and 2007. Microseismicity (circles) was recorded by the network CRLNET (black triangles) and relocated by Lambotte et al. [2014]. Red circles represent the studied microearthquakes occurring in 2003–2004. The yellow dashed line locates the microseismicity transition between the highly seismic western zone and the quiescent eastern zone. Historical earthquakes (blue framed dates) are from Papazachos et al. [1997] and Bernard et al. [1997]. Focal mechanism is from Bernard et al. [1997]. Main active faults have been compiled by Moretti et al. [2003], Palyvos et al. [2005], Bell et al. [2008] and *M. Ford* (personal communication). The red box corresponds to the map of Figure 3.2.

3.2 Data and methods

3.2.1 Seismotectonics and seismological data

The Corinth rift is a highly active seismic region, with six earthquakes of magnitude $M_S > 6$ during the last century, all related to major normal faults developed by the back-arc extension of the Hellenic subduction and the dextral shear of the North Anatolian Fault [e.g., Armijo et al., 1996; Palyvos et al., 2005]. In the western rift, the last damaging earthquake occurred in 1995 (M = 6.2 [Bernard et al., 1997]) and activated a low angle, north-dipping blind normal fault beneath the Gulf. On the southern coast, the last large earthquakes were felt in 1861 and 1888 [Boiselet, 2014; Papazachos et al., 1997] respectively activating the north-dipping Helike and Aigion faults (Figure 3.1). Revisiting and integrating instrumental and historical earthquakes, Boiselet [2014] finds that there is around 50% chance to expect a $M_S > 6$ in the next 30 years in this region.

A permanent dense seismic network with 12 short-period three-component stations, the Corinth Rift Laboratory Network (CRLNET), has been installed since the years 2000–2001 in the western part of the rift. It has recorded about 10,000 earthquakes per year with $M_W > 1.0$, and the activity is strongly clustered in time and space (http://crlab.eu/). The swarms last days to months and extend from 1 to 10 km long, so that the daily seismicity rate ranges from ten events per day in quiet periods to several hundreds during swarms. A clear drop in microseismicity rate is observed to the East, delimited by a NS discontinuity in the fault system (Figure 3.1). This discontinuity has the same strike as the Hellenic nappe stack [Jolivet et al., 2010] inherited from the convergence tectonics, that constitutes the upper 5–10 km of the crust.

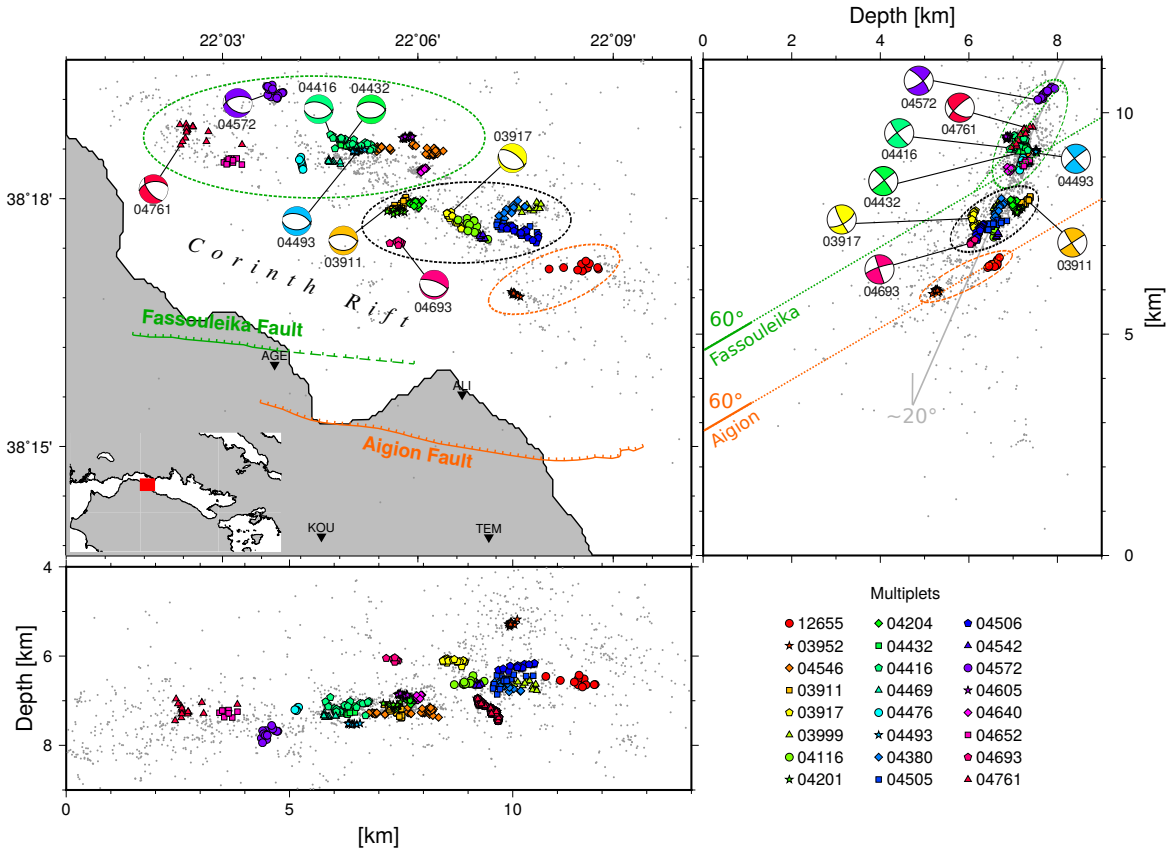

Figure 3.2 – Map, EW and NS vertical sections of the 2003–2004 swarm. The 24 main multiplets have specific colored symbols. The background microseismicity is represented as gray dots. The Aigion and Fassouleika faults dipping about 60° at surface are the two main structures illuminated at depth by respectively 2 (dashed orange ellipses) and 11 (dashed green ellipses) multiplets. A third structure (dashed black ellipses) between these faults is highlighted by the remaining multiplets and assimilated to a relay zone. Focal mechanisms are from Godano et al. [2014].

Recently, a detailed analysis of the microseismicity (multiplet identification, double-difference hypocenter relocation, focal mechanism determination) between 2000 and 2007 in the western rift, has revealed the complex internal structure of the main microseismic, 1–3 km thick brittle layer, that gently dips to the north between 5 and 9 km depth [Godano et al., 2014; Lambotte et al., 2014], questioning the original model of a major, crustal detachment proposed by Rigo et al. [1996]. This multiplet database, with highly correlated waveforms, provides the opportunity to better understand the fault zone structure and the seismic-aseismic coupling processes during swarms.

Here, we focus on the largest swarm (October 2003–June 2004) in which 24 multiplets were recorded, with more than 7 events in each of them (Figure 3.2). They consist of 411 earthquakes, with magnitudes up to 2.9 (b-value $\simeq$ 1.2), located at a depth of about 7 km, within the main seismic layer (Figure 3.1). Their absolute location error is less than 1 km, and their relative one is about 10 m [Lambotte et al., 2014]. Composite focal mechanisms for multiplets have been determined by jointly inverting the P polarities with the Sv/P, Sh/P, Sv/Sh amplitude ratios of direct waves [Godano et al., 2014].

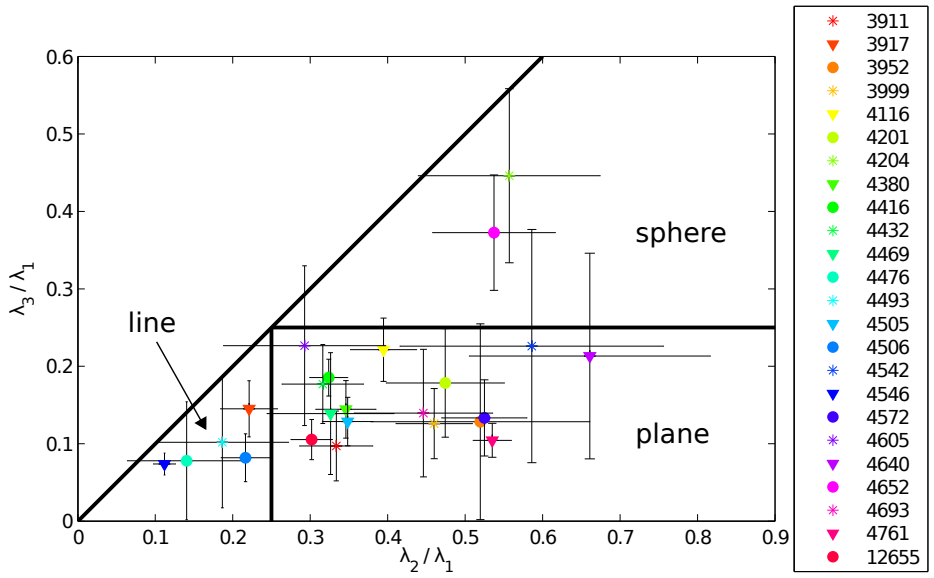

Figure 3.3 – Multiplet geometry. Representation of the geometry-type (linear, planar, spherical) areas as a function of the ratios between eigen-axis lengths of the best-fitting ellipsoid of a multiplet.

3.2.2 Multiplet geometry and pore pressure changes

Ellipsoid geometry

The geometry of the 24 multiplets (length, thickness, orientation of the best-fitting plane) was defined by calculating ellipsoids containing 95% of earthquakes. From the ratio between eigen axis lengths (λ_i) of the best-fitting ellipsoid, we classified the multiplets in three groups by setting thresholds L_{ij} [Asanuma et al., 2001]:

$$\begin{gathered}1.\ \text{Linear}: \lambda_2/\lambda_1 < L_{21} \text{ and } \lambda_3/\lambda_1 < L_{31}\\ 2.\ \text{Planar}: \lambda_2/\lambda_1 > L_{21} \text{ and } \lambda_3/\lambda_1 < L_{31}\\ 3.\ \text{Spherical}: \lambda_3/\lambda_1 > L_{31}\end{gathered}$$

where i and j are the ellipse axes. The critical values L_{ij} are all fixed to 1/4 after a visual pre-analysis of ellipsoid forms. The Figure 3.3 shows a representation of the geometry classification.

Planar multiplets suggest ruptures along an unique fault plane or an en-echelon globally planar structure. Linear multiplets could be associated to the intersection of two fault planes, and spherical multiplets are assimilated to ruptures on non-coplanar en-echelon structures. The uncertainties on the length of the ellipsoid axes are estimated taking as minimal size (respectively maximal size) the size of the ellipsoid containing 90% (respectively 99%) of earthquakes.

From the eigen vectors of the major and intermediate ellipsoid axes, one can determine the dip and azimuth of the best-fitting plane of the multiplet. The uncertainties on the angles are estimated by randomly perturbing the location of multiplet events by at most 10 m and computing 1,000 new combinations of earthquake multiplets. We took the standard deviation of the resulting dip and azimuth solutions from the mean solutions, assuming a Gaussian distribution. The results are summarized in the Table 3.1.

We can see that most of the planar multiplets show small dip and azimuth uncertainties (around 5°) because of the well-constrained multiplet plane. Nearly all horizontal multiplets have a poor resolution in fault azimuth, but this is due to the parametrization which is not relevant in such a

case. As expected, linear multiplets often have a poorly constrained dip or azimuth, and spherical multiplets show high uncertainties for dip and azimuth.

The best fitting-plane of multiplets 03911, 04416, 04432, 04572, 04693, and 04761, which are planar, are similar to the fault plane of the focal mechanisms computed by Godano et al. [2014] (misfits mean and max respectively of 8° and 20° for the strike, and 14° and 30° for the dip). The two other multiplets 03917 and 04493, which are linear, show a focal mechanism fault plane consistent with the Aigion or Fassouleika fault plane, but their best-fitting plane follows another orientation. This is certainly related to their linear character, for which the determination of a best-fitting plane is not a good feature. However, their major eigen-vector can be used to see if the mulitplet events follow the fault plane solution or define a different non-parallel direction. The 03917-multiplet is within its fault plane (only 3° of misfit), whereas the 04493-multiplet is 19° off the plane. It might indicate that the latter is at the intersection of two different structures.

Table 3.1 – Characteristics of the 24 multiplets. Mulitplet identification number (ID), number of events N, duration Δt [days], spatial dimension (ellipsoid major a, intermediate b and minor c axis length [km]), angles of the best-fitting plane (azimuth ϕ [°], dip θ [°]), and geometry type. The uncertainties for a parameter "p" are expressed as an acceptable range of values delimited by p_{min} and p_{max}.

ID	N	Δt	a [a_{min}; a_{max}]	b [b_{min}; b_{max}]	c [c_{min}; c_{max}]	ϕ [ϕ_{min}; ϕ_{max}]	θ [θ_{min};θ_{max}]	Shape
03911	29	5.2	955 [854; 1150]	319 [285; 384]	93 [83; 112]	259 [255; 262]	55 [52; 58]	plane
03917	20	72.8	1194 [1068; 1438]	264 [236; 318]	173 [155; 209]	312 [237; 361]	29 [13; 51]	line
03952	14	61.3	341 [305; 411]	177 [159; 214]	44 [39; 53]	124 [117; 127]	72 [65; 76]	plane
03999	13	1.5	953 [853; 1149]	439 [392; 528]	120 [107; 145]	274 [269; 281]	45 [39; 50]	plane
04116	14	7.6	1074 [960; 1294]	424 [379; 510]	238 [213; 286]	201 [165; 251]	11 [7; 29]	plane
04201	12	1.9	621 [555; 748]	295 [263; 355]	111 [99; 134]	268 [259; 276]	57 [44; 64]	plane
04204	19	2.3	417 [373; 502]	232 [208; 280]	186 [166; 224]	227 [114; 292]	2 [2; 55]	sphere
04380	14	5.4	1164 [1041; 1402]	403 [360; 485]	168 [150; 203]	287 [264; 305]	25 [20; 35]	plane
04416	23	36.4	1828 [1635; 2203]	592 [530; 714]	339 [303; 408]	283 [162; 314]	75 [61; 83]	plane
04432	15	10.8	853 [763; 1028]	270 [241; 325]	151 [135; 182]	283 [225; 315]	67 [47; 77]	plane
04469	11	4.4	549 [491; 662]	179 [160; 216]	76 [68; 92]	98 [67; 143]	58 [38; 70]	plane
04476	7	6.2	565 [505; 680]	79 [71; 96]	44 [39; 53]	300 [231; 339]	23 [19; 65]	line
04493	10	1.8	508 [454; 612]	95 [85; 114]	52 [46; 62]	81 [42; 161]	32 [21; 51]	line
04505	22	9.6	1378 [1232; 1660]	480 [429; 579]	177 [159; 214]	271 [264; 275]	67 [58; 72]	plane
04506	20	8.3	1390 [1244; 1675]	301 [269; 363]	114 [102; 137]	260 [241; 274]	20 [15; 27]	line
04542	10	1.0	291 [261; 351]	171 [153; 206]	66 [59; 79]	268 [236; 286]	31 [23; 42]	plane
04546	48	19.8	3037 [2716; 3659]	340 [304; 410]	224 [201; 270]	98 [73; 140]	25 [13; 36]	line
04572	17	2.2	878 [785; 1058]	461 [412; 555]	117 [105; 141]	262 [257; 267]	45 [41; 49]	plane
04605	15	3.2	426 [381; 513]	125 [111; 150]	96 [86; 116]	264 [128; 305]	57 [28; 70]	plane
04640	10	3.6	330 [295; 397]	218 [195; 262]	70 [63; 85]	227 [191; 252]	70 [61; 77]	plane
04652	12	12.3	613 [548; 738]	329 [294; 397]	228 [204; 275]	270 [185; 308]	53 [36; 77]	sphere
04693	7	2.6	524 [469; 632]	234 [209; 282]	73 [65; 88]	282 [224; 328]	41 [31; 53]	plane
04761	16	3.5	1966 [1758; 2368]	1051 [940; 1267]	205 [184; 247]	274 [265; 279]	40 [36; 44]	plane
12655	13	7.4	1660 [1485; 2000]	501 [448; 604]	175 [156; 211]	275 [263; 285]	49 [43; 58]	plane

Pore pressure diffusion

We calculated the internal diffusivity of each multiplet by assuming a pore pressure diffusion process and analyzing the spatio-temporal variations of seismicity. Based on Darcy's law and poroelasticity with a viscous fluid, the pore pressure perturbation p due to high-pressure fluid intrusion in the rock mass can be described by the diffusion's equation:

$$\frac{\partial p}{\partial t} = D\nabla^2 p \tag{3.1}$$

where D is the hydraulic diffusivity, typically ranging between 0.01 and 10 $m^2.s^{-1}$ in the earth crust [Scholz, 2002], and proportional to the permeability. When applied to seismicity induced by a transient injection of fluid from a point-like source, and considering a homogeneous isotropic medium, the distance (radius) d to the diffusing pressure front triggering the seismicity can be approximated by

$$d = \sqrt{4\pi D t} \tag{3.2}$$

where t is the relative start time of the injection [Shapiro et al., 1997].

The application of this model to natural earthquakes is however not straightforward because (1) the location of fluid source and its geometry is unknown and (2) earthquakes must occur at an early stage of the pore pressure diffusion to resolve the time dependence of the radius as $\sqrt{t}$ [Pacchiani and Lyon-Caen, 2010]. The initial propagation of pore pressure could be seismically silent. Here, diffusion coefficients are estimated considering the first event of the multiplet as an injection point and assuming an isotropic pore pressure diffusion. This starting point approximates the place of first fracturation, connecting the fluid reservoir to the activated faults.

3.3 Results

3.3.1 Fault and multiplet location

In the following we show, with the joint analysis of multiplet location, geometry and focal mechanisms, that the swarm is mostly related to the activation of the two parallel north dipping normal faults of Aigion and Fassouleika, outcropping on the southern coast of the rift. First, the southern border of the large microseismically active zone (Figure 3.1) matches at depth the youngest Lambiri-Selianitica-Fassouleika-Aigion fault system [Lambotte et al., 2014]. On a smaller scale (Figure 3.2), the first and easternmost two multiplets (12655 and 03952) are located in the downdip continuity of the Aigion fault, near its eastern edge, considering the reported dip angle of 50-60° inferred from the AIG10 borehole [Cornet et al., 2004] and the 2000–2007 microseismicity [Lambotte et al., 2014]. The westernmost multiplets (04761 and 04652) are coincident with the downdip continuity of the onland Fassouleika fault scarp assuming a similar dip angle. Eastward, the location of eight multiplets with similar normal focal mechanisms and depths, shows a tight alignment with the two previous ones, potentially outlying an eastward, yet unmapped, off-shore extension of the Fassouleika fault. Eleven other multiplets appear to be located in between the above clusters, showing a complex geometry of the Aigion-Fassouleika (AF) fault system at depth and suggesting the activation of a relay zone between these two en-echelon faults. These events seem to draw a third fault zone, with similar dip and azimuth as the AF fault system.

The 2003–2004 multiplets are located within the large scale microseismic layer identified by Lambotte et al. [2014] at the intersection with the AF fault system. Considering that: (1) the planar 04572-multiplet about 1.5 km north of the main structure has a ~45° dipping plane; (2) the normal focal mechanisms of the Fassouleika multiplets show dip angles slightly lowering with depth, from 60° to 50° [Godano et al., 2014], and (3) no microseismicity is reported beneath the seismogenic layer [Lambotte et al., 2014], we propose that the AF fault system roots in this layer. The complexity and the thickness of the multiplet structures (Table 3.1) would then be consistent with the broadening of the fault damage zone at its root [Kim et al., 2004].

3.3.2 Migration of the microseismic activity

Along and across fault migration

The spatio-temporal analysis of microseismicity shows an overall migration from ESE to WNW at around 50 m.day^{-1}, as already estimated by Bourouis and Cornet [2009]. This globally westward (over 10 km) and slightly downward (1 km) migration highlights the successive activation of the Aigion fault, of the relay zone, and of the Fassouleika fault. The swarm starts with the eastern-most 12655-multiplet, and first propagates upwards along the Aigion fault to the 03952-multiplet (see Figure A.2). The latter, tightly clustered and breaking the same patch of 50 m diameter [Duverger, 2014]), remains active during a whole month, suggesting repeater-like behavior, and thus some

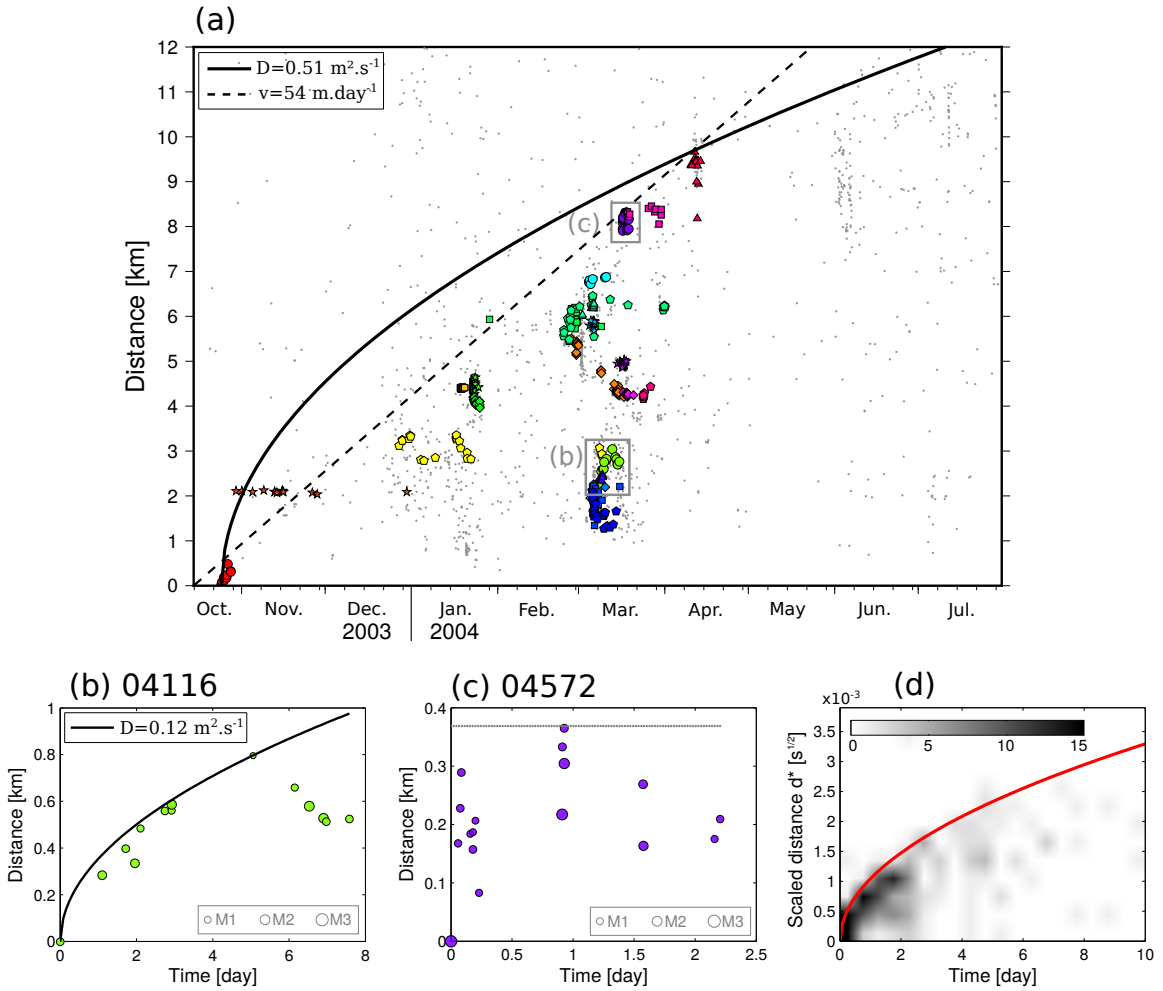

Figure 3.4 – Microseismicity migration. (a) Distance-time graph considering the first event of the 2003–2004 crisis as the spatial origin. Colored symbols indicate the events of the 24 main multiplets. Gray dots show the background microseismicity. The black curve represents the theoretical diffusion law (Equation 3.2) with a diffusivity of 0.51 $m^2.s^{-1}$. The dotted line shows a constant migration velocity of 54 $m.day^{-1}$. (b) Example of diffusion (04116-multiplet). (c) Example of fast activations (04572-multiplet). (d) Space-time event density for the 18 multiplets associated with a diffusion law, considering the first event of each multiplet as the origin. For each multiplet i with diffusivity D_i, the y-axis is defined by $d^* = d/\sqrt{D_i} = \sqrt{4\pi t}$.

aseismic creep. The activity then jumped a few kilometers to the WNW, 500 m within the hanging wall. From then on, small migrations started from central to western multiplets within the relay zone, whereas the main migration continued north-westward, activating multiplets on the Fassouleika fault. The illumination of the central multiplets on the latter led to a back-propagation of activity to the eastern multiplets of the relay zone, whereas the main migration reached the western-end of the Fassouleika fault (Movie S1). From Equation 3.2 [Shapiro et al., 1997] the global diffusivity is about 0.5 $m^2.s^{-1}$ for the whole seismic crisis (Figure 3.4.a), but one notes a better fit with simple constant migration velocity. The latter could be favored by an increased permeability of the fault zone resulting from its dilatancy during the creep [e.g., Cappa, 2009] induced near the pore pressure front.

Small scale migration on subfaults

At a smaller scale, we could estimate the internal diffusivity for 18 of the 24 multiplets (Figure 3.4.b and Figure S1 in Annex A). The 6 remaining multiplets (04432, 04505, 04506, 04572, 04640, and

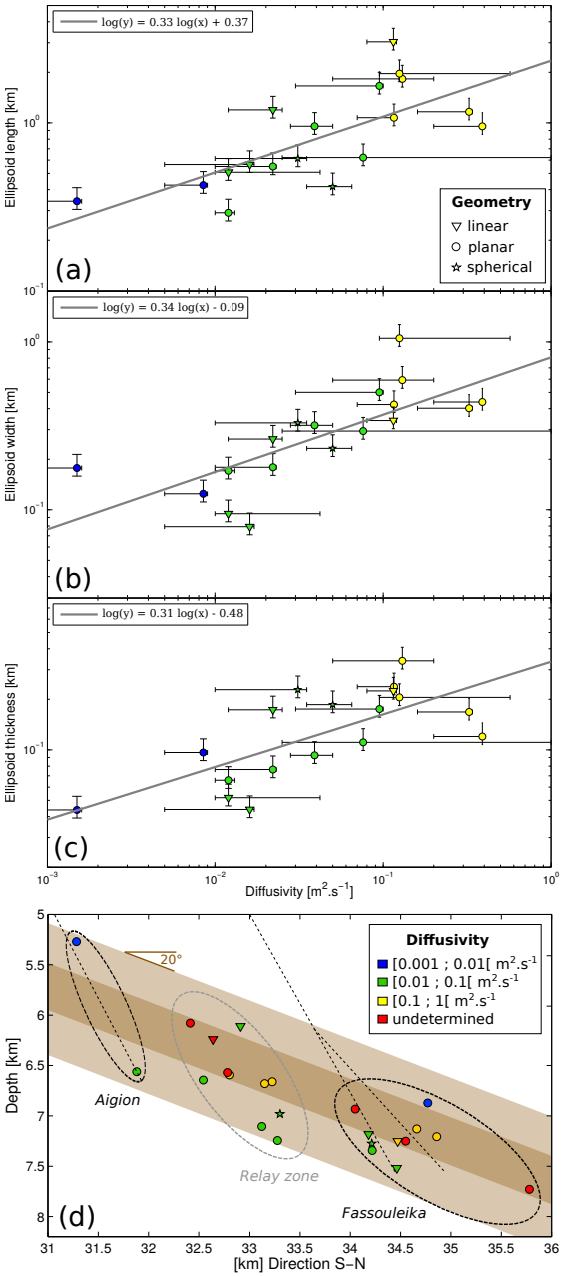

Figure 3.5 – Relation between intra-diffusivity, dimensions, and location of multiplets. Ellipsoid length (a), width (b) and thickness (c) of multiplets versus intra-diffusivity of multiplets in log-log scale. (d) Multiplet mean location in depth along the SN section. Undetermined diffusivities (red) correspond to the 6 multiplets showing nearly simultaneous ruptures along large distances. They reflect fast phenomena assimilated to very high diffusivities. High diffusivities (red-yellow) are concentrated in a 400 m thick, ~20 ° dipping layer (dark brown) central to the microseismogenic zone (light brown).

04693) show nearly simultaneous distant ruptures (Figure 3.4.c and Figure S1), so that no diffusion law could be adjusted to them. The estimated diffusivity values range between 0.001 to 0.4 $m^2.s^{-1}$ (Table 3.1) and present a positive correlation (cubic root scaling trend) with the multiplet dimension, as shown in Figure 3.5.a–c. We also note that for the subfaults, the diffusivity pressure front triggers most of the activity during 2–3 days (Figure 3.4.d), providing a possible evidence for a back front [Parotidis et al., 2004].

Internal diffusivity was then jointly analyzed with the geometry and location of multiplets (Figure 3.5.d). Using fitting ellipsoids and their aspect ratios, 18 multiplets are defined 'planar', 5 'linear', and 2 'spherical' (see Section 3.2.2 for details). With this classification, the geometry does not seem to be correlated with the intra-diffusivity or the multiplet epicentral position. However, on a SN vertical section, multiplets with high diffusivities (≥ 0.1 $m^2.s^{-1}$), or with nearly simultaneous activations, are concentrated within the core of the microseismic layer, along a thin band about 400 m thick, dipping 20°, whereas multiplets with lower diffusivities (< 0.1 $m^2.s^{-1}$) are above or below this band.

3.4 Discussion

3.4.1 Origin and diffusion mode of the fluids

The global and intra-multiplet diffusivities (0.5 $m^2.s^{-1}$ and 0.001–0.4 $m^2.s^{-1}$, respectively) are typical values of fluid diffusion found in fault zone contexts at crustal depth [Scholz, 2002]. In the geothermal Vogtlang/Bohemia region, Parotidis et al. [2003] report similar space-time swarm patterns, modeled with a diffusivity of 0.27 $m^2.s^{-1}$. In Corinth rift, the migration velocity of 50 m/day (~2 m/h) compares with that of a pore pressure front diffusion [e.g., Chen et al., 2012b], but is significantly smaller than that estimated for creeping faults, on the order of 100–1000 m/h [e.g., Roland and McGuire, 2009]. However, the multiplets found with nearly simultaneous distant ruptures suggest stress transfer or creep propagation. There is thus some evidence for marginal local creep or earthquake triggering by stress transfer, but the global swarm activity appears to be dominantly fluid-driven.

A few processes can lead to a slow build up of pore pressure at large crustal depths. A meteoric water overpressure effect is proposed by [Bourouis and Cornet, 2009] for the 2003-2004 swarm. However, our observation of an upward propagation of the seismicity in the early stage (from 12655-multiplet to 03952-multiplet) updip the Aigion fault contradicts this hypothesis. The overpressurized reservoir is thus probably at depth, either fed by upgoing mantellic fluids produced by the African subducting plate 50 km beneath the rift (as proposed by Bourouis and Cornet [2009] for the 2001-swarm), or by metamorphic processes within phyllosilicate-rich rocks in the seismogenic zone which may release structural water by dehydration reactions [Latorre et al., 2004].

Whatever the process for a slow pore pressure increase near the root of the fault system, it has eventually led to large-scale hydroshear processes on preexisting faults, triggering the detected microseismicity. These processes were possibly accompanied by transient creep, as was reported for Soultz [Bourouis and Bernard, 2007]. This large scale fracturation along several successive 0.1 to 1 km subfaults, is expected to have increased the local permeabilities within the fault system, which may explain the persistence of a large migration velocity.

3.4.2 Fault zone structure and the geological seismogenic layer

The detailed multiplet geometries provide new insights on the AF fault system. Our proposed system, consisting of two main subparallel en-echelon normal faults both dipping around 50–60°, provides the simplest explanation of the multiplet activity. The termination depth of both faults also fits standard values of aspect ratio (fault length-to-width ratio) [Wells and Coppersmith, 1994], with a 8–10 km length and 8–10 km width. Considering a Fassouleika fault restricted onland, a more complex fault model might also be proposed in which the north-eastern multiplets mark the south dipping Trizonia fault at depth, consistent with the nodal planes of focal mechanisms (within 15° dip angle).

At subfault scale, the cubic-root dependence of the multiplet size with its diffusion coefficient suggests that the larger the multiplet is, the higher the degree of fracturation is, increasing the permeability. This may arise from scale-dependent permeabilities [Guéguen et al., 1996], as larger fractured rock volumes statistically sample more permeable paths. The reported highly fractured permeable layer, around 400 m thick, centered within the microseismically active layer, may be the core part of a thicker (1–2 km) brittle geological layer of the Hellenic nappe stack [Jolivet et al., 2010]. Indeed, according to Latorre et al. [2004], the regional velocity change at 5–7 km depth seen from seismic tomography data could correspond to the tectonic contact between the karstic Gravrovo-Tripolitza limestone and the low-permeability Phyllite-Quartzite geological series. The latter, called Phyllade nappe, consists of phyllites, schists and quartzites with local intercalation of metavolcanic rocks [Koukouvelas and Papoulis, 2009]. Latorre et al. [2004] emphasized that

the specific characteristic of this geological unit, as well as its depth, may explain the seismicity concentration at about 6–8 km depth. Our study then strongly suggests that the intersection of the AF system with this layer produces a fractured zone building a long narrow permeable corridor in a low-permeability bulk, explaining the 1D pore pressure migration. The presence of a higher diffusivity in the core of this layer might be enhanced by the fault terminations, as faults tips are generally associated with high damage zones.

3.4.3 High pore pressure reservoir

The tomographic images by Gautier et al. [2006] also show a high $\frac{Vp}{Vs}$ anomalous zone at 8–9 km close to the bottom of the microseismic layer near the root of the Aigion fault, possibly revealing the top of a high pore pressure reservoir. This interpretation requires that the bulk of the geological layer sitting on top is impermeable and acts as a cap, except, temporarily along the channels created by the cross-cutting faults.

A schematic diagram (Figure 3.6) shows our interpretation of the mechanisms involved during the 2003–2004 swarm. We propose that slow changes of either strain or fluid pore pressure conditions near the deep fault system eventually reached a strength limit leading to a sudden permeability increase. This would create a hydraulic connection between a deeper reservoir, capped by the Phyllade nappe, and the bottom of the Aigion fault plane, following a process similar to the fault-valve model of Sibson [1992]. The pore pressure migration would then have continued along the most permeable paths, in the fractured corridor built within the geological layer and maintained by the seismic cycle of the AF fault system.

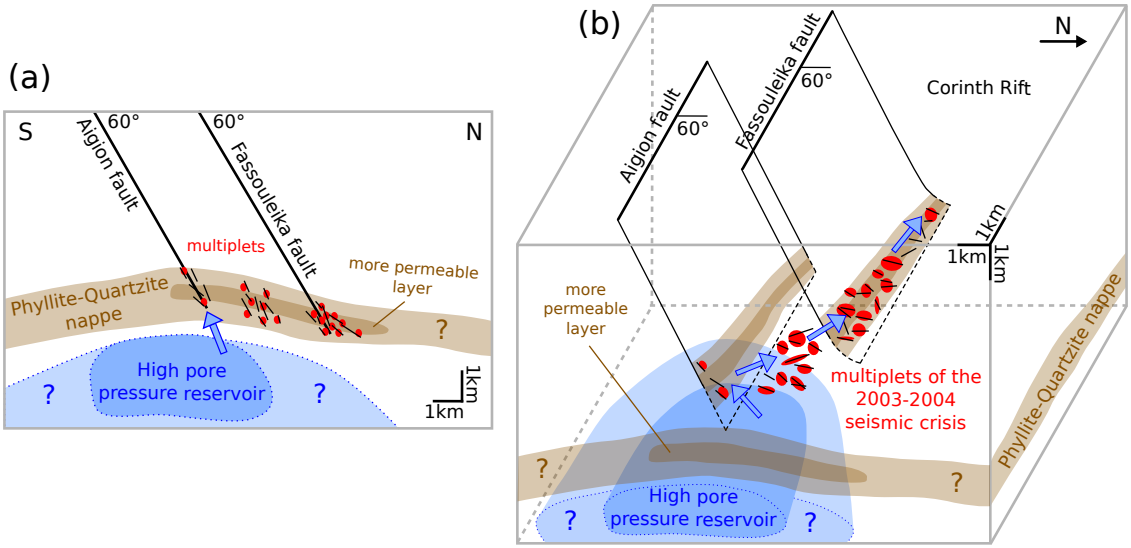

Figure 3.6 – Sketch of proposed mechanisms for the 2003–2004 swarm. (a) SN section. (b) 3D view. The intersection of a Hellenic nappe with the AF system creates permeable corridors allowing the microseismicity diffusion forced by a deep capped high pore pressure reservoir. A fault-valve behavior [Sibson, 1992] may initiate the seismic crisis.

3.5 Conclusion

The detailed analysis of the multiplets activated around 7 km in depth during the 2003–2004 seismic swarm in the western Corinth rift reveals a hydro-mechanical process, involving the migration

of a pore pressure transient over 10 km along a complex, permeable, fractured structure. It reaches an average velocity of 50 m/day and a diffusivity of 0.5 $m^2.s^{-1}$. This structure is defined by the intersection of two major normal faults with a deep low-permeability geological layer, possibly the Phyllade nappe. The highest local diffusivities, appearing in the core of the seismic layer, can be related to the largest subfault structures defined by the multiplets, and to the highest damage near the tip of the fault. The high $\frac{Vp}{Vs}$ region imaged by tomography below the main seismic layer is most likely a signal of high pore fluid pressure. This reservoir, capped by an impermeable layer, would be sporadically connected to the root of the faults above by sudden permeability changes of fractured channels. The pore pressure source, as well as the amount of aseismic creep in the area, still have to be investigated in more detail, in particular for quantifying their potential to trigger a large earthquake on the AF system. More refined tomographic images along with new studies of the most recent swarms in this area are still needed for a better characterization and quantification of the permeable paths and of the fluid pressure sources. Finally, this multiscale, high resolution approach of natural microseismicity diffusion is also relevant for the study of microseismicity induced by man-made fluid-injection, bringing valuable information on fault structure and permeabilities, useful for production and safety purpose.

Chapitre 4

Structures tectoniques actives et évolution des multiplets de 2000 à 2015

Sommaire

Dans ce chapitre, nous analysons les 16 années de données sismiques enregistrées par le réseau dense du CRL (*Corinth Rift Laboratory*), en utilisant les méthodes d'inter-corrélation de formes d'ondes et de relocalisation par double différence. L'objectif est d'améliorer la résolution de la localisation des hypocentres des microséismes de la partie occidentale du rift de Corinthe en exploitant et tirant bénéfice des propriétés des multiplets, afin d'imager finement les structures actives en profondeur.

Dans le but d'extraire les multiplets de la microsismicité globale du golfe, nous décrirons le prétraitement nécessaire aux données et les paramètres de calcul, puis nous présenterons la méthode d'identification et de classification utilisée. Nous introduirons en même temps la méthode de double différence et les paramètres choisis.

Ensuite, nous analyserons en détail la radiographie des failles et l'évolution des multiplets sur les 16 années disponibles, avant de discuter les variations spatio-temporelles de la microsismicité, permettant de mieux comprendre la déformation actuelle du rift ainsi que les aspects d'aléa sismique.

Les différentes parties de ce chapitre seront très prochainement soumises à publication dans le journal *Geophysical Journal International*.

4.1 Introduction

The Corinth rift has been studied for more than two decades, in particular on geological [e.g. Armijo et al., 1996], geodetic [e.g. Avallone et al., 2004; Briole et al., 2000] and seismological aspects [e.g. Bernard et al., 2006; Lambotte et al., 2014; Latorre et al., 2004; Pacchiani and Lyon-Caen, 2010]. However its seismic activity coupled with its deformation processes remains largely misunderstood and raises several mechanical questions.

The Corinth rift is an active asymmetric graben extending E–W over 100 km, where south coast uplifts of several millimeters per year over at least the last 0.3 My [e.g. Armijo et al., 1996; Rohais, 2007; Vita-Finzi, 1993]. The fault system (Figure 4.1) is mainly composed of onshore antithetic normal faults, with the main active faults cropping out on the southern coast and dipping north 40-60°. Some active offshore faults have also been identified in the middle of the gulf [Bell et al., 2008; Moretti et al., 2003; Stefanos et al., 2002, e.g.]. On the northern coast, the south dipping normal faults have been less extensively studied. Currently, the north-south extension of the rift is inhomogeneous, with a higher extension rate of around 15 mm.yr^{-1} in the western part than in the eastern part (10 mm.yr^{-1}) [Avallone et al., 2004; Briole et al., 2000]. The Corinth rift has one of the highest strain rate (about 10^{-15} s^{-1}) in the world. This deformation is the consequence of the back-arc extension due to the Hellenic subduction in the south and the dextral detachment of the North Anatolian Fault [Armijo et al., 1996]. In the history of the rift activity, its deformation has progressively been translated northward and dropped former long normal faults. The western tip of the gulf is the only part of the Corinth rift which has showed evidence of strike-slip motion [Beckers et al., 2015].

From a geological point of view, the first 5-10 km of the crust is made of the Hellenide nappe stack, composed of a succession of five different carbonate nappes. Three of them outcrop in the western and central Corinth rift (Figure 4.1). These geological structures are inherited from the past east-west convergence during the Miocene. They may have influenced the sedimentation and the fault segmentation [Ghisetti and Vezzani, 2004] and may play a role in the lateral variability of the seismicity distribution [Duverger et al., 2015; Lambotte et al., 2014].

The Corinth rift has been shaken by a few destructive M > 6 earthquakes per decade, making it one of the most seismically active region in Europe. For instance, in the 19^{e} century, two historical earthquakes that occurred in 1817 and 1888 have been associated to the Aigion fault and one that

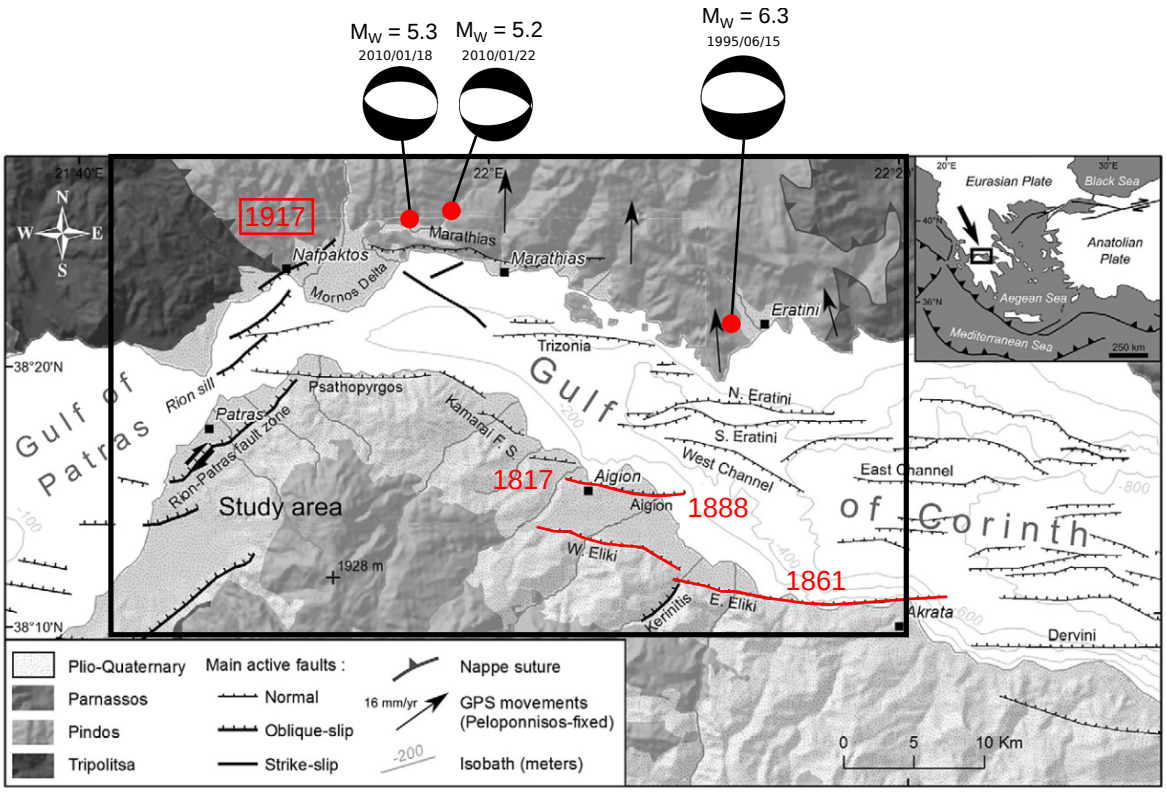

Figure 4.1 – Tectonic map of the central and western part of the Corinth rift. Onshore active faults are from Ford et al. [2013, 2009]; Palyvos et al. [2008, 2005], main offshore faults are from Beckers et al. [2015]; Bell et al. [2009]; Flotté et al. [2005]; Taylor et al. [2011]. Isobaths are from Bell et al. [2008] and GPS measurements are from Avallone et al. [2004]. Epicenters and focal mechanisms of magnitude M > 5 earthquakes are from Bernard et al. [1997]; Sokos et al. [2012]. Historical earthquakes of magnitude M ≥ 6 affecting faults in the study area (black frame) are mentioned in red by dates [Albini et al., 2017]. The distribution of the onshore Hellenide nappes and the Plio-Pleistocene sediments are drawn and described in the legend. The insert shows the Hellenic subduction in the south and the dextral detachment of the North Anatolian Fault. Modified from Beckers et al. [2015].

occurred in 1861 to the Helike fault [Albini et al., 2017] (Figure 4.1). However, some large recent earthquakes of the region do not seem to be associated to one of the principal fault planes visible at the surface. This is especially the case for the major earthquake (M_W6.3) in 1995, which occurred on a low-angle north dipping blind fault and has been felt in the city of Aigion [Bernard et al., 1997]. The analysis of the doublet of magnitude $M_W > 5$ earthquakes in 2010 emphasizes a link with shallow steep dipping fault structures, but has not been associated to any known major normal faults [Sokos et al., 2012]. The fault plane extensions at depth are not well constrained or sometimes totally unknown, so that linking an earthquake to a fault remains complicated even nowadays.

The microseismic activity follows a swarm organization, with alternation of intensive crisis and more quiescent periods. The controlling factor of these seismic swarms is still not well understood, but some crises have been explained by fluid circulations or pore pressure diffusions [Bourouis and Cornet, 2009; Duverger et al., 2015]. The microseismicity is mainly concentrated into a 3 km-thick layer below the gulf, slightly dipping north at very low angle (15°) [e.g. Gautier et al., 2006; Lyon-Caen et al., 2004; Rigo et al., 1996], which has fed a debate on the presence of either a large-scale detachment at 6-9 km depth acting as a shear zone [Bernard et al., 2006; Rigo et al., 1996], or a brittle-ductile transition zone [Hatzfeld et al., 2000]. The detachment has been interpreted as an inherited crustal-scale detachment [Jolivet et al., 2010] or a newly formed blind detachment [Lambotte et al., 2014]. Whatever the case, the observed normal faults at the surface seem to root into this layer, since almost no seismicity is observed below 9 km depth.

Using more than 200 000 events of moment magnitudes ranging from 1 to 4 in this paper, the objectives are (1) to present new insights into the western deep structures and their relationships with the faults observed at the surface, (2) to characterize the spatio-temporal evolution of the microseismicity, (3) to identify the interactions between seismic and aseismic mechanisms, and more generally, (4) to better assess the seismic hazard in the region. To do so, we performed waveform cross-correlations and a double-difference relocation coupled with a multiplet classification to identify small-scale structures within the microseismicity and to characterize their reactivity through years. Thanks to the seismological network extension, the idea is to extend the study of [Lambotte et al., 2014] to the westernmost part of the Corinth rift and perform an homogeneous analysis of the 16 years of data. After a description of the seismic network stations and datasets used, we explain the different steps of the relocation process and the multiplet extraction. Then we present the high-resolution images of the global relocated microseismicity, describing fault geometries at depth. Moreover, we statistically analyze the spatio-temporal evolution of the multiplets to propose different mechanisms or stress responses across the rift. We finally discuss the active fault structures in terms of possible mechanical sources and seismic hazard.

4.2 Data and methods

We take advantage of the dense distribution of recorded events within the western Corinth rift over the last two decades to obtain a high-resolution image of the microseismicity at depth. We proceed in three main steps: (1) cross-correlation of valuable waveforms, (2) relocation of the whole seismicity using a double difference technique and (3) identification of multiplets by hierarchical clustering. Here, we describe the dataset used and the different stages of the processes.

4.2.1 Seismic network and waveform dataset

We use the entire seismic archive, 16 years of data recorded by the *Corinth Rift Laboratory* network (CRLNET), from spring 2000 to winter 2015. This database includes around 225 000 events, slightly less than 14 million digital waveforms (800 Gb) recorded at about 15 different permanent or temporary stations in average. The first permanent stations of the *Corinth Rift Laboratory* (CRL) network have been installed in 2000 in the western part of the rift around the city of Aigion by a French CNRS team. Between 2000 and 2009, the network covers a 30×30 km area with 12 permanent stations recording at 125 Hz, equipped with three-component seismometers. From 2010, 4 new three-component velocimeters recording at 100 Hz have been installed further west to especially monitor the activity of Psathopyrgos zone. In 2013, an antenna with 7 broadband stations has been installed in Magoula, Central Greece, on the northern coast. Nowadays, the CRL network covers a 60x40 km area (Figure 4.2).

The CRLNET also includes 7 stations recording at 100 Hz equipped with broadband seismometers operated by the University of Athens (KALE and LAKA), and the University of Patras (ANX, EFP, SERG, UPR and VVK).

A post-trigger algorithm, based on a STA/LTA (short-term average/long-term average) ratio, is used to extract events from the continuous CRL stations. It detects an event when more than three stations trigger at about the same time (within 2 s) and picks the P and S phases when possible. Details on the detection and picking algorithms are available in Bourouis and Cornet [2009]. All events are automatically located using hypo71 software [Lee and Lahr, 1972], the 1-D velocity model of Rigo et al. [1996] and a V_P/V_S ratio of 1.80. Part of the dataset (around 10 %) has been manually picked for specific studies. In this case, we prefer to use manual picks than automatic ones. Inaccuracies in the phase picks and errors in the initial model used to predict the data affect the hypocenter locations errors. These last ones vary from several hundreds meters to few

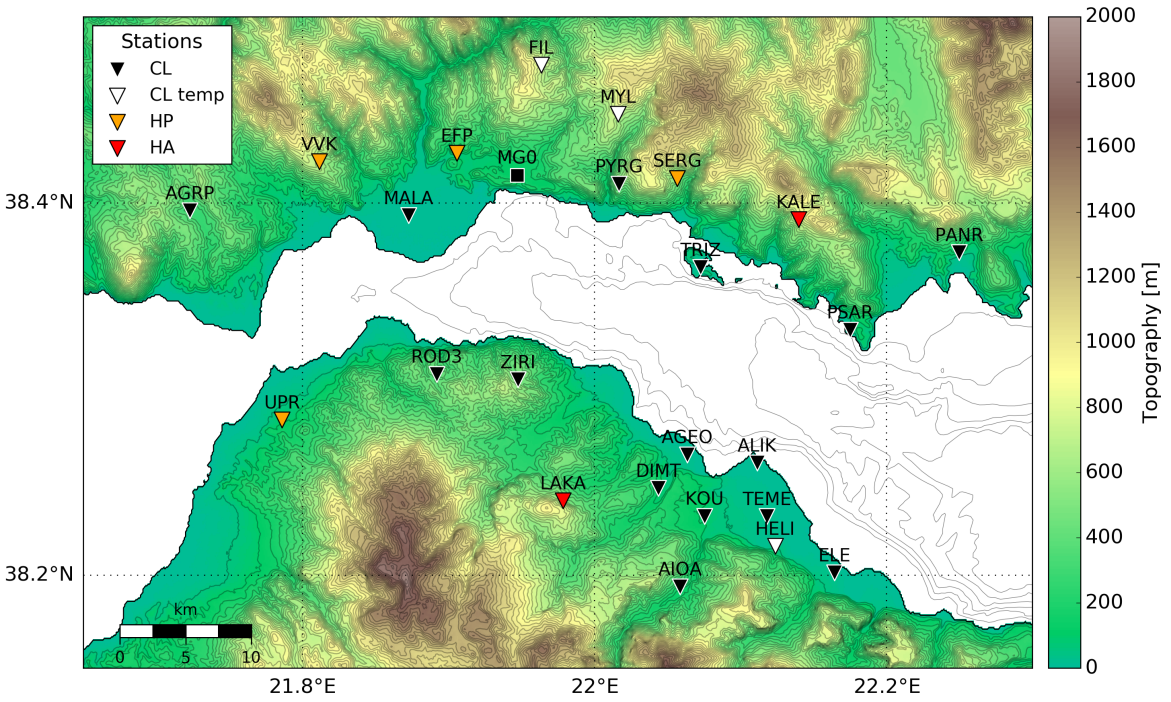

Figure 4.2 – Map of the seismic stations used for the cross-correlations and the relocation. Black triangles are CNRS stations. Among them, the easternmost stations (ALIK, AGEO, AIOA, DIMT, ELE, KOU, PANR, PSAR, PYRG, TEME, TRIZ) started recording in 2000–2001 but ELE was removed in 2006, KOU in 2011 and HELI was installed later in 2013. FYL and MYL were temporary stations used in 2010 to record the aftershocks of two M=5 earthquakes occurring in January 2010 in the area. ROD3 and ZIRI started recording in 2010, AGRP and MALA in 2012. MG0 (black square) is a CNRS antenna with 7 broadband seismometers set up in 2013. Orange triangles are stations operated by the University of Patras (one of these stations, ANX, is off-map, further north). Red triangles are stations from the University of Athens.

kilometers for events in the area covered by the network, with depths less well constrained than epicenters. The average standard errors for events outside the network can reach 5 km [Lambotte et al., 2014]. These errors are many times larger than the spatial dimension of micro-earthquakes themselves. Indeed, magnitude 1 to 4 earthquakes have source dimension typically ranging from 10 to 1000 m. The moment magnitude of events has been computed by spectral inversion of the seismograms [Satriano et al., 2016]. Thus, studying the seismic hazard of active faults or the physical properties of these earthquakes is hampered by these location uncertainties.

4.2.2 Computation of waveform cross-correlations

Here, we want to take advantage of the density of events recorded in the Corinth rift. A common signal processing tool, the cross-correlation can be used to both (1) identify multiplets by quantifying the similarity between different event waveforms, and (2) perform a relocation at local scale using the differential phase arrival times between earthquakes [e.g. Waldhauser and Schaff, 2008]. Such differential times are simultaneously inverted for estimating more precisely the distance between events [e.g. Got et al., 1994; Waldhauser and Ellsworth, 2000].

Cross-correlation method

The methodology used here takes advantage of the definition of a multiplet, which is a set of seismic events spatially close, occurring on parallel (coplanar or not) fault planes and so producing identical focal mechanisms. These events generate similar waveforms, which share common ray

paths between the source and the receivers. Sometimes, an individual asperity could also rupture several times in the observational period. In this case, the asperity generates the same waveforms, which follow exactly the same ray paths until the receivers. In this case, we called this group of repeated events, a repeater.

The recorded waveforms, at a station S, depends on four different terms:

$$S = F * G * R + N \tag{4.1}$$

where $*$ represents the convolution operation, F is the source function, G is the response of the medium due to the traveling wave, otherwise known as the medium's Green's function, R is the seismic station's receiver response, and N is random additive noise.

Considering a multiplet, the differences between waveforms recorded at a same station are mainly related to the random noise N and the medium response G. Nevertheless, we could consider that the pathway differences are negligible due to the spatial proximity of the different sources compared to the distance traveled to the station. Moreover, if we suppose that the properties of the medium do not change during the observational period, G remains the same for events within a multiplet. Finally, the waveforms of different events observed at different times that originate from the multiplet should be identical ± N.

To then quantify this similarity between two event waveforms $s_1(t)$ and $s_2(t)$ recorded at the same station, we use the time-domain cross-correlation function, which is defined as:

$$cc_f(\tau) = \frac{\int s_1(t) s_2(t+\tau) dt}{\int s_1^2(t) dt \int s_2^2(t) dt} \tag{4.2}$$

The delay τ for which the correlation coefficient CC = $max(c(\tau))$ measures the timelag between the two seismograms (Figure 4.3).

The terms in Equations 4.1 and 4.2 are considered continuous. However, recorded signals at the seismic stations are discretely sampled. We then define the seismic signal, $s(t)$, where the time is $t = n\,\Delta t$, n is the sample index $\in \mathbb{N}$, and Δt is the constant sampling rate. In the discrete domain, the cross-correlation function CC_f can be defined as:

$$CC_f(\tau) = \frac{\sum_n s(t_1 + n\Delta t)\; s(t_2 + n\Delta t + \tau)}{\sqrt{\sum_n s(t_1 + n\Delta t)^2 \; \sum_n s(t_2 + n\Delta t)^2}} \tag{4.3}$$

This representation of CC_f is only true if the mean of $s(t)$ is equal to zero. The cross-correlation coefficient CC is defined between -1 and 1. A coefficient equal to -1 indicates that the two waveforms are completely anti-correlated and 1 indicates that the two waveforms are completely correlated. For two multiplet events, the cross-correlation coefficient should be higher than 0.7–0.8. For two repeater events, it should be extremely close to 1, about 0.95.

Cross-correlation processing and optimization

Measuring arrival time differences by cross-correlation requires the choice of windows around phase arrival times for a pair of events. A battery of tests were conducted by Lambotte et al. [2014] to define correlation parameters that produce robust delay time measurements in an efficient manner for the Corinth rift. Based on these tests and some readjustments linked to the evolution of the CRL network from 2010, we choose the following input parameters to run uniformly across the entire network.

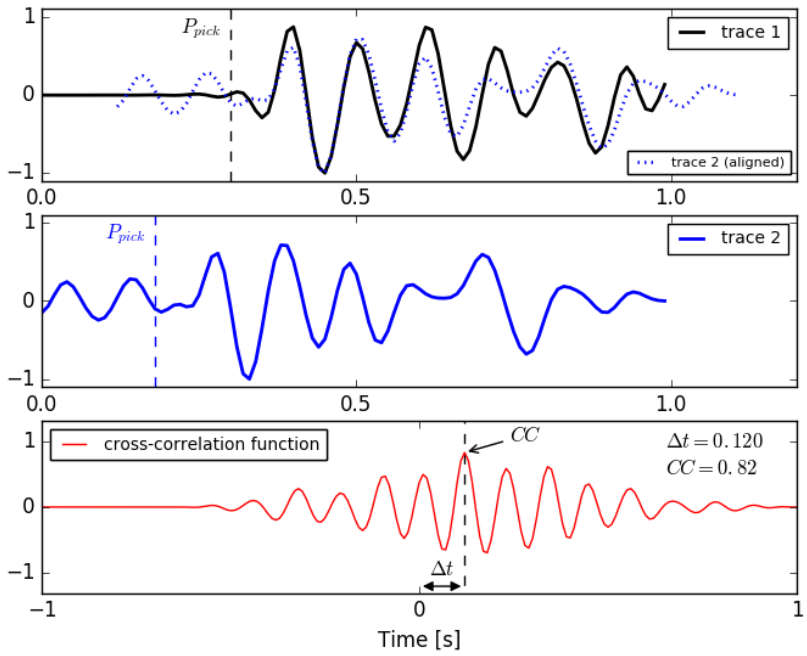

Figure 4.3 – Synthetic time domain cross-correlation. The black curve is the vertical component of an event from the database (2003.11.17-00.26.17) recorded at the station AGEO, with a high signal-to-noise ratio. The trace has been cut around the P-phase. The selected window starts 0.3 s before the P-arrival and lasts 1 s. Below, the blue curve is a synthetic trace obtained by adding random noise to the real trace, and the selected window is shifted by 0.12 s. The third panel shows the cross-correlation function (in red) of the two traces. To do so, padding zeros have been added before and after both traces in order to optimize the computation time. The second trace is successively moved along the first one and the correlation coefficient is estimated at each sample time. The final cross-correlation coefficient CC is the maximum of the function, here 0.82, and the corresponding time is the recovered time-shift between the two traces. The dashed blue line on the top panel is the shifted synthetic trace, aligned with the original one.

— Since the sampling rate at some given stations varies from 125 Hz to 100 Hz in the observational time (2000–2015), we downsampled all our seismograms at 100 Hz to standardize the database.

— Seismograms were filtered between 1.5 and 15 Hz. The instruments are reliable in this frequency band [Lambotte et al., 2014]. Moreover, according to Schaff and Waldhauser [2005] who studied California data with a similar size problem as ours, filtering from 1.5 and 15 Hz increases the number of useful cross-correlation measurements reducing long-period instrument noise and less similar high frequencies.

— Correlation measurements were made on 1 s time-window lengths for the P-wave train, and 2 s for the S-wave train. The waveform windows begin 0.3 s and 0.5 s before the P- and S-pick arrival time, respectively.

— The P-windows were extracted from the vertical component and the S-windows were computed on the two horizontal components (East and North).

— Lag times up to 0.5 s for the P- and 1 s for P- and S-windows are looked for.

Cross-correlations are computed first at the time resolution of one sample, which is 0.01 s for our data, and finally at subsample time resolution using a local polynomial fit (Figure 4.4). This procedure enables the measurement of delays within millisecond precision, and allows better estimations for large delays [Schaff et al., 2004].

Numerically cross-correlating all events with each other in the case of 225,000 events in the database, would be impractical because of the size of the problem. To reduce it and for the purpose of the relocation procedure described in section (4.2.3), we first divide the western Corinth rift into 10

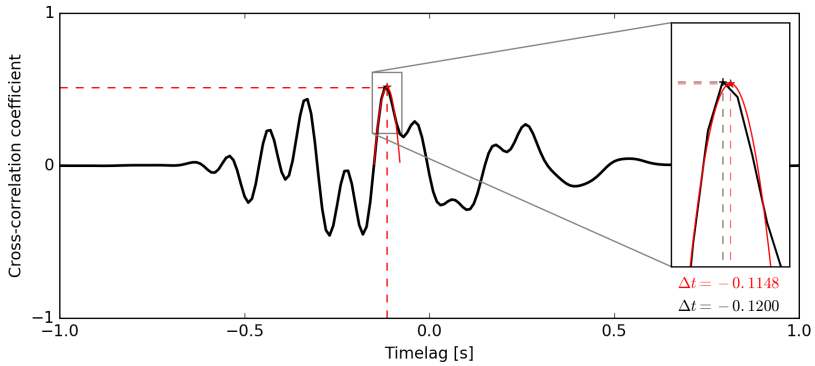

Figure 4.4 – Subsamble timelag resolution of the cross-correlation timelag. A polynomial fit is estimated locally in order to refine the timelag estimation in the cross-correlation measurement.

rectangles (Figure 4.5.b). The edges of boxes were chosen to lie as much as possible in region of sparse seismicity (Figure 4.5.a) and they overlap to ensure the spatial continuity in the seismicity.

In order to reduce the computational time, we do not cross-correlate every event with every other event of the same area, but only event pairs less than 5 km apart. This radius was chosen taking into account the preliminary hypocenter location uncertainty and the known degradation of the waveform similarity with interevent separation distance. We also scan the database event by event in occurrence time order, avoiding computation duplications.

A total of 15 billion cross-correlation measurements (P-waves on vertical component and S-waves on the two horizontal components) were performed. The computations were carried out on 10 nodes of the S-CAPAD [1] cluster, where each node is equipped with 2 Intel Xeon 2.90 GHz processors (2 x 8 cores), with 4 GB of RAM per core. Cross correlations were performed at a rate of about 30 million measurements per CPU hour.

Since the correlations operate on a station by station basis, they are parallelizable and can use any free processors. To reduce the storage volume of the outputs, binary output files were saved in HDF5 format for each station and each component per station. The results kept are the events list, event pair indexes, differential travel-times and cross-correlation coefficients.

The total processing time including input/output operations was approximately four weeks for the 10 areas, and the resulting cross-correlation measurement database is about 6.7 GB in size.

4.2.3 Double-difference relocation

The resulting cross-correlation time-shifts are then used to perform a high-precision relocation using double-differences of travel times [e.g. Got et al., 1994; Hauksson and Shearer, 2005; Waldhauser and Schaff, 2008].

HypoDD method

hypoDD is a software developed by Waldhauser and Ellsworth [2000] to determine high-resolution hypocenter locations over large distances. The inverse problem is solved by incorporating absolute travel-time measurements and/or cross-correlations P and S wave differential travel-time measurements between pairs of adjacent events recorded at common stations. This reduces the errors due to unmodeled velocity structures along the path.

1. Service de Calcul Parallèle et de Traitement de Données en sciences de la Terre
http://webpublix.ipgp.fr/rech/scp/index.php

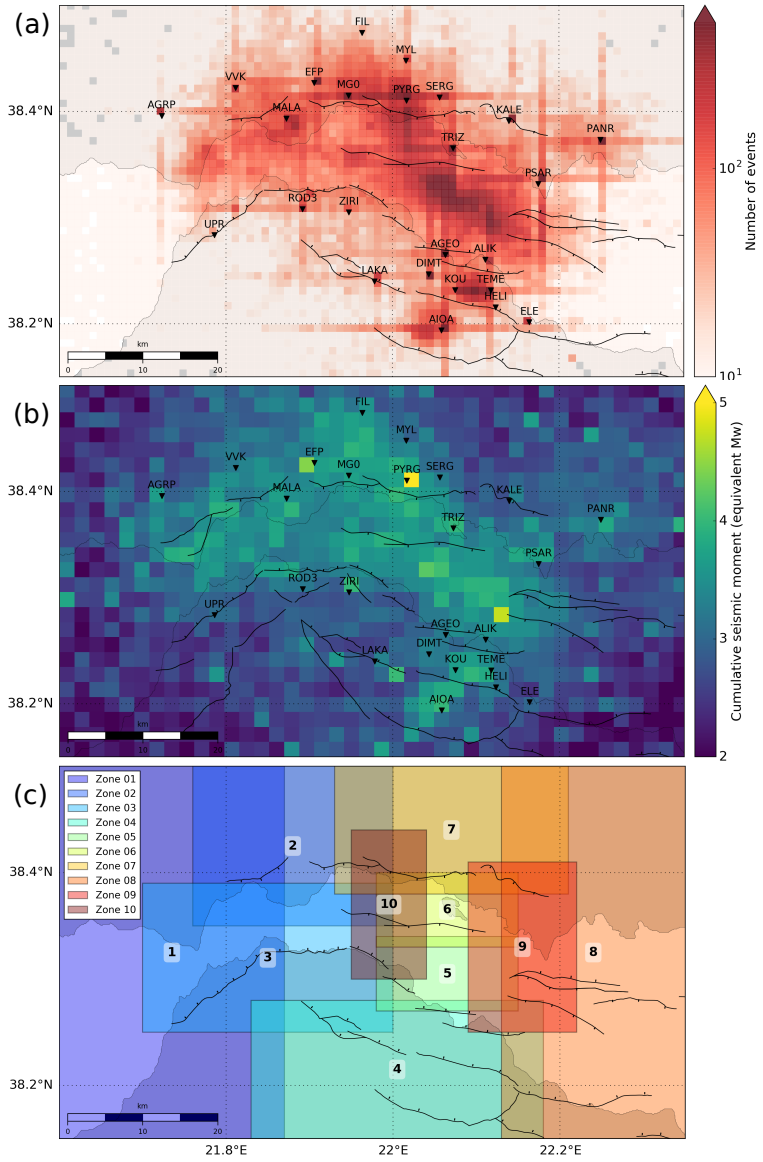

Figure 4.5 – Density maps over 15 years of seismicity in the western Corinth Rift and delimitation of zones for the relocation. (a) Map of the spatial seismicity density. The grid resolution is 1×1 km. The color represents the number of events per square-km in log-scale. The location of events is the original one obtained by hypo71. (b) Map of the cumulated seismic moment expressed in equivalent magnitude (M_W). The grid resolution is 2×2 km. (c) Colored boxes indicate areas used to parallelize the relocation procedure. They have been designed taking into account the seismic density and are overlaid to ensure the continuity in the relocated seismicity.

We use a damped least-square inversion method to minimize the residuals between observed and theoretical travel times differences (= double-differences). As in Lambotte et al. [2014], we solve the forward problem with the 1–D velocity model already used for routine absolute locations [Rigo et al., 1996] and the V_P/V_S ratio of 1.8.

The dataset contains the differential times based on catalog picks (automatic and manual) combined with the cross-correlations measurements for both P and S waves. The different types of data are a priori weighted as a function of their quality. Catalog data are weighted using the signal-to-noise ratios (SNRs) of the waveforms. SNRs are computed as ratios between the maximum absolute value of data window and noise window. SNRs of the P-phase are computed on the vertical component, using the 1 s length filtered P-window as signal and the 0.2 first seconds of this trace as noise (the P-arrival is at 0.3 s). SNRs of the S-phase are computed both on the East and North horizontal components, using the 2 s length filtered S-window as signal and the 0.4 first seconds of this trace as noise (the S-arrival is at 0.5 s). Then, SNRs are reduced between 0 and 1 using a logistic function with the equation:

$$f(x) = \frac{\mathrm{L}}{1 + e^{-k(x-x_0)}} \tag{4.4}$$

The logistic function is a common sigmoid curve, where L is the curve's maximum value, k is the steepness of the curve and x_0 is the x-value of the sigmoid's midpoint (Figure 4.6). We fixed L = 1,

k = 2.5 and x_0 = 3.0 after comparing the SNR with the pick quality (assigned by the operator for manual picks and by default for automatic ones) and the location quality (given as outputs by hypo71). In order to take into account the difference in accuracy between automatic and manual picks [Lambotte et al., 2014], we downweight the automatically picked data by increasing the mid-point of the sigmoid, x_0 to 3.5. The weight assigned to a pair of events for the catalog phase data is the smallest reduced signal-to-noise ratio. Cross-correlation data are weighted by their squared cross-correlation coefficient without any difference between P and S waves. Finally, since the S-phase weights (either for the catalog data or cross-correlated data) are computed on the north and east horizontal components for each event pairs, we keep the component with the highest weights.

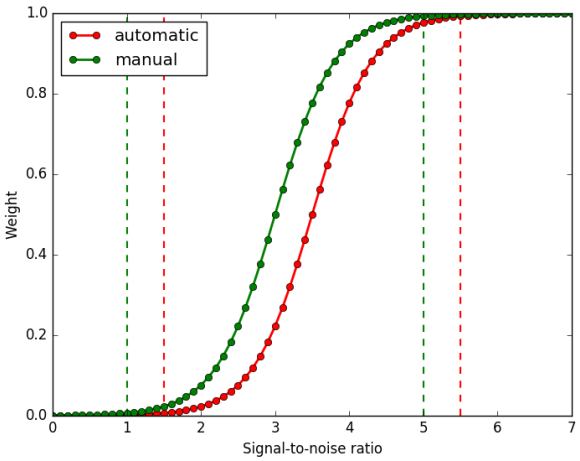

Figure 4.6 – Logistic functions used to weight catalog data. The signal-to-noise ratios of waveforms were reduced between 0 and 1 using a logistic function which is a sigmoid curve (see Equation 4.4). The constants L, k and x_0 were respectively set to 1, 2.5 and 3.5 for the manually picked data. The automatically picked data were downweighted by decreasing x_0 to 3.0 because of their poorer quality.

Relocation strategy

We parallelize the relocation process, similarly to Hauksson and Shearer [2005] by generating 10 rectangular boxes (Figure 4.5.c), because we could only fit travel-time data from a maximum of 30,000 earthquakes into each hypoDD inversion. As stated before, the cells are chosen in order to keep dense cluster of events in one cell, as much as possible. Since the boxes overlap, part of the hypocenters are calculated several times (as many time as the number of boxes they belong to). The final hypocenter is a weighted average of the different available hypocenters. The weight assigned to each solution is proportional to the number of linked (cross-correlated) events that the considered event has in each box.

For the relocation process, we exclude events having poorly constrained locations. The location quality is indicated in the hypo71 output from excellent to poor based on the RMS (in s), the vertical and horizontal errors (in km), the number of phase readings, the largest azimuthal gap and the distance to the closest station. For the automatically located events, we remove quality D events (31 % of the event catalog). Because of the network broadening in the observational time, we only keep events having at least 5 phases recorded at 3 different stations or more among data before 2010, and we keep those having at least 8 phases recorded at 6 different stations or more among data in 2010 and later (60 % of the total number of located events).

For the phase-pick differential-time catalog, we require pair wise connected events with a link strength of 6 differential times, and define strongly connected neighbor events, as pairs with 8 differential times. We restrict the number of neighbors to 100 per event within 5 km distance. Differential times from stations within 50 km from an event pair's centroid are used, and we save a maximum of 100 differential times per pair. These selective parameters generated a catalog of 115,000 events, a bit less than 24 billion pairs, with 187 million P-wave and 115 million S-wave differential time observations.

For the cross-correlation differential-time catalog, event pairs having at least 5 CC equal or greater than 0.85 are retained, resulting in 70,000 events, 736,000 pairs, 8 million P-wave and 6 million S-wave cross-correlation pair measurements.

First, we relocate each event by using 10 iterations that include the phase-pick differential times with a weight of 1.0, and the cross-correlation differential times with a weight of 0.01. After 5 iterations, a residual cut-off of six times the standard deviation is applied to remove outliers. Second, we continue the relocation process for 10 iterations, where the picks are given a weight of 0.2, the correlations are given a weight of 1.0 and a threshold of 4 km between cross-correlated linked pairs is applied. Third, we finish with 15 iterations, where the picks are down-weighted to 0.01, a threshold of 4 km between phase-pick linked pairs is applied, and the maximum distance between cross-correlated linked pairs is decreased to 2 km. A single damping factor is fixed at 80 for all the 10 grid cells.

In total, we relocate around 94,000 events (Figure 4.7.b) from the 115,000 selected (Figure 4.7.a) between 2000 and 2015 in the western Corinth rift. The new hypocenters show improved clustering both horizontally and vertically, creating a more focused picture of the complex distribution of seismicity. The hypoDD program does not estimate hypocentral errors directly and it was not feasible to carry out detailed error estimates here because of the large dataset size. Nevertheless, some statistical tests using a bootstrap technique have previously been done on a smaller dataset by Lambotte et al. [2014] to assess the relative relocation errors. According to the authors, which used the same relocation approach, the maximum relative relocation uncertainty is about 30 m in the center of the rift where the density of events and the quantity of cross-correlations is high, and larger at the edges where the network coverage is not good.

4.2.4 Classification of earthquake multiplets

We also use the cross-correlation coefficients to identify multiplets. Multiplets can provide additional information on the geometry of microstructures and are useful to characterize seismically active structures [e.g. Pacchiani and Lyon-Caen, 2010; Rietbrock et al., 1996]. Here, we present the adopted multiplet extraction strategy.

Event pair similarity

To classify events in multiplets, both manually and automatically picked events have been combined. Waveform similarity of P and S phases are evaluated using cross-correlation coefficients between pairs of events located in a same area 5 km apart (see Section 4.2.2). Here, we computed a similarity coefficient per event pair (i, j) using an average of the cross-correlation coefficients for P and S-phase weighted by the reduced signal-to-noise ratios, at the common stations:

$$Z_{ij} = \frac{\sum_k cc^{\mathrm{P}}_{ijk}\, w^{\mathrm{P}}_{ijk} + cc^{\mathrm{S}}_{ijk}\, w^{\mathrm{S}}_{ijk}}{\sum_k w^{\mathrm{P}}_{ijk} + w^{\mathrm{S}}_{ijk}} \tag{4.5}$$

where i and j are the two considered events, k is the common station, cc_{ij} is the cross-correlated coefficient of the event pair (i, j), w_i is the reduced signal-to-noise ratio of event i (see Equation 4.4), and $w_{ij} = min(w_i, w_j)$. With this formula, a high signal-to-noise ratio gives a high weight to the cross-correlation coefficient whatever its value. This increases the gap between similar and dissimilar events. On the contrary, a low signal-to-noise ratio does not highly affect the final similarity coefficient.

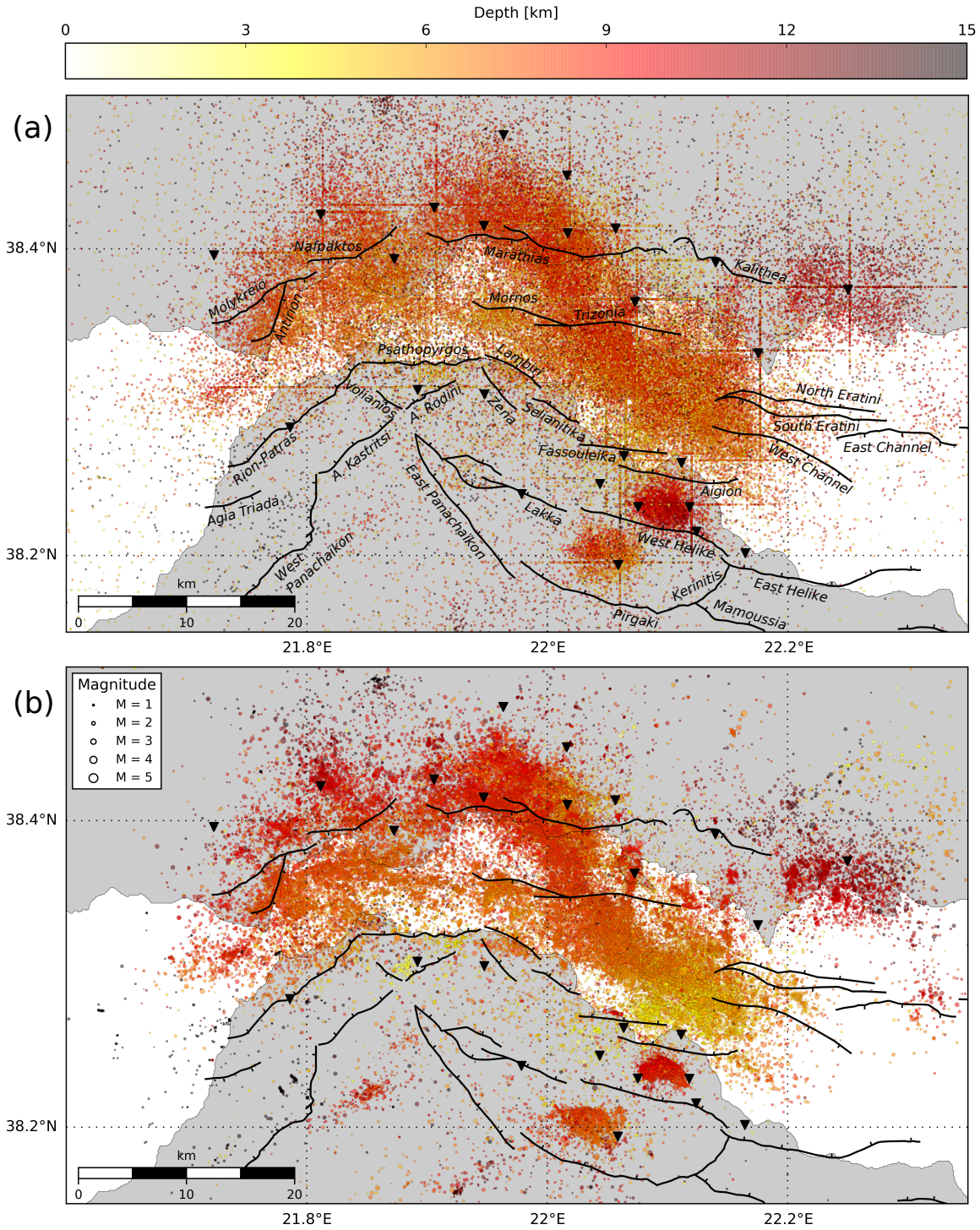

Figure 4.7 – Maps of original and relocated earthquakes. (a) Map of selected earthquakes for the relocation (n=115,000) from 2000 to 2015, recorded by 4 or more stations (triangles) with at least 6 picked phases. These events are plotted at their original location obtained with hypo71. (b) Map of the relocated earthquakes (n=94 000) computed with hypoDD. Dot size is proportional to the magnitude. Warm colors represent the depth of events. The black lines are the main normal faults of the region reported in Beckers [2015].

Finally, we obtaine a matrix of similarity coefficients Z_{ij} for all event pairs per area. Since coefficients $Z_{ij} = Z_{ji}$ (symmetric matrix) and $Z_{ii} = 1$ by definition, only values of the upper triangle are computed without the diagonal. This condensed similarity matrix is converted into a condensed dissimilarity matrix $D = 1 - Z$ to serve as a metric for the hierarchical clustering algorithm.

Hierarchical clustering

The hierarchical clustering is a method of cluster analysis, which seeks to build hierarchy of sets of observations from distance matrices. We used an agglomerative algorithm (or 'bottom up' approach) which starts with all individual observations and tries to link each data point to its nearest neighbor, making a family. It offers the advantage of creating a complete range of nested cluster solutions. While the groups are forming, a linkage method is needed to determine the distance between emergent clusters. We chose an average linkage criterion (or UPGMA : Unweighted Pair Group Method with Arithmetic Mean [Sokal, 1958]), which is the mean distance of the pairwise distances between cluster elements. The linkage between two clusters $\mathscr{A}$ and $\mathscr{B}$ can be written as:

$$L = \frac{1}{|\mathscr{A}|\,|\mathscr{B}|} \sum_{i \in \mathscr{A}} \sum_{j \in \mathscr{B}} d(i,j) \tag{4.6}$$

where $d(i,j)$ is the distance, or dissimilarity in our case, between events i and j. This computation allows to create a dendrogram, which is a figurative tree diagram illustrating the arrangement of observations.

Finally, in order to generate clusters, we have to select a distance cut-off (dissimilitude cut-off in our case) in the dendrogram to divide the dataset into multiplets. Another way to see the problem is to determine the number of clusters we want.

However, the similitude matrix or the dendrogram can not be visualized with our large dataset of around 30,000 events per rectangle. To deal with this issue and estimate a proper threshold for our study, we analyze a smaller dataset including already well-known multiplets. We mix events from two multiplets of the 2003-2004 seismic crisis, which was analyzed in Duverger et al. [2015], with random selected events of the same spatial area. We obtain a total of 52 events with magnitude ranging from M = 0.7 to M = 2.4. We repeat exactly the same processing steps as for the global dataset, and we obtain the similarity matrix and the dendrogram presented in the Figure 4.8.

With only the visualization of the similarity matrix sorted by link strength, we can identify at least a small well-defined cluster in the lower right corner and a larger cluster less constrained in the upper left corner. This last one could also be divided into two distinct families. When looking at the dendrogram, we observe the tree of connections between all events with the different gathering steps. We succeed in recovering the two known multiplets for $D_c = 0.32$. The other random events are single events. If we decrease a little bit D_c to 0.30, the larger multiplet is split in two. With this test, we see that a small change in D_c could strongly modify the number of extracted families, but the kernel of each family will always be preserved.

The threshold value for multiplet classification will strongly depend on the purpose of the study we want to conduct. In order to allow microstructure studies and obtain an accurate image of individual multiplet geometry, the similarity cut-off ($S_c = 1 - D_c$) has to be quite strong, around 0.8. A weaker criteria, around 0.7, results in the classification of more events in clusters valuable for spatio-temporal studies. However, below 0.7, event waveforms cross-correlate quite easily and the algorithm accepts some dissimilar event pairs. A stronger criteria ($S_c = 0.9$) results into highly correlated clusters, close to repeater behavior.

A noise cross-correlation test was also performed on each station to quantify the confidence of similarity coefficient and help in the truncation process (see Supplementary Section 4.A). The

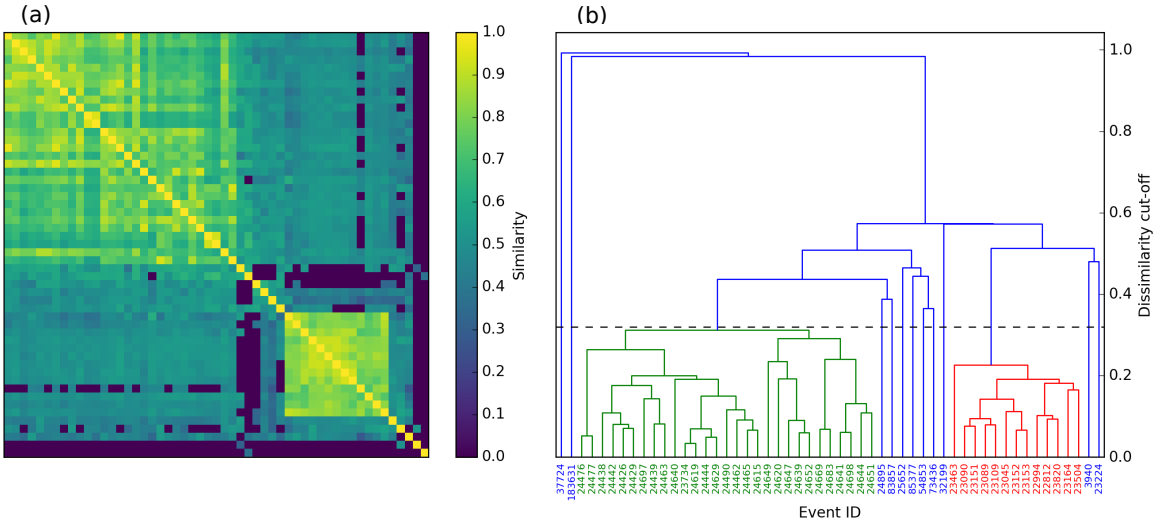

Figure 4.8 – Similarity matrix and dendrogram. (a) This matrix contains similarity values for each event pairs computed for events of two known multiplets from the 2003-2004 seismic crisis and random events from the CRL catalog. (b) The hierarchical clustering dendrogram computed from the matrix. This figurative tree shows a truncated dendrogram forming two distinct clusters (green and red) and isolating the remaining events (blue). The horizontal dashed line depicts the dissimilarity cut-off used (D_c = 0.32) to retrieve the known multiplets. The remaining events do not correlate (for the considered threshold) with other events.

average cross-correlation coefficient of noise windows is around 0.4 and can tend towards 0.5 for some stations (AGRP, ELE, KOU for instance) possibly due to their resonance characteristics caused by site effects. The average probability over all stations to have a CC ≥ 0.5 is greater than 10%.

Extracted families

Here, we first quantify the number events classified in multiplets and in doublets as a function of the dissimilarity cut-off D_c (Figure 4.9). We observe that the maximum number of families created is obtained for a similarity cut-off S_c of 0.7 or 0.8 (D_c of 0.3 or 0.2). This means that high threshold (low D_c) deletes some families and reduces the number of events per family (rising the proportion of doublets among multiplets), whereas a lower threshold (higher D_c) tends to merge families together. The proportion of doublets among multiplets goes from 15 % for D_c = 0.5 to almost 75 % for D_c = 0.1 in average on all zones.

We choose a S_c = 0.8 to perform the structural analysis (see Section 4.3), the following description of multiplets or doublets will then correspond to this threshold value. In this case, 70% of the events of the CRL database are classified in multiplets, among those 66 % are in doublets.

In order to distinguish repeaters from multiplets, we conduct a more detailed analysis with a stronger threshold. Among families obtained with a 0.8 similarity cut-off, we cross-correlate multiplet events with a 5 s waveform window encompassing the P- and the S-phase together. Indeed, repeater events should preserve the differential time between the P- and S-phase apart from the high waveform similarities. We then apply a high similarity threshold of 0.9 to construct repeater families.

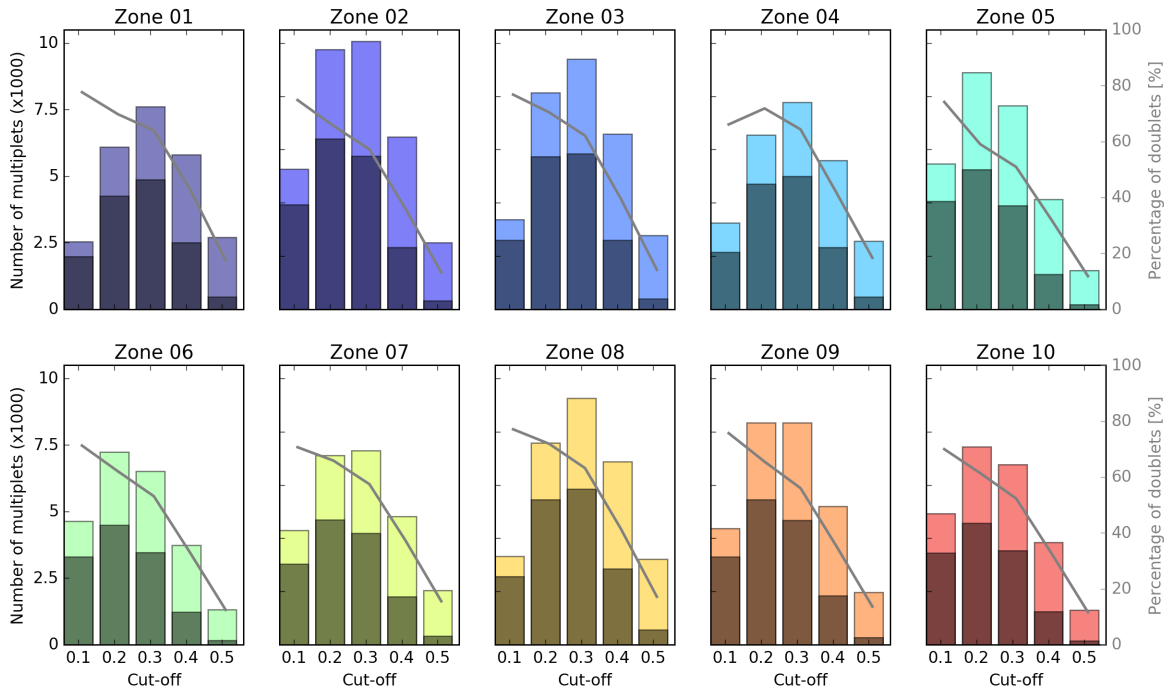

Figure 4.9 – Number of families created as a function of dendrogram truncation. Histograms of the number of multiplets (colored) and doublets (shaded) for each zone as a function of the dissimilarity cut-off. The gray line stands for the percentage of doublets among multiplets. The different zone numbers are defined in the Figure 4.5.c

4.3 Results

After the relocation stage and the multiplet extraction, we obtain a high-precision image of the microseismicity at depth with the clusterization of families of similar earthquakes. The Figure 4.7.b presents the entire western Corinth rift relocation map over 16 years, with two vertical cross-sections oriented N-S and E-W. Firstly, we clearly observe that the seismicity is not distributed homogeneously over the length and width of the gulf. The seismicity is mainly concentrated between 5 and 10 km depth with few activity above 4 km.

For the presentation of the results, we divided the studied area in three main sectors: the central zone (ZC), the western zone (ZW), and the westernmost zone (ZM), which correspond to different seismic rate and spatial organization of the microseismicity (Figure 4.10.a). We also introduced some acronyms for specific structures which will be described in this section: the North Eratini fault zone (NEZ), the Transition zone (TZ), the Trizonia Island zone (IZ), the Aigion–Fassouleika fault zone (AFZ) and the Rion–Patras and Psathopyrgos fault zone (RPZ).

In order to guide the description of these structures, we present 8 vertical sections across the rift in the Figure 4.11 and a dozen more in the Supplementary Figure 4.31. The spatial extension of these cross-sections are presented on the map, Figure 4.10.b.

4.3.1 Large-scale microseismicity patterns

The absence of shallow events makes difficult to evaluate the geometry of faults at depth and to constrain their dips. However, analyzing thinly clustered events in several cross-sections help to define and interpret their geometry. The first global observation looking at the different cross-sections (Figure 4.11) is that the biggest events (M > 3) are often located just under or in the deeper part of the main clusters.

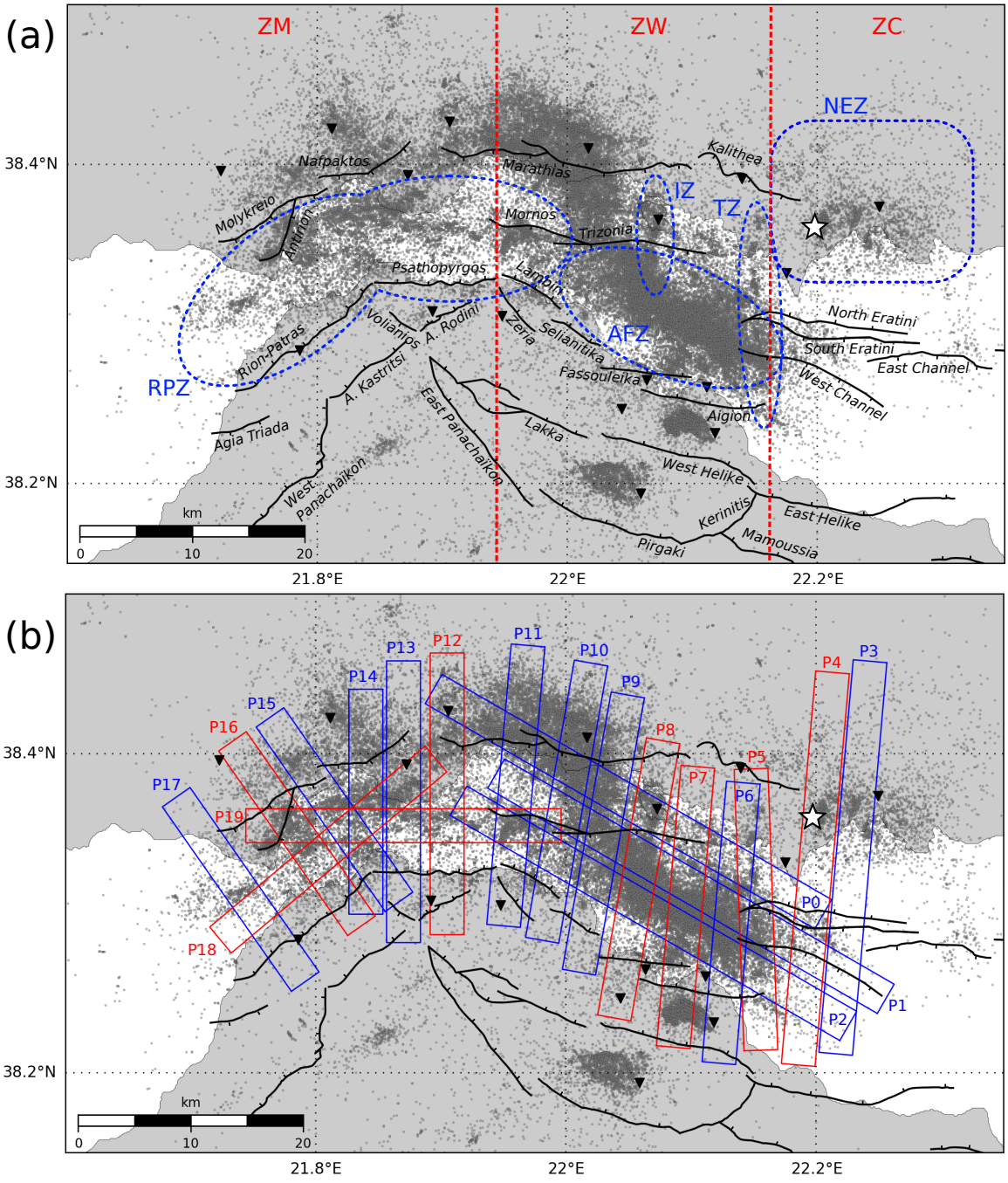

Figure 4.10 – Main structures discussed and clusters illuminated by the relocated seismicity. (a) Location of the different sectors delimited with red lines and the main structures / clusters (blue ellipses) discussed in this section. The initials are associated to names defined and used in the text. The black lines are the main normal faults of the region reported in Beckers [2015]. (b) Location of the cross-sections detailed in Figure 4.11 for the red rectangular boxes, and in the Supplementary Figure 4.31 for the blue rectangular boxes. The gray dots are the relocated earthquakes. Black triangles indicate the seismic stations. The white star locates the M_W6.3 1995 earthquake.

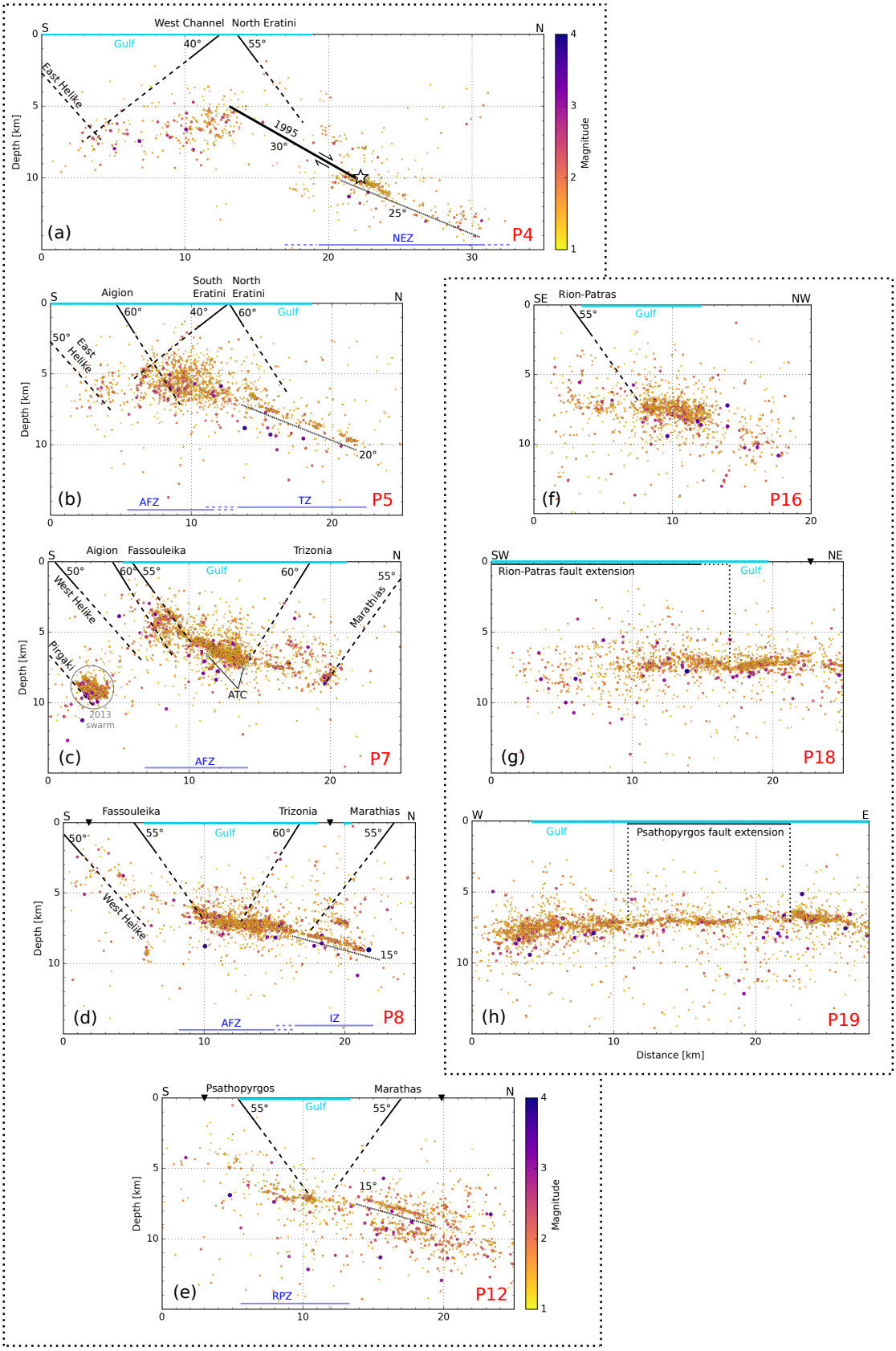

Figure 4.11 – Vertical cross-sections along the western Corinth rift. They are identified by red rectangles in Figure 4.10.b. Bold black lines indicate the major onshore and offshore faults, with dashed extrapolation of the surface dip at depth. Light blue lines at the surface represent the offshore rift. Black triangles at the surface are the seismic stations. Dark blue lines at panel bottom represent the extension of zones defined in Figure 4.10.a and in the text (NEZ: North Eratini Zone; TZ: Transition Zone; IZ: Trizonia Island Zone; AFZ: Aigion-Fassouleika Fault Zone; RFZ: Rion-Patras Fault Zone). The color scale corresponds to the moment magnitude of events. The white star in (a) locates the M_W6.3 1995 earthquake, which ruptures a blind fault plane dipping ~30° and drawn in bold black line.

The central part (ZC) versus the western part (ZW)

The western part (ZW) concentrates a mean of more than 10 events per day since 2000 and up to hundreds of events during swarms. Its seismicity is mainly located in the middle of the rift, offshore (Figure 4.10), between 4 to 10 km depth, in a 1–2 km thick layer gently dipping north (Figure 4.11.c-d). Seismicity structures are complex and highly variable over short distances.

On the contrary, the central part (ZC) shows a lower seismicity rate with a seismic gap in the middle of the rift (Figures 4.10 and 4.11.a). Few small swarms are located under the northern coast at a depth larger than 10 km, in a 1 km thick layer, dipping 25°N (NEZ). The seismicity continues deeper further north, reaching almost 15 km depth. The fault system of ZC is shifted to the north compared to ZW, and its seismicity is deeper. This clear discontinuity in the seismic activity and the tectonic settings occurs over a small distance range (5 km) and will be described in more details as TZ in the Section 4.3.2.

The northern seismicity of the ZW mainly corresponds to the aftershock sequence after a doublet (M_W5.3 and 5.2) occurring in January 18th and 22nd 2010, close to the Efpalio city [Ganas et al., 2013; Sokos et al., 2012]. These events are the largest occurring in the western Corinth rift since the Aigion one of M_W6.3 in 1995. Hypocenters of the first and second main shocks are respectively relocated at (38.428° N, 21.890°) at 11.5 km depth and (38.441°,21.964°) at 10.5 km depth. Our epicenter locations are in agreement with the previous estimates reported and compiled in the Table 1 of Ganas et al. [2013]. Our depth estimate of the January 18th event is among the deepest proposed in other studies, which are ranging from 2 km to 12 km. The constant pattern retrieved over all studies is that the second mainshock is systematically shallower than the first one. According to Sokos et al. [2012], the rupture of the first event most likely occurred on a 55° blind south-dipping nodal plane whereas its aftershocks and the second event are connected to a north-dipping structure. The results of our global relocation do not more precisely validate these interpretations, so we attempted another relocation of the aftershock sequences independently. However, these new results did not bring new valuable information compared to others. The aftershocks are located between 5 and 9 km depth and it is hard to associate them with any structure at depth. Sokos et al. [2012] noticed that aftershock clusters seem to be bounded by NE-SW strike-slip faults marked by earthquake strike-slip mechanisms at the western and eastern termination of the sequence. Our results support these observations in that our relocated aftershocks stay confined in the same spatial area.

The westernmost part (ZM) versus the western part (ZW)

In the westernmost part of the rift (ZM), the seismicity seems more thinly clustered than in the western part (ZW), where larger and laterally extended swarms are observed. This visual impression has to be nuanced by the fact that no station was installed before 2010 in the ZM. If we only consider data above the completeness moment magnitude $M_c = 1.2$, from 2011 when the network covers the full area, we do not observe denser and larger spatially continuous swarms in the ZW than in the ZM, but sequences of small clusters detached from each other.

Clusters in the ZM are mainly associated to the E-W Psathopyrgos fault and the NW-SE Rion–Patras fault, which follow the south coastline (Figure 4.7). The lateral extension of clusters is also parallel to the two faults. The seismicity is mainly located between 5 and 10 km depth, in a really thin layer of about 200 m around Psathopyrgos fault (Figure 4.11.e), but in a 2 km thick layer around Rion–Patras fault (Figure 4.11.f), both gently dipping to the N-NW. The westernmost seismicity is a bit less well resolved at depth due to the network coverage, possibly explaining the larger thickness.

Moreover, we observe a seismic gap between the western part of the Marathias fault and the Mornos fault (Figure 4.7), at the transition between the ZW and the ZM. Either the seismicity occurs north of the Marathias fault, under the northern coast and follows the coastline, or it occurs

along a E–W line in the continuity of the mapped-extension of the Trizonia–Mornos faults, following likely the Psathopyrgos fault plane at depth (Figure 4.11.e-h).

4.3.2 Fault zone structures

The North Eratini fault zone (NEZ), a deep structure

The North Eratini fault zone presents a specific seismic behavior linked to the blind offshore fault which ruptured in 1995 [Bernard et al., 1997; Lambotte et al., 2014]. The deep seismicity located at more than 10 km depth under the northern coast seems to be in the continuity of this low-angle rupture plane dipping north ~30° [Bernard et al., 1997] (Figure 4.11.a). Moreover, according to Lambotte et al. [2014] the multiplets at the root of the fault show a similar dip around 30°. Either the microseismicity occurs directly on the deeper part of the blind fault plane, which then could be longer than previously proposed, or the microseismicity nucleates at the edges of the fault plane and delineate its depth termination. This new relocation makes some deeper events appear further north than previously shown in Lambotte et al. [2014], which are also in the continuity of the seismic layer. The extension of the North Eratini fault dip (55°) at depth also coincides with the southern limit of the microseismicity.

The transition zone (TZ), a structural boundary

The ZC and the ZW are clearly separated by a thin structure oriented N–S shallowly dipping north and containing numerous clusters (Figure 4.10). This discontinuity is not only visible in the seismicity distribution as already mentioned, but also in the geomorphological structures. This was already discussed by Lambotte et al. [2014], who identified a northward shift of the whole normal fault systems by 5-10 km at the transition between the Trizonia, the Aigion, and the West Helike faults with the North Eratini, the South Eratini and the East Helike faults. The E–W fault extension of the Lambiri–Fassouleika–Aigion fault system ends at the TZ. Moreover, Lambotte et al. [2014] noticed that the structural boundary coincides with the transition between a narrow part of the rift with shallow bathymetry further west (the Channel and the Delphic Plateau), and an older, wider, deeper part of the rift further east (the Mornos Canyon leading to the Corinth abyssal plain) [Heezen et al., 1966].

The integration of the 2008–2015 data to the 2000-2007 dataset used in Lambotte et al. [2014] better highlights the discontinuity. The TZ is more clearly outlined by a north-south line of persistent clusters, which form a swelling of ~ 2 km high (Supplementary Figure 4.31.b-c). This seismic alignment also delineates the western boundary of the 1995 earthquake rupture plane [Bernard et al., 1997], where no or very few microseismicity has been recorded since. The origin and the nature of this structure is not yet well understood, but it has the same orientation as the Hellenic nappes [e.g Jolivet et al., 2010] inherited from the past convergence during the Miocene.

The Trizonia Island zone (IZ), a second parallel structural boundary

As for the TZ, the Trizonia Island zone (IZ) shows a north-south alignment of several clusters, with sparse seismicity on each side (Figure 4.10). At depth, we observe that this deeper seismicity is contained in a very thin layer, around 200 m thick, and is gently dipping north 15° (Figure 4.11.d). On the contrary, the seismicity under the gulf is concentrated on a 1-2 km thick layer, almost flat, which grips the root of the Fassouleika fault on the southern coast. The change from a thick flat layer under the gulf to the northern thinner layer of the IZ seems to coincide with the projection of Marathias fault plane at depth dipping 55°. The IZ is a mimic of the TZ in terms of seismicity alignment, but does not seem to be associated to a fault system discontinuity.

The Aigion and Fassouleika fault zone (AFZ), a shallower activity

In the AFZ, the microseismicity clearly outlines the Aigion fault and the Fassouleika fault up to 3-4 km depth (Figure 4.11.c). The dip of the structures is consistent with the one observed at the surface (50-60°), also constrained by the AIG10 borehole [Cornet et al., 2004] which is crossing the Aigion fault at 1 km depth, and is consistent with the geometry and the fault plane solutions of multiplets [Duverger et al., 2015; Godano et al., 2014]. The faults are rooting in the dense seismic layer, 1-2 km thick, less dip. The fault system is better outlined by the microseismicity over the whole 2000–2015 period than it has been shown in previous studies over a restricted observational span [e.g. Lambotte et al., 2014]. Some kilometer-long structures are observed in the seismic layer but with an antithetic direction (ATC in Figure 4.11.c), parallel to the Trizonia fault plane extension. The Trizonia fault seems to behave as a limit of the thick seismic layer, which further north becomes a really thinner layer aligned on a 15° dip plane as for the TZ and the IZ (Figure 4.11.c).

The Rion-Patras and Psathopyrgos fault zone (RPZ), a connection between two gulfs

We have seen that the microseismicity in the westernmost part of the Corinth rift could appear to be less dense, but this is actually the effect of the late widening of the network. The two main normal faults on the southern coast of the rift, the Rion-Patras and the Psathopyrgos faults, meet at the surface with a high angle change in strike. The observed microseismicity is mainly following these structures. The relocated clusters are aligned on a E-W straight line parallel to the Psathopyrgos fault, in the middle of the rift, and then turn parallel to the Rion-Patras fault, following the coast line at N45°E. We also observe some seismicity under the Rion-Patras fault, in its footwall, which is possibly connected to the inland Kastrisi fault or related to the Hellenic nappe stack (Figure 4.11.f).

The cross-sections (g) and (h) of the Figure 4.11, which are parallel to the Psathopyrgos and the Rion-Patras, present nice pictures of the seismicity occurring along the two fault planes. The known surface extension of the Psathopyrgos and the Rion-Patras faults are reported on the cross-sections. The seismicity is mainly located around 7 km depth in a layer varying from hundred-meter-thick to kilometer-thick. The location of the south-westernmost seismicity is not well defined due to the poor seismic network coverage there, explaining the large depth sparsity in the Figure 4.11.g. We notice a change in the seismicity at 17 km on the same cross-section which possibly images the junction between the two faults. The projection of this change at the surface does not fall on the Rion-Patras fault trace. However, on the Figure 4.11.h, we clearly identify the seismicity extending along the Psathopyrgos fault which corresponds perfectly with its mapped surface extension. In this section, the seismicity is concentrated in a very thin flat layer of 100 m thick at 7 km depth with different small clusters. Further west and further east, the seismicity gets thicker.

4.3.3 Spatio-temporal evolutions

Migration velocity during swarm activity

In the western Corinth rift, migrations of microseismicity have already been observed and some of them during swarms have been analyzed in details. For instance, in 2001, the spatio-temporal evolution of the Agios-Ionis earthquake swarm was modeled by Pacchiani and Lyon-Caen [2010] assuming a fluid-driven seismicity. The 2003–2004 seismic crisis occurring along the Aigion and Fassouleika faults was associated to an hydroshear process caused by pore pressure migration [Duverger et al., 2015]. In 2006-2007, another swarm with westward migration [Lambotte et al., 2014] occurred in the middle of the gulf, and in 2009 another swarm activity migrated eastward along the Selianitika and Lambiri faults.

Here, we present some results on the 2014 year which showed two main strong activities, one in the westernmost rift along the Psathopyrgos and Rion-Patras faults, and another in the middle of the gulf along the Kamarai fault system. During these seismic crises, different orders of migration velocities are observed. All migration velocities mentioned in the following text are projected along the E-W axis, which is the main migration direction at first order. The discussed migration velocities are then smaller or equal to real ones.

Firstly, we describe the westernmost 2014–swarm. In July, we observe a first slow (~0.08 km.day^{-1}) westward migration of the microseismicity, which started at the western extremity of the Psathopyrgos fault (Figure 4.12). A second shallower eastward migration at a velocity of 0.27 km.day^{-1} occurred from mid-August along the Psathopyrgos fault. From mid-September, a new, faster, bilateral migration started close to the junction between the Rion-Patras fault and the Psathopyrgos fault, with several magnitude M_W3 events. The eastward velocity reaches ~3 km.day^{-1} along the Psathopyrgos fault. Both westward and eastward velocities of this bilateral migration are of the order of few km.day^{-1}. Contrary to previous swarm activities in this region, the two main faults seem to be connected and are activated as a continuous fault system during this crisis.

Secondly, we are interested in the 2014-swarm which developed from June to December along the Kamarai fault system (Figures 4.13 and 4.14). It started with relatively deep swarm, at 7-8 km depth, which occurred just after a M_W4.1 earthquake. This event is either located at the western extremity of the Fassouleika fault or on the Trizonia fault, the focal mechanism is compatible with both. The nodal planes of the focal mechanism of this event are compatible both with the play of the Fassouleika fault and the Trizonia fault. Looking at the vertical cross-section (Figure 4.14.b), the event is relocated in the continuity of the Trizonia fault extension at depth, thus we favor a fault plane dipping south. Almost instantaneous aftershocks propagated to the north-east 3 km away from the mainshock. Knowing that a magnitude 4 event has a rupture dimension of about 1 km, this denotes a strong postseismic effect. These aftershocks would deserve a more specific analysis to highlight a possible afterslip, which is beyong the scope of this discussion. Then, the seismicity front migrated eastward at 1 km.day^{-1} for 2 more kilometers (Figure 4.13.c), while another slower migration at about 0.05 km.day^{-1} continued during almost 3 months. Two different order of migration velocities are observed here. During the slow migration, the seismic activity jumped eastward, with events a bit shallower (6 km depth) to finally come back deeper and fill in the emptiness. From mid-August, another westward migration at 0.05 km.day^{-1} occurred along the Fassouleika fault extension and lasted more than 2 months. The seismic rate slowed down at the end of October just before the birth of a M_W4.7 event located at 5.5 km depth, which triggered an intense and shallower swarm on the Aigion fault (Figure 4.13.d). Aftershocks are present instantaneously on the shallow part (around 4 km depth) of the Aigion fault, with a lateral extension of about 8 km. A eastward propagative front of the aftershocks is observed at a velocity of several hundred meters per day. When the activity on this fault slows down, the Fassouleika fault remains active with the same westward migration at a velocity of 0.05 km.day^{-1}. The two faults seem to play alternatively and independently.

At depth, the seismicity from June to November starts below 7.5 km and migrates progressively upwards at first order until 6.5 km, before the activation of the more superficial crisis in November, ranging from 3.5 to 7.0 km depth.

Relationship between shallow and deep seismicity

With the last 2014–swarm, we saw that the superficial activity along the Aigion-Fassouleika fault system occurred because of a relatively shallow M_W4.7 earthquake. Globally, over the 2000–2015 period in the Corinth rift, events shallower than 5 km depth seem to follow the main swarm activities (Figure 4.15). We also often notice that mainshocks triggered shallower aftershocks either instantaneously or with a migration pattern. Moreover, we observe that the biggest events ($M_W > 3$)

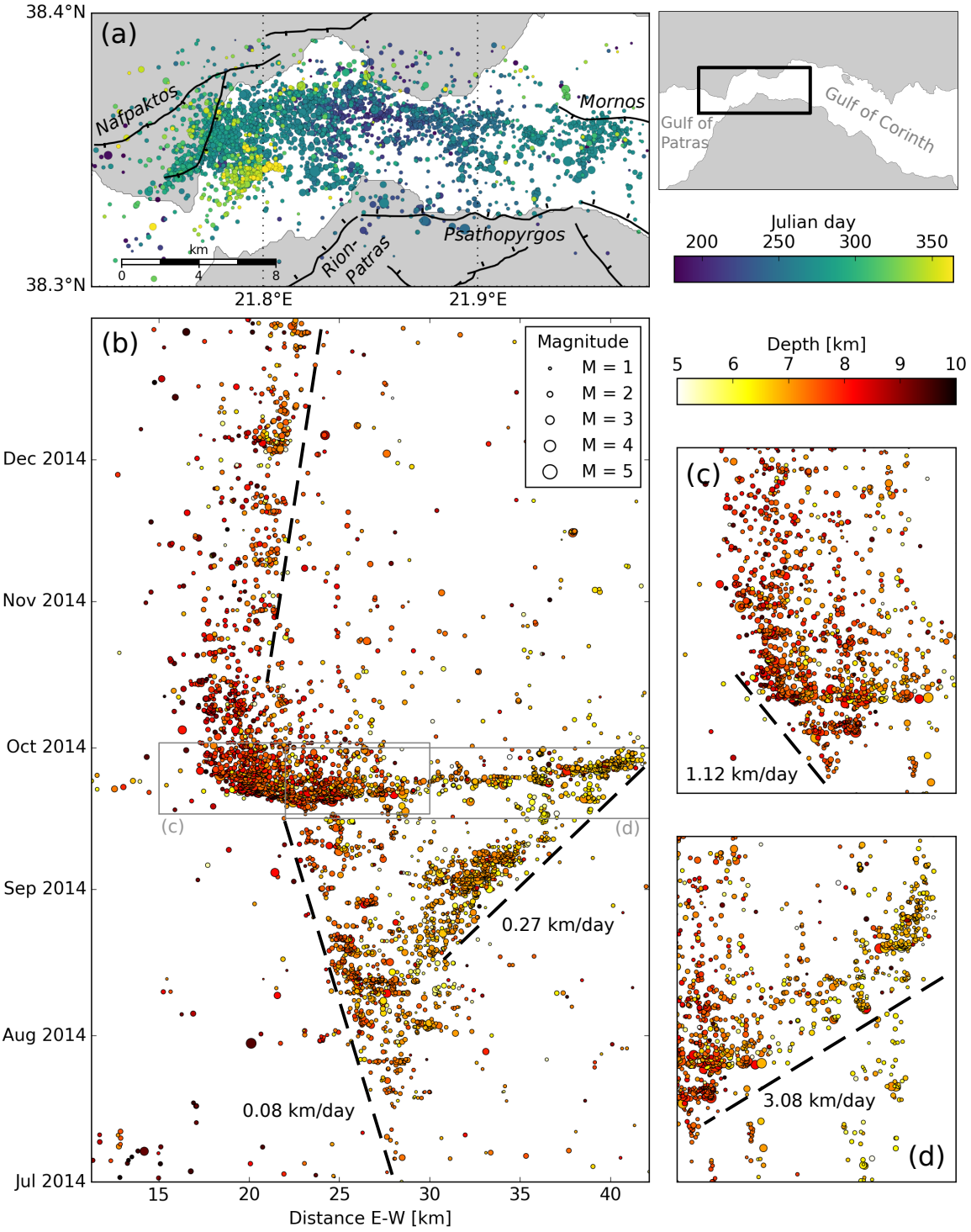

Figure 4.12 – Seismic migration velocities during the westernmost (ZM) swarm in 2014. (a) Map of the seismicity migration along the Psathopyrgos, Nafpaktos and Rion-Patras faults. The colorbar represents the time in Julian days of 2014. (b) Temporal evolution of the microseismicity along the longitude. The size of points is proportional to the event magnitude. (c) and (d) are zooms in migrations represented by light gray frames in (b). Black lines represent the main migrations seen with the corresponding velocities in km.day^{-1}. The colorbar represents the event depth.

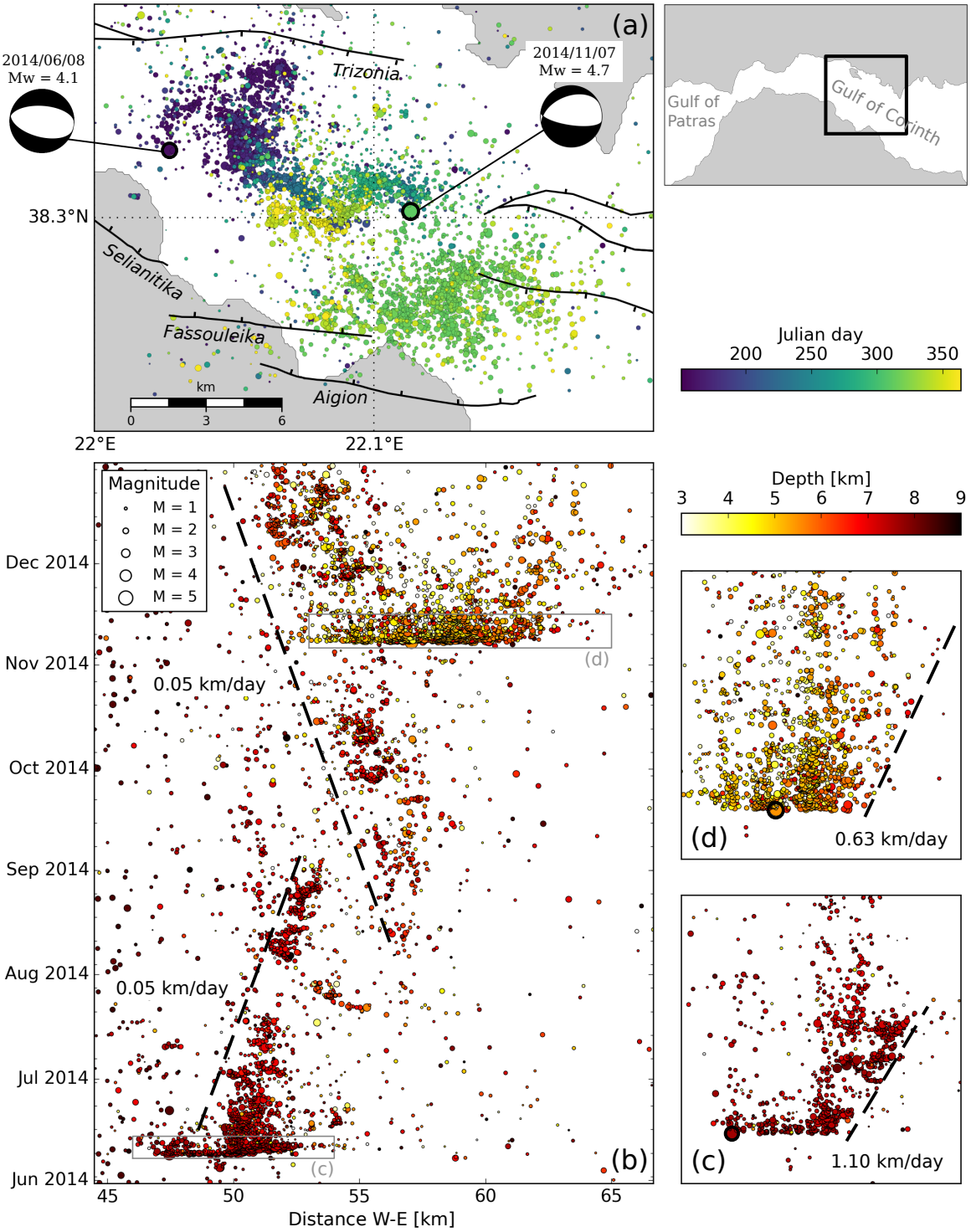

Figure 4.13 – Seismic migration velocities during the western (ZW) swarm in 2014. (a) Map of the seismicity migration along the Selianitika-Fassouleika-Aigion fault system. The colorbar represents the time in Julian days of 2014. (b) Temporal evolution of the microseismicity along the longitude. The size of points is proportional to the event magnitude. (c) and (d) are zooms in specific migrations, represented by light gray frames in (b). Black lines represent the main migrations seen with the corresponding velocities in km.day^{-1}. The colorbar represents the event depth.The colorbar represents the depth of events.

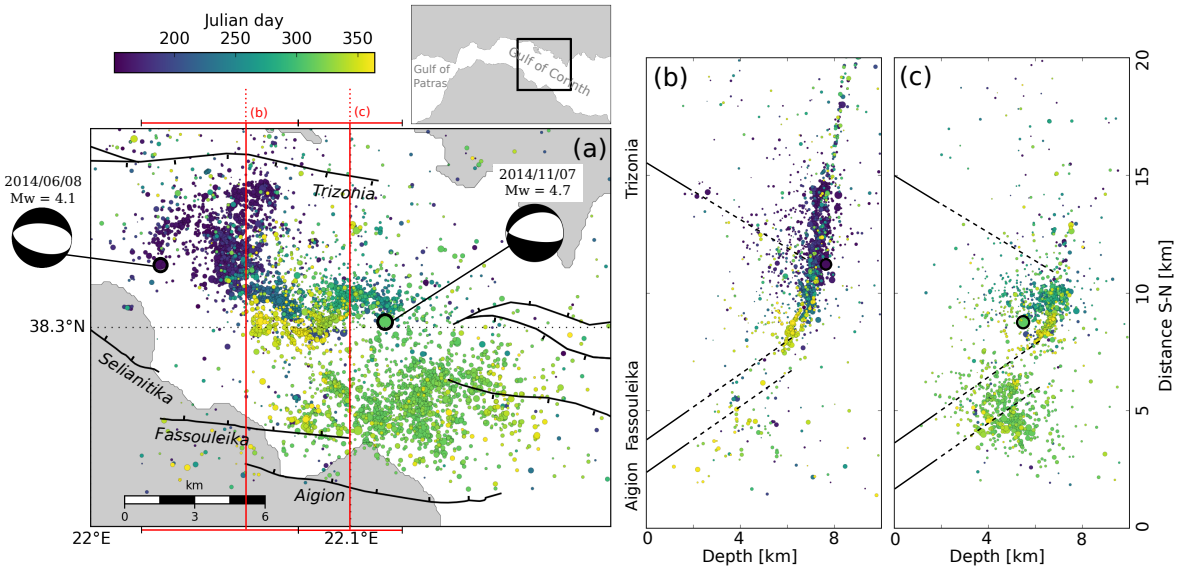

Figure 4.14 – Vertical sections of the seismicity during the western (ZW) swarm in 2014. (a) Exactly the same map as in the Figure 4.13. The red lines delineate the two cross-sections displayed in (b) and (c) with their lateral extent. The colorbar represents the time in Julian days of 2014. (b) Vertical section oriented south-north crossing the events occurring at the beginning of the crisis. (c) Vertical section parallel to the first one, further east, crossing the events occurring later during the crisis.

are localized deeper than the global microseismicity (Figure 4.16). This characteristic may be due to the relocation process, in that M ~ 3 events have a different frequency content than smaller events, thus are possibly less well correlated to them. However, relative location errors on the biggest events are very similar to their neighbor events in the swarm, so we are still confident in their relocated position. If we trust the relocation results, this means that fault planes are larger in the deeper part of the thick layer than inside. We suggested different interpretations: (1) this could reflect a geological heterogeneity or a lithological variation, with for instance a brittle or finely stratified limestone in upper part against a massive limestone in the deeper part; (2) it could be a sign of a mechanical evolution of the layer, with an intense fracturing of the medium linked to the rooting normal faults. The shear-stress layer would be more fractured with smaller structures in the upper part than in the deeper part, where the fault planes are better preserved with a higher magnitude potential.

Long-term and short-term multiplets and repeaters

We map all multiplets composed by at least 10 relocalized events with a similarity threshold of 0.8, which represents more than 1 000 families (Figure 4.17). The first observation is that multiplets are localized in dense seismic area. The lower number of multiplets found in the ZM is likely related to the recent installation of seismic stations there.

Some of the multiplets are clustered in time, others last several years (Figure 4.17.b). Godano et al. [2015] noted that multiplets with a regular or persistent activity are located under or close to the northern coast of the Corinth Gulf, at the root of the 1995-fault. We therefore analyze the temporal activity of our major multiplets in order to check these observations over the double time period (16 years) available. We classified the multiplets into two groups: “long-term” and “short-term”. The long-term multiplets are regularly activated throughout the observational period or for at least several years. Almost all the multiplets in the ZC and along the TZ belong to the long-term ones, that supports Godano et al. [2015]’ observations. Multiplets in the IZ, as well as the ones located at the border of the silent patch between the Mornos fault and the Marathias fault, are also long-term multiplets. On the other hand, the short-term or burst-type multiplets appear

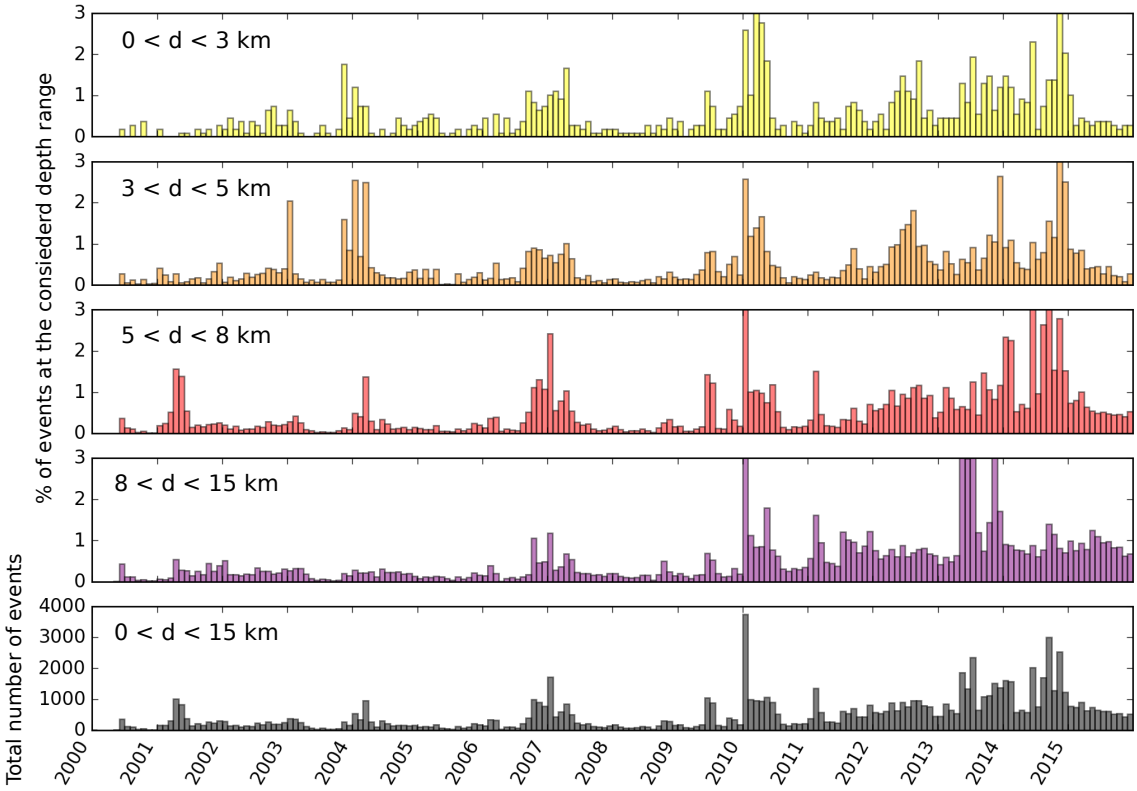

Figure 4.15 – Histograms of seismic activity for different depths. Time bins are computed every month.

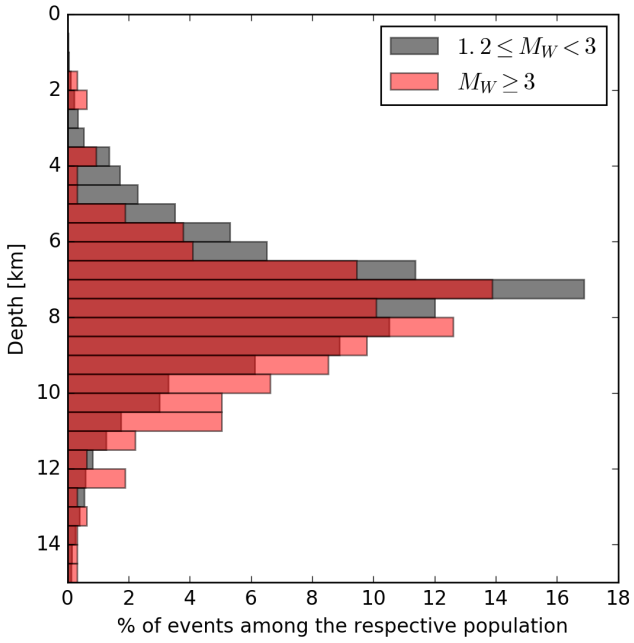

Figure 4.16 – Histogram of event depths. The black bins are for $1.2 \leq M_W < 3$ events, whereas the red bins correspond to $M_W \geq 3$ events. The biggest events are deeper than the remaining microseismicity.

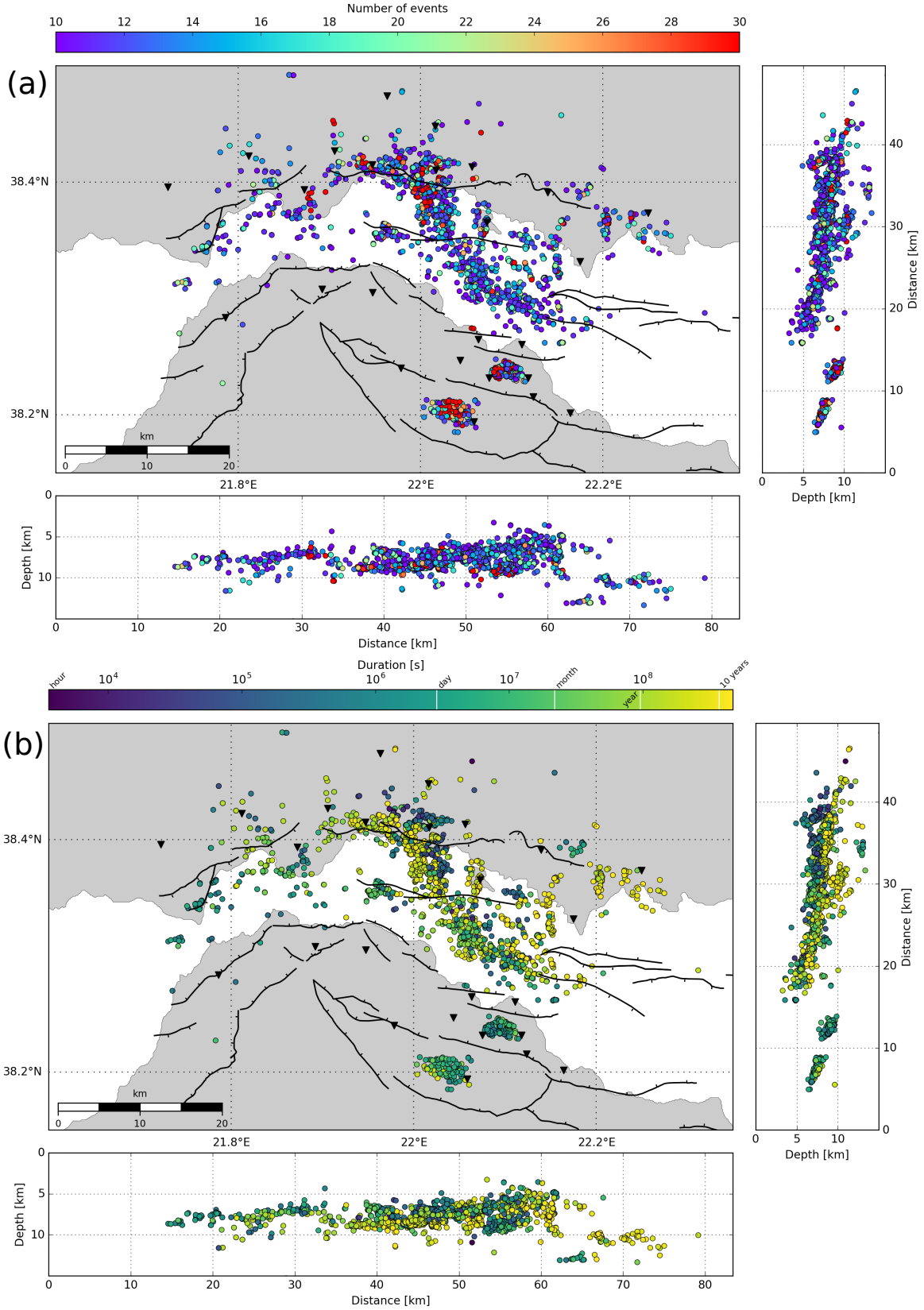

Figure 4.17 – Maps of the multiplets having more than 10 events. Circles represent the mean relocation of multiplet events. (a) Colors indicate the number of events per multiplet. (b) Colors represent the duration of multiplets in log-scale, i.e. the time in seconds between the first and the last event of the family. White vertical lines in the colorbar mark several temporal points of reference: 1 hour, 1 day, 1 month, 1 year and 10 years.

only for a short period and do not activate again later. In the AFZ, multiplets mainly belong to this burst-type. They last less than 1 year and often occur during seismic crises or during aftershock sequences with no further reactivation during next swarms.

Furthermore, on cross-sections of the Figure 4.17, we can see that long-term multiplets are systematically deeper than the short-term ones.

To complete this temporal analysis, we computed the interevent times t_r inside each repeater to characterize the recurrence of repeater-events (Figure 4.18). We remind that repeaters have been extracted using a 0.9 similarity threshold for a 5 s window encompassing the P and S-waves together. First, we have 30 % of events from the database which are inside repeaters (45% of multiplet events in repeaters). For the presentation of the results, we only kept repeaters with at least 5 relocalized events. It represents more than 1000 families. We used the periodicity definition of Lengliné and Marsan [2009] and computed the mean interevent time (T_0) as the mean of the time intervals between successive events.

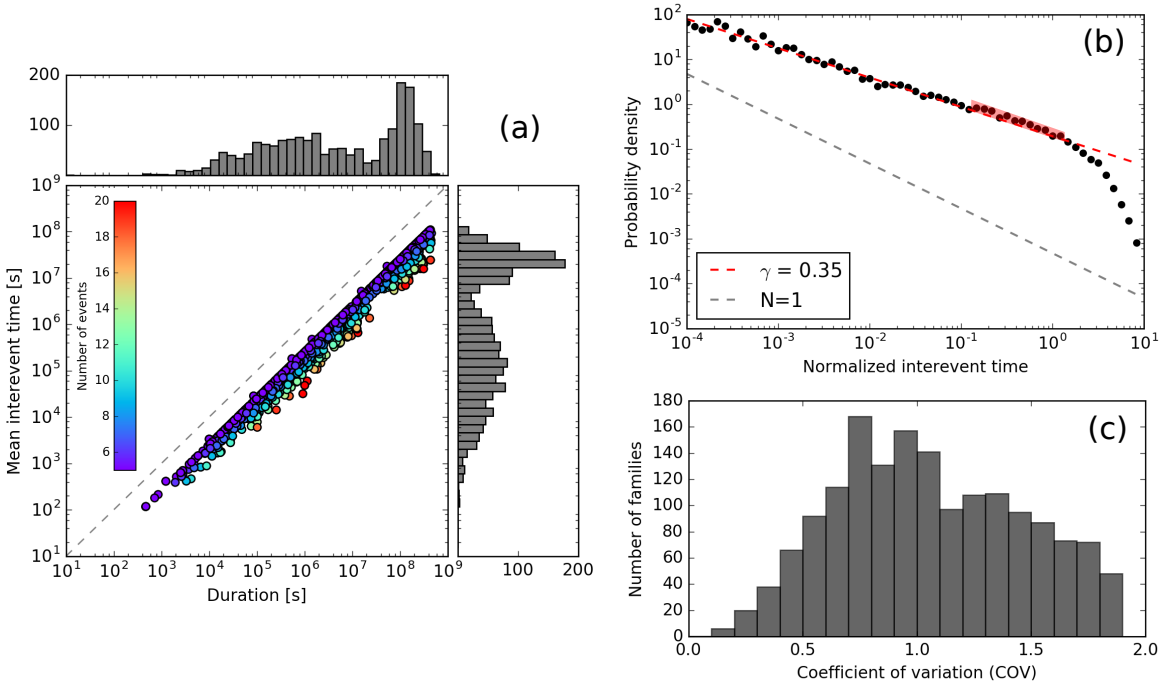

Figure 4.18 – Analysis of the interevent times of repeaters with at least 5 events. (a) Mean interevent time as a function of duration and their respective histograms. (b) Probability densities for normalized interevent times, $T_r/\overline{T_r}$. The red dashed line displayed is the fitted $T_r/\overline{T_r}$ gamma-law decay. The grey dashed line represents the number of samples equal to 1. (c) Histograms depicting the COV distribution of repeaters.

First of all, we observe that long-term repeaters have higher mean interevent times than short-term repeaters (Figure 4.18.a). For a same number of events per family, this relation is trivial but in the general case, it is not. The important feature is the dispersion of the interevent times for a given repeater duration or number of events. The histograms show a bimodal distribution of their mean interevent times and their durations. For each repeater, we defined the normalized interevent times as t_r/T_0, which are then sorted by time bins over all families. To obtain a probability density, the number of recurrence times falling in each time bins is divided by the length of the time bin and by the total number of normalized interevent times. These steps amount to consider a gamma-distribution:

$$\rho(t_r) = A\left(\frac{t_r}{T_0}\right)^{\gamma-1} \exp\left(\frac{t_r}{T_0}\right) \tag{4.7}$$

where A is a constant [Hainzl et al., 2006]. If $\gamma = 1$, then the seismic activity follows a Poisson–law, i.e. a random occurrence of events with no interactions (background). These events occur at a

known mean frequency independently of the elapsed time since the previous event. On the other hand, if $\gamma = 0$, the seismic activity follows an Omori–law [Omori, 1894] expressing the delayed interactions between a mechanical disturbance generated by an earthquake and the seismic rupture of the nearby faults. In other words, it characterizes the mainshock–aftershock sequences. Finally, if $0 < \gamma < 1$, then the seismic activity is clusterized with a high number of events in a given time without particular interactions, and if $\gamma > 1$, it follows a regular seismic cycle.

We represent the probability density function of the normalized interevent times and fitted the data by a gamma–law decay (Figure 4.18.b). We find $\gamma \approx 0.35$, typical of cluster activity, and observed a decrease similar to an Omori–law decay. We also notice a really small bump between 10^{-1} and 10^{0} s with a factor of 1.25 compared to the linear log-log decay. The dynamics of earthquakes seems then dominated by interactions between asperities rather than steady stress accumulation on a single asperity. We can distinguish three different regimes: (1) about 65% of the events are in clusters (temporal interactions between events of Omori-type), (2) less than 35% follows a Poisson-law (random background seismicity) and (3) the remaining events occur quasi-periodically (red frame in Figure 4.18.b).

We further investigate the data in order to potentially identify the periodic or quasi-periodic earthquake recurrences, typical of repeater behavior. To do so, we compute coefficients of variation (COV) as the standard deviation of the interevent times divided by the mean interevent time by repeater. A COV of 0 implies a perfectly periodic recurrence, whereas a COV of 1 is characteristic of a Poisson sequence. The COV values obtained are mostly lower than 1, with a majority between 0.5 and 1 (Figure 4.18.c). This is consistent with the fitted gamma-law decay seen in the probability density function. However few repeaters show a very low COV value, that is expected in case of periodicity. We then plot some sequences of these repeated events in the Figure 4.19. This behavior can be interpreted as the result of a constant stressing rate acting on the asperities [Lengliné and Marsan, 2009] and could suggest aseismic slip. The families often last several years, but we also observed an example of really short-term repeater, lasting less than half a day with a COV equal to 0.2. We observe that low COV–value repeaters correspond mainly to the long-term repeaters. They are concentrated in the same zones as seen before, that is to say the ZC, along the TZ and the IZ, and around the patch with no seismicity between the Mornos and the Marathias faults. On the other hand, the AFZ concentrates many high COV–value repeaters, as well as the 2001–cluster and the 2013–cluster further south.

The events of repeaters should have similar moment magnitudes, and there must exist a relation between the mean recurrence time and the mean moment of a repeating sequence. To test this assumption, we computed the mean magnitude moment and the standard deviation of the repeaters compared them with its mean recurrence time (Figure 4.20). No trend is highlighted and long interevent times spread over the same magnitude range as the short ones.

We also tested two classical models of seismic hazard: (1) the time-predictable model, for which the rupture threshold is known but not the stress drop, and (2) the slip predictable model, for which the stress drop is known, not the rupture threshold. For consecutive events of a repeater, we compared then either the magnitude of the first event to the interevent time or the magnitude of the second event to the same interevent time (Figure 4.21). However, no valuable information have been emphasized from these tests. We thus constrain this analysis for only the quasi-periodic repeaters (COV<0.4). These sub-group of repeaters mirrors the magnitude distribution of the whole repeater population but not the inter-event time distribution. Recurrence times of the quasi-periodic repeaters are large, 70% of them are larger than 10^{-7}s, i.e. $\sim$ 4 months. Moreover, for this population of large interevent times, we observe a trend consisting in an increase of the delays with an increase of the magnitudes of either the 1st or 2nd event. This population are probably real repeaters in the sense that a same asperity breaks, more or less regularly.

The bimodal distribution of the repeaters' duration and interevent time recurrences is likely associated to their spatial location. The hole in the distribution at around 4 months is the signature of

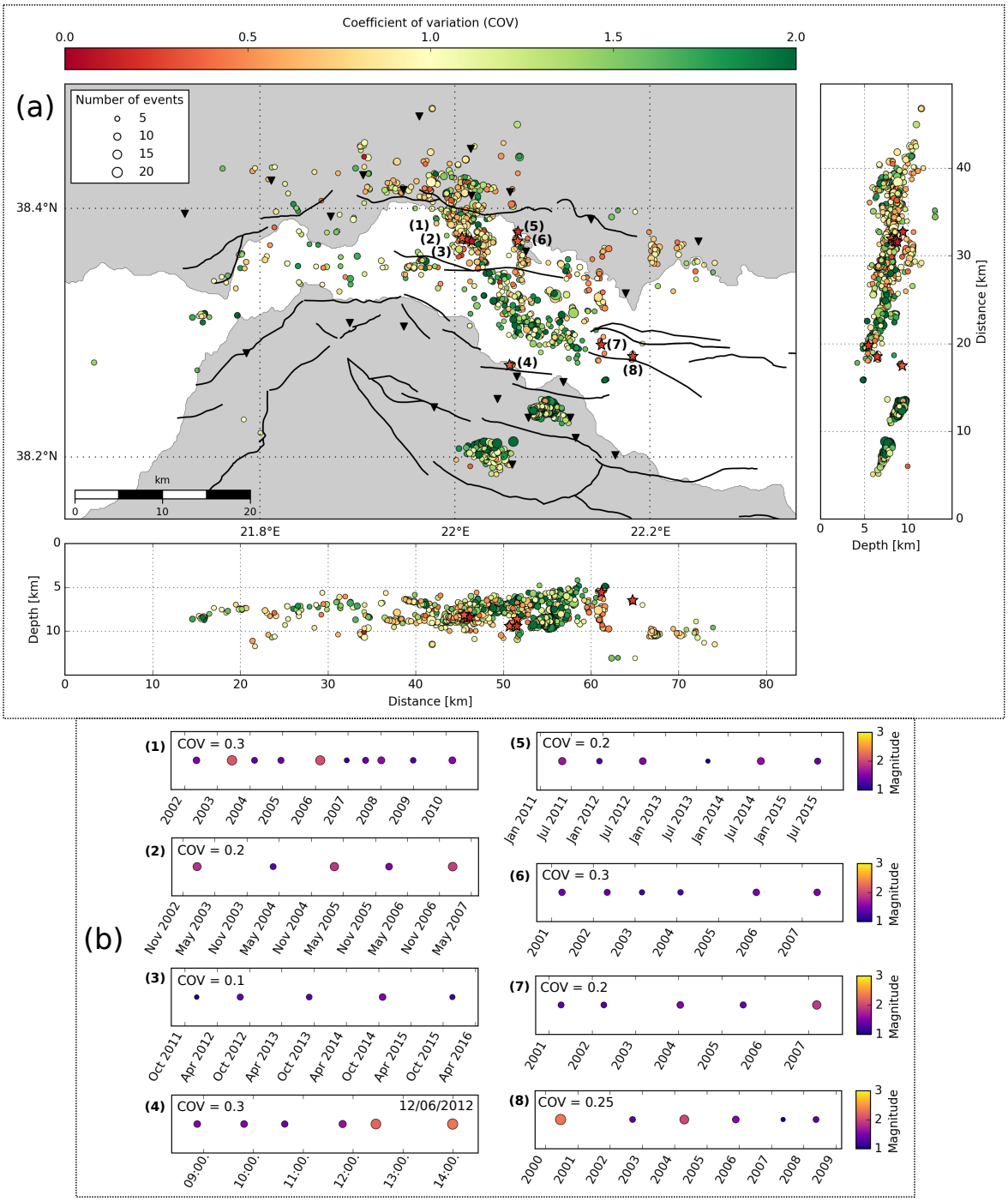

Figure 4.19 – Periodicity of repeaters. (a) Map and north-south, east-west cross-sections of repeaters having more than 5 events. Each circle represents a repeater, which is located at the mean relocation of its events. The colors indicate the coefficient of variation (COV) of the interevent times for each repeater. A COV equal to 0 means that the repeater is fully periodic. A COV equal to 1 means that the repeater interevent times are random. A larger COV corresponds to repeaters having some longer interevent times compared to its mean interevent time. (b) Temporal occurrences of events from some quasi-periodic repeaters. The color and the size of circles are proportional to the event magnitude. These particular repeaters are identified by stars and numbers on the map and cross-sections.

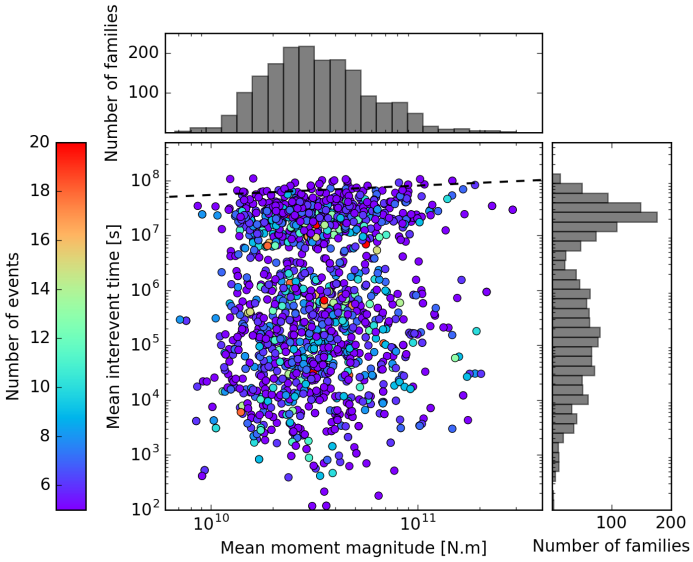

Figure 4.20 – Variation of the mean recurrence time of a repeater as a function of the mean moment of the repeater events. The line is the $\log(\overline{T_r}) = 4.85 + 0.17\log(\overline{M_0})$ relation reported by Nadeau and Johnson [1998], where $\overline{T_r}$ is the mean recurrence time in seconds and $\overline{M_0}$ is the mean seismic moment of the repeater in dyn.cm (1 N.m = 10^7 dyn.cm).

the swarm rhythm in a same area. The short-term multiplets and repeaters occur during a specific seismic crisis, whereas events from long-term multiplets or repeaters occur during different crises, spaced out of several months even years in a same region.

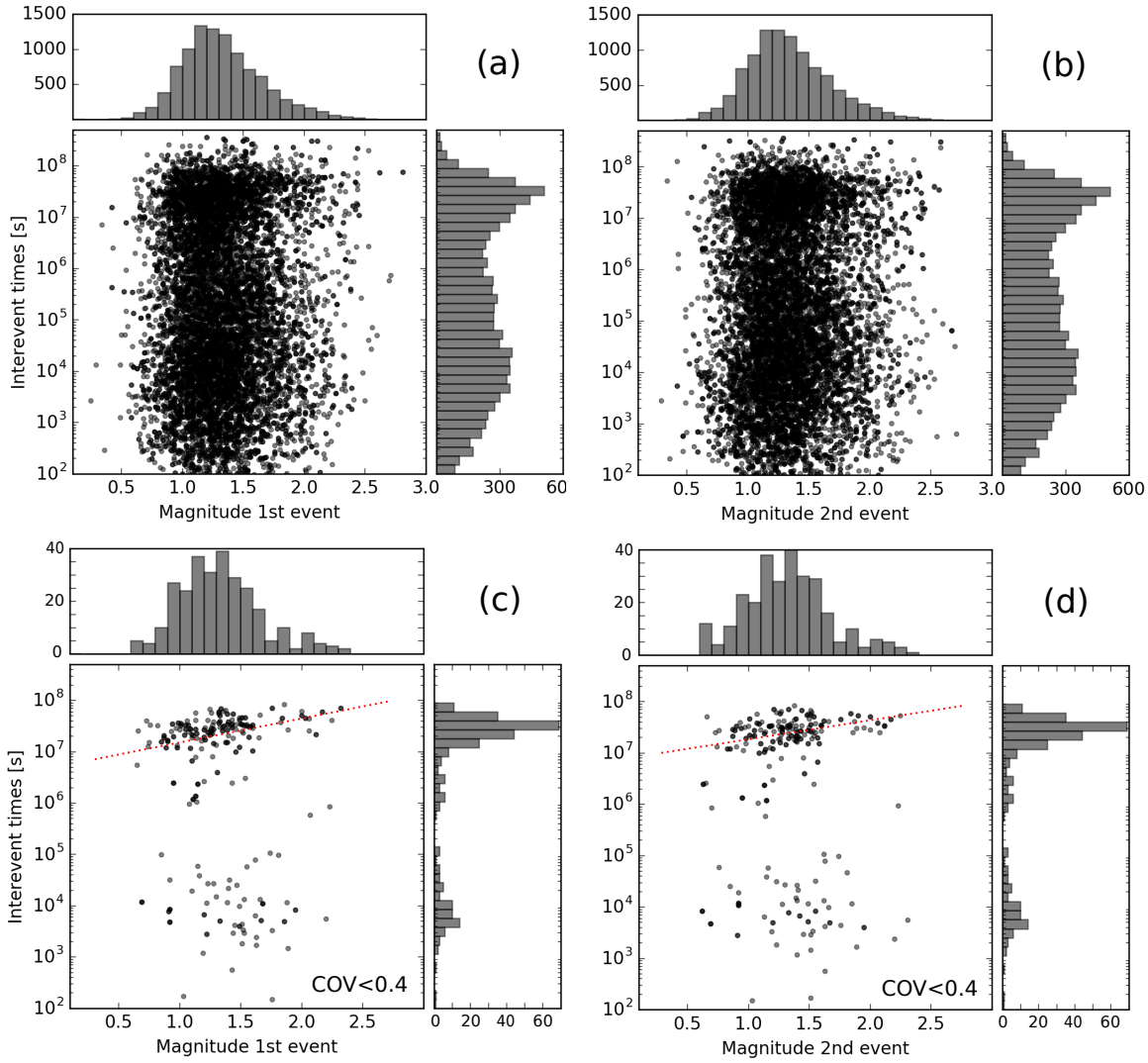

Figure 4.21 – Recurrence time data of repeaters versus simple seismic cycle models. (a) The interevent times of repeaters as a function of the magnitude of the first event (mainshock). We investigated a dependance of the time knowing the past event. This is equivalent to the time-predictable model. (b) The interevent times of repeaters as a function of the magnitude of the second event (triggered). We investigated a possible dependency of the necessary time to triggered the future event knowing its magnitude (stress drop). This is equivalent to the slip-predictable model. (c) and (d) are the same as (a) and (b) respectively for a sub-population of quasi-periodic repeaters (COV ≤ 0.4). The red dashed lines illustrate a positive trend among repeaters with large interevent times.

4.4 Discussion

The relocation of this large dataset of more than 200,000 earthquakes was challenging because of the intense computational task required for the analysis of waveforms and parametric data. To accomplish the processing, we had to make choices such as dividing the region in several areas, deciding the distance threshold for cross-correlations, determining damping values for the double-difference relocations, and selecting a dissimilarity cut-off for multiplet classification. Although our results could probably be improved by studying limited areas individually [Duverger et al., 2015; Kapetanidis et al., 2015; Pacchiani and Lyon-Caen, 2010] and by optimizing configuration parameters for each processing step, the results of this study provide a uniform look across the whole western Corinth rift. Thus, this new precisely located catalog of events can be used to analyze spatial and temporal seismicity patterns across the whole highly active western rift.

4.4.1 The fault systems of the southern coast

Active faults

The relocation allows a more detailed interpretation of the activity of the faults close to the south shore. The former southern faults do not seem to be extinct since some seismicity is observed in the dip continuation of the West Helike and East Helike faults. The 2001–swarm occurred on the Pirgaki and Kerinitis faults [Lambotte et al., 2014], and the 2013–swarm seems to also be associated to the Pirgaki fault [Kapetanidis et al., 2015]. The northward migration of fault activities [Ford et al., 2013; Goldsworthy and Jackson, 2001; Palyvos et al., 2005] in favor of the Kamarai fault system (Aigion–Fassouleika–Selianitika-–Lambiri) has probably reduced their slip rates, which is consistent with geological [Flotté, 2003] and GPS observations [Avallone et al., 2004]. Moreover, further west, we have seen some microseismicity in the footwall of the Rion-Patras fault, which is either associated to the inland Kastrisi fault or to a geological feature. Indeed, the Hellenic nappe pile is locally enhanced by south dipping normal faults [Flotté, 2003] on the norther coast and further south-east to the location of the seismicity.

Driving mechanisms

The seismicity is concentrated in 1–2 km thick active layer in the middle of the rift, and contains numerous multiplets with a wide range of strikes and dips [Godano et al., 2015; Lambotte et al., 2014]. This layer has a high variability of internal structures along the rift over short distances. We looked for the line of the maximum gradient of this thick microseismic layer and found a plane roughly oriented N260°E, dipping 5-10°N.

Along the Kamarai fault system, characterized by a high concentration of burst–like multiplets, we systematically observed seismic migration velocities of the order of tens or hundreds meters per day during seismic crises. This is for instance the case during the 2014–swarm which has shown two migrations at 50 m.day^{-1} in between the aftershock sequences. This area has already been associated to fluid pore pressure migration during the 2003–2004 seismic crisis [Duverger et al., 2015], and the computed migration velocities compare with that of a pore pressure front diffusion [e.g., Chen et al., 2012b].

The Aigion fault, which roots into this seismically active layer at about 6 km depth, shows some shallower microseismic activity (~3 km depth) which was not seen in previous studies. It may indicate that the deeper part of the fault is continuously creeping over years while the upper part is partly locked, but can also creep from time to time. This interpretation can be supported by InSar observations [Elias, 2013], which showed creep on the Aigion fault with an uplift rate of about 2 mm.year^{-1}.

4.4.2 The 1995–fault rupture

The observation of deep events at almost 15 km depth in the downdip extension of the 1995 blind rupture plane could be interpreted as a longer fault extension at depth than previously established. The relatively thick distribution of events under 10 km depth may be related to a diffuse deformation zone and define a damaging zone, consistent with a not fully grown detachment proposed by Lambotte et al. [2014]. They interpret the shallow north-dipping layer defined by the microseismicity in the ZC as an immature detachment, not yet connected to the ductile middle crust.

We also notice that the seismicity rate is constant since 2001, which is incompatible with the hypothesis of afterslip after the 1995, M_W6.3 earthquake. We propose then that the observed deep microseismic activity is a witness of the tectonic loading of the fault. Godano et al. [2014] showed that the multiplet–866, located at the border of the 1995-fault, has a maximum cumulated coseismic slip over the period 2000–2008 of ~10 cm. If we consider that (1) the tectonic loading rate across the rift is constant since 1995, which has been shown by GPS measurements [Avallone et al., 2004], (2) this blind fault is mainly accommodating the deformation prior to the West Channel and the Eratini faults, and (3) the multiplet–866 is a weak seismogenic patch surrounded by a locked fault, which is consistent with the location of the maximum slip at the center of the multiplet [Godano et al., 2014], we could have accumulated about 20 cm of slip deficit on the fault plane over 20 years. However this slip value is large and does not seem consistent with the current estimated dimension of the fault plane. The high slip rate observed on the multiplet–866 [Godano et al., 2014] rather suggests creep on the fault surface allowing rapid stress reloading of some asperities and repeated earthquakes with quite short delays at depth. Moreover, according to Igarashi et al. [2003], repeating earthquakes of regular–type usually occur on the plate boundary and are caused by repeating slips of small asperities surrounded by stable sliding areas. These observations are in favor of a termination of the 1995–fault plane between 10 and 15 km depth, and we may consider that the deeper part of the fault is creeping whereas the upper part corresponding to the 1995–rupture is completely locked. However, we can not say if a major rupture could affect the whole fault plane at the same time, including the microseismically active part at depth.

4.4.3 Seismicity gaps and regular multiplets in the western rift

Lateral changes of seismicity rate

The change in seismicity rate between the central and western rift marked by the TZ also coincides with a change in the rift geomorphology as already mentioned. In the western part, the gulf is shallower and the seafloor relief is marked by the Trizonia fault scarp [Beckers et al., 2015], whereas the central part is deeper and marked by the Eratini and West Channel horsts [Bell et al., 2009]. This change has been attributed to a difference in the geology of the basement [Taylor et al., 2011].

Two parallel structures (TZ and IZ) oriented north-south are illuminated by long-term and well-defined multiplets and some quasi-periodic repeaters, northward of the thick seismically active layer. They are separated by 10 km of very low seismic activity and image a thinner layer (~ 0.2 km), slightly dipping north with a dip of 10–20°. They may delineate the border of a structural plane at depth.

Thanks to the westward extension of the network and the 15 years of seismic data, an another seismic gap is revealed further west, between the Mornos and the Marathias faults. This gap is also surrounded by regular multiplets lasting several years.

In the middle of the gulf, along the Kamarai fault system, it seems that the asperity of a repeater is excited for a short time and never break again later, thus disappear. This phenomena could be interpreted as (1) a gradual abrasion of the roughness of the asperity leading to a loss of the seismic

behavior of the asperity, (2) the mechanical blocking of the asperity at one point, (3) the release of the whole accumulated energy to the point of exhaustion, or (4) the alteration of the surrounded field after each small ruptures resulting in a decorrelation of the waveforms. The first hypothesis assume that each repeatitive rupture alters and smooths the friction coefficient of the fault patch until that it becomes aseismic and can slip continuously. The second possibility proposes that the fault geometry or the configuration around the asperity changes locally, either because of the different ruptures themselves or because of an another displacement possibly caused by slow slip at a different time for instance, and thus prevent new fast motions. The third assumption is based on the energy accumulation and release. We can assume a constant shear loading due to the long-term tectonic or to surronding slow slip. However, the long-term tectonic loading is very likely to small to generate such deformation rate at this short time-scale. Indeed, if we consider a loading rate of 10 mm.year^{-1} [e.g Armijo et al., 1996] over 1 km, we obtain a deformation rate of $\dot{\epsilon} = 10^{-5}$ year^{-1}, but an asperity releasing a shear stress drop of about 1 MPa ($\epsilon = 10^{-4}$) in average [e.g. Godano et al., 2015] would need 10 years to be realoaded. A slow slip is thus preferred and could amplify the local shear strain much more effectively, leading to the complete release of the accumulated energy stored in the asperity until exhaustion. We also can assume an increase of the pore pressure leading to a decrease of the effective normal stress, which could trigger the rupture. In this case, 5 events with stress drop of about 1 MPa would require an overpressure of 5 MPa or 50 bars to be generated. This high value is probably not reasonable for natural fluid pressure perturbations but has already been observed in fluid injection environment [e.g. Cornet et al., 1997]. Finally, the slow slip mechanism is the most likely source for the energy exhaustion. The last interpretation was the possible decorrelation of the waveforms due to changes around the fault zone. The perturbations have to been relatively strong to sufficiently modify the surrounding field and perturb the waveforms generated by a single asperity. With the help of fluid circulations and pressure modifications, the ruptures on the asperity might be seen differently in the seismic records, but we are less convinced by this hypothesis.

If we consider that a part of the repeater population is actually not real repeaters in the sense that a same asperity breaks but several neighbor asperities break successively, the interpretation slightly differs. The small fractures break because of favorable conditions becoming unfavorable after the crisis (permeable paths for fluids?). This aspect could inform on the rock volume fracturability knowing the number of events.

The thin seismic layer and its multiplets

Therefore, we wonder if the highlighted thin layer with seismic gaps may correspond to blind faults bordered by some asperities activated by creep, or to a geological interface. In order to try to answer this question, we identify precisely this thin layer in 10 cross-sections (Supplementary Figure 4.31.d–m) across the rift, picking the depth of the upper and lower points delineating the layer. We image the surface in 3D, materializing consecutive triangle planes between points (Figure 4.22.a). We notice different plane orientations, but at first order we interpolated these points by a unique plane, minimizing the square of the sum of the vertical distances between the points and the plane. We obtain a surface with a strike angle of N295°E and a dip angle of 10°N. The maximum distance between a picked point and the interpolated plane is 0.7 km (Figure 4.22.b–c).

At a second order, we can identify a step at depth between points located in the central rift (ZC) and the western rift (ZW). We then interpolate independently the 4 points from the ZC and the remaining points from the ZW. We find two planes quasi-parallel with similar strike angles (N290°E) and dip angles (9°N) separated by less than 1 km at depth.

We interpret these consistency over the rift length as the possible existence of a geological surface at depth. The vertical displacement of the surface could correspond to a limit in the nappes of the Hellenides at the transition zone (ZT). However, we still observe steep variations of triangle plane

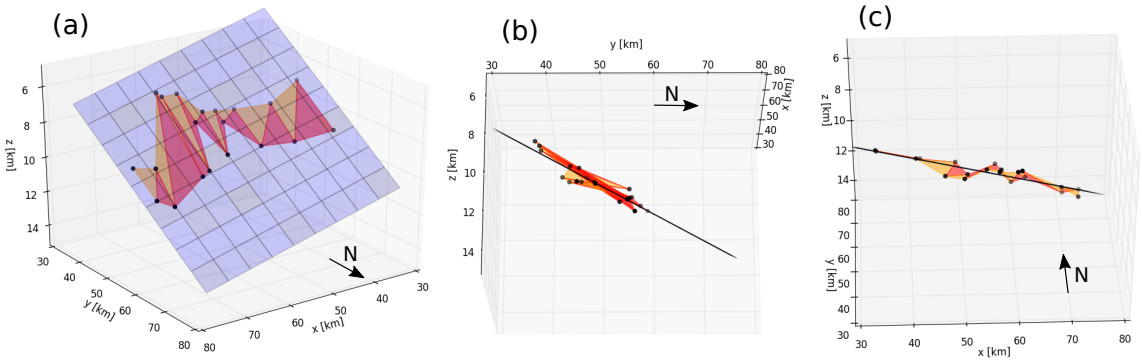

Figure 4.22 – Interpolation of the thin layer of microseismicity. The black points correspond to the picked upper and lower depth of the thin microseismicity on 10 cross-sections (Supplementary Figure 4.31 from P3 to P12). We reconstructed the layer surface by compiling the consecutive triangle surfaces (orange and red) between points. We interpolated these points by a 3D-plane, minimizing the square of the sum of vertical distances of the points to the plane. This plane is oriented N295°E 10°N. The vertical scale is exaggerated. (a), (b) and (c) show 3 different views of the layer surface and the interpolated plane.

orientations around the mean interpolated plane at smaller scale. These fluctuations could be assimilated to the roughness of the surface intersected by several faults with different orientations.

As the strike of the interpolated plane is similar to the strike of the old normal faults of the south coast (West Helike, Lakka), we do not reject the possibility of a major tectonic structure on which faults root. The interpolated plane outcrops around 15 km south from the mapped Marmoussia fault (at the south limit of our map). A possibility to make this plane coincide which the faults at the surface would be to have a large fault with a dip angle shallower at depth, which has already been observed for some major ancient faults on the southern coast with 10–15° dip angle [Flotté et al., 2005].

4.4.4 Influence of the Patras rift on the Corinth rift

We have described the along strike change in the E-W evolution of the fault extension of the Kamarai fault system and the faults on either side of the Nafpaktos basin. Particularly, we observed a 45° change in strike between the Psathopyrgos fault and the Rion-Patras fault (an angle of 135° between the two mapped fault extension). The questions raised here are then:

— how the connection at depth between these two faults is structured ?

— do the faults play independently or does the seismicity propagate along both planes continuously ?

The fine analysis of the microseismicity results enable us to partly answer these questions. The first one is entirely treated here but the second one is mainly discussed in the Section 4.4.6.

Fault connection

First of all, in the Figure 4.11.g, we have seen that the microseismicity occurring at depth on the Psathopyrgos fault plane is confined in the north-south projection of the known surface fault extension of 12 km long. The seismicity further west goes deeper and the layer gets thicker. With this view, we guessed that the intersection at depth between the Psathopyrgos and the Rion-Patras fault planes could be drawn as a north-south line at the surface. In this case, the geometry of this contact imposes a higher dip angle for the Rion-Patras fault (Figure 4.23). Indeed the mathematical relation between the dip angles of the two faults (α for the Psathopyrgos fault and β for the

Rion–Patras fault), knowing the angle (θ) between the fault traces at the surface is, for this geometry :

$$\tan(\beta) = \frac{1}{\cos(\theta)\ \tan(\frac{\pi}{2} + \alpha)} \tag{4.8}$$

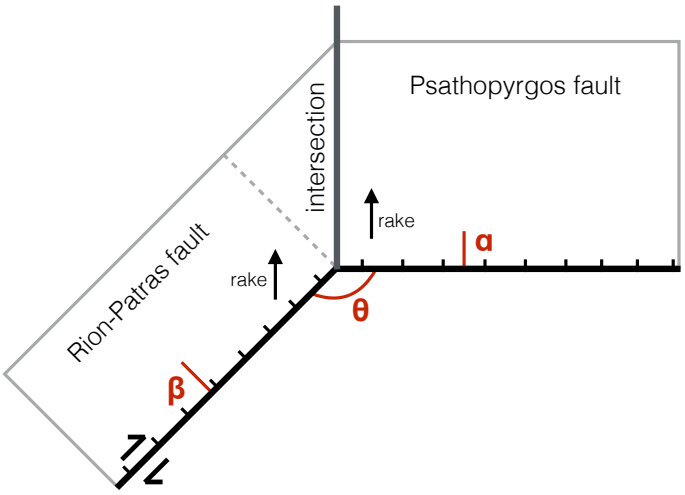

Figure 4.23 – Geometry of the depth contact between the Psathopyrgos and the Rion-Patras faults. α is the dip angle of the Psathopyrgos fault. β is the dip angle of the Rion-Patras fault. θ is the angle at the surface between the two fault extension (θ = 135°).

Then, if we consider a dip angle between 50–55° for the Psathopyrgos fault, as observed at the surface, we obtain a ~60° dip angle for the Rion-Patras fault, which is not inconsistent with the field observations and the microseismicity at depth. A steeper dip angle for the Rion-Patras fault also explains the deeper seismicity observed further west to the Psathopyrgos fault, at a same distance to the fault, on the cross-sections of the Figure 4.11.g. Moreover the fact that the edge delineating the intersection at depth between the two faults is oriented north-south is compatible with the slip of the hanging wall on its foot wall without internal deformation, and the oblique play of the Rion-Patras fault. The strike-slip component of the fault has been suggested by several authors from different types of data [e.g. Beckers, 2015; Elias, 2013; Hatzfeld et al., 2000; Parcharidis et al., 2011; Rigo et al., 1996].

Indeed, from microseismicity analyzes, Hatzfeld et al. [2000]; Rigo et al. [1996] documented pure strike-slip and oblique-slip earthquake focal mechanisms in the Nafpaktos Basin, between the Rion-Patras fault and the Nafpaktos fault on the northern coast. Beckers et al. [2015] showed for the first time evidence of strike-slip movements on offshore faults in the same area thanks to seismic acquisition, and finally InSAR data suggested that the Rion-Patras fault is creeping with about 4 mm.yr^{-1} normal slip and some right-lateral motion [Elias, 2013; Parcharidis et al., 2011]. Furthermore, the strongest earthquake in the area was the 1993 M_W5.4 Patras earthquake, which showed a strike-slip mechanism [Papazachos et al., 1997]. However, this earthquake has been attributed to the Saravali fault, a parallel and further south fault than the RPZ. A submarine study has nevertheless exhibited different features (pockmark field, tilting Holocene sediments) located in the continuity of the Rion-Patras fault [Flotté et al., 2005; Hasiotis et al., 1996].

However, the percentage of slip between normal-slip and strike-slip mechanism is still unknown. With our interpretated contact geometry between the Psathopyrgos fault and the Rion-Patras fault, we are able to propose an estimation of this partition, assuming no deformation in the hanging wall or the foot wall. Indeed, in order to have a mechanically compatible slip (no creation of empty space when the fault blocks are moving) with the Psathopyrgos fault, the rake angle of the Rion-Patras fault, should be parallel to the one of the Psathopyrgos fault, which is oriented north-south. In this geometrical configuration, the Rion-Patras rake angle (λ) is defined as:

$$\lambda = -\arccos\left(\frac{\sin(\alpha)}{\sin(\beta)}\right) - 90° \tag{4.9}$$

We obtained a rake angle[2] of −115°, which gives about 30% of normal slip against 70% of right lateral strike-slip.

Temporal evolution of the fault systems

In terms of temporal evolution of the fault system, the northward migration of the deformation accommodation from inland old southern faults to the presently active coastal southern faults [Ford et al., 2013; Goldsworthy and Jackson, 2001; Palyvos et al., 2005], caused a 25 km northward shift of the Corinth rift, and a NE-SW strike-slip movement joining the Patras and the Corinth gulfs. The formation of these dextral trending transfer-faults started 0.9 Ma ago [Flotté et al., 2005], with the activity of the Panachaïkon faults. The initiation of the Psathopyrgos fault is estimated around 0.4 Ma, followed by the successive propagation to the SE of normal faults of the southern coastline [Ford et al., 2016]. The NE-SW strike-slip trending then translated to the Rion-Patras fault around 0.2 Ma [Flotté et al., 2005], reaching the shore and catching up the Kamarai fault system.

This temporal organization of the Rion-Patras-Psathopyrgos fault system is compatible with the proposed geometry of the faults. Indeed, thanks to analog experiments, Schlagenhauf et al. [2008] showed that normal fault growth starts with a rapid lateral lengthening in a short-term period, followed by a longer phase of slip accumulation with almost no lengthening. The length of Psathopyrgos fault was thus already defined and a priori stable when the Rion-Patras joined the fault system. At its growth, the Rion-Patras fault showing an oblique play, adjust its extension to catch up the normal play of the previously defined system, if we consider that the whole slip is accommodating on the fault plane with no zone of diffuse deformation.

We can add here that the seismicity rate in the Patras rift is very low, as for the eastern part of the Corinth rift (Figure 4.24), whereas the deformation is present all along the two gulfs. Almost the whole microseismicity activity is recorded in the western Corinth rift, and reasons for this behavior are still not well understood.

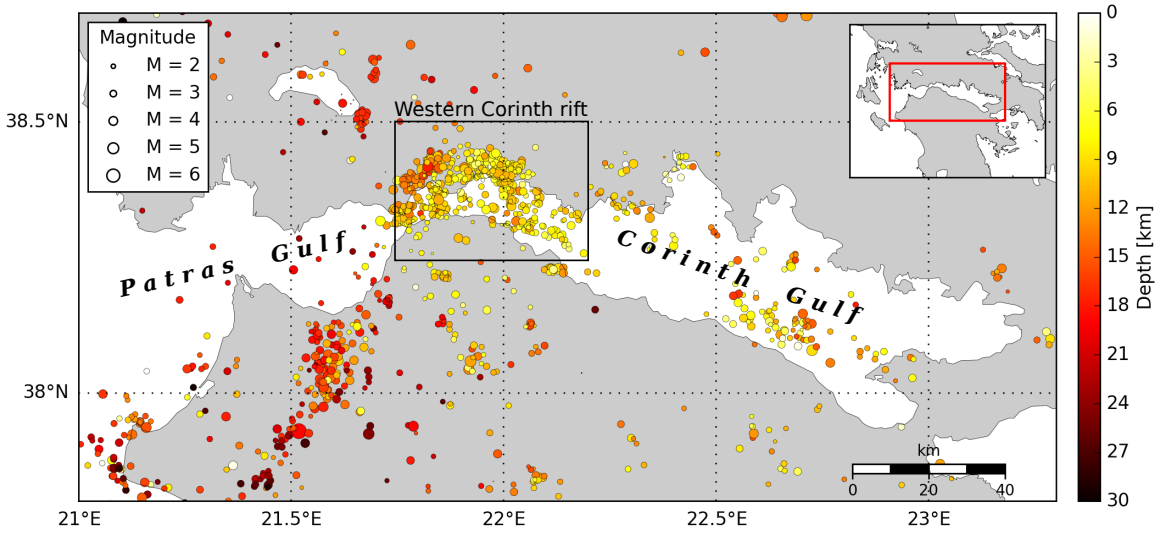

Figure 4.24 – Microseismicity map recorded by the NOA network in the Patras Gulf and the Corinth Gulf. The magnitude M > 2 earthquakes from 2006 to 2015 are shown. The colors represent the event depth.

2. Convention on rake angle: left-lateral strike slip: 0°, rigth-lateral strike-slip: 180°, normal slip: -90°, reverse slip: 90°

4.4.5 Swarms associated to slow transient

We have seen that the westernend region was equipped with seismic stations starting in 2010. So, most seismic events occurring in this zone before 2010 and recorded by the CRL network had not enough constrained locations to undertake a structural analysis. However, in 2002-2003, a swarm recorded in the Patras University catalog has activated the Psathopyrgos fault zone. The activity lasted for several weeks and produced 6 events with $M_L > 3$. The particularity of this swarm is that a slow transient deformation was detected by a dilatometer located on Trizonia Island, about half an hour before the largest event (December 3rd, $M_L = 3.5$) of the swarm [Bernard et al., 2006]. According to the authors, the slow slip event has an equivalent moment magnitude M_W ranging between 4.5 and 5.5. It had been thus assimilated to a special silent slow mainshock, triggering the following seismic swarm sequence.

Among the multiplet catalog, we identified a multiplet of 6 events including an event of M_W2.4, occurring on December 4th 2002, which is a replica aftershock of the largest event of the swarm. The multiplet contains events from 2011 and 2014. The similarity of the waveforms made a specific relocation of the 2002 earthquakes possible with the newly recorded and well located events from 2011 to 2015, and thus would enable us to better analyze the structure of the fault patch activated during the 2002–swarm. We thus created a dataset of about a thousand events containing the 200 events of the 2002–swarm and well constrained events of 2011–2015 in the same area. These last events are selected on the basis of a maximum location change of 100 m before and after the global relocation undertaken. We repeat the relocation process for this specific dataset and obtain a map of the relocated 2002–swarm events (Figure 4.25).

Compared to the western 2014–swarm, the 2002–swarm is relocated further south in the footwall of the Rion-Patras fault. Primary locations were slightly further north-west but still directly under the fault. The main encountered difficulty in this relocation was the network evolution and few events recorded at a same station for the two distinct periods. We are still quite confident in these results knowing that the largest events of 2002 are well recorded by several stations in common with 2014 events and may constrain the relocation of the others by double-differences.

4.4.6 Seismic hazard

The relocated seismicity allows to define which faults are regularly active, or triggered or silent. The depth is better constrained with the precise location of the seismicity helping modelers to define the root depth of the faults. In terms of fault extent, the seismicity patterns enable us to confirme the re-evaluated extension length of the Psathopyrgos fault (12 km) found by Beckers et al. [2015]. We added a geometrical connection between the Psathopyrgos fault and the Rion–Patras fault system based on the microseismicity distribution at depth, which imposes a precise mix of striking–normal mechanism for the Rion Patras fault. The 30% of normal component and 70% of rigth lateral strike-slip could be validated with InSAR and GPS data, where displacements are measured. Moreover, new realistic scenarii of dynamic rupture [Durand et al., 2014] could be considered thanks to this geometrical link between the two faults, and we could test numerically if ruptures can propagate from one fault to another. It brought valuable information as inputs for the seismic hazard modeling.

Seismic hazard related to the coastal faults has been studied by Boiselet [2014]. The last major EQs in the western rift ruptured faults that are blind (i.e., Aigion 1995 EQ, [Bernard et al., 1997]) or that were not described as a major structure (i.e., Efpalio sequence, [Sokos et al., 2012]). The new seismic gap revealed in the westernmost part with some repeaters around looks like the locked rupture plane of Aigion 1995 and is possibly a zone to monitor. It is possible that another minor or unknown structures rupture.

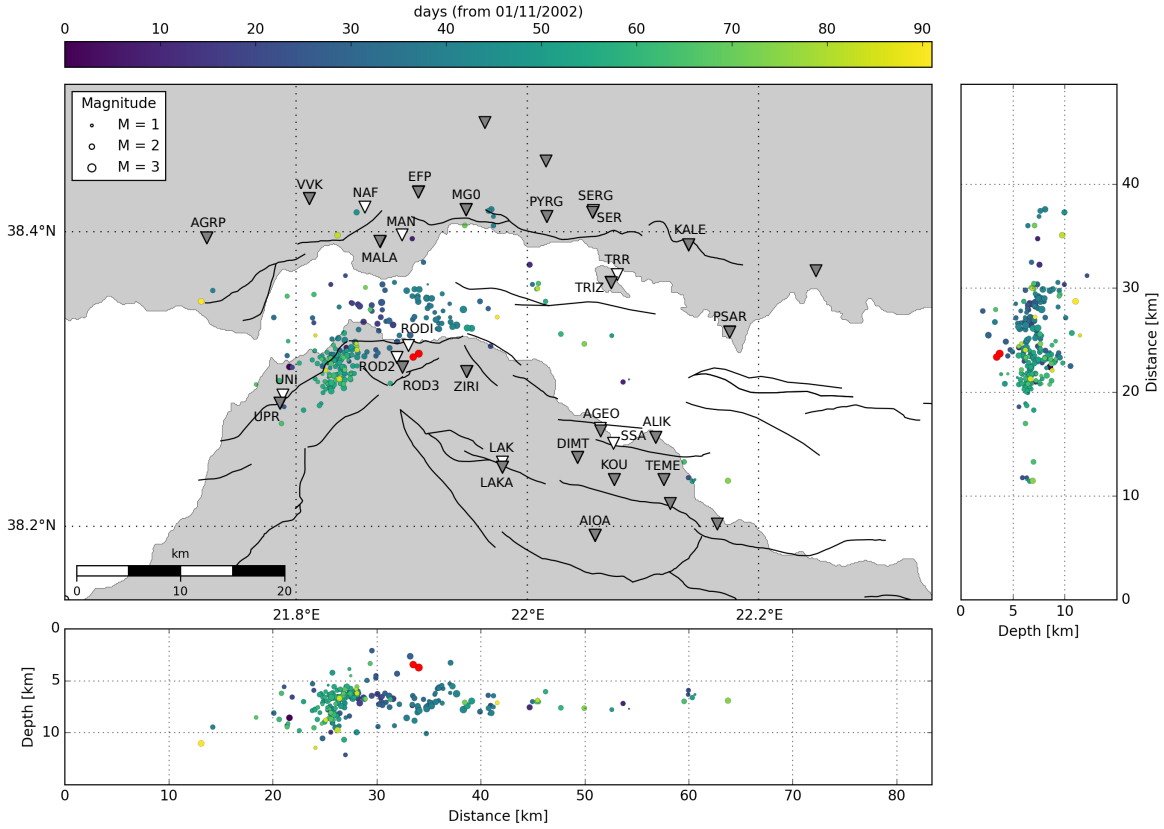

Figure 4.25 – Map of the relocated 2002–swarm. The two red circles are the largest event M_L3.5 of the 2002–swarm occurred on December 3rd [Bernard et al., 2006] and its replica of M_W2.4 on December 4th. The colorscale represents the temporal evolution of the 2002–swarm in days from November 11th 2002. The stations used for the relocation are represented by upside down triangles. White triangles are stations which recorded only during 2002, so no double-differences at these stations can be computed with the 2011-2014 events used to better relocate the 2002-swarm. The westernmost gray stations were not yet installed in 2002 so did not record the swarm events.

These analyzes of multiplets and repeaters also bring data to better constrain seismic hazard models. Modelers need such information in order to quantify the amount of aseismic slip, microseismic slip and large earthquake slip of the different faults. However numerous questions remain regarding the most appropriate way to assess seismic hazard in this area.

4.5 Conclusion

The regional seismicity patterns in the western Corinth rift have been highlighted thanks to the relocation of the micro-earthquake hypocenters, using a double-difference method. In detail, when compared to the former study of Lambotte et al. [2014], the spatial correlation between the dense microseismicity and active structures has been improved, the hypocenters become more thinly clustered at depth and families more sharply defined. The extension at depth of the known geometry of the fault planes at the surface is consistent with the spatial distribution of the microseismicity.

The detailed analysis of the spatio-temporal activity of multiplets and repeaters has highlighted strong spatial variation of family behavior interpreted as different mechanical responses over the rift length. The zones under the gulf tend to generate many micro-earthquakes organized in intense but short-lived swarms. These areas are interpreted to be sensitive to pore pressure variations and fluid circulation. On the contrary, the zones at the edges of former major rupture planes

or of low seismicity rate regularly generate highly correlated seismic events which repeat over long-term period (several years). They are probably affected by slow aseismic slip occurring along a structure shallow dipping north.

The results also point out the interest of maintaining a permanent network of stations over long periods of time. They suggest to gather geodetic measurements with seismological data to cross-check geometrical aspects and help the mechanical interpretations.

We explored diverse aspects in terms of structures and mechanisms thanks to the relocalized microseismicity and the defined families, but many more fine spatio-temporal studies, with migration velocity computation for instance, can be undertaken in the future, to better understand the sources of the highly fluctuating seismicity rate of the western Corinth rift. Moreover, we used a 1-D velocity model for the relocation, but a 3-D model of the Corinth rift crust could improve the initial locations and facilitate fine relocations of this inestimable database.

As direct perspectives from this study, it would be interesting to compare the slow transient episode in 2002 with the 2014–swarm looking into the dilatometer data and GPS data, at the time of the highest activity to see if another transient event would be detectable. Indeed, the relatively fast migrations observed in the westernmost part, especially along the Psathopyrgos fault, of few kilometers per day (hundreds meters per hour) compares with that for creeping faults, on the order of 100–1000 m/h [e.g., Roland and McGuire, 2009].

4.6 Bilan

Ce chapitre fait le bilan de l'ensemble des résultats obtenus à l'aide des inter-corrélations des formes d'ondes des évènements enregistrés par le réseau CRL. Ces inter-corrélations ont permis de générer une base de données de multiplets pour chacun des 10 secteurs définis dans la région d'étude, recensant les familles de séismes aux mécanismes de rupture semblables, proches spatialement, quel que soit le temps inter-évènement. Une sous-base de données, par secteur également, contenant les repeaters a été constituée, regroupant les évènements extrêmement similaires qui ont rompu un même patch sismogène. Les inter-corrélations ont également servi de données d'entrées pour la relocalisation globale des séismes.

Les deux bases de données ainsi que les nouvelles localisations précises permettent d'analyser finement les différents comportements sismiques des zones de faille du rift de Corinthe. Les zones sous le golfe ont tendance a générer beaucoup de microséismes sous forme d'essaims intenses mais éphémères temporellement. Elles sont interprétées comme étant sensibles aux variations de pression de pore et aux circulations de fluides à des profondeurs crustales. D'autres zones au contraire, surtout en bordure de précédents plans de rupture majeurs, ou de zones faiblement sismiques, génèrent régulièrement des séismes fortement corrélés qui se répètent sur de longues périodes de temps. Ces dernières zones sont sûrement affectées par du glissement lent.

Les difficultés premières rencontrées ont été le développement de la méthode de calcul des inter-corrélations et les choix à définir pour traiter les plus de 200 000 évènements présents dans la base de données CRL. Le développement des codes en Python a été réalisé en étroite collaboration avec Sophie Lambotte qui avait déjà préparé un certain nombre de fonctions pour lire les formes d'ondes (au format SAC), les méta-données de CRL (dataless, fichiers de phases, fichiers de localisations, etc.) et optimiser numériquement le calcul d'inter-corrélation. La stratégie de traitement des données et de stockage des résultats, ainsi que la phase de parallélisation du code, ont été établies ensemble et réalisées par moi-même. Étant donné la disponibilité du cluster de calculs S-CAPAD de l'IPGP, j'ai pu mettre en place des routines afin de lancer les calculs sur plusieurs nœuds. Deux étapes de parallélisation ont donc été appliquées, une première au sein même des codes Python, et une seconde sur le cluster de calculs.

4.A Statistics on cross-correlation data

The following figures illustrate the characteristics of the cross-correlation data computed to set appropriate processing parameters. The Figure 4.26 presents histograms of events that correlate with at least another event at the indicated cross-correlation threshold. For the different stations presented, two on the southern coast (AGEO and DIMT) and two on the northern coast (PSAR and TRIZ), we notice that more than 99% of the events correlate for the P-phase with another event in a 5 km radius, at a threshold CC ≥ 0.5. In comparison with the cross-correlation measurements done on 1 s noise windows (Figure 4.27), we can say that a CC < 0.5 is not meaningful and comparable to noise. Indeed, the mean value of CC for noise windows on the vertical component is around 0.4 depending on the station.

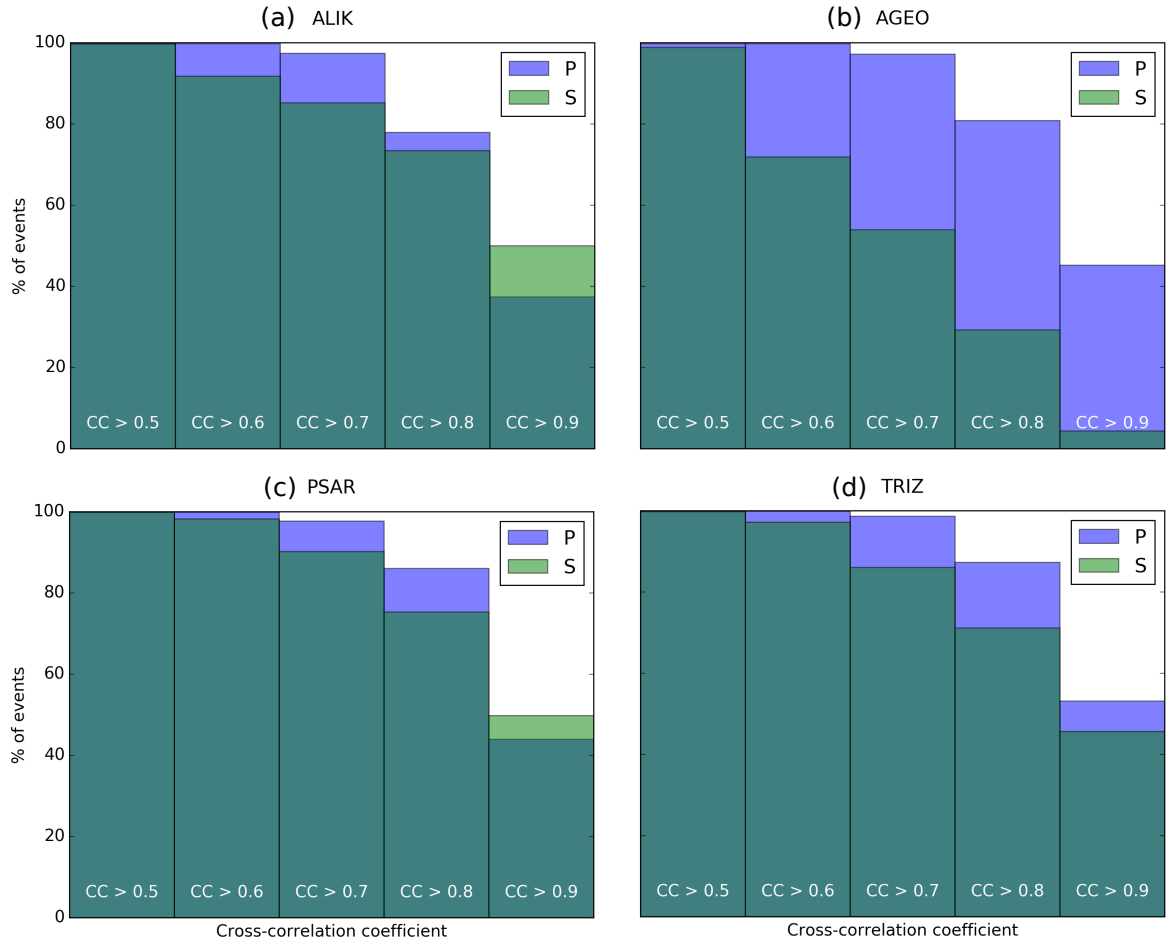

Figure 4.26 – Percentage of cross-correlated events. Histogram of events that correlate with at least another event of its zone at the different cross-correlation thresholds between 0.5 and 0.9 for the P-wave train at the station (a) AGEO, (b) PSAR and (c) TRIZ. Almost all events cross-correlate at a threshold of 0.5 for the P-phase. The histograms have been done for the events of the zone05. Stations ALIK and AGEO are on the southern coast whereas PSAR and TRIZ are on the northern coast.

In average for all stations of the CRL network, on the vertical component, we have 1.2% chance to have CC ≥ 0.7, 0.2% chance to have CC ≥ 0.8 and 0.03% chance to have CC ≥ 0.9 (Figure 4.27.e). We consider that a pair of events having a CC ≥ 0.7 begins to be a significant value in our study, especially knowing the alteration of CC with decreasing SNR, with increasing separation distance and with increasing magnitude difference. These notions are precisely broached in the three next subsections.

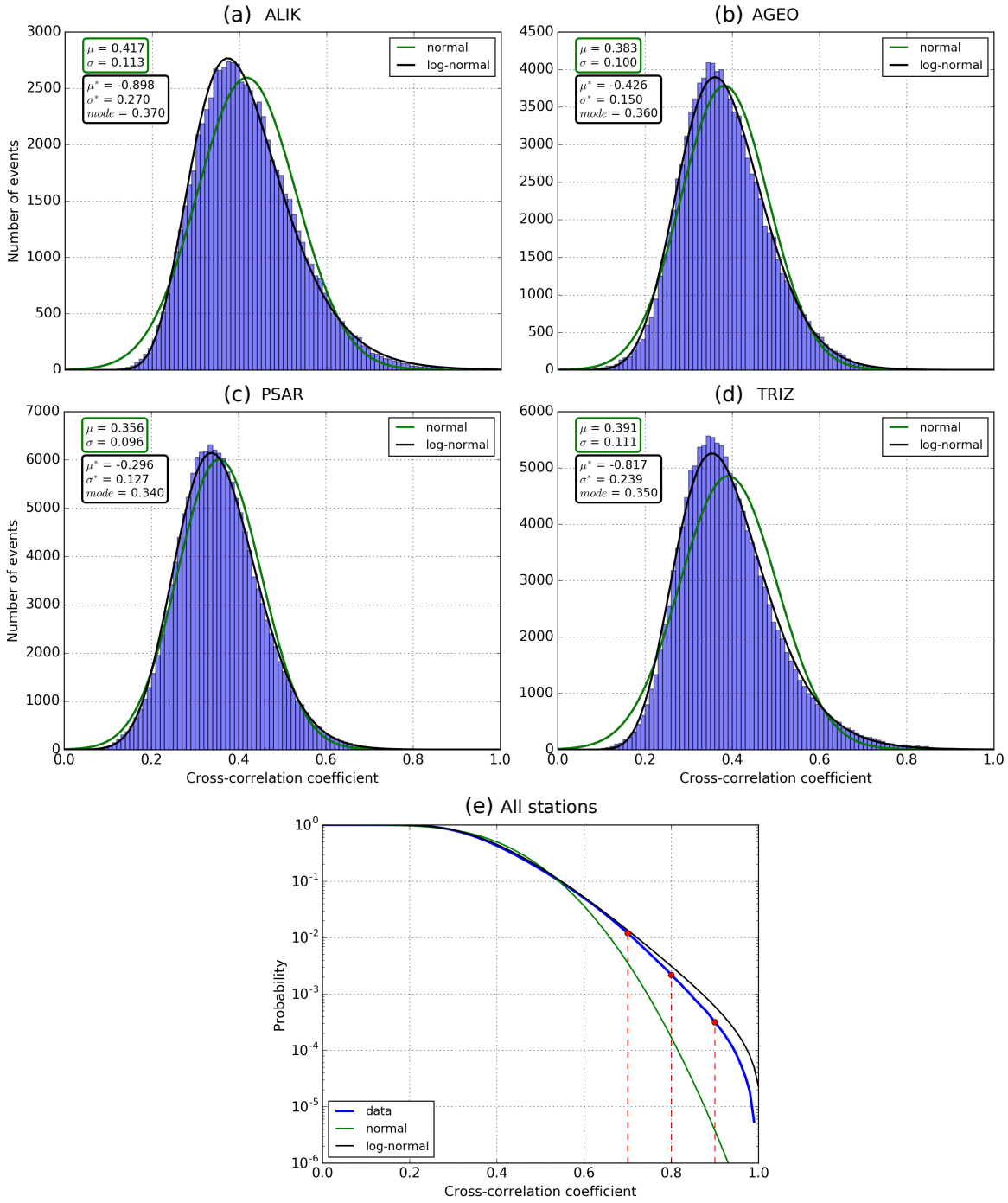

Figure 4.27 – Cross-correlation of noise windows. Histograms of CC estimated randomly on a thousand 1 s noise windows extracted on the vertical component before the P-phase arrival, for (a) ALIK, (b) AGEO, (c) PSAR, and (d) TRIZ. The mean μ and the standard deviation σ of the best-fitting normal distribution (green curve) are given for each station. μ^* and σ^* are the parameters of the best-fitting log-normal distribution (black curve), given with the *mode*, which is the most representative value of the distribution. The average mean of CC fluctuates around 0.4 for CRL stations. Systematically, log-normal distributions better fit the data. (e) This graph represents survival functions, which give the probability for an observation to exceed a CC_{lim}, computed for all stations of the CRL network. The survival function can be written as $S(x) = 1 - \Phi(x)$, where Φ is the cumulative distribution function. In other words, to obtain the blue curve which corresponds to the data, we cumulatively sum the number of observations per bin in the histogram gathering all station observations, from the last bin to the first bin, divided by the total number of observations. The green and black lines are respectively the best-fitting normal and log-normal survival functions.

4.A.1 Correlation measurements as a function of signal-to-noise ratio

In order to estimate the impact of the signal-to-noise ratio (SNR) on the cross-correlation measurements, we performed a synthetic test designing a thousand noisy traces from a real waveform of the database. The reference trace has a high SNR (above 100). We added a random percentage of white noise to the trace, filtered it in the frequency band of the reference trace (1.5–15 Hz), and shifted it in time of Δt = 0.12 s, to create noisy traces. Then we cross-correlated each pair (reference trace, noisy trace) to retrieve the cross-correlation coefficient CC and the timelag Δt (Figure 4.28).

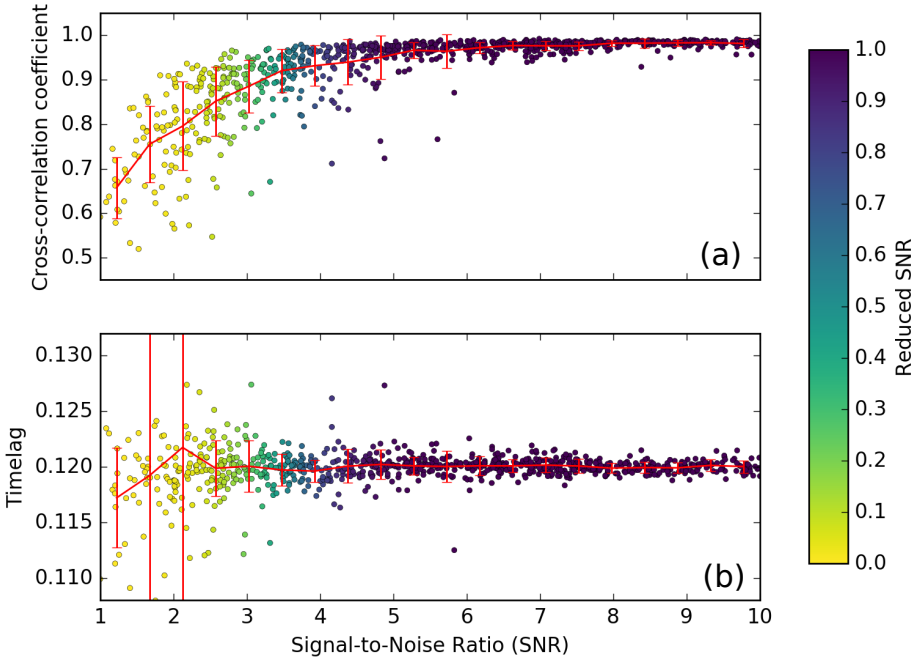

Figure 4.28 – Synthetic case showing the influence of signal-to-noise ratio (SNR) on cross-correlation coefficient (CC) and time-shift Δt. (a) CC as a function of SNR. (b) Δt as a function of SNR. The colorbar corresponds to the reduced signal-to-noise ratio introduced with the Equation 4.4. We used an original trace from the CRL dataset (trace 1 presented in Figure 4.3) as input and computed a thousand noisy traces adding random white noise. Then we cross-correlated the original trace to each noisy trace to retrieve a CC and a Δt. The SNR values are estimated from the noisy traces. Red curves present the mean value of (a) CC and (b) Δt for each SNR bin with the standard deviation as error bars.

We observed that the lower is the SNR of the implemented trace, the weaker is CC and the less constrained is Δt. CC can drop to 0.6 when SNR is close to 1 and Δt is not well retrieved when SNR < 3. The reduced SNR (see Equation 4.4) has been computed in order to take into account this degradation. Low weights are attributed to data with low SNR for the relocation and the classification in multiplets. On the contrary, for SNR ≥ 4, we find CC > 0.9 and Δt really close to the implement timelag (0.12 s). The reduced SNR quickly increases from 0.2 to 0.8 between 3 < SNR < 4, when CC goes above 0.9.

4.A.2 Correlation coefficient as a function of event pair distance

Here, we want to quantify the effect of the inter-event separation distance in the CRL network on the estimated cross-correlation coefficient. The Figure 4.29 shows several representations of the distribution of CC as a function of inter-event distance. In order to perform the plots, we randomly selected 1 million pairs of events among the computed cross-correlated pairs for the P-phase on the vertical component of TRIZ station. The contours of the distribution of CC versus event pair

distance (Figure 4.29.c) has been estimated at different confidence level. This kind of representation has regularly been used in other similar studies [e.g. Aster and Scott, 1993; Schaff and Waldhauser, 2005]. For instance, at 2 km inter-event distance, 90 % of event pairs have CC > 0.6 for this distance bin. We observed a decrease of CC values with an increase of the separation distance at the station TRIZ. This is related to the breakdown of the waveform similarity with distance. The more waveforms originate from distant sources, the more they have chance to travel within different crustal structures which alter differently the waveforms. The change of pathway (length, direction, dip angle) itself affects the recorded waveforms.

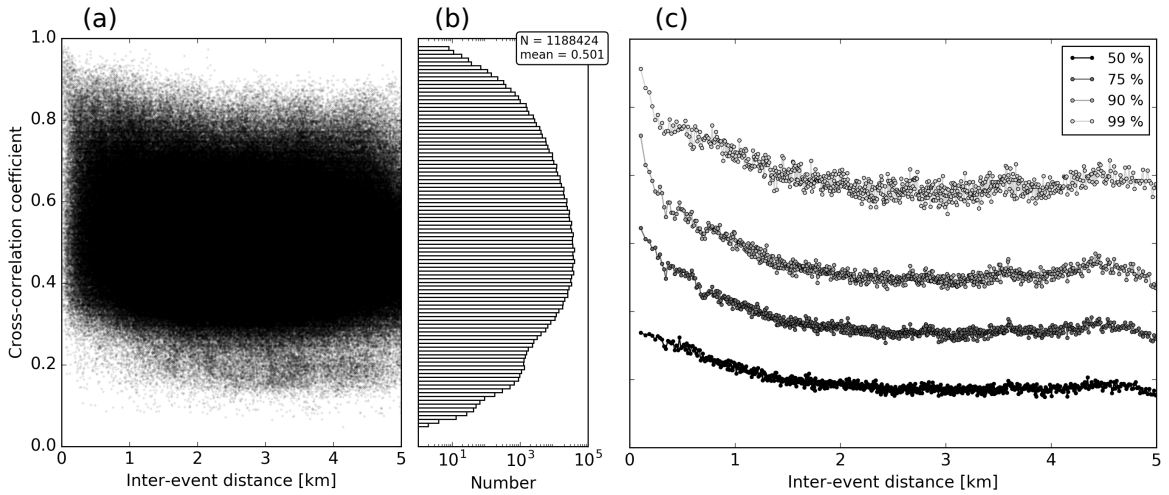

Figure 4.29 – Influence of the event separation distance (Δ) on cross-correlation coefficient (CC)**.** (a) Scatter plot of CC as a function of Δ. Each dot is an observation plotted with a transparency coefficient to show the huge amount of data. (b) Histogram of the distribution of CC with the number of observations in log-scale. The total number of data N is higher than 1 million, and the mean CC is 0.5. (c) The different curves are contours of confidence levels defined in the legend. They are computed by dividing the x-axis into bins of equal number of data, representing by each circle (1500 observations per bin). The data are evaluated on the P-phase for station TRIZ, where the breakdown of the waveform similarity with increasing distance is well observed.

Note that, as a general rule, high similarity of waveforms for event pairs requires the events to be not farther apart than about one-quarter of the dominant wavelength λ [Geller and Mueller, 1980]. In our case, for a P-wave velocity of 6 km.s^{-1} (the mean P-wave velocity of the Corinth rift crust at 5-10 km depth) and for dominant frequencies in a 1.5 to 15 Hz band, this distance would be from 0.1 to 1 km. However, several studies of seismic waveform coherence [e.g. Harris, 1991; Hutchings and Wu, 1990] indicate that the $\lambda/4$ guideline is too restrictive in some cases, and that appreciable coherence can exist for inter-hypocenter separations of up to a few times λ. Indeed, if the mechanisms are similar and path effects are consistent for a common station or if the crustal structure is relatively homogeneous, the waveforms are expected to be similar for greater inter-event separation distances. For the station TRIZ for instance, we can see that an inter-event distance of 2–3 km captures most of the useful cross-correlations (Figure 4.29.c). The distance threshold chosen of 5 km is longer than the quarter wavelength rule, but with these arguments and knowing the uncertainties on initial hypocenter locations computed with hypo71, we prefer to keep a generous radius to measure cross-correlations. This enables us to try to estimate differential travel times between pairs of initially mislocated earthquakes, which could provide an improvement over phase picks and help in their relocation.

4.A.3 Correlation coefficient versus magnitude difference

The dependency of correlation coefficients CC on the difference in magnitude (ΔM_W) is shown in Figure 4.30. For $\Delta M_W \geq 1$, CC values decrease linearly with increasing difference between event

pairs' magnitudes. The larger is the magnitude difference, the more different is the frequency content of the recorded waveforms, so the lesser is the similarity between the events. Up to $\Delta M_W 1$, CC values are quite stable or increase slightly especially for AGEO station (Figure 4.30.a). This rise is actually due to the fact that the small magnitude differences mainly come from very small magnitude event pairs, which have noisier seismograms.

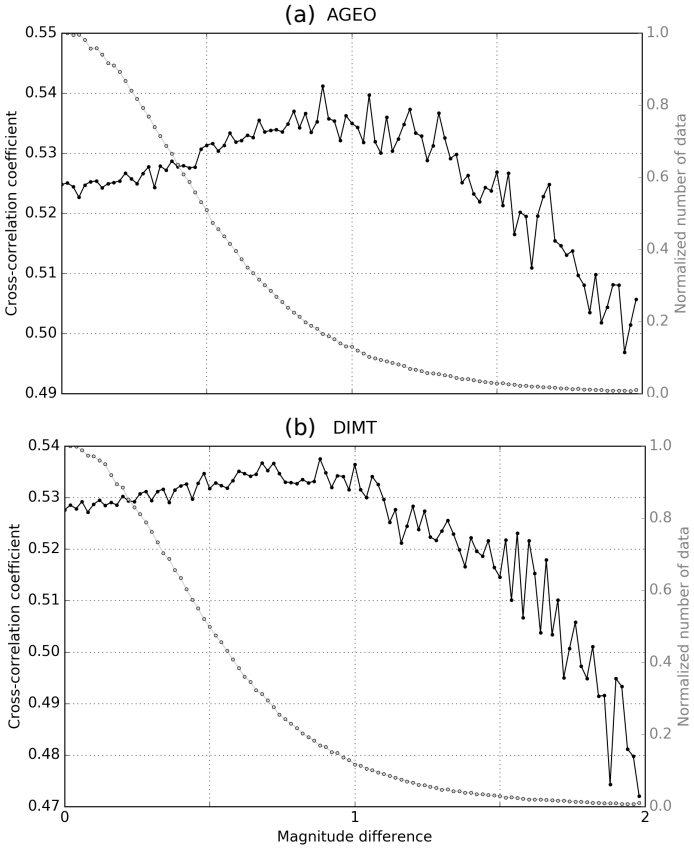

Figure 4.30 – Influence of the magnitude difference on cross-correlation coefficient. Red curves represent the mean of CC computed by dividing the x-axis into bins of equal length (ΔM_W = 0.2). The CC are evaluated on the P-phase for thousands random pairs of events recorded at the station (a) AGEO and (b) PSAR.

Above a magnitude difference of 2, we have almost no data since the huge majority of events in the database have a magnitude between 1 and 3. We can also note that the largest magnitude events ($M_W \approx 5$) of our database do not well correlate with microearthquakes because of the difference in their dominant frequency range.

Our results show that the ability for two events to produce similar waveforms in the frequency band 1.5–15 Hz depends on the quality of their recorded signals, on the distance between their hypocenters and the difference between their magnitudes.

4.B Additional cross-section images

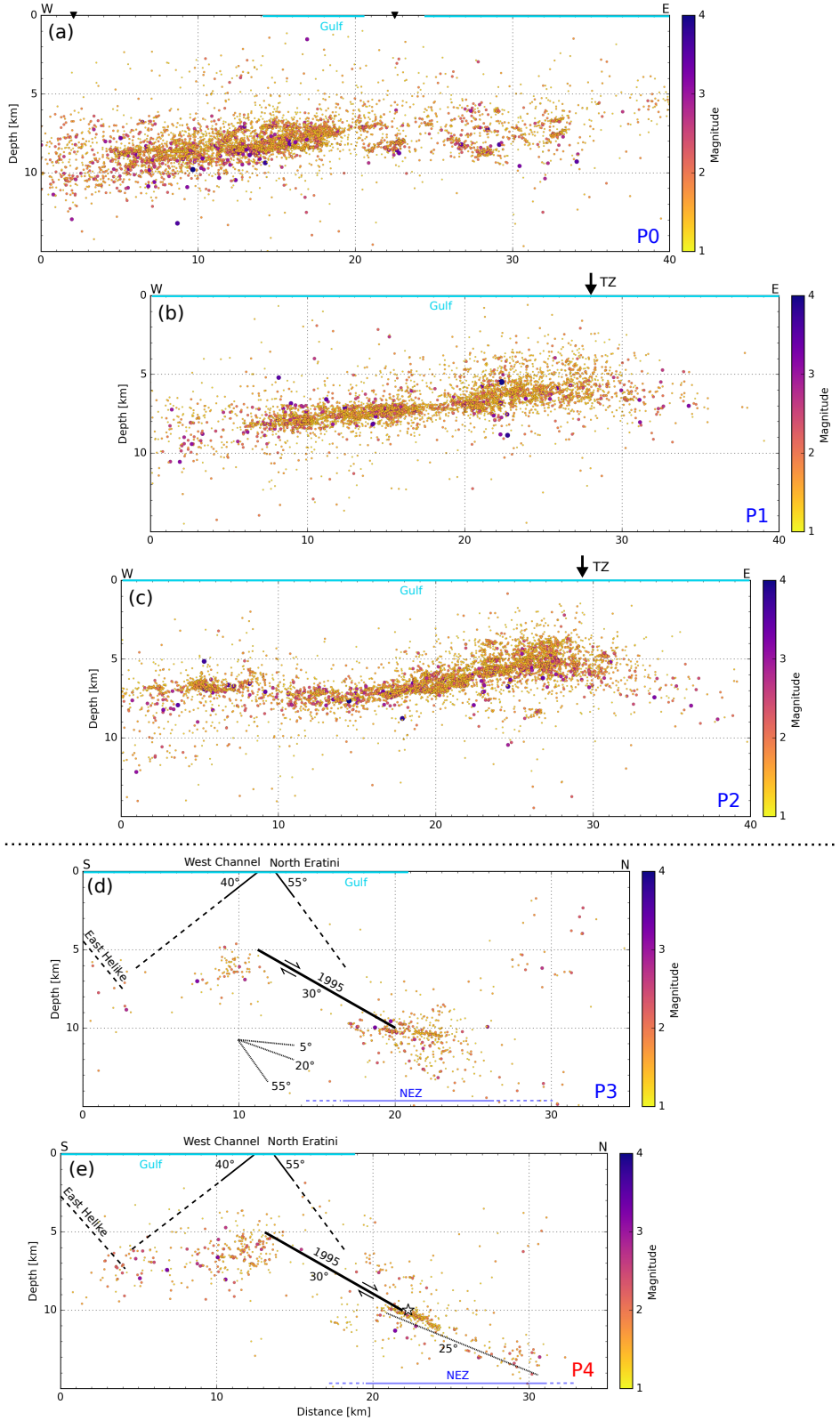

Figure 4.31 – Additional vertical cross-sections along the western Corinth rift. They are identified by blue and red rectangles in Figure 4.10.b. Bold black lines indicate the major onshore and offshore faults. Light blue lines at the surface represent the offshore rift. The color scale corresponds to the moment magnitude. Dark blue lines at panel bottom represent the extension of zones defined in Figure 4.10.a and in the text (NEZ: North Eratini Zone; TZ: Transition Zone; IZ: Trizonia Island Zone; AFZ: Aigion-Fassouleika Fault Zone; RFZ: Rion-Patras Fault Zone). The black arrows in (a), (b) and (c) are the location of the swelling at the transition zone (TZ in Figure 4.10.a). The white star in (e) is the location of the M_W6.3 1995 earthquake.

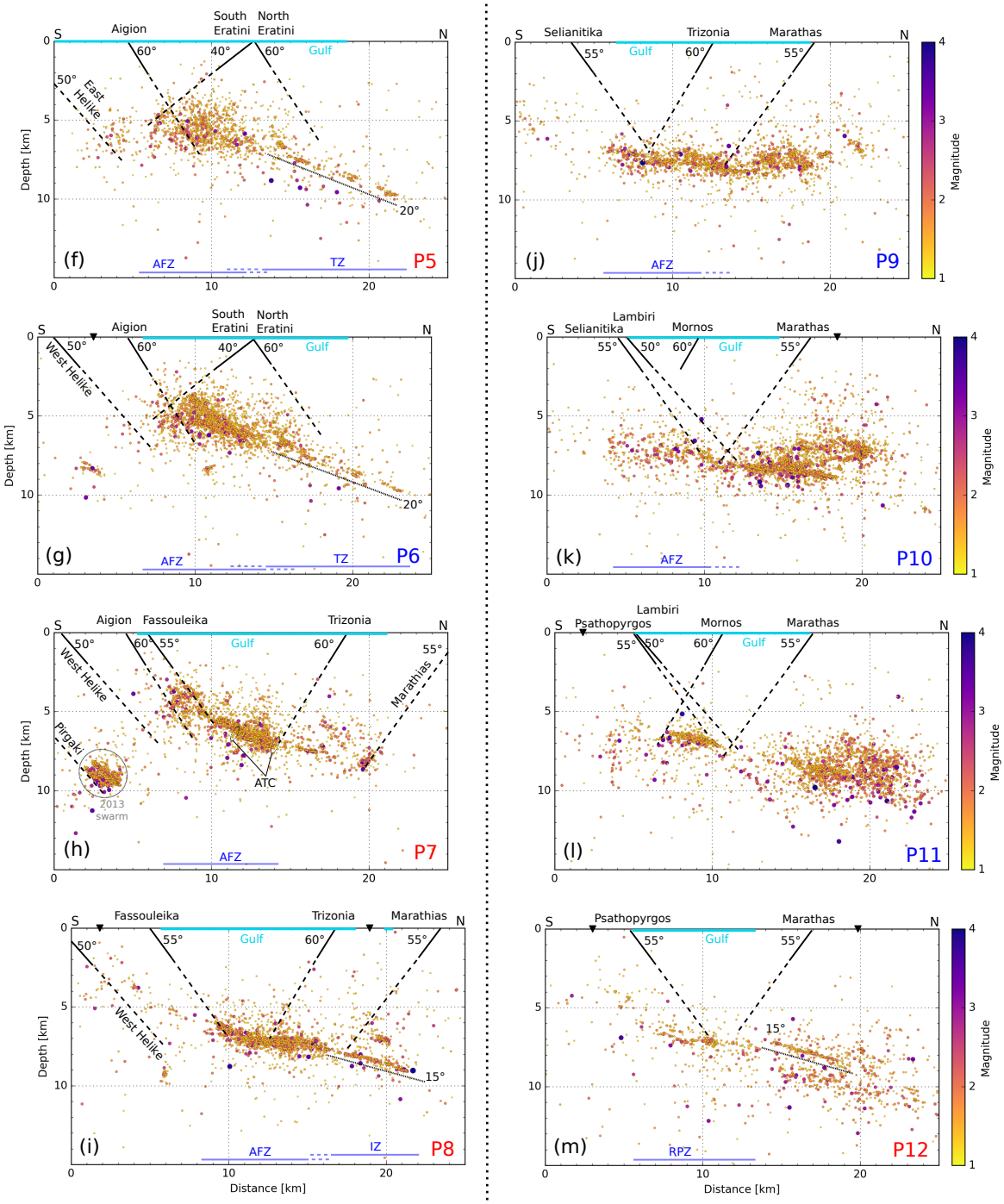

Figure 4.32 – Additional vertical cross-sections along the western Corinth rift (continued).

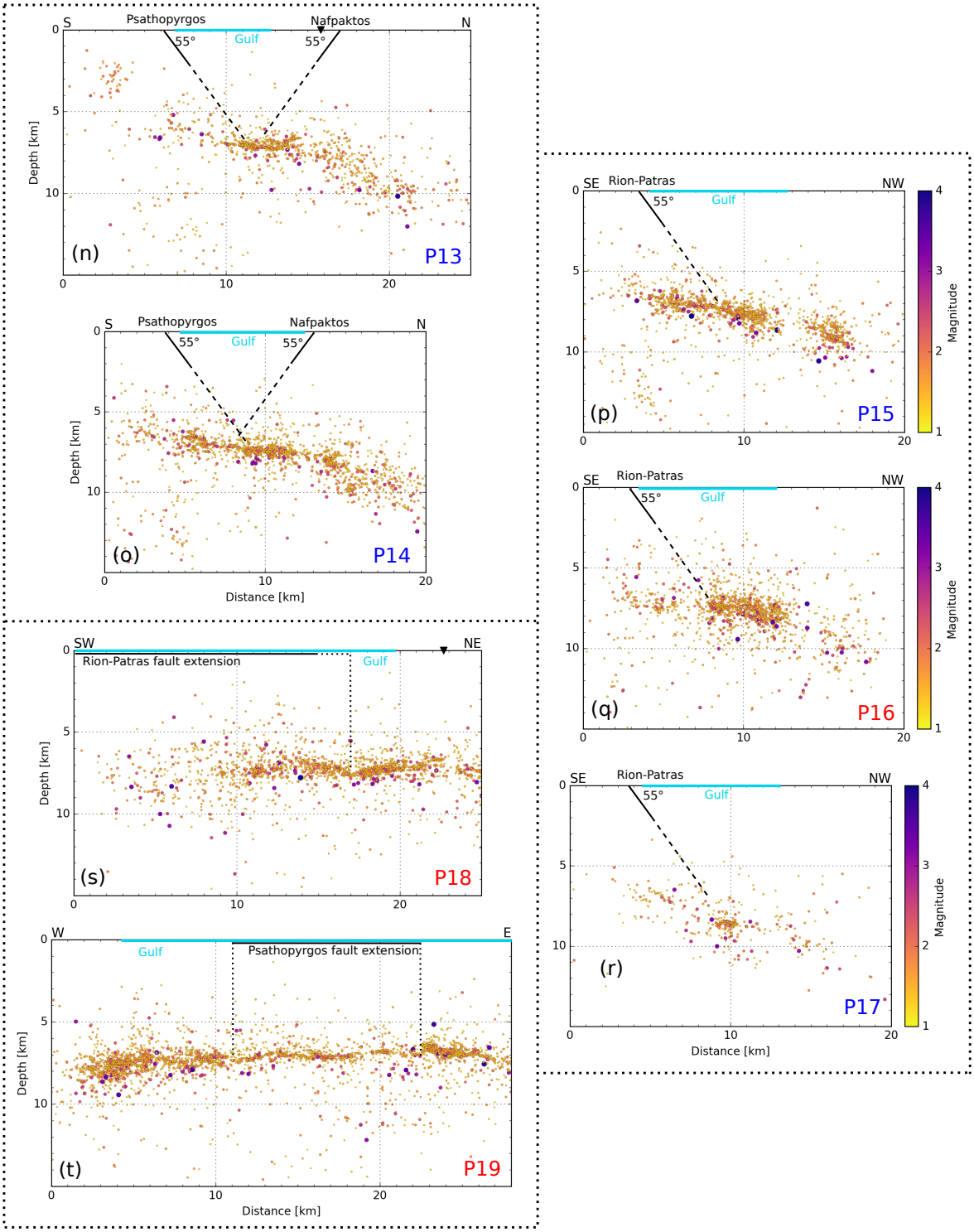

Figure 4.33 – Additional vertical cross-sections along the western Corinth rift (continued).

Chapitre 5

Déclenchement dynamique de la microsismicité du rift de Corinthe

Sommaire

Dans le premier chapitre, nous avons vu que les changements de champ de contraintes après un tremblement de terre peuvent affecter la sismicité proche et/ou lointaine via les contraintes statiques et/ou dynamiques. Dans les deux chapitres précédents, nous avons remarqué que les essaims de microséismes se produisant au sein du rift de Corinthe sont pour certains couplés à des migrations de pression de pore et pour d'autres à des glissements lents transitoires. Cependant, les mécanismes régissant l'augmentation ou la diminution des pressions de fluides dans la croûte restent encore non identifiés, tout comme l'apparition de certaines crises sismiques. Il est donc nécessaire d'explorer d'autres pistes, et éventuellement des causes à plus grande distance. C'est l'objet de ce chapitre dans lequel nous allons rechercher des possibles effets de déclenchement dynamique. Nous traitons le problème à plusieurs échelles en incluant des forts séismes télésismiques ($M \geq 7.5$), des séismes de magnitude modérée ($M \geq 6$) de la région (Grèce, Turquie) et des séismes régionaux proches de magnitude élevée ($M \geq 5$) en comparaison avec l'activité microsismique du golfe. De manière générale, en sommant l'ensemble des séismes sélectionnés comme potentielle source de déclenchement dynamique, le rift de Corinthe ne semble pas être sensible aux perturbations transitoires. Cependant, en analysant individuellement certains grands séismes, le passage de leurs ondes de surface à travers le rift semble corrélé à un changement de sismicité principalement au milieu du golfe.

5.1 Introduction

The triggering of events by the propagation of seismic waves generated by distant earthquakes, i.e. the dynamic triggering, has been first observed after the M = 7, 1992 Landers earthquake. Geothermal areas across the western United States [Anderson et al., 1994; Hill et al., 1993] have been activated with a clear increase of local seismicity following the arrival of the Landers wave trains. Out of geothermal or volcanological context, after the 1999 M = 7.2 Izmit earthquake, Brodsky et al. [2000] observed an overall increase of seismicity in Greece, in a continental context. Since then, several dozens cases of dynamic triggering following large earthquakes have been documented in different tectonical contexts worldwide [e.g. Fischer et al., 2008; Gomberg and Johnson, 2005; Gonzalez-Huizar et al., 2012; Prejean et al., 2004]. The propagating waves of a mainshock induce transient Coulomb stress changes, which are generally strong enough to trigger slip on prestressed fault [Gomberg et al., 1997].

Sometimes, dynamic triggering is also observed long after the passing of traveling waves, up to weeks after. This phenomenon is currently not well understood but several possibilities have been proposed to explain the mechanisms: (1) Parsons [2005] suggested that the dynamic stress waves damage frictional contacts of fault zones; (2) Brodsky et al. [2003] showed that fluid inside the fault zones could be pressurized by the passing waves, leading to a decrease of the effective stress on faults; or (3) the propagating waves trigger slow aseismic slip at the root of faults making microseismic ruptures easier on localized patches.

The Gulf of Corinth in Greece is an active continental rift in extension, opening at a velocity of about 10 mm.year^{-1} in the eastern part and 15 mm.year^{-1} in the western part. This high and inhomogeneous extension rate is the consequence of the back-arc extension of the Hellenic subduction and the dextral detachment of the North Anatolian Fault. Its north-south opening rate results into a high microseismicity level following a swarm organization with alternation of intensive crises and more quiescent periods. These numerous swarm activities are not explained currently and make the area a good target to explore the possibility of dynamic triggering. Our objectives are to better understand the processes involved in the microseismic behavior of the western rift and to attempt to identify particularly sensitive local areas to dynamic transient or large earthquake characteristics resulting in systematic dynamic triggering of the region.

5.2 Data and methods

Dynamic triggering has been more observed for large earthquakes (M ≥ 7.0) at distances of several thousand kilometers, but we will integrate significant earthquakes at different spatial scales in this study, gathering very large teleseismic earthquakes, moderate regional earthquakes and some noteworthy local earthquakes. After the presentation of the selected earthquake (SEQ) datasets and the microseismicity catalog of the western Corinth rift, we will detail the waveform processing steps and the statistical measure used.

5.2.1 Teleseismic, regional, and local events

Large teleseismic earthquakes

Firstly, we would like to investigate very large teleseismic earthquakes which occurred during the observational period 2000–2015. The first notable and well-known earthquakes that we think of are the M_W = 9.0, 2011 Tohoku-oki earthquake, which triggered a tsunami and caused loss of life and damage in Japan, the M_W = 8.8, 2010 Maule earthquake, which is the largest earthquake on the Southern Hemisphere since 1960, and the M_W = 9.1, 2004 Sumatra earthquake.

The March 11th 2011 Tohoku-oki earthquake is particularly interesting as it triggered seismic activity all around the world. A search for changes in local and global seismic rates after the passing waves of the large earthquakes conducted by Gonzalez-Huizar et al. [2012] revealed potential cases of instantaneous triggering in the United States, Russia, China, etc. based on the analysis of global seismic networks. Large surface waves generated by the Tohoku-oki earthquake circumvented the globe, so local and regional seismicity far from the source region could have been possibly impacted.

The February 27th 2010 Maule earthquake has been shown to trigger tremors and SSEs in Mexico with the arrival of the different S-waves and during the passing of Love and Rayleigh waves [Zigone et al., 2012], tremors in Cuba [Peng et al., 2013], but also Antartica icequakes [Peng et al., 2014]. The relation with classic seismic ruptures seems to be less obvious than for other large earthquakes but the diversity of interactions already noticed is interesting and deserves our attention.

The December 26th 2004 Sumatra earthquake was pointed to trigger seismic swarm at the chain of arc volcanoes in Alaska at more than 11,000 km away from the source, during the passage of the Rayleigh waves [West et al., 2005]. It activated deep low-frequency tremors in Japan, related to fluid flow along the Nakai subduction zone [Miyazawa and Mori, 2006], and also triggered non-volcanic tremors along the San Andreas Fault, during the later part of compressional waves but with clearer evidence during the period of surface waves [Ghosh et al., 2009].

For a statistical study, we select worldwide M ≥ 7.5 earthquakes reported in the ANSS earthquake catalog at depth shallower than 100 km. We remove 6 aftershocks or precursors from this catalog which occurred less than 3 hours before or after the mainshock. The Figure 5.1.a shows locations, occurrence times, and magnitudes of the 71 remained selected teleseismic earthquakes.

Moderate regional earthquakes

The extension of the Corinth rift is related to the dextral detachment of the North Anatolian Fault (NAF) in the north-east and the Hellenic subduction in the south-west. At regional scale, the Corinth rift is surrounded by many different fault systems accommodating the deformation due to the different plate motions. These active faults regularly generate moderate earthquakes of magnitude around 6 at hundreds kilometers from the rift. Therefore, we add 20 regional events of

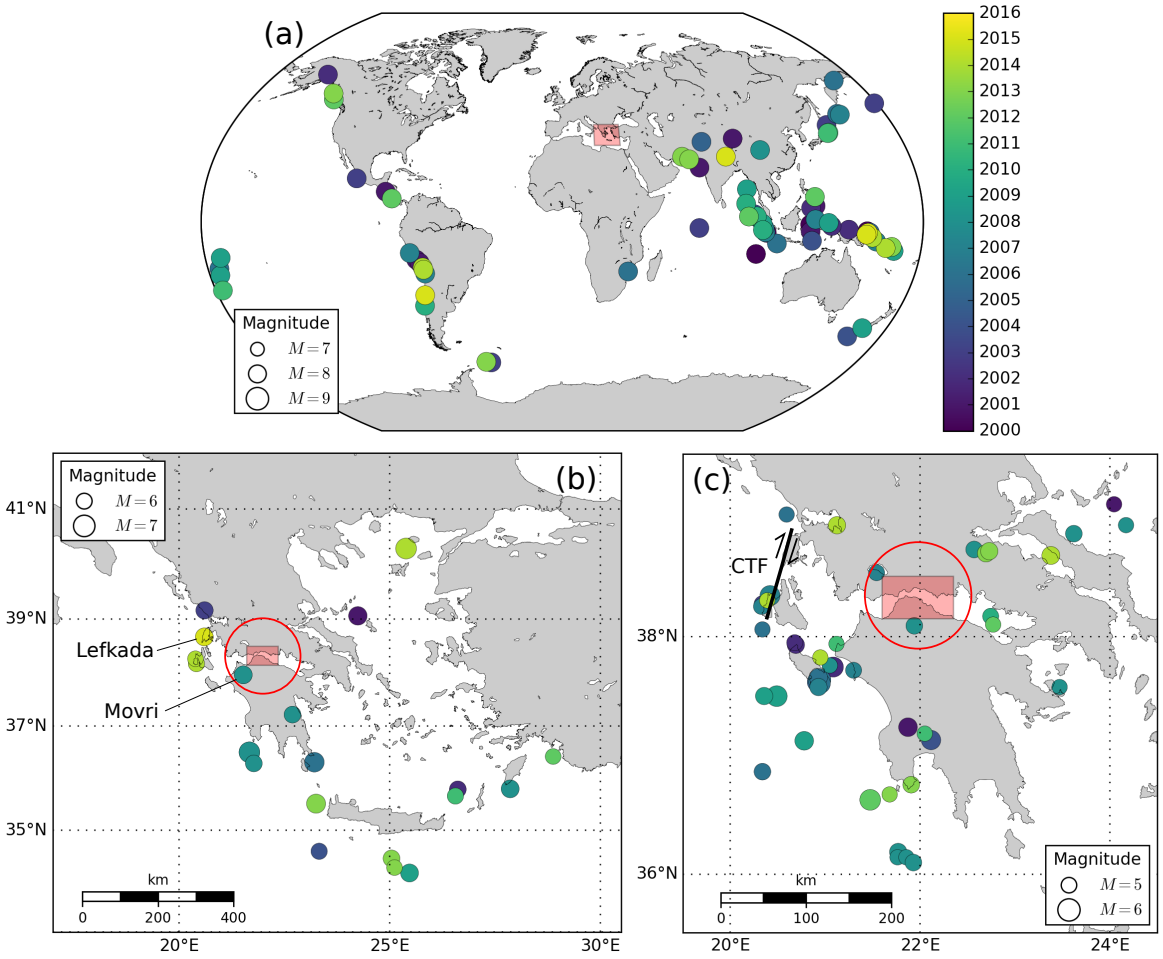

Figure 5.1 – Epicenters of selected earthquakes considered as possible sources of dynamic triggering (SEQ). (a) Worldwide map of large earthquakes (M ≥ 7.5) reported by the ANSS. (b) National map of moderate earthquakes (M ≥ 6.0) at a maximum distance of 1000 km from the center of the studied zone. (c) Regional map of moderate earthquakes (M ≥ 5) at a maximum distance of 500 km. The circle sizes are proportional to the event magnitude and the colors correspond to the event year. The events inside the red circles are not included in the stack analysis because of their relatively short distance to the Corinth rift.

M ≥ 6 occurring at distances between 100 km and 1000 km from the center of the western Corinth rift located at 22.00°E, 38.35°N (Figure 5.1.b), and 45 regional events of M ≥ 5 in a radius included between 50 and 500 km (Figure 5.1.c).

Some regional events are not included in this selection for the statistical analysis because of their proximity and their possible static effect on the local microseismicity. It is the case of the M_W = 6.4, 2008 Movri earthquake, which took place in a region free of strong seismicity, and ruptured a N-NW strike-slip fault about 30 km south of the city of Patras [Serpetsidaki et al., 2014]. It is the closest M ≥ 6 event to the Corinth rift occurring during the observational time period. We also do not integrate two M ≥ 5 regional events: the 2007-04-10 M_W5.1 event occurring just further north to the gulf at less than 50 km, and the 2008-02-04 M_W5.2 event just further south (see red circles on Figure 5.1).

Among these regional earthquakes, a recent activity draw our attention and will be analyzed individually: the M_W = 6.4, 2015 Lefkada earthquake which broke an asperity 12 years after, in between the two large sub-events of the 2003 M_W = 6.2 Lefkada doublet [Sokos et al., 2016].

Noteworthy local events

The Corinth rift exhibits large fault mirrors in the landscape, even sometimes crossing entire Greek towns. The fault system (Figure 4.1) is mainly composed of onland antithetic normal faults. The main active faults crop out on the southern coast and their dip angles are oriented north 40-60°. The Corinth rift has been shaken by a few destructive M ≥ 6 earthquakes during the last centuries, and several M > 4 have been recorded by the CRL network since its installation in 2000.

Between 2000 and 2015, the Efpalio doublet in January 2010, respectively of M_W = 5.3 and M_W = 5.2, ruptured often blind or not well known fault planes in the western Corinth rift. The two strong earthquakes occurred near the town of Efpalio on the northern coast, 4 days apart, and showed shallow normal focal mechanisms. The mainshocks triggered an intense sequence of aftershocks, whose a cluster triggered by the first mainshock was connected to a north-dipping structure where the second mainshock occurred [Sokos et al., 2012]. These two events are obviously not included in the catalog of SEQ for the statistical analysis, because of their direct impact on the local microseismicity rate. They triggered aftershock sequences mainly because of increasing static stresses. However, they will be analyzed independently more precisely.

Local microseismic catalog

The seismicity of western Corinth rift is mainly characterized by dense swarms, with about 220,000 microearthquakes of moment magnitude ranging from 1 to 4, recorded between 2000 and 2015. This swarm behavior are proposed to be induced by under-pressure fluids circulating at depth [e.g Bourouis and Cornet, 2009; Duverger et al., 2015; Pacchiani and Lyon-Caen, 2010], or to be associated to an aseismically slipping layer at 7–10 km depth in which asperities are embedded [e.g. Dublanchet et al., 2015].

We compute the number of events per day of the *Corinth Rift Laboratory* (CRL) catalog and the cumulative seismic rate over the 16 years available (Figures 5.3 and 5.2) for $M_W \geq 1.2$ events located in a maximum radius of 40 km from the center of the western rift. The moment magnitude threshold value corresponds to the completeness magnitude of the CRL catalog. Details on its computation can be found in the Annex C. Firstly, the increase of the background seismicity rate (gradient) observed from 2010 is due to the westward extension of the CRL network, with the installation of about 10 new stations.

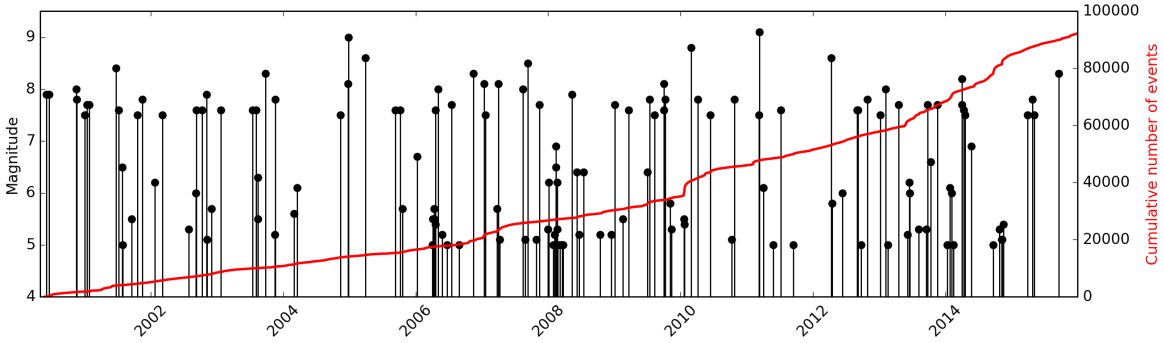

Figure 5.2 – Cumulative number of microearthquakes recorded by the CRL network. Same local events (in red) and SEQ (in black) as in Figure 5.3.

5.2.2 Wave propagation and processing

We perform an analysis for different time lengths (i.e. 3 hours, 24 hours, 3 days and 15 days in this study) before and after the theoretical arrival time of the surface waves of every selected earthquake considered as possible triggering source (SEQ). We compute the arrival time of the surface

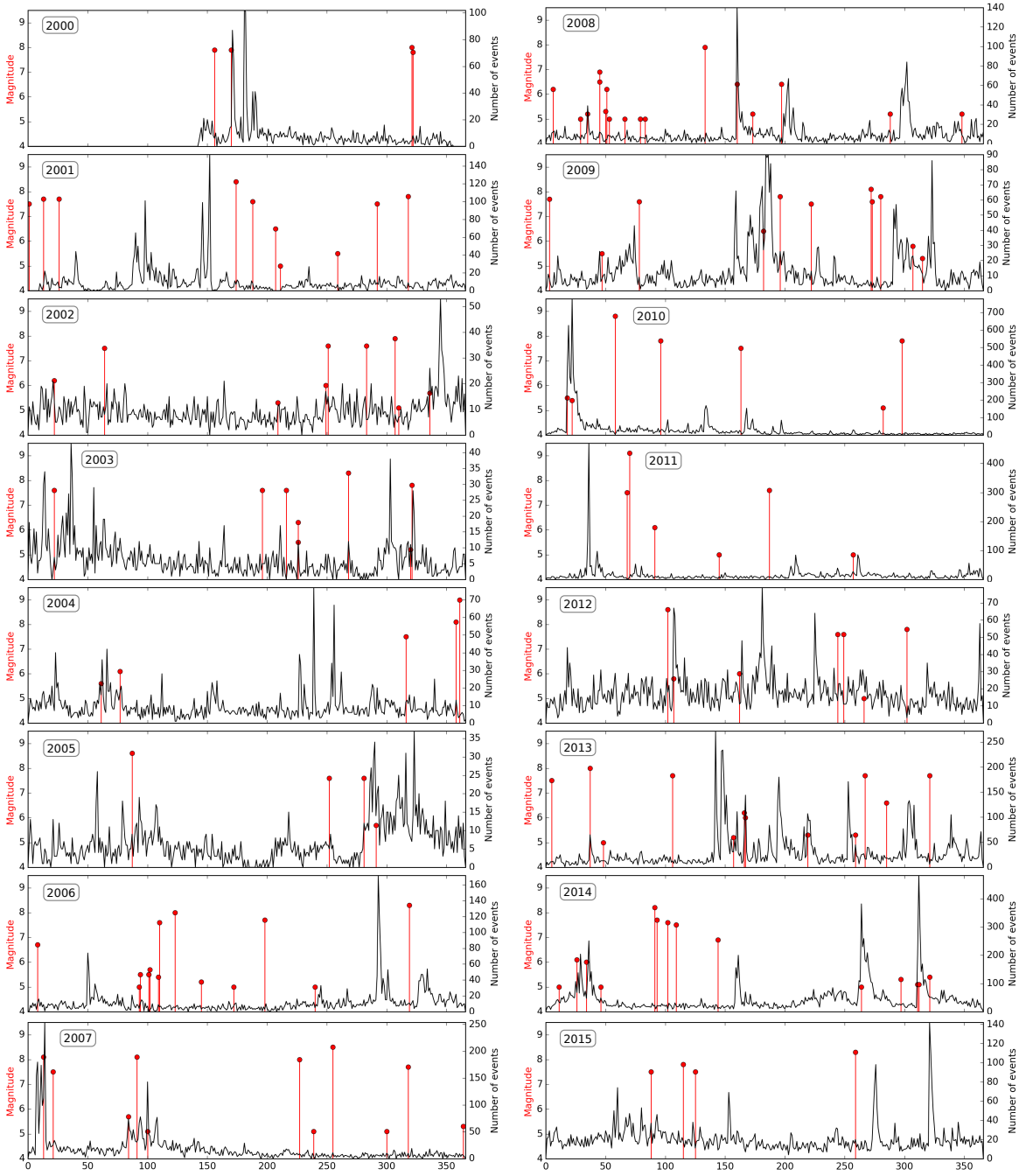

Figure 5.3 – Histogram of the number of microearthquakes per day recorded by the CRL network. Only the events of magnitude higher than the completeness magnitude (M_C = 1.2) of the catalog from 2000 to 2015 are retained (black curve). The selected potential triggering sources are represented by red lines at their occurrence time and their magnitude are specified with red circles.

waves considering a Rayleigh wave velocity of $V_R = 3.81$, extracted from PREM model at a period of 40 s.

We systematically remove aftershocks or precursors occurring during the same 24 h interval from the mainshock in order to not multiply the cumulative number of events in the stack histogram. The stack histogram is computed by defining the time origin as the surface wave arrival time for each SEQ and stacking the number of events per bin over the given time length of each indivual SEQ histogram together. In order to compare stack histograms over different time length, we normalize them by dividing the sum by the mean number of events before the arrival time of the SEQ surface waves. It gives an estimation of the seismicity rate change after the passing surface waves.

As DE BARROS et al., submitted to GRL, we also define the ratio R by dividing the number of events falling in the second half window (after the SEQ) by the total number of events counted in the considered time span. This ratio is used as a quantitative indication of the changes in the microseismicity rate: a value around 0.5 means a constant activity before and after the SEQ, while a ratio close to 1 indicates a strong increase of the number of events afterwards.

Moreover, we remind here some notions about the distribution of events in time. The Poisson's law is a discrete probability law, which describes the behavior of the number of events occurring in a given time span. If the distribution of the seismicity in time follows a Poisson'law, it means that events are randomly distributed in time, with a known mean frequency (seismicity rate) independent of the elapsed time since the last event. This behavior is opposed to the Omori's law, which describes the delayed mechanical interactions between a fault rupture and its neighbor faults. This law predicts an exponential decrease of the number of aftershocks occurring after a mainshock in its neighborhood. Seismic swarms are still a different process from the Poisson's law or the Omori's law. They are characterized by a high concentration of events in space and time without any particular mainshock at the beginning of the seismic sequence. A manner to represent the distribution of the time intervals between successive events in a specific region showing swarm activity is to consider a gamma-distribution:

$$\rho(T) = A\left(\frac{T}{T_0}\right)^{\gamma-1} \exp\left(\frac{-T}{T_0}\right) \tag{5.1}$$

where A is a constant and T_0 is the mean time interval between two successive events [Hainzl et al., 2006]. When $\gamma = 1$, the process completely follows a Poisson's law. When $\gamma = 0$, it follows an Omori's law with a mainshock and aftershocks. If $0 < \gamma < 1$, then we have a clustered behavior with both mechanical interactions and randomly distributed events. Finally if $\gamma > 1$, the process is regular with a seismic cycle pattern.

5.3 Results

5.3.1 Statistical stack analysis

Globally, we find no clear evidence of statistical increase of the Corinth rift microseismicity, both in the short-term (hours) or in the long-term (several days) period, after the passing surface waves of the global SEQ catalog (Figure 5.4). We estimate no increase at all for the daily seismicity rate over ±15 days, even a slight decrease not significant, but an increase of about 25% for the hourly seismicity rate and about 80% for the first 3 hours (left panels of the Figure 5.4). However, the number of local events detected ±3 hours from SEQs in the CRL catalog is relatively low compared to the initial 138 stack SEQs. Moreover, the distribution of R-ratios does not highlight clear shift from the natural variability of the local seismicity, whatever the given time span (Supplementary Figures 5.24 and 5.23). For the ±3 hours time length, only 13 SEQs respect the criteria of more than 10 local events to compute the R-ratio and the normalized stacked histograms. Thus, this

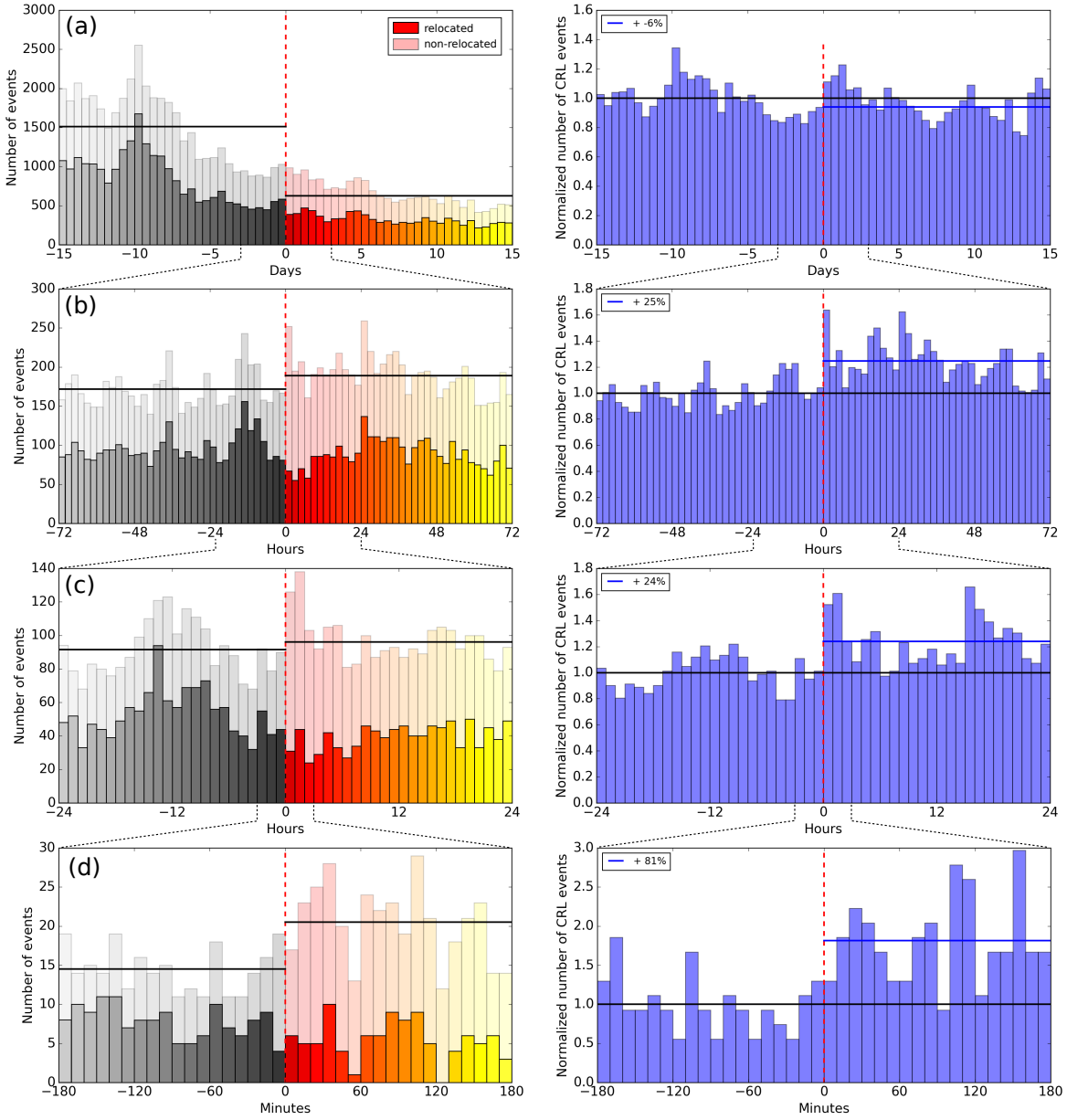

Figure 5.4 – Cumulative and normalized histograms of the number of events before and after the reference events (SEQs). The observational time is (a) 15 days, (b) 3 days, (c) 24 hours, (d) 3 hours before and after the considered SEQ (red vertical dashed line). On the left, there are stacked histograms of the number of local events before and after each SEQ. The horizontal black lines represent the mean number of events before and after the SEQs. The transparent bins correspond to non-relocated events. The colors enable to identify events before (gray scale) or after (warm color scale) the SEQs, which will be used to locate them on maps in the following figures. On the right, the stacked histograms are normalized by the mean number of events recorded before each SEQ. The horizontal blue lines show the mean number of events after the passing surface waves of the SEQs normalized to the mean number of events in the first half window (black lines).

time span is not really reliable for the CRL catalog, but we can see that 3 over the 4 SEQs with R-ratio>0.8 are likely outsiders and may correspond to triggering earthquakes. We also compare the R-ratio of each SEQ with their hypocentral distance and azimuth computed from the center of the western Corinth rift, and their magnitude and number of local events detected in the ±15 days time length (Supplementary Figure 5.25). Plots are particularly scattered. We observe high R-ratios > 0.65 (more than 1 σ higher from the mean of the natural variability of the local seismicity) for some SEQs arriving from azimuths between N30° to N100° and N250° to N310° whatever their distance or number of associated local events. However, in the same azimuthal ranges, we also find SEQ events showing low R-ratios (< 0.35), thus the mean of R-ratios in sliding azimuthal window stay confined in range 0.35–0.65 except at N290°.

We separate the different categories of SEQ (teleseismic and regional) to try to differentiate their relative impact (Figure 5.5). The same histograms with normalized number of events are shown in the Supplementary Figure 5.22, and the R-ratio distributions of the different categories in the Supplementary Figure 5.26.

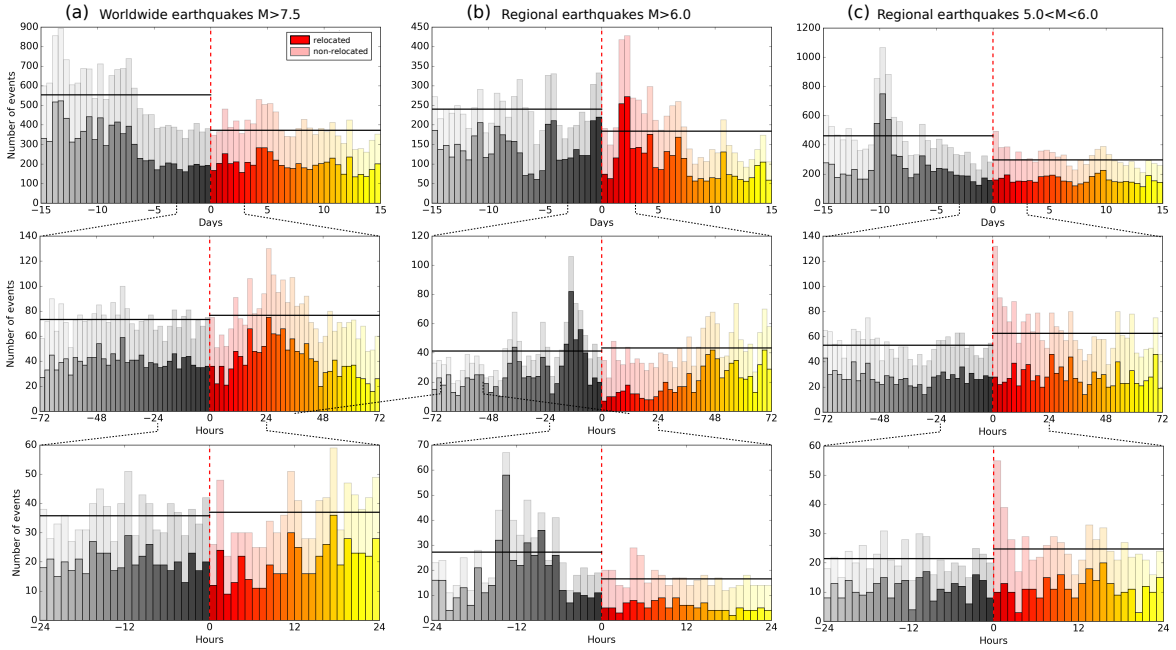

Figure 5.5 – Cumulative histograms of the number of events before and after the reference earthquakes according to their distance. Colors and markers are the same as in the Figure 5.4. (a) Stack for the worldwide M ≥ 7.5 SEQs. (b) Stack for the regional M ≥ 6 SEQs. (c) Stack for the regional 5 ≤ M < 6 SEQs.

Teleseismic events

If we only consider the 71 teleseismic events, no particular trend is observed in the histograms (Figures 5.5.a and 5.22.a). The distributions of the R-ratios follow Gaussian distributions centered on those of the natural activity of the rift with identical or larger standard deviations (Supplementary Figure 5.26.a and 5.23), without any more reliable information.

Regional events

For the 20 regional events of M ≥ 6, the results are similar to the teleseismic events in terms of histograms. We do not identify strong evidence of local seismicity variation during the seismic wave trains (Figure 5.5.b), except that for the R-ratios (Supplementary Figure 5.26.b) we observe a slight shift of the distribution to higher R-ratios for the ±3 days and ±24 hours time spans which

Table 5.1 – Regional Lefkada events. These events have been compared and studied by Sokos et al. [2016].

Date Time	Longitude (°)	Latitude (°)	Depth (km)	M_W	R-ratio
2003-08-14 05:14:55	20.60	39.16	10	6.2	1.0
2015-11-17 07:10:07	20.60	38.67	20	6.4	0.9

are not particularly convincing due to the low amount of events and the quite high standard deviations. But two events have really high R-ratios (R > 0.9) at more than 3 σ from the natural mean for ±24 hours, which possibly illustrate cases of dynamic triggering. They correspond to the Lefkada events (Table 5.1).

Together, the two episodes of moderate earthquakes in 2003 and 2015 ruptured the entire 40 km of the Lefkada Segment [Sokos et al., 2016] of the Cephalonia-Lefkada Transform Fault (CTF) zone (see Figure 5.1). The second event will be analyzed in the next section with a comment on the first one.

On the other hand, we observe an increase of the number of local events in the first hours following the passing surface waves for the 45 stacked regional events of 5 ≤ M < 6 (Figure 5.5.c). This trend is well seen for the initial hypocenter locations but not with the relocated catalog which contains about half of the total number of local events. These potentially triggered events are often located in the middle of the gulf, along the Kamarai fault system (Aigion-Fassouleika-Selianitika-Lambiri) following the southern coast (Figure 5.6).

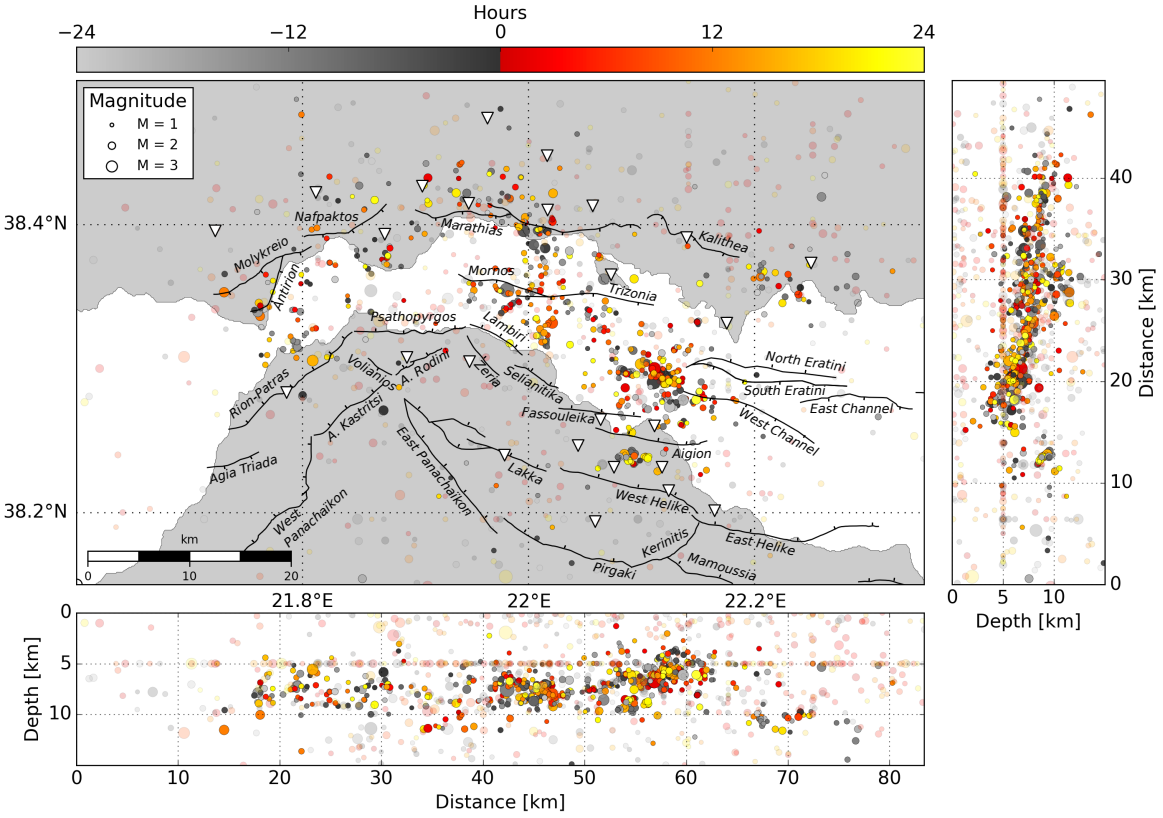

Figure 5.6 – Microseismicity map preceding and following the passing surface waves of the regional SEQ with 5 ≤ M < 6. The colorbar is proportional to the time, in gray for events 1 day before the surface wave arrivals and in warm colors 1 day after. Transparent events are non-relocated events. The major faults are mapped in black [Beckers, 2015] and the seismic stations are represented by upside-down white triangles.

5.3.2 Dynamic triggering by individual teleseismic earthquakes

Tohoku earthquake

For the Tohoku earthquake, we observe a small increase of the cumulative number of microseismic events recorded in the western Corinth rift few hours after the passing surface waves and a higher seismicity rate during the next days (Figure 5.7.a). The cumulative number of local earthquakes is more explicit with a slowdown of the microseismicity rate during the 2 days preceding the zero time and an acceleration few hours later (Figure 5.7.b). Moreover, the Tohoku earthquake shows a R-ratio of

— 0.67 for ±15 days,

— 0.81 for ±3 days,

— 0.88 for ±24 hours.

The computation of a gamma-law distribution of the interevent times of the triggered events gives a gamma value of 0.85, i.e. a swarm behavior with only 15% of mainshock-aftershock interactions against 85% of randomly distributed events (Figure 5.7.c).

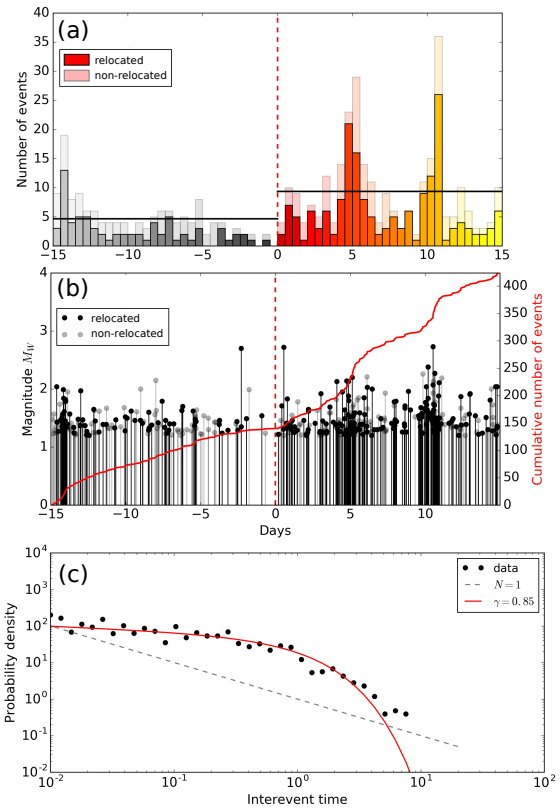

Figure 5.7 – Statistics on the Tohoku earthquake (M_W9.0, 2011). (a) Histogram of the number of events per 12 hours bins. The vertical red dashed line represents the arrival time of the Tohoku surface waves and defined the time reference. Black lines are the mean number of events 15 days before and 15 days after the Tohoku earthquake. The transparent histogram includes non-relocated earthquakes. (b) Cumulative number of events (red curve) taking into account the non-relocated events (transparent), and magnitudes of these events in time (vertical lines). (c) Probability density to trigger an event for a given time interval following the last event. We represent the distribution of the successive interevent times of the events after the passing surface waves, normalized by the mean interval time in log-log scale. We fitted the data (black circles) by a gamma-distribution (red curve). The gamma-value is around 0.85 indicating a swarm behavior with a majority of independent events and 15% of mechanical interactions of the type mainshock–aftershocks. The gray dashed line corresponds to the number of observations equal to 1.

The map of the triggered events (Figure 5.8) shows activities first in the middle part of the gulf close to city of Aigion with a thinly clustered swarm during the first days, then some events and clusters further north close to the Trizonia Island, and finally on the northern coast further west.

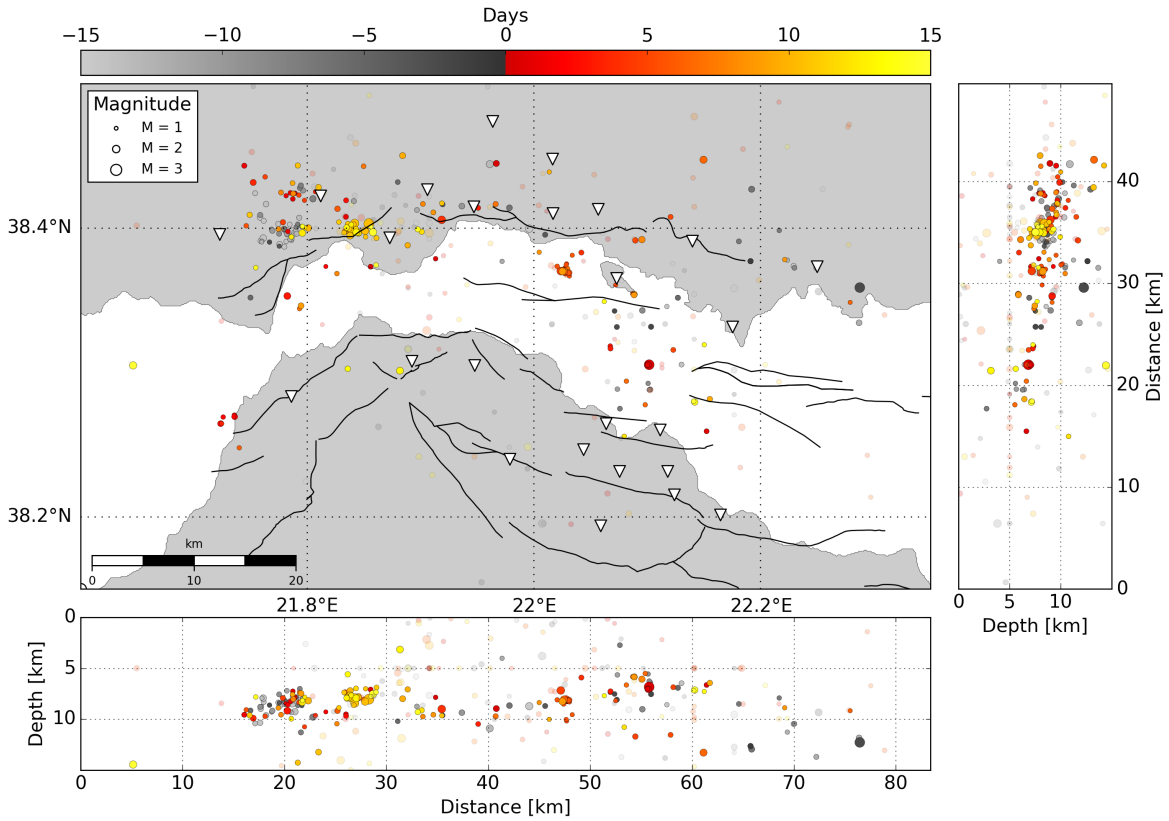

Figure 5.8 – Microseismicity map preceding and following the passing surface waves of the Tohoku earthquake (M_W9.0, 2011). The colorbar is proportional to the time, in gray for events 15 days before the surface wave arrivals and in warm colors 15 days after. Transparent events are non-relocated events. The major faults are mapped in black and the seismic stations are represented by upside-down white triangles.

Maule earthquake

For the Maule earthquake, on the contrary, we observe a gap in the CRL microseismicity just after the arrivals of the surface waves and during several hours (Figure 5.9). The microseismic activity restarts approximately one day later with a bit higher intensity. In opposition to the Tohoku earthquake, the Maule passing ways seem to interrupt a swarm in the middle of the gulf, along the Kamarai fault system (Figure 5.10), whereas the seismicity of the northern coast seems to continue.

Sumatra earthquake

For the December 2004 Sumatra earthquake, whereas several regions have shown triggering responses to different kinds of its passing waves [Velasco et al., 2008], we did not observe any significant variation in the microseismic rate or in the number of events in the Corinth rift. No valuable information can be highlighted here with the CRL catalog. More detailed analyses and a refined catalog would be needed to further investigate the situation, especially during this period when the CRL network counted only 12 seismic stations. We can add that the Sumatra earthquake did not trigger systematically significant activity during its large amplitude surface waves yet observed in specific geothermal regions known to be triggered by dynamic waves, as at the Long Valley Caldera in California for instance [Aiken and Peng, 2014]. Some possible explanations of this absence of change in the Corinth rift microseismicity would be (1) that the amplitude of the Sumatra seismic waves may be not as high as in other areas in the world due to geometrical configuration (azimuth-distance) for instance, (2) the Corinth fault systems is not oriented in a

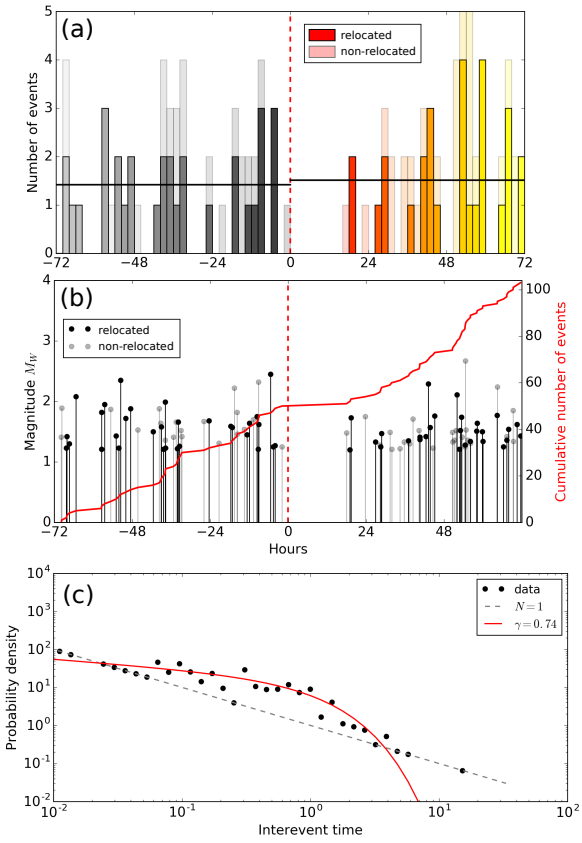

Figure 5.9 – Statistics on the Maule earthquake (M_W8.8, 2010). Subplots similar to Figure 5.7.

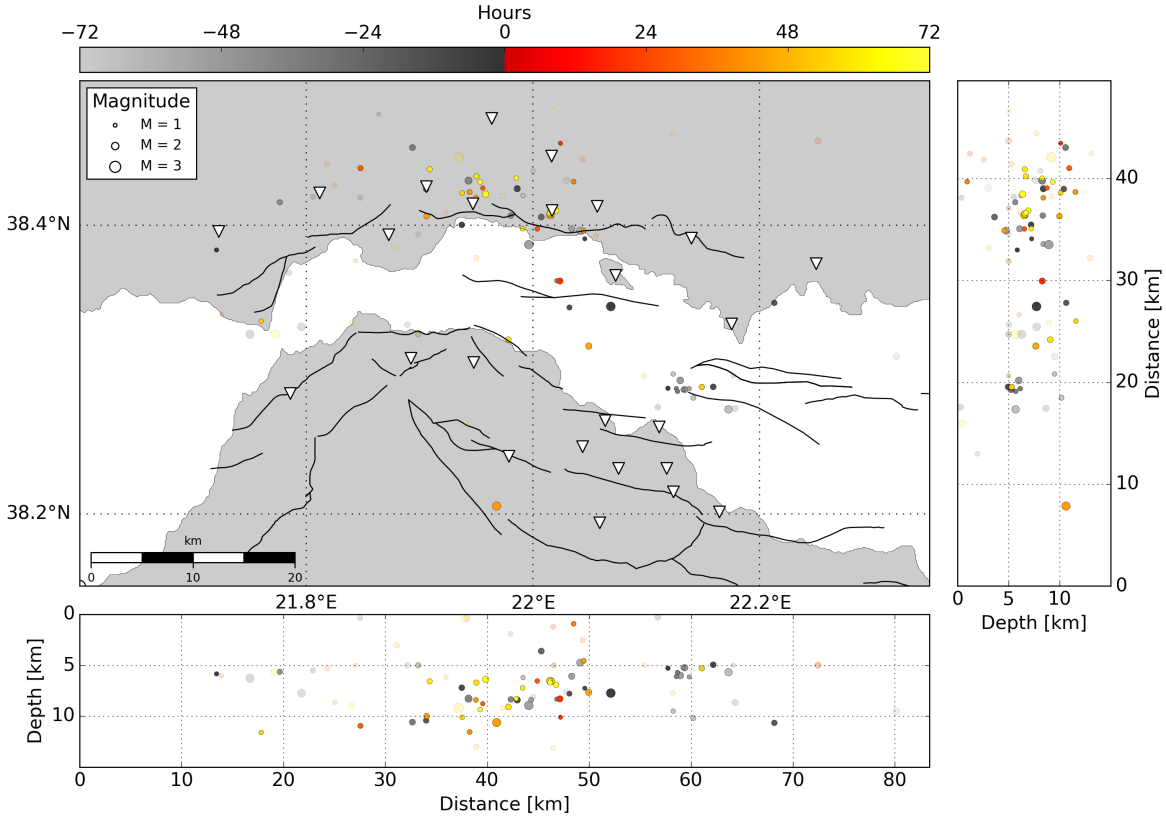

Figure 5.10 – Microseismicity map preceding and following the passing surface waves of the Maule earthquake (M_W8.8, 2010). Legend and markers similar to Figure 5.10.

privileged direction to be affected by the incoming waves, or (3) that the Corinth region previously loss accumulated stress by experiencing a prominent activity prior to the Sumatra earthquake. This last possibility could be investigated more deeply because we know that the central part of the western Corinth rift encountered a highly active seismic crisis from October 2003 to July 2004 [Duverger et al., 2015] and a relatively quiet period all along the year 2005 (Figure 5.3).

5.3.3 Dynamic triggering by individual regional earthquakes

Movri earthquake

The Movri earthquake occurred on June 8th 2008 during an unusual sequence of large earthquakes in Greece [Durand et al., 2014]. The authors showed an increase of the seismicity at regional scale, with several M > 6 earthquakes and they denoted a raise in the microseismicity rate in the western Corinth rift at the timescale of several years (Figure 5.11). The sequence of large regional ruptures starts on January 6th 2008 with the M_W = 6.2 Leonidio earthquake (Figure 5.12 #1) located in the south-eastern Peloponnese. The microseismic activity of the Gulf of Corinth is relatively quiet and does not change significantly during this earthquake with a mean of about 10–15 events per day, but the number of M > 5 raised in Greece after this earthquake (Figure 5.3). The activity remained relatively low for several days until the 4th February where a peak in the microseismicity activity is noticed with around 40 events per day during 2 days. This peak corresponds to a M > 5 event occurring less than 50 km south from the Corinth rift. Then, we observed a small bump on February 13th and 14th corresponding to the M_W = 6.8 Methoni earthquake (Figure 5.12 #2 and #3) occurring further south of the Peloponnese, in the Mediterranean Sea. On February 20th, a third large shock of M_W = 6.2 hits the same area at shallower depth [Durand et al., 2014] with a strike-slip mechanism (Figure 5.12 #4) showing no particular influence on the local microseismicity.

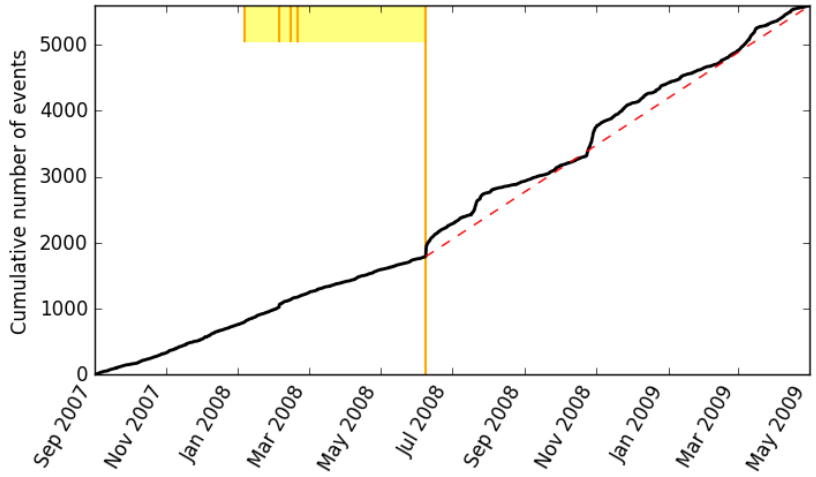

Figure 5.11 – Cumulative number of $M_W \geq 1.2$ events recorded by the CRL network between 2007 and 2009. As in Durand et al. [2014], we observed the change in the seismicity rate at large temporal scale after the sequence of M > 6 earthquakes in Greece. The yellow colored slot indicates the duration of this sequence and the orange vertical lines their occurrence time.

Finally, the June 8th Movri, also named Andravida or Achaia-Elia earthquake (Figure 5.12 #5) localized at 22 km depth [Serpetsidaki et al., 2014] is the clearer evidence of seismic interactions with the Corinth rift, due to the occurrence of more than 300 microseismic events in 1 day (Figure 5.13) recorded by the CRL network. The Movri earthquake ends the sequence of M > 6 events and lies in the continuation of the North Anatolian Fault, as well as the western Corinth rift. We distinctly observe a mainshock-aftershocks sequence with an Omori's law decay in the first 24 hours of the histogram and the time-magnitude distribution (Figure 5.13.a-b) and the gamma-value of the interval times of about 0.4 reinforced the result.

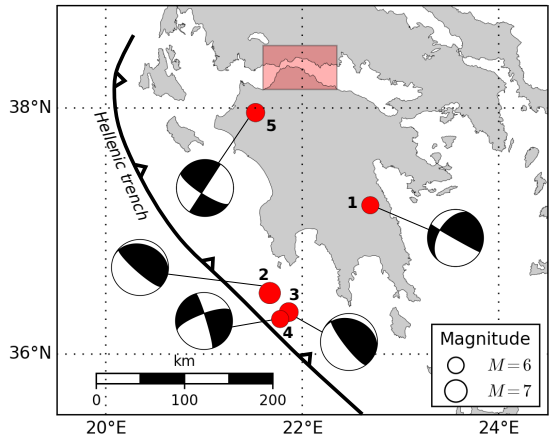

Figure 5.12 – Map of the M > 6 earthquakes sequence in 2008. Focal mechanisms are from Zahradnik et al. [2008] and www.geophysics.geol.uoa.gr. The red rectangle outlines the studied western Corinth rift.

However, after the relocation of the CRL events by double-differences, a large majority of the microearthquakes present in the catalog were actually localized outside the western Corinth rift or not in the central part of the gulf. The triggered events seem to be localized inland on the southern coast (Figure 5.14), and further south closer to the mainshock, on the growing strike-slip fault system [Serpetsidaki et al., 2014]. Some events are on the contrary located in the middle of the rift, close to the Trizonia and Mornos faults, but they probably correspond to the natural daily activity already present before the earthquake. The question of dynamic or static triggering is still an open question here, since the distances between the observed microearthquakes and the mainshock are not large enough to conclude (less than 50 km). The microseismicity recorded by the CRL network is close to a regional microseismicity (not local), but the differences between the S- and P-arrival times at the stations were lower than 3 s, to pass the $T_S - T_P$ threshold condition.

Lefkada earthquake

For the 2015 Lefkada earthquake, the behavior is roughly the same as for the Movri earthquake. The CRL network has recorded around 200 earthquakes in 24 hours (Figure 5.15), with a clear increase of microseismicity rate over several days. However very few events have been relocated and thus most of them are located in the north-western part of our map (Figure 5.16). Concerning the 2003 Lefkada earthquake, almost exactly the same pattern as the 2015 one is observed. No local event has been detected in the 24 hours prior the 2003 earthquake, and about a dozen events occurred after in the CRL catalog, but all of them are not relocated. They occurred in the westernmost part of the Corinth rift. We think that these local events do not come from the western Corinth rift fault systems but belong to strike-slip structures further north-west. Nevertheless, the distance between the Lefkada earthquakes and these small events (more than 150 km apart) suggests that at least a part of them could be dynamically triggered.

Efpalio doublet

The Efpalio doublet occurred on the northern coast with two relatively shallow mainshocks located at about 5–6 km and 8–9 km depth respectively [Sokos et al., 2012]. Both events triggered aftershocks in a radius of about 10 km (Figures 5.17 and 5.18). Several attempts of relocation of the mainshocks and aftershocks have been performed [Ganas et al., 2013; Sokos et al., 2012] but the results remain difficult to interpret and the chosen solutions do not converge between the different authors. We also undertook a relocation of the Efpalio sequence combined with the microseismicity recorded by the CRL network during the crisis (see Chapter 4), without obtaining any more clarification on possible structures. However, it has been shown that the aftershock clusters are bounded by strike-slip faults at their western and eastern ends [Sokos et al., 2012].

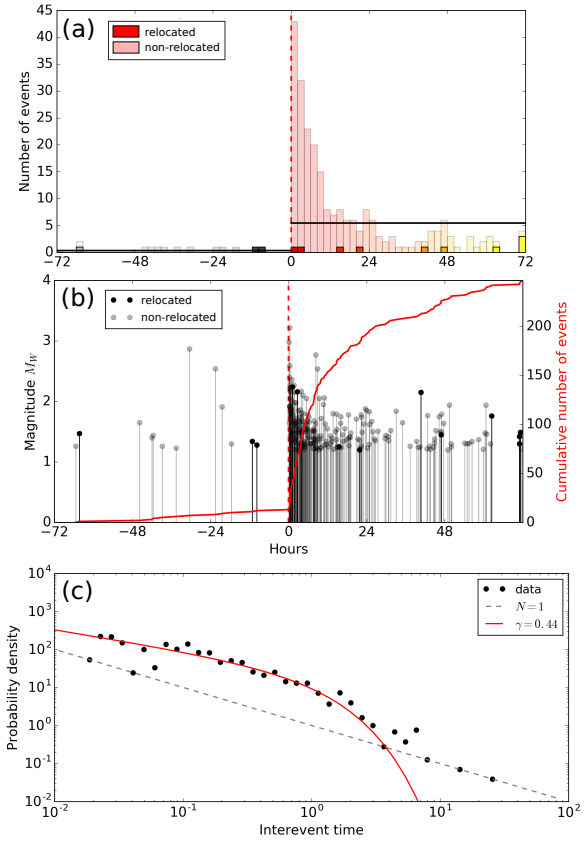

Figure 5.13 – Statistics on the M_W6.4 Movri earthquake. Subplots similar to Figure 5.7.

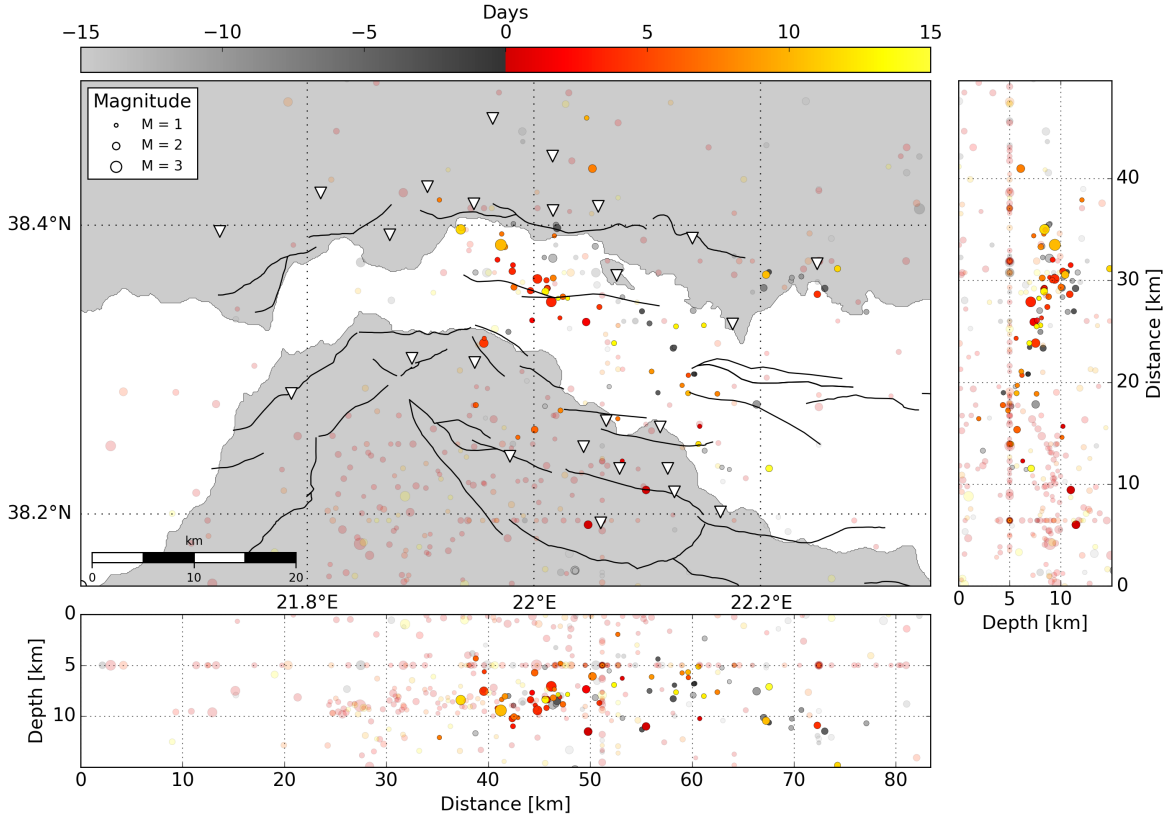

Figure 5.14 – Microseismicity map preceding and following the passing surface waves of the Movri earthquake (M_W6.4, 2008). Legend and markers similar to Figure 5.10.

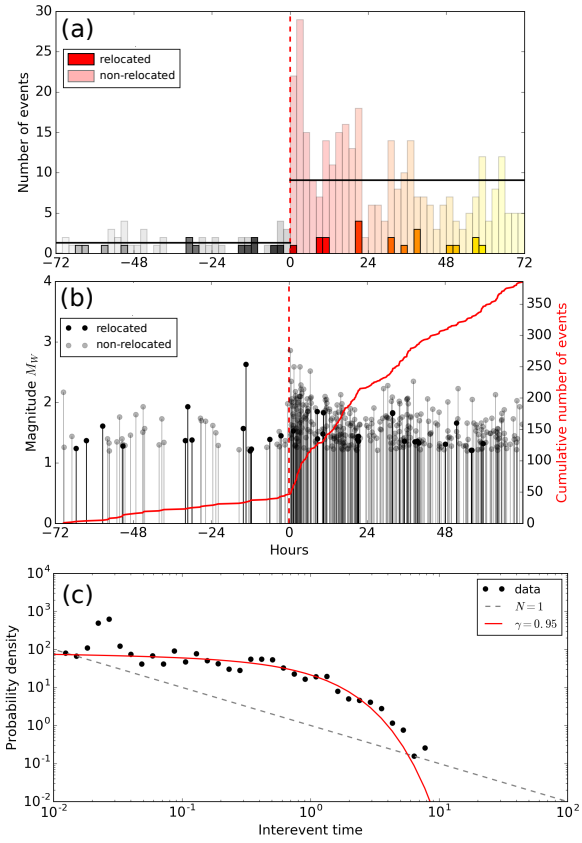

Figure 5.15 – Statistics on the M_W6.4 Lefkada earthquake. Subplots similar to Figure 5.7.

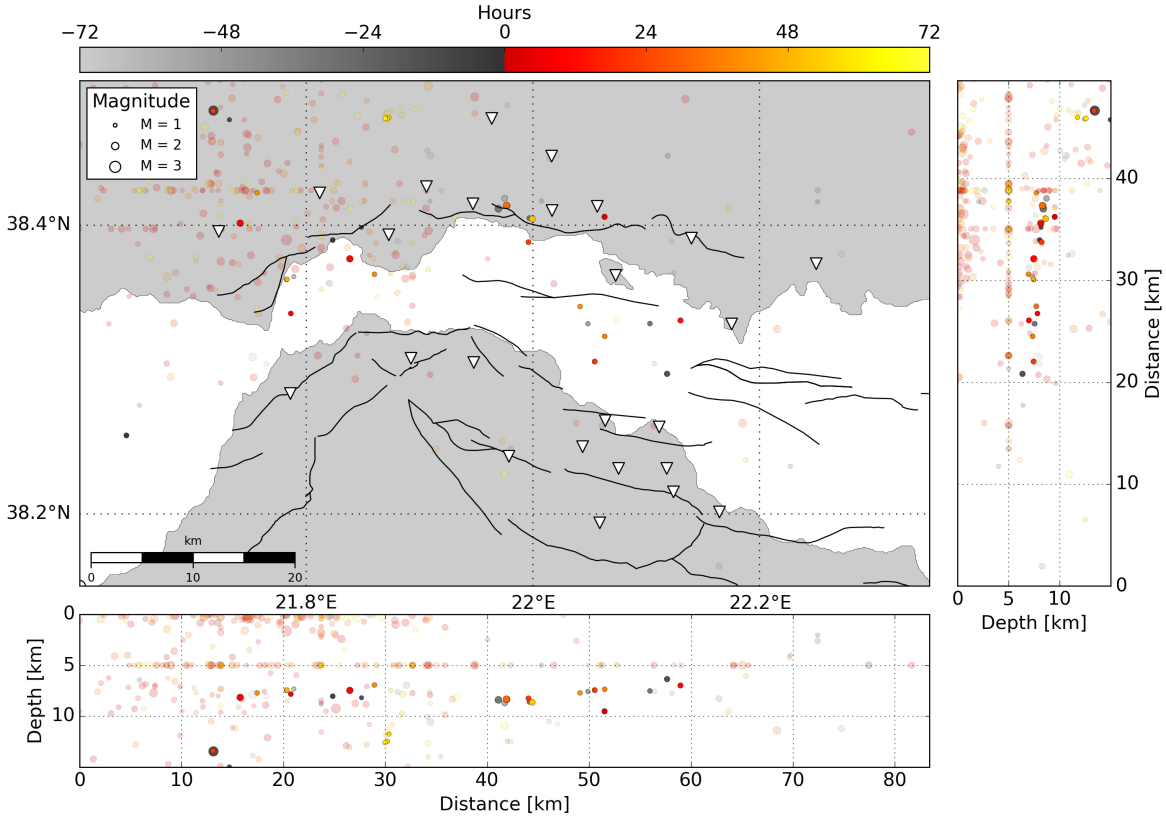

Figure 5.16 – Microseismicity map preceding and following the passing surface waves of the Lefkada earthquake (M_W6.4, 2015). Legend and markers similar to Figure 5.8.

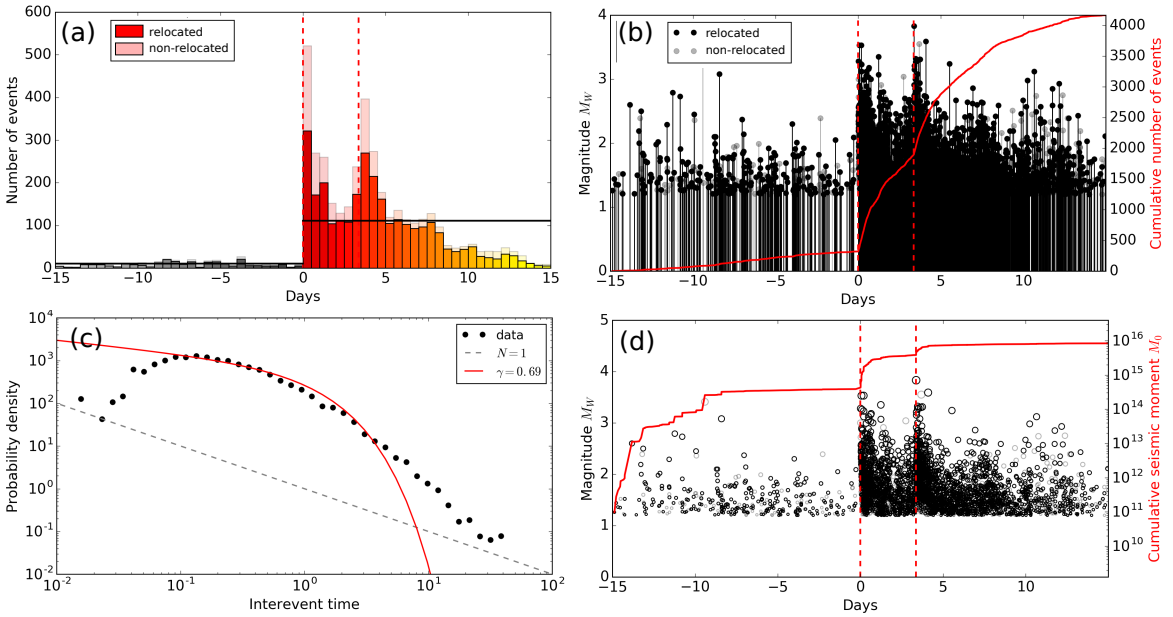

Figure 5.17 – Aftershocks of the Efpalio doublet. Subplots similar to 5.7.

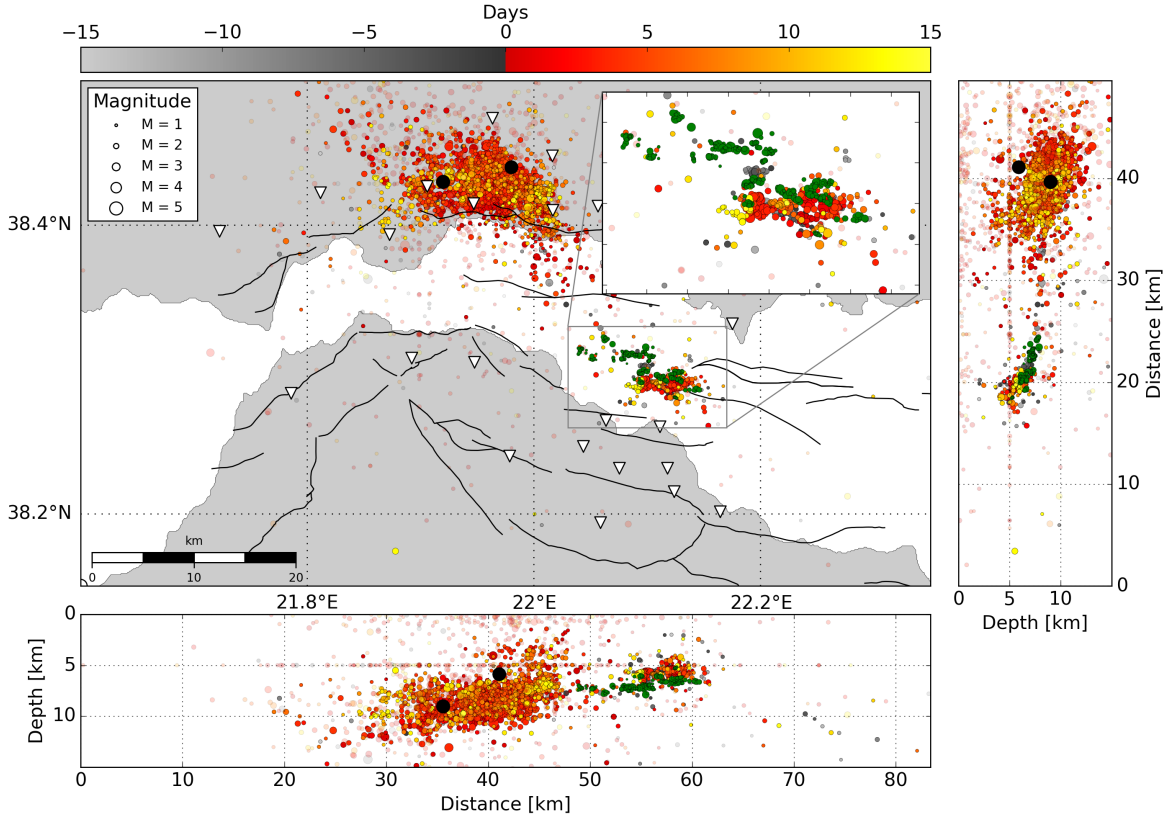

Figure 5.18 – Microseismicity map preceding and following the doublet of Efpalio (M_W5.3 and M_W5.2, 2010). Legend and markers similar to Figure 5.8. Black circles are the two Efpalio earthquakes occurred on January 18th and 22nd. Green circles represent the multiplet events of the 2003–2004 seismic crisis.

Independently of the well-observed static triggering of aftershocks, we notice the activation of a small cluster located 30–40 km apart in the middle of the rift, linked to the Kamarai fault system (Figure 5.18). This cluster is localized in the same area of the 2003–2004 seismic crisis, described in the Chapter 2 and represented in green on the map.

We notice that the observed swarm was active prior to the first mainshock, but its activity was decreasing during the 4 days before, until the first rupture which seems to more intensely reactivate the cluster in the next few days (Figure 5.19). The gamma-distribution clearly shows a swarm behavior with a gamma-value of about 0.3. Moreover, looking at the spatio-temporal evolution of the sequence, we observe a westward migration of the microseismicity front at about several hundreds meters per day starting about 15 days before the first mainshock and a stop with a back-migration 2 days before (Figure 5.20). At the occurrence of the M_W5.3 January 18th earthquake, an another westward migration, slightly faster of the order of a kilometer per day, starts and lasts until January 22nd, date of the second M_W5.2 earthquake. After that, the swarm remains active with the occurrence of several smaller clusters more randomly distributed in space-time domain.

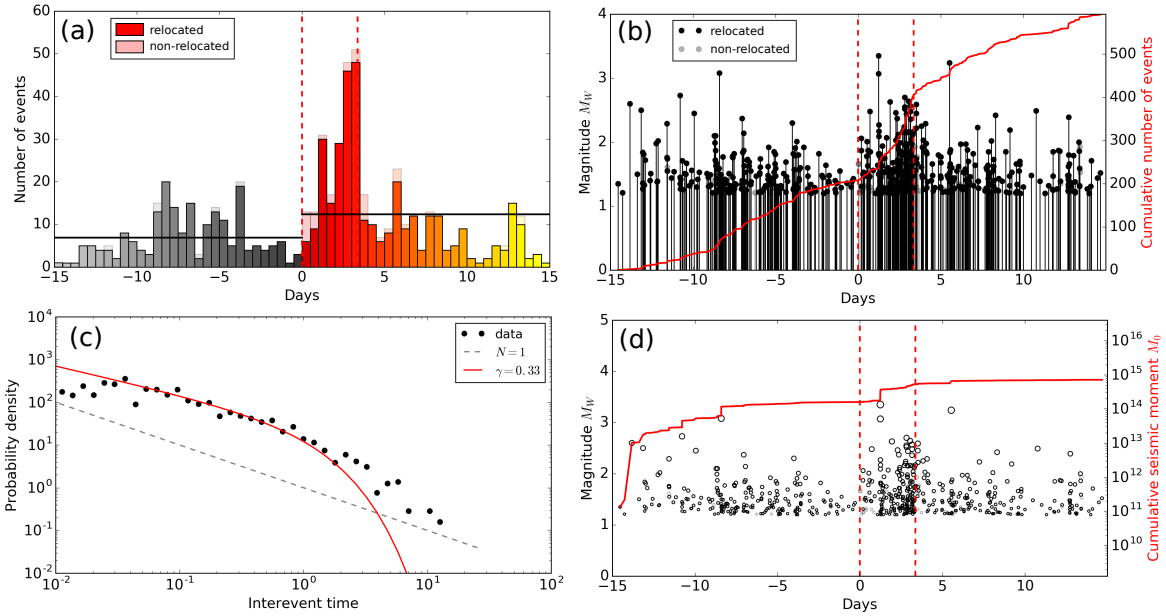

Figure 5.19 – Swarm reactivated by the Efpalio doublet. (a,b,c) subplots similar to 5.7. (d) Magnitudes of events (circles) and cumulative seismic moment (red curve). The red vertical dashed lines are the times of the two mainshocks.

The cumulative distribution of the number of events inside the swarm clearly shows a phase with an acceleration and a slow-down just before the first mainshock, and then a stronger increase of the number of events until the second mainshock. The last one seems to stop or at least slow-down the activity of the swarm, whereas the first one magnifies it slightly just after its rupture time and much more with a delay of about 24 hours.

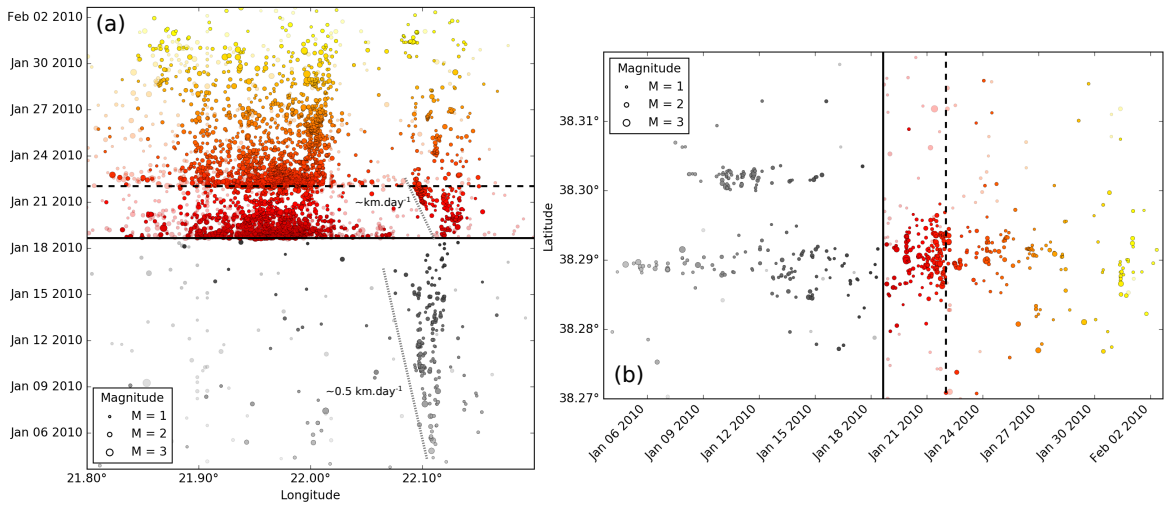

Figure 5.20 – Spatio-temporal evolution of the swarm reactivated by the Efpalio doublet. (a) Time as a function of longitude in degrees. (b) Latitude in degrees as a function of time. As for the previous figures, the colorscale is adjusted to the timescale and transparent circles represent non-relocated events.

5.4 Discussion

We identify several worldwide earthquakes which potentially triggered microseismicity in the western Corinth rift, during and after the passing of the surface waves. In some cases, the link between increasing seismicity rate and arrivals of the waves is not well defined due to the delay between each other. This is also the case for the stack analysis. Several mechanisms have already been invoked to explain cases of delayed triggering [Hill and Prejean, 2015], including (1) the damaging of the frictional contacts Parsons [2005], (2) pressurized fluid inside fault zones and pore pressure diffusion Brodsky et al. [2003], (3) slow aseismic slip, as already mentionned in the Introduction 5.1.

For the remaining SEQs, we have seen a slight increase of the local seismic rate, but this change is not persistent over the different time scales. The increase number of local events is not large enough for the small time lengths to be significant. Moreover, the constant Rayleigh wave velocity implemented for all SEQs may have a delay impact in this analysis and may especially arbitrary rise the number of events just before the predicted arrival time if the real velocity is higher and a direct triggering is occurring. We did not look either for an influence of the body wave traveling faster than the surface waves whereas they might also trigger some local events.

5.4.1 Initial catalog of hypocenters

In attempt to observe more direct triggering cases without large delays, we need (1) to look into the continuous data to determine the real arrival time of the SEQs, filtering the waveforms with a low frequency bandpass filter, (2) to thinner detect events in a short observational time span (typically of few hours) in order to catch up some masked events and improve the statistical confidence. Indeed, the automatic method used to detect local events and based on an overpassing threshold value may miss some small local events because of high regional activities or other passing waves hiding the onset of the local events. Moreover the explored CRL catalog only contains located events with a magnitude estimate, whereas some other events have been detected but the recorded waveforms are not good enough to pick the phase arrival times, estimate a location or estimate the source parameters. Matched-filtering technique would be a really interesting solution to detect much more events during seismic crisis periods for instance, especially knowing that a catalog of event families have been created (see Chapter 4).

We also have seen that a huge number of events have not been relocated in the Corinth rift. This absence of relocated hypocenter for an event is either due to events, which do not respect the initial conditions of phase number, or weak links with its neighbors. For the Movri earthquake for instance, most catalog events are actually not well located and integrated in the western Corinth rift microseismicity whereas they did not belong to this specific region. This explains their rejection in the relocation process.

5.4.2 Transient stress across the rift

We almost systematically observed activity along the Kamarai fault system, either stopped or triggered for the discussed cases. This area of the western Corinth rift has been suggested to be particularly sensitive to fluid pore pressure, with evidence of microseismic migrations at similar velocity as pore pressure front diffusion, especially during the 2003–2004 swarm [Duverger et al., 2015]. Our results reinforced this assumption knowing that transient stress induced by the traveling seismic waves may influence the pore pressure inside fault crevices, thus trigger the rupture of asperities.

Moreover, Canitano et al. [2017] observed seismic seiches in the rift of Corinth triggered by the passing seismic waves of the Tohoku earthquake. Indeed, unusual water level fluctuations were recorded by a tide-gauge located on the Trizonia island, and evidenced as initiated by the S-waves and then enhanced by the surface waves. Given this highlighted correlation, we might also expect changes in the pore pressure conditions at crustal depth, possibly explaining the occurrence of some delayed events in the middle of the gulf.

5.4.3 Dynamic or static stress?

At relatively short scale, the distinction between static and dynamic triggering is more difficult. Indeed, static triggering occurs within a few fault lengths of a mainshock rupture and results from slip-induced changes in the local stress field, whereas dynamic triggering occurs from the rupture location to large remote distances and results from the field perturbations caused by traveling seismic waves. We wonder here if the cluster reactivated by the Efpalio doublet is either dynamically triggered as proposed or statically triggered.

Sokos et al. [2012] has shown a map with the modeled static stress caused by the first event of the Efpalio doublet (Figure 5.21). This stress is concentrated in one or two fault length distance (10 km) and seems to be honestly too small to trigger activity at about 40 km south-east, in the direction of the swarm. We are quite confident in the dynamically triggering case thanks to this model, and because of the location of the cluster in a area sensitive to fluid.

5.4.4 Mechanisms of the Corinth rift fault systems

Dynamic triggering often appears on faults close to failure and thus often gives information on the stress state of analyzed faults. For the western Corinth rift and the analyzed teleseismic and regional earthquakes, only few possible dynamic cases have been shown, whereas we selected the strongest events as possible triggering sources. If we are confident in the CRL catalog and try to explain this relatively weak response with a simple mechanical interpretation, we can suppose either that (1) the faults are discharged at the time of the passing surface waves, (2) the incoming waves are not properly oriented in favor of the fault play, or (3) rupture directivity effects [e.g. Gomberg et al., 2004; Husker and Brodsky, 2004; Pankow et al., 2004] sometimes shadow the Corinth rift region. However, the selection of earthquakes explored the whole range of possible azimuths with

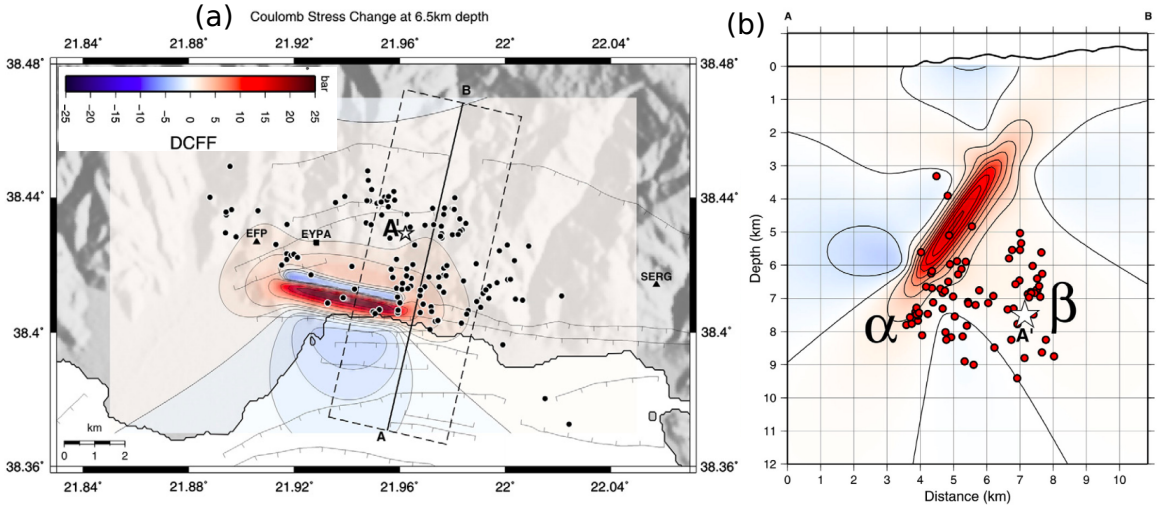

Figure 5.21 – Coulomb stress change due to the first event of Efpalio doublet. (a) Map view at 6.5 km depth, i.e. 2 km below the centroid depth of the event. (b) Vertical cross-section of the assumed south dipping fault plane. The red circles are the early aftershocks. The white star is the second mainshock. From Sokos et al. [2012].

different focal mechanisms and some large earthquakes occur during swarms, when the fault systems are destabilized and should normally be more excited.

That is, authors [e.g. Prejean et al., 2004; Stark and Davis, 1996] have noticed that some areas do not appear to require a certain amount of time to be stress recharged and for triggering to recur. Moreover, Prejean et al. [2004] precise that some regions are more susceptible to large-scale triggering than others, and especially the extensional environments, as Corinth, because fractures closer to the vertical can be opened by relatively low-stress changes leading directly to unstable rupture [e.g. Hough and Kanamori, 2002]. Low-stress perturbations could also trigger more easily in hydrothermal system regions because high pore pressures decrease the effective normal stress of the fault system [e.g. Brodsky et al., 2003; Hill and Prejean, 2015]. Finally, we think that the normal faults of the western Corinth rift would have variable stress drop characteristics, so that only a low percentage of them could be triggered because of a low effective stress.

5.5 Conclusion

The Corinth Gulf is an active rift system characterized by dense seismic activities with some larger M_W6 earthquakes per century. With such numerous swarms and its extensional context, it is a really good target to look for dynamic triggering cases. We explored a wide catalog of large teleseismic, moderate regional and strong local earthquakes, in comparison to the microseismicity recorded by the CRL network.

Globally for the 71 teleseismic earthquakes occurring between 2000–2015, no significant increase of the seismicity rate or of the activity is revealed across the rift. We did not find relevant changes either in the seismicity rate for the 20 stacked selected M > 6 regional earthquakes. Globally, the normal faults of the western Corinth rift do not seem to be efficiently affected by dynamic stress to make nucleate micro-earthquakes during the time of passing surface waves. Apparently, the dynamic variations of stress generated from far and large earthquakes do not alter the friction coefficients of the faults.

However, we identified some individual cases of dynamic triggering by teleseismic earthquakes, especially the Tohoku earthquake. This is the most probable case, with its R-ratio of 0.88 (at 3 standard deviation from the average, i.e. less than 1% chance) for a time span of ±24 hours. Among

others, it activated several micro-earthquakes in the middle of the gulf during the first twenty hours, thinly clusterized in space. The fact that the Tohoku earthquake triggered some seismicity in the Corinth rift whereas the closer and moderate regional earthquakes seem less effective could also be due to the long duration of its passing surface waves. The surface waves of the closer events travel across the rift on a shorter period. We also discovered some examples of dynamic triggering at smaller scale, inside the western Corinth rift itself with the Efpalio doublet. Moreover, these examples showed the systematic activation of the middle part of the gulf, along the Kamarai fault system. Therefore, we suggested that this area is mainly influenced by fluid pore pressures and then are easily affected by small variations of stress induced by remote earthquakes.

For the largest events, it would be interesting to see if we can observe the incoming waves in the continuous waveforms recorded by the CRL network in order to measure the amplitude of the surface waves, and determine whether the level is really sufficient to dynamically trigger local events. Indeed, the dynamic triggerability depends on the amplitude of the seismic waves, but the arrival azimuth of the passing waves could also be a controlling factor. For other perspectives, it would be interesting to compare the gamma-distribution of the triggered local events with the R-ratio value, in order to detect abnormal behavior. Indeed, we have seen that for the Tohoku earthquake, the triggered sequence of local events shows a relatively high γ-value corresponding to a large population following a Poisson's activity. This behavior is not common in the way that we expect more a swarm activity with mechanical interactions after a large earthquake. For the Tohoku earthquake, the Poisson activity seems to be slightly amplified. We then propose to couple analyses of gamma-values and R-ratios by representing both parameters in a 2-D diagram for instance, to reveal possible abnormal cases and help in the determination of dynamic or static triggering.

5.A Supplementary figures

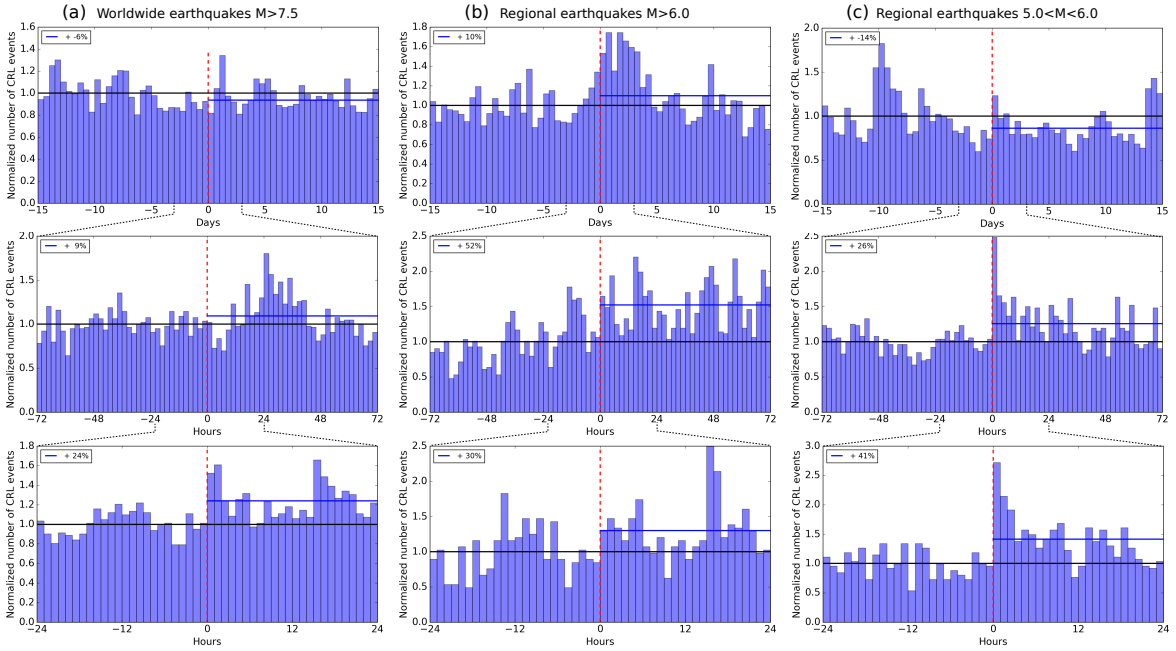

Figure 5.22 – Cumulative and normalized histograms of the number of events before and after the reference earthquakes according to their distance. Same as the Figure 5.5 except that the histograms are normalized by the mean number of events before the passing surface waves of the SEQs.

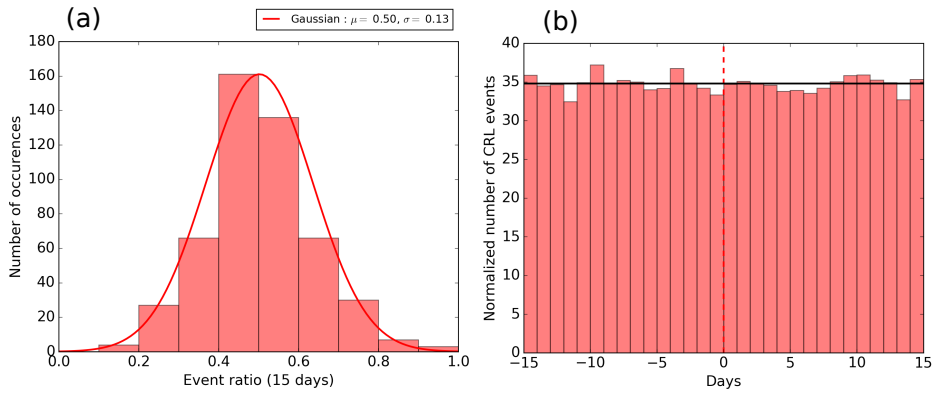

Figure 5.23 – Natural variability of the local seismicity. (a) Histogram of the R-ratios. (b) Histogram of the number of events before and after a reference time. We estimate the natural variability by randomly selecting 500 times a reference time in the observational time catalog (from 2000 to 2015). The 500 windows of 30 days contain at least 10 events from the CRL catalog. The R-ratios are computed as the number of events in the second-half of the windows over the total number of events. The fitted Gaussian distribution is centered on $\mu = 0.5$, with a standard deviation of $\sigma = 0.13$ (red curve). The fitted distributions for the other time spans (±3 days, ±24 hours and ±3 hours) give the same values with uncertainties: $\mu \pm 0.01$ and $\sigma \pm 0.01$. This curve is especially used in the Supplementary Figures 5.24 and 5.26 to show the natural variability of the microseismicity. (b) It shows how the normalized cumulative number of events varies with time on the 30-day windows. Here, the variability is small compared to the mean number of events per day (~35) without any clear changes in the number of events.

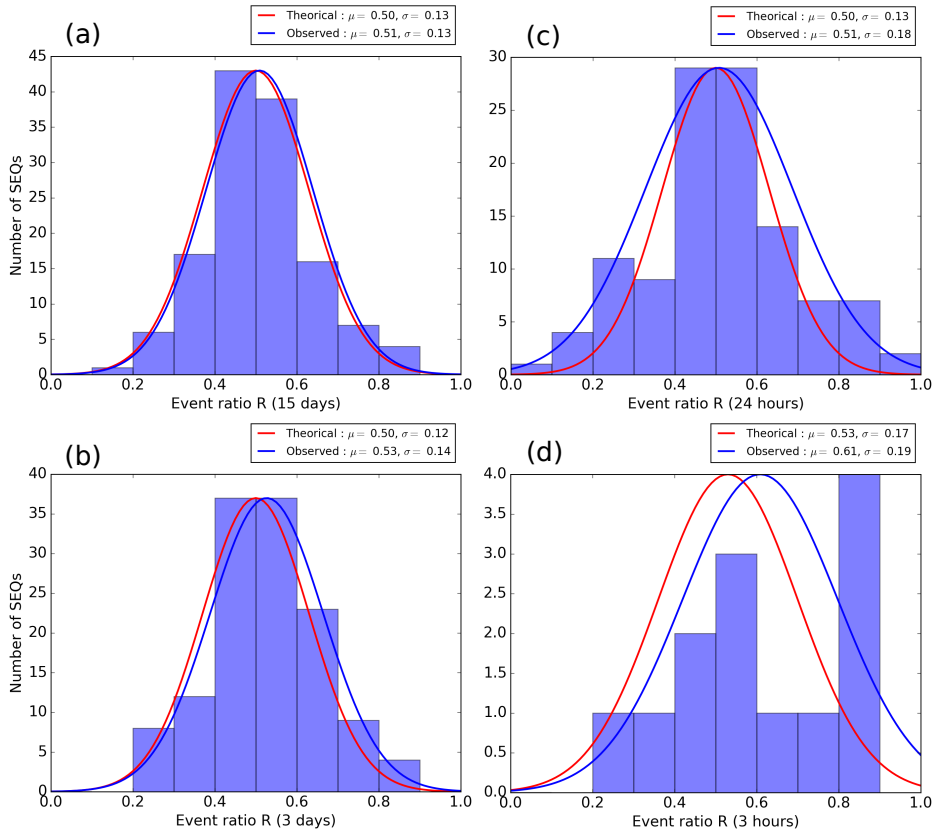

Figure 5.24 – Distribution of R-ratios of the selected reference events (SEQs). Each SEQ with more than 10 events in the considered time length (a) 15 days, (b) 3 days, (c) 24 hours and (d) 3 hours. The blue curve is the best-fitted gaussian of the distribution. The red curve is the gaussian distribution of the natural variability of the seismicity represented in the Supplementary Figure 5.23. For the time span (d) ±3 hours, only 13 SEQs have a sufficient number of local events to compute the R-ratio. This time span is thus not particularly reliable.

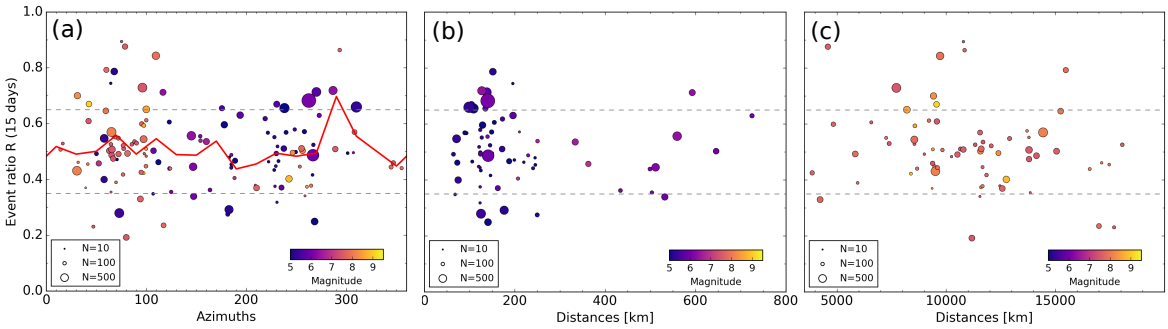

Figure 5.25 – R-ratios and spatial distribution of the selected reference events (SEQs). We compute the R-ratio for a time length of 15 days before and after the SEQs. (a) Event R-ratio versus SEQ azimuths. The red curve is the slidding average of R-ratios every 20°. (b) Event R-ratio versus regional SEQ hypocentral distances. (c) Event R-ratio versus teleseismic SEQ hypocentral distances. The colorscale stands for the magnitude. The size of circles corresponds to the number of events recorded in the second half of the time interval (+ 15 days).

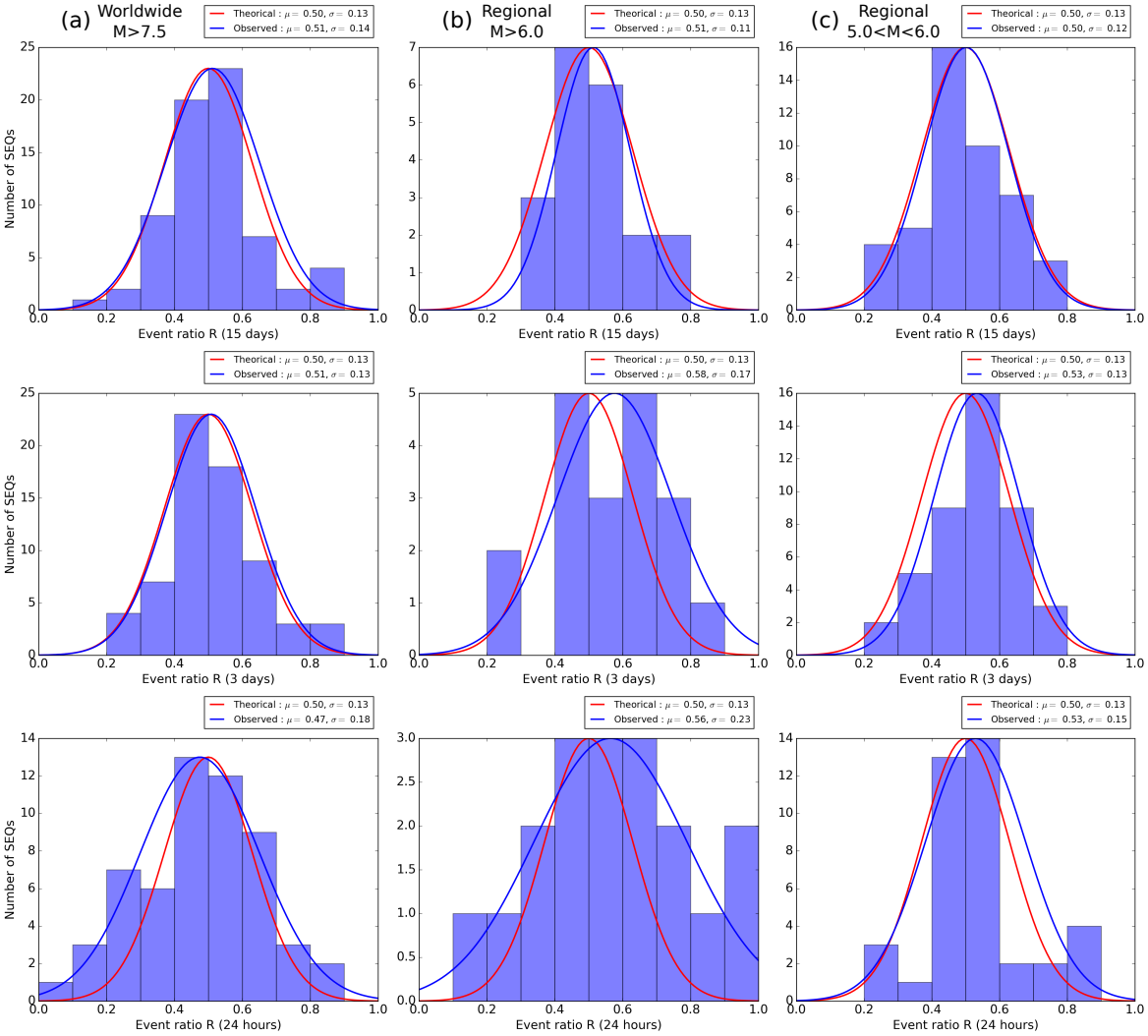

Figure 5.26 – Distribution of R-ratios of the teleseismic and regional SEQs). We compute the R-ratio for (a) teleseimic SEQs, (b) regional M ≥ 6 SEQs and (c) regional 5 ≥ M < 6, with more than 10 events in the considered time length (top) 15 days, (middle) 3 days, (bottom) 24 hours. The blue curve is the best-fitted gaussian distribution. The red curve is the gaussian distribution of the natural variability of the seismicity represented in the Supplementary Figure 5.23.

Chapitre 6

Analyse de l'initiation de la rupture de microséismes

Sommaire

Des observations récentes ont montré des différences de comportement dans l'initiation de la rupture entre les petits et les grands séismes. Elles offrent de nouvelles perspectives sur la compréhension des processus de nucléation des évènements sismiques, et permettraient de développer la future génération de systèmes d'alerte, basés sur des méthodes de traitement des signaux en temps réel pour identifier l'extension de la rupture et la taille finale du séisme. Ce chapitre présente les résultats obtenus grâce à une initiative collaborative avec l'Université de Naples afin de regarder si les caratéristiques de nucléation des forts séismes ($5 \leq M \leq 9$) mises en évidence par Colombelli et al. [2014] se retrouvent chez les séismes de plus faible magnitude. La richesse des petits évènements sismiques enregistrés par le réseau CRL, des magnitude 1 à 5 en moyenne, nous donne l'occasion d'utiliser cette base de donnée pour tenter la comparaison, voire l'extension des résultats de Colombelli et al. [2014] à cette gamme de magnitude. La méthodologie de traitement et de calculs utilisée pour les données du rift de Corinthe est quasi-identique à celle développée par l'équipe italienne, à ceci près que les paramètres sont adaptés à chacun des jeux de formes d'ondes des séismes analysés. Cette étude permet, en plus d'établir une potentielle loi déterministe sur l'ensemble de la gamme de magnitude (de 1 à 9), d'essayer de distinguer des comportements particuliers au démarrage de la rupture en fonction du type de forçage la déclenchant. Le fort taux de sismicité et la diversité des interactions sismiques et asismiques rencontrées au sein de rift de Corinthe en font un lieu d'étude adapté et privilégié pour tenter de répondre à ces questions mécaniques.

Les différentes parties de ce chapitre seront prochainement soumises à publication dans le journal *Geophysical Research Letter*.

6.1 Introduction

The predictability of the final size of an earthquake whereas the rupture of the fault plane has not finished is a highly debated scientific problem. Better understanding how the seismic rupture nucleates and evolves is crucial for risk mitigation actions and for our understanding of fault system behaviors. Opposite points of view have been proposed on whether the starting of the rupture process is identical whatever the final earthquake magnitude [e.g Ellsworth and Beroza, 1995].

According to the "cascade model" [e.g Brune, 1979], the rupture initiates with a common nucleation phase on a limited region of the fault plane and continues across the fault plane as long as the conditions are favorable. The final size of the earthquake is then controlled by the local friction conditions and the geometrical discontinuities of the fault surface [Wesnousky, 2006]. In this case, the earthquake magnitude can not be established until the end of the rupture. This implies that the rupture process is not deterministic. On the contrary, some recent studies from the last decades [Beroza and Ellsworth, 1996; Colombelli et al., 2014; Ellsworth and Beroza, 1995; Iio, 1995; Olson and Allen, 2005] have reported a possible scaling between the rupture nucleation characteristics and the earthquake final size. In this case, it would be possible to predict the earthquake magnitude before the rupture is complete. The rupture process would have a deterministic nature to some degree. However, this relationships is still difficult to evidence for plenty of reasons: intrinsic mechanical complexity of the initial stage, different timescales and frequency contents between small and large earthquakes, propagation effects, different numerical characteristics of records, etc.

With almost no processing of the seismograms to not deteriorate the data relative to the growth phase of the earthquake, Colombelli et al. [2014] showed evidence for a difference in rupture initiation between intermediate and large earthquakes occurring in Japan. The magnitude range investigated was for $5 \leq M \leq 9$. Thus in this present study, we first want to investigate smaller events to observe whether the trend is preserved for lower magnitudes, using the same methodology. To do so, we focus on the western part of the Gulf of Corinth, which is a young active continental rift showing one of the highest deformation rate in the world. Its intense and irregular microseismic

activity coupled with the occurrence of some M > 5 events per decades makes it an opportune region. The dense seismic array and small distances between the sources and the stations enable to record and locate microseismic events, and to be partly less affected by propagation effects. This study also takes the advantage of the diversity of seismicity pattern encountered in the Corinth rift to investigate the dependency of small rupture initiations on driven mechanisms, such as fluid circulation or pore pressure diffusion, slow aseismic slip, or long-term tectonic stress. With this aim in mind, we analyze 3 different families of events previously identified and evidenced as originating from different triggering forcing.

The ability to distinguish a small seismic shock from a large one through the first tenths of a second from the seismic observations raised a high interest for seismic hazard assessment. Besides the earthquake hazard aspect, defining the origin mechanisms of the rupture with the nucleation characteristics, in short delay, could be useful both for a better understanding of the earthquake triggering and mechanical interactions in different regions in the world, and for production and safety purpose in industrial areas.

6.2 Data and methods

6.2.1 The Corinth rift

The western Corinth rift is monitored since 2000 by the *Corinth Rift Laboratory* (CRL) network composed by several dozens of permanent seismic and geodetic stations. Its high microseismic activity is due to a very large extension rate of about 15 mm.year^{-1} resulting from the back-arc extension of the Hellenic subduction to the south and the dextral detachment of the North Anatolian Fault. The reliefs and geomorphological aspects of the gulf are governed by antithetic fault systems outcropping both offshore in the middle of the gulf [Bell et al., 2008; Moretti et al., 2003; Stefanos et al., 2002, e.g.] and onshore [Armijo et al., 1996; Ford et al., 2009]. The landscapes are shaped by the fault scarps dipping north on the south coast [Ford et al., 2016; Palyvos et al., 2005] and south on the north coast. The continental north-south opening generates highly irregular seismic activity with about a dozen events per day in quiescent periods and up to hundreds of events per day during seismic crises. Dense seismic swarms have been recording between 2000 and 2015 resulting in about 220,000 microearthquakes of moment magnitude ranging from 1 to 5. Some authors show that this swarm behavior might be induced by pressurized fluids migrating at depth [e.g Bourouis and Cornet, 2009; Duverger et al., 2015; Pacchiani and Lyon-Caen, 2010], while others [e.g. Dublanchet et al., 2015] associated these swarms to aseismic slip on a deep layer in which asperities are embedded.

6.2.2 Data selection

We use 4 different datasets in this analysis. The first one, called $\mathscr{D}$, is a large homogeneous set of selected and relocated earthquakes ranging from magnitudes 1 to 5 in order to supplement the study of Colombelli et al. [2014]. We also select three particular families of events (Figure 6.1):

— $\mathscr{M}_1$ is a persistent multiplet containing more than 100 events, located at the border of a locked fault plane. It has been analyzed by Godano et al. [2014] for its events occurred from 2000 to 2008 and has been extended by hierarchical clusterization method encompassing events from 2000 to 2015 (see Chapter 4).

— $\mathscr{M}_2$ contain seven events from the 2003–2004 seismic crisis located in the middle of the gulf [Duverger, 2014]. The analysis of the spatio-temporal evolution of this multiplet shows a bilateral migration of its events following a pore pressure diffusion law (see multiplet #04476 in the Annex A.2).

— $\mathscr{M}_3$ contain ten events with very similar waveforms (cross-correlation coefficients $C_C > 0.9$ for a 5 s waveform window encompassing the P- and the S-waves together) and regular recurrence times of about 6 months. The family is actually a repeater lasting several years, probably linked to an aseismic slow slip on the sub-fault plane surrounding the asperity (see Chapter 4).

We remind that a multiplet is a group of events spatially close, occurring on parallel sub-faults (coplanar or not) and showing identical focal mechanisms. Several seismological studies are using these families in the western Corinth rift in order to better understand the mechanical processes involved there [Duverger, 2014; Godano et al., 2014; Lambotte et al., 2014]. A repeater is considered here as an unique asperity breaking sometimes partially, more or less regularly, and generating extremely similar waveforms. Few regular repeaters have been extracted and evidenced in the western Corinth rift by cross-correlation measurements and statistics on their recurrence times.

These four datasets have been selected to contain high quality events, that is to say events having a majority of P- and S-phase picked manually at each station and relocated. We include records up to 50 km from the seismic stations. The moment magnitude of events has been computed by spectral inversion of the seismograms [Satriano et al., 2016]. The corner frequency, stress drop measurements also arise from this spectral inversion considering a Brune's model [Brune, 1970] and a constant rupture velocity.

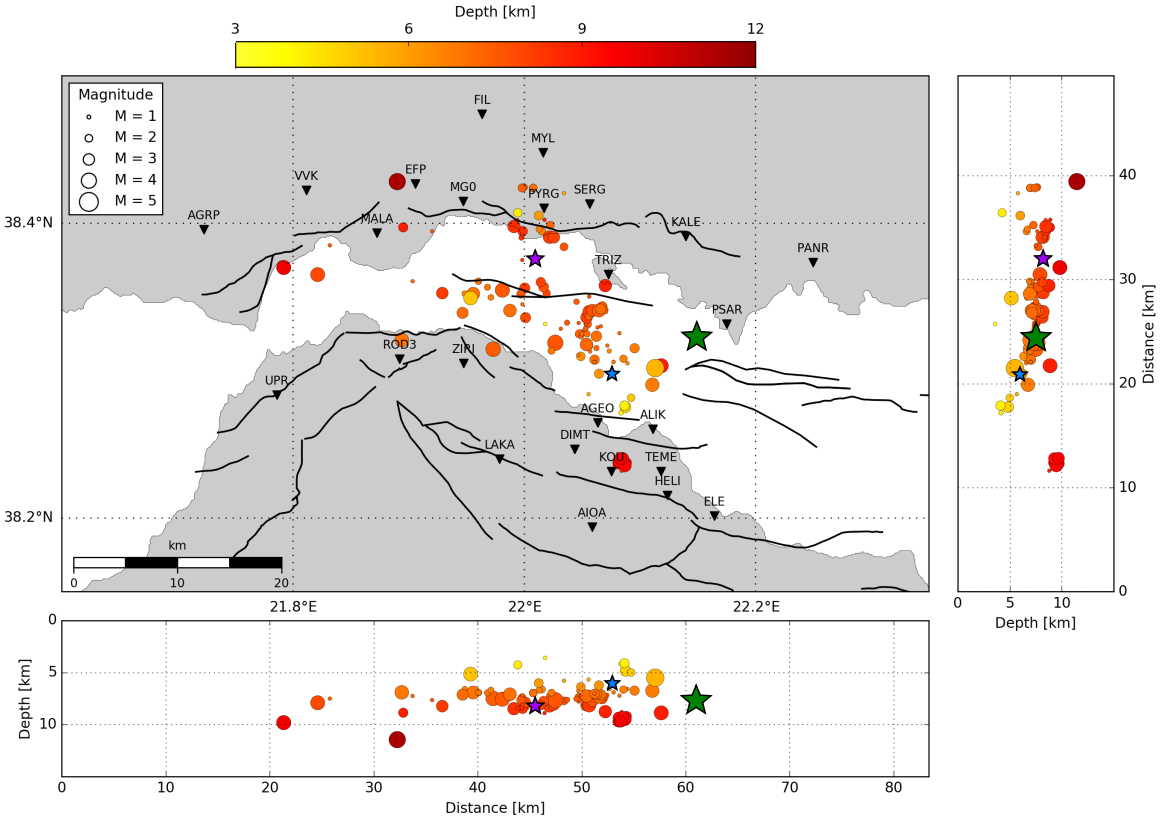

Figure 6.1 – Seismic events and stations map. The distribution of stations used (black triangles) and the hypocentral locations of the selected events from the first dataset (warm circles) and the three multiplets (green, blue, purple stars). The size of circles is proportional to the event magnitude, and the warmed colors represent the depth. The black lines are the main normal faults of the region reported in Beckers [2015].

We also composed the dataset $\mathscr{D}$ by adjusting as much as much the number of events per magnitude bin and per distance bin, in order to obtain a relatively homogeneous dataset (Figure 6.2).

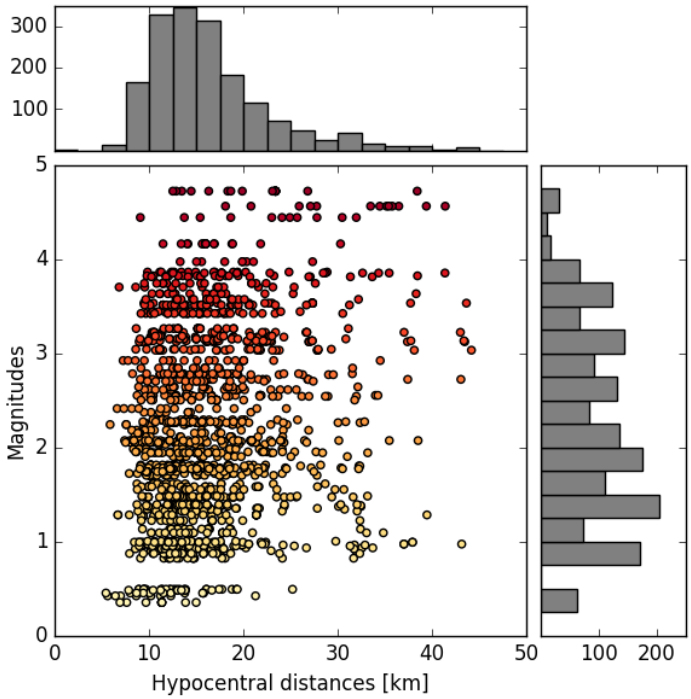

Figure 6.2 – Spatial and magnitude distribution of the first dataset. A hypocentral distance limit of 50 km is used. The colors scale with the magnitude. The histograms represent the number of records distributed over hypocentral distances and magnitudes of events.

6.2.3 Data processing

We adopt the methodology of Colombelli et al. [2014] by configuring the processing of data for the microseismicity recorded in the western Corinth rift by the CRL network. The codes were translated from a combination of SAC and bash commands to Python in order to take advantage of the Obspy library, which is a user-friendly and seismological-dedicated tool. We also parallelized the code to treat all events independently and run almost 8 times faster (8 cores used) than with the original serial implementation. The CRL database of event waveforms is stocked in SAC format, in counts unit. The sampling rate of the seismograms used in this study is 100 Hz. We first convert the raw count data in raw velocity data (cm.s^1), dividing the waveform by the station sensitivity registered in the dataless files. The mean value and linear trend are removed. Then, a non-causal, high-pass Butterworth filter with a cutoff frequency of 1 Hz is applied to remove the long-period drift present in the recorded data at some stations. These low frequencies could come from diurnal changes in ground conditions, or seasonal variations, or they are sometimes linked to the observatory conditions around the instrument.

For the dataset $\mathscr{D}$, the P-wave onsets are manually picked from the vertical component of the velocity records. For the three multiplets, we used the cross-correlation measurements to aligned the waveforms together and adjust their P-phase arrival times. For each family, we define a reference event by station as the maximum magnitude event recorded at each station. Since a large magnitude event is usually recorded at more stations than smaller events, the same event is often the reference event for the majority of stations. These referent events are manually picked on the vertical component of the velocity records for the corresponding station.

We then measure the peak velocity amplitude (P_V) on the filtered P-wave signals over a progressive expanding P-wave time window (PTW) [Colombelli et al., 2014]. The window starts at 0.01 s (1 sample) after the P-wave onset time T_P and extends until a given maximum PTW and before the expected arrival of the S-phase. To avoid the inclusion of the S-waves in the considered PTW, when the S-arrival time T_S is not noticed, we estimate it at each station using the following relation:

$$T_S - T_P = b\,R \tag{6.1}$$

where R is the hypocentral distance (in km). The coefficient b was derived through a linear regression analysis with the records from our datasets already having a manual S-pick (Figure 6.3). We

adopted a maximum PTW of 0.5 s for each event, based on the expected duration of the source ruptures and the smallest lapse time between P- and S-waves.

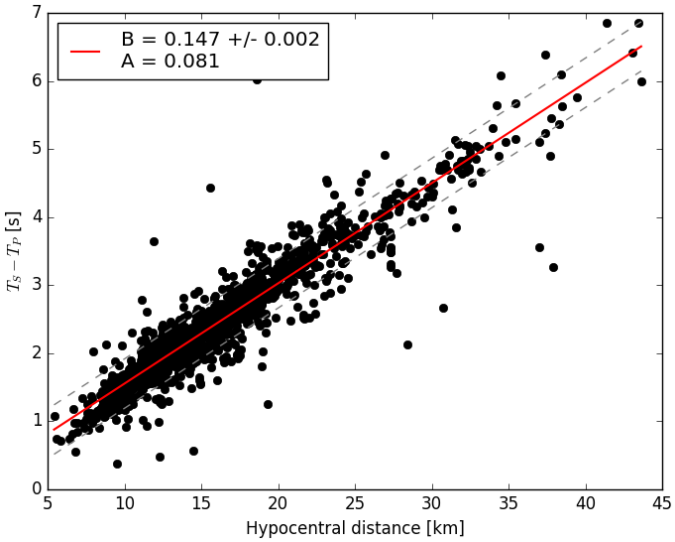

Figure 6.3 – Difference in arrival times of P- and S-waves as a function of the hypocentral distance. Linear regression (red line) to estimate the slope b in the Equation 6.1. The intercept a from the regression is 0 as expected. The dashed gray lines represent the standard deviation from the regression.

Attenuation correction

We correct the geometrical attenuation effect to compare the observed P_V values of an event recorded at different stations, with the following equation:

$$\log P_V = A + B\,M + C\,\log R \tag{6.2}$$

where M is the event magnitude, R is the hypocentral distance (in km) and P_V is the peak velocity amplitude (in cm) measured at a fixed PTW of 0.3 s. In this equation, the single term log(R) accounts for both the geometrical spreading and the anelastic attenuation [Colombelli et al., 2014]. We estimate the coefficients A, B and C through a non-weighted linear regression analysis. The Figure 6.4 shows the regression results of P_V as a function of the magnitude and corrected for the hypocentral distance, with the computed values of the three coefficients.

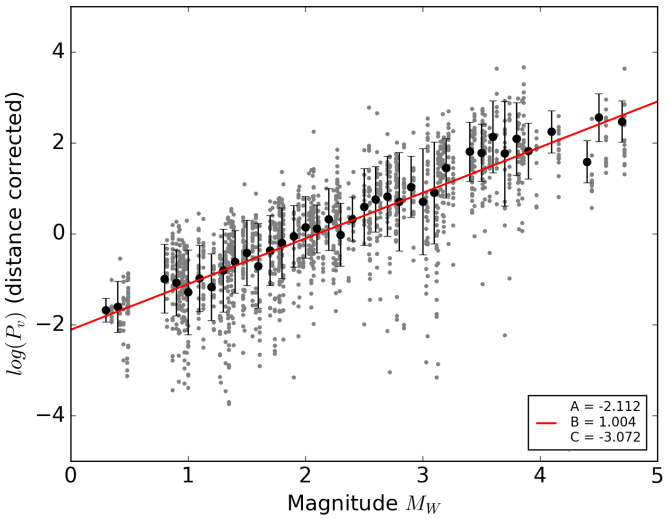

Figure 6.4 – Attenuation correction. Non-weighted linear regression to estimate the coefficients A, B, and C in the Equation 6.2 and correct the relation from the attenuation effects. The gray dots are the regressed data points ($\log(P_V) - C\log(R)$) corresponding to a P_V measurements at 0.3 s after the P-arrival time at every station, corrected from the hypocentral distances. The black circles are the mean of data in 0.1-long magnitude bins. The error bars represent the standard deviation of data per magnitude bin.

Computation of average peak velocity

As the nucleation phase of the rupture is growing exponentially in the framework of linear slip weakening models [e.g. Ampuero et al., 2002], for each event, we compute the logarithmic PTW–

curve (abbreviated LPW–curve) by averaging all the available data at each time window, after correcting the observed P_V values at different stations for the geometrical attenuation effect. We also required at least five data points to be used at each PTW. The average computation stops either when the the number of data points is not sufficient or when the PTW reaches its maximum time limits, whichever condition occurs first [Colombelli et al., 2014]. To model the LPW–curves, we use a piecewise linear fit function inverted for five unknown parameters: two corner times (T_1 and T_2), the slopes of two first lines (B_1 and B_2) and the final plateau value (P_L). Examples of fitted-curves for three representative events are displayed in the Figure 6.7.

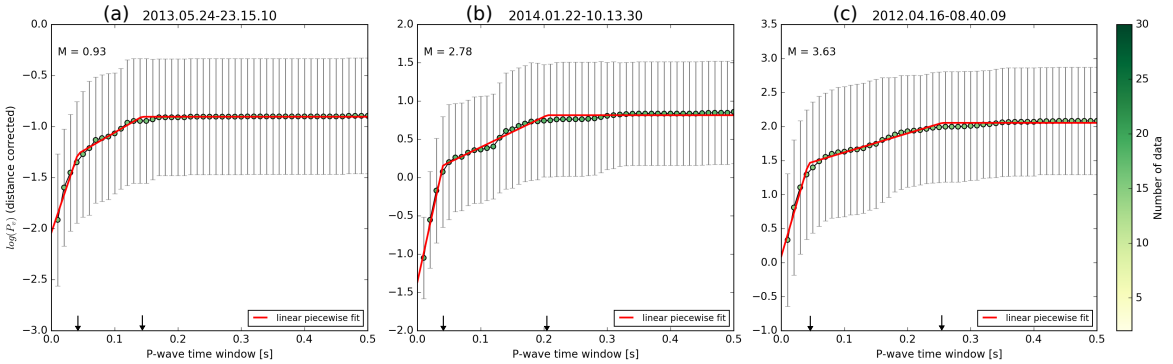

Figure 6.5 – Average peak velocity P_V in log-scale as a function of the PTW and piecewise linear fit model for three representative events. (a) Event 2013/05/24-23:15:10 M = 0.93. (b) Event 2014/01/22-10:13:30 M = 2.78. (c) Event 2012/04/16-08:40:09 M = 3.63. In each panel, the circles are the observed data, with the color scale indicating the number of data used to compute the average peak at each PTW. The grey error bars are $\pm 1\sigma$, the standard deviation. The solid red line is the best fit function obtained using the piecewise linear model, and the dark arrows mark T_1 and T_2 the two corner times of each event.

6.3 Results

Taking into account the characteristics of the Corinth rift microseismicity, the number of analyzed earthquakes used in the dataset $\mathscr{D}$ ensures a relatively good data sampling in magnitude bins (Figure 6.2). First, we will focus on the results of this large dataset before analyzing the smallest and specific families of events.

6.3.1 Temporal evolution of the average peak velocity

For each event of the first dataset, we obtain increasing LPW–curves showing a high gradient at the beginning which progressively diminishes until a stabilization of the curve around a plateau value P_L scaling with the magnitude. The saturation time T_2 resulting from the piecewise linear fit generally increases with the magnitude too (Figure 6.5). These observations validate the hypothesis that averaged LPW-curves approximate the Moment Rate Function (MRF) and the P_L is reached at the peak of the MRF assuming a triangular shape for it [Colombelli et al., 2015].

As our main interest is the rupture initiation, we focus the following on the parameters T_1 and B_1 which are possibly linked to it. We did not retrieve the same log-linear correlation between these parameters and the magnitude as obtained by Colombelli et al. [2014] for larger events. We observe a log-linear increase of B_1 as a function of the magnitude in our case (Figure 6.6.b), instead of an decrease. We also notice a slight deviation to the log-linear trend for our largest magnitudes ($M_W > 4$), with a possible stabilization of the logarithm of the slope B_1. This opposite trend may (1) sign a radical change in the rupture nucleation behavior operating between small and large earthquakes, with an inversion of the curve around magnitude 4–5, (2) show that the Greek events are not following the same relation as the Japanese ones, (3) indicate that we are not scanning the

same phase in the rupture process. Indeed, different fault systems or tectonic regions in the world might have their own rupture process characteristics depending on the forcing type for instance. As we explore smaller magnitude events, the nucleation phase of the rupture is probably hiding in the first hundredth of a second, even less for the smallest ones. We thus likely analyze the beginning of the rupture propagation phase rather than the nucleation on the asperity.

Moreover, the log-linear decrease of T_1 with the magnitude observed by Colombelli et al. [2014] is not recovered either with our events. We did not find a particular relation except a potential independence of first breakpoint time to the magnitude (Figure 6.6.a).

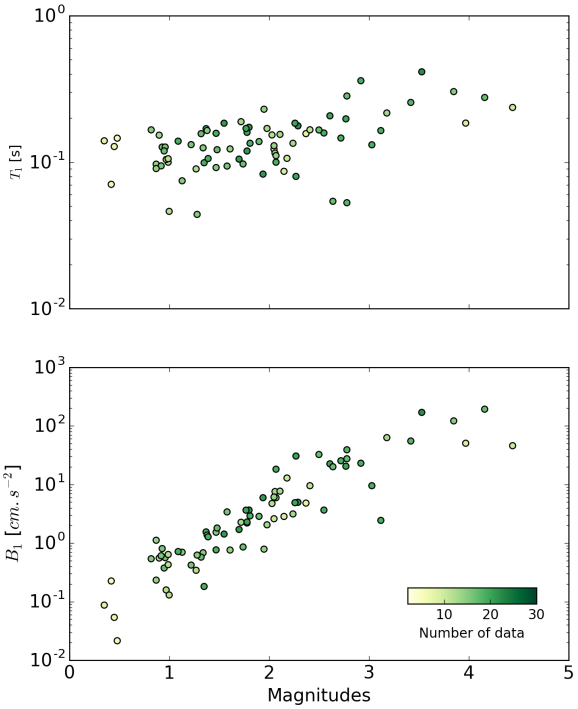

Figure 6.6 – Fit parameters T_1 and B_1 in the average peak velocity in log-scale. (a) First-corner time of the linear piecewise fit model as a function of the magnitude for all events for the first dataset. (b) Slope of the first-line segment of the piecewise linear fit model as a function of the magnitude. The color scale indicates the number of data points used to compute the average peak velocity at the time T_1. Error bars for individual data points are smaller than the symbol size.

Instead of analyzing the logarithm of the average P_V in time which is justified by assuming an exponential growth of the rupture, we prefer to come back to the analysis of the average P_V in time, which seems to show a linear increase in our case. We perform exactly the same analysis interpolating the first 3 points of the average PTW–curves (not LPW–curves) by a linear function in order to estimate the new slope B_1' at the early beginning of the rupture process (Figure 6.7). The slope value does not change according to the number of points taking into account to fit linearly the data (Supplementary Figure 6.15).

The log-linear correlation obtained between B_1' and the magnitude gives a gradient of ~ 0.8 (Figure 6.8). The individual estimated parameters are particularly accurate in terms of errors and masked by the size of the circles in the plot. The scaling with the magnitude seems robust (correlation coefficient $R^2 = 0.84$) even if a clear dispersion of the data appears. Our observations indicate an increase of B_1' of approximately 3 orders of magnitude in the range M_W 1–4.

6.3.2 Reliability of the depicted tendencies

Several factors described by Colombelli et al. [2014] may have influenced the shape of the PTW–curves. They have listed the :

— earthquake depth,

— high pass-filter,

— propagation effect related to the crustal structures.

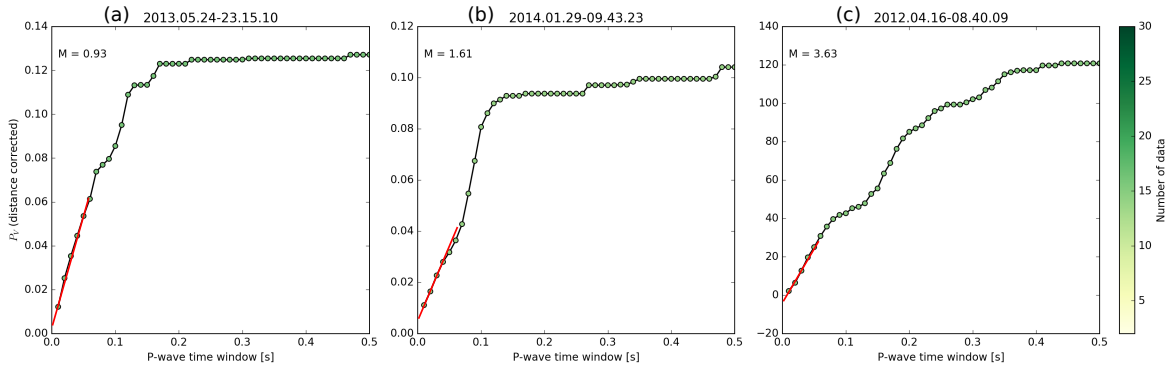

Figure 6.7 – Average peak velocity P_V as a function of the PTW and linear fit of the first points for three representative events. (a), (b) and (c) are the same events as in the Figure 6.5. In each panel, the circles are the observed data, with the color scale indicating the number of data used to compute the average peak at each PTW. The solid red line is the best fit function obtained for the first 4 points of the curves giving the slope B_1'.

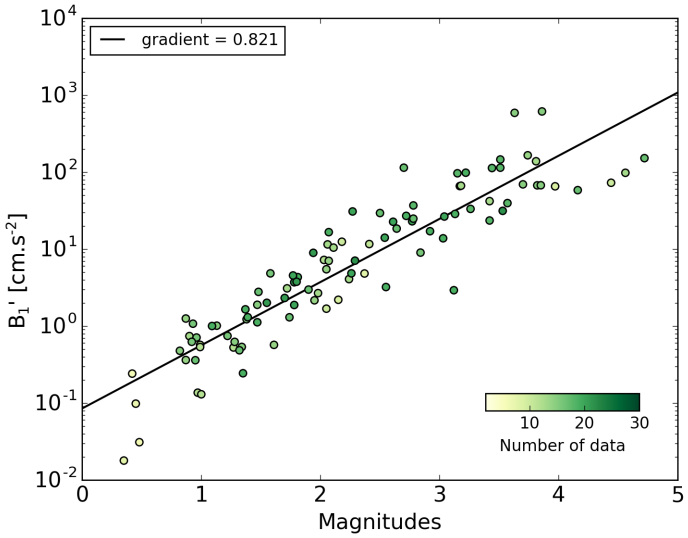

Figure 6.8 – Fitted parameter B_1'. Slope B_1' of the linear fit of the first 4 points in the PTW–curves as a function of the magnitude. The solid black line shows the best fit linear function (R^2 = 0.84) and the dashed lines represent the 95% confident intervals. Error bars for individual data points are smaller than the symbol size. The gradient of the linear fit is $\beta = 0.82 \pm 0.04$

In our case, we explored events in a smaller region extended over 50 km x 20 km. Attenuation effects and site effects may be strongly affect the amplitude of the seismograms recorded in velocity, especially because of the fault system complexity of the western Corinth rift and the different geological layers [e.g Ford et al., 2016; Le Pourhiet et al., 2004]. Since higher frequencies attenuate faster than low frequencies, we expect an increase of the initial slop with the magnitude as the observed behavior. To understand if these effects are responsible for the different initial slopes, we analyze several events of same multiplets (extremely spatially close events with the same focal mechanism). We estimated in the same manner the parameters B_1 and T_1 (see the next sections) and a trend with magnitude is still observed evidencing that this trend is not controlled by the distance range.

The earthquake depth with the frictional properties and the source mechanism might impact the evolution of the amplitude with time recorded at the stations. However our data are comprised in a 5 km range, so almost no change in the fragile/ductile state is possible at the depth of the events (~ 7 km). The microseismicity of the rift is mainly characterized by normal focal mechanisms constrained by parallel fault planes so we did not expect strong variations for different events at a same station. We exclude this hypothesis, as well as because of the analysis of the multiplets.

Differences between stations are however noticed. We thus perform a test computing the attenuation correction for the whole stations individually. The robustness of the coefficients A, B and C used in the Equation 6.2 over each station is displayed in the Supplementary Figures 6.13 and

6.14. We add the number of records as the size of symbols in the last figure to illustrate the weight of each station in the final correction. We re-estimate the parameters T_1 and B_1 of the piece-wise linear fit taking into account the 33 different values of the three coefficients obtained for the stations. The trend of the slope of the average peak velocity with magnitude is still preserved.

To discard the filtering effect, we perform a test by repeating the processing steps without the high-pass filtering operation. With a visual observation, no distortion of the shape of the LPW–curves were noticed. We compute again the different piece-wise linear fit parameters (T_1, B_1, T_2, B_2 and P_L) and no change in the trend with magnitude is observed, as for [Colombelli et al., 2014], even if the values are less constrained.

An another factor which could strongly impact the measurements of the velocity amplitude is the recording sample rate of the seismograms. We build PTW–curves at data sample resolution (0.01 s) and can not measure velocity variation at higher frequencies. Thus we might loose thinner crucial information for the smallest events to characterize the very beginning of the rupture process and particularly the nucleation phase which is likely in the noise.

6.3.3 Relations between measures in velocity, magnitude and stress drop

Here, we try to complement the results with other relations between the initiation of the rupture and the final source parameters to see if we still conserve a trend. We measure the average P_V at 0.3 s ($P_V(0.3)$), which corresponds to the end of the rupture for the majority of events, and compare it with the slope B_1' estimated in the first hundredth of a second (Figure 6.9). We clearly observe a log-linear relation with a gradient of ~0.94 (almost 1) between these two measures, which seems also dependent on the magnitude and the stress drop.

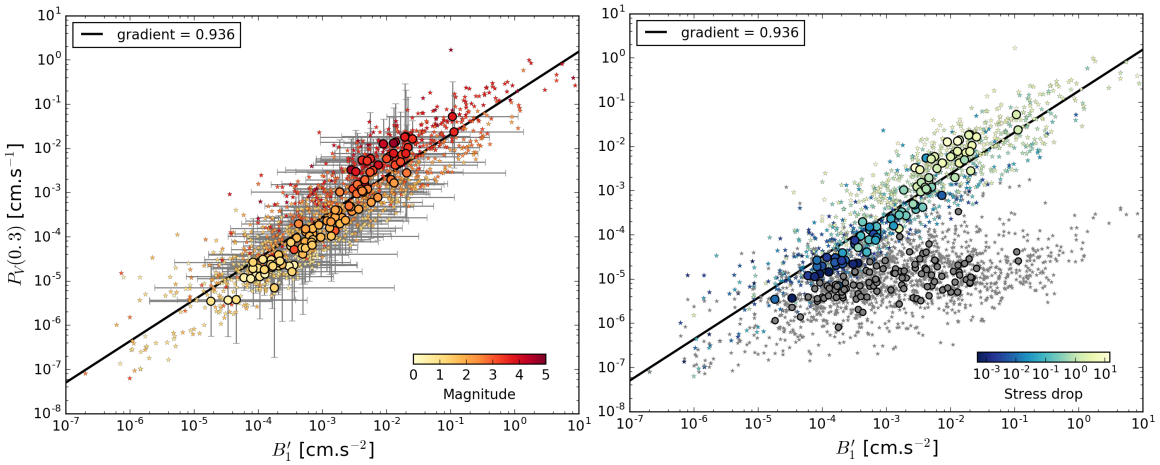

Figure 6.9 – Peak velocity measurements as a function of the slope B_1'. The color-scale is proportional to the magnitude in (a) and to the stress drop in (b). The colored stars are the whole peak velocity measurements at each station for each event. The colored circles are the average peak velocity by event at 0.3 s after the P-arrival time. The error bars in (a) are the standard deviation among the slope (horizontal) and the average peak (vertical) for the different measures at the stations per event. The gray stars and gray circles in (b) are respectively the noise data and noise mean data for each event.

We then look at $P_V(0.3)$ and B_1' as a function of the stress drop, and still observe a positive log-scale correlation between these parameters with respectively a gradient of 0.74 and 0.57 (Figure 6.10).

Finally, to check the reliability of these last tendencies and better understand the observed strong variation in stress drop between the different events, we compare the final source parameters, i.e. the seismic moment as as function of the stress drop (Figure 6.11), which were previously estimated by a spectral inversion and a simple Brune's model [Satriano et al., 2016].

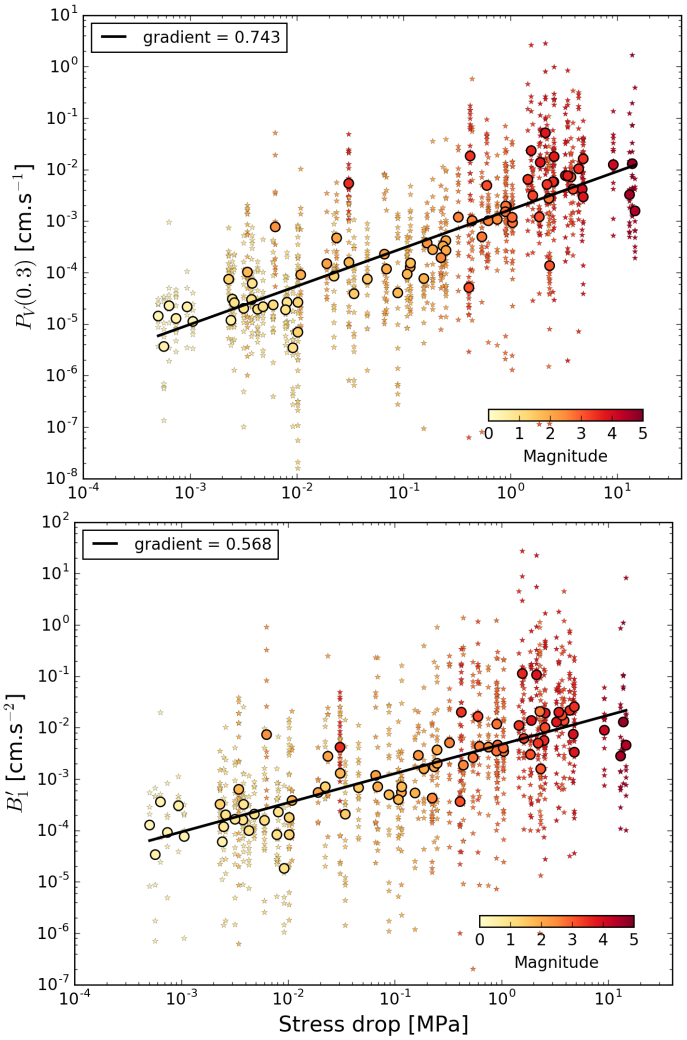

Figure 6.10 – Peak velocity measurements as a function of the stress drop. (a) The circles are the average peak velocity by event at 0.3 s after the P-arrival time $P_V(0.3)$ (cm.s^{-1}) as a function of σ (MPa). (b) The circles are the slope B_1' (cm.s^{-2}) as a function of σ (MPa). The stars are the data for each event at each station. The black lines are the best fit over the average data points. The gradient of these lines are estimated to ~ 0.7 for (a) and ~ 0.6 for (b).

We estimate a log-linear gradient of ~1.25 (5/4) between the stress drop and the magnitude, in opposition with the commonly accepted self-similar scaling [e.g Abercrombie, 1995; Shaw, 2009].

6.3.4 Application to multiplets

Concerning the different multiplets, we repeat the measurements of the slope B_1' at the very beginning of each PTW-curve and compare it with the event magnitude (Figure 6.12.a–c).

The positive log-scale correlation obtained between B_1' and the magnitude for the dataset $\mathscr{D}$ is conserved for the three multiplets. The three populations are quite superimposed in the Figure 6.12.d, however the gradient of the best log-linear fit slightly varies between datasets: ~ 1.1 for $\mathscr{M}_1$, ~ 1.25 for $\mathscr{M}_2$ and ~ 1.6 for $\mathscr{M}_3$ compared to 0.8 for $\mathscr{D}$. The more there are large magnitudes in the dataset, the lower is the gradient. The fluid-driven multiplet has the maximum gradient.

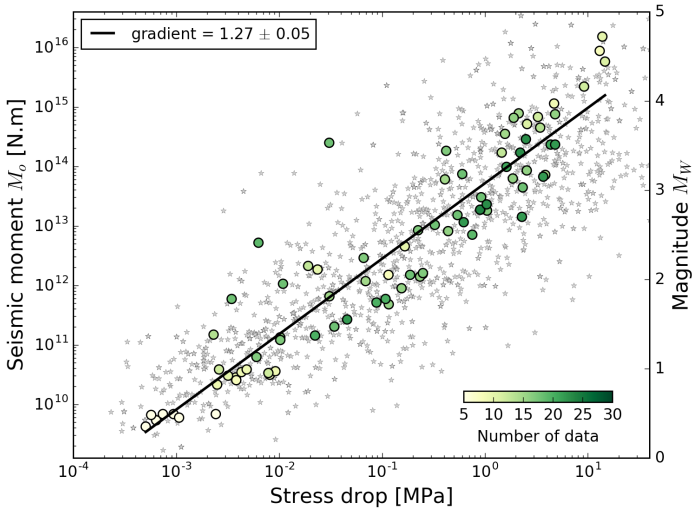

Figure 6.11 – Seismic moment as a function of the stress drop. (a) The circles represent the average seismic moment and average stress drop by event. The stars are the measurements for each event at each station. The black line is the best fit over the average data points. The gradient is estimated to ~ 0.66, making a strange relation $M_0^{1/2} \propto L^3$ with L the source dimension.

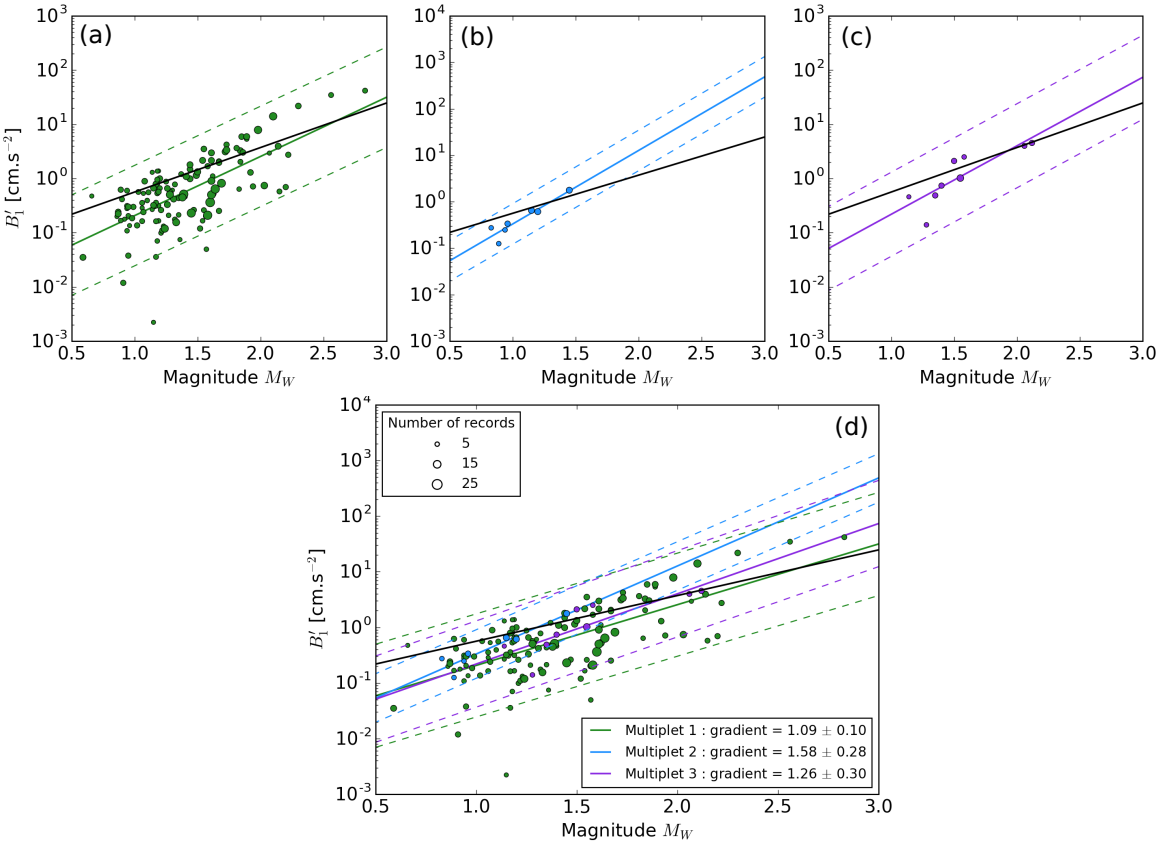

Figure 6.12 – Positive correlation of B_1' with magnitude on the three multiplets. Slope B_1' of the linear fit of the first 3 points in the PTW–curves as a function of the magnitude for (a) the large multiplet $\mathscr{M}_1$, (b) the multiplet $\mathscr{M}_2$ linked to pore pressure, (c) the repeater $\mathscr{M}_3$. (d) This plot gather the three previous ones. The solid black line shows the best fit linear of the first large dataset ranging magnitude 1 to 5. The colored solid line represent the best linear fit of each dataset. The dashed lines represent the 95% confident intervals.

6.4 Discussion

The nucleation time of small earthquakes is from 0.01 to 0.8 s according to Beroza and Ellsworth [1996] for magnitude ranging from 1 to 5, which is comparable with our estimates of T_1 (Figure 6.6.a). However, for the magnitude $M_W 1$, we are at the sampling rate accuracy thus our estimates of T_1 are very likely overestimated. On the opposite side, for our three events with $M_W > 4$, we may be close to the used 0.5 s threshold in PTW. We fixed this maximum time-window length according to the observed T_1 by Colombelli et al. [2014] for events with magnitude $M_W < 5.5$ which are all below 0.5 s. Thus, we may be at the resolution limit for the piecewise linear fit methodology and we possibly underestimate T_1 for our three largest events, especially knowing the exponential growth of the rupture duration with magnitude. Finally the increase in T_1 observed between $M_W 2$ to 4 may be the reliable trend, which would be in agreement with the positive scaling of nucleation duration with the total seismic moment evidenced by several authors [e.g. Beroza and Ellsworth, 1996; Colombelli et al., 2014].

6.4.1 Static stress drop estimation

Here we come back to the classical relations between source parameters to investigate the non–self-similarity observed of our data. The seismic moment M_0 can be expressed as:

$$M_0 \sim \mu \, \Delta u \, S \tag{6.3}$$

where μ the rigidity, Δu the average slip and S the fault area. Δu is related to the stress drop $\Delta\sigma$ by:

$$\Delta u \sim C \, \frac{\Delta\sigma}{\mu} \, L \tag{6.4}$$

where C is a geometric constant, and L is the characteristic length of the fault area. Substituting the Equation 6.4 in Equation 6.3 and assuming $S = L^2$, we obtain:

$$\begin{aligned} M_0 &\propto \Delta\sigma \, L^3 \\ \log(M_0) &\propto \log(\Delta\sigma) + 3 \log(L) \end{aligned} \tag{6.5}$$

However, our observations give:

$$\log(M_0) \propto \frac{5}{4} \log(\Delta\sigma) \tag{6.6}$$

Then, subtracting the Equation 6.5 to the Equation 6.6 gives:

$$M_0 \propto L^{15} \tag{6.7}$$

This means that the rupture length does not vary or very little with the seismic moment, which is contradictory with the theory and the observations. As the stress drop computation comes from the measurement of the corner frequency in spectral domain in the routine codes, we think that the estimation of the final stress drop is not reliable for the smallest events due to the Nyquist frequency. Indeed, the maximum corner frequency authorized value is imposed by the sampling rate (100 Hz) and thus about 50 Hz limiting the minimum source length authorized. This issue was already pointed out by Godano et al. [2014] on CRL events and similar problems were described by Ide and Beroza [2001] for the apparent stress. We then dramatically underestimate the stress drop values for the smallest magnitude events. The slope between seismic moment and stress drop should be much more steep, and vertical in case of self-similarity.

We also precise that the stress drops determined by Godano et al. [2014] for the multiplet-866 events included in the $\mathscr{M}_1$ are about a factor two higher than our stress drop estimates, only due to the model difference (see Supplementary Section 6.B).

For the next discussions, we will then not consider final stress drop estimations.

6.4.2 Mechanical models

In this section, we attempt a mechanical interpretation of our observations. The far-field displacement of the P-waves due to a point source dislocation is [Aki and Richards, 2002]:

$$u_P(t) = \frac{1}{4\pi\rho\alpha^3} A^{FP} \frac{1}{R} \dot{M}_0(t - \frac{R}{\alpha}) \tag{6.8}$$

where ρ is the density of the crust, α is the P-wave velocity, A^{FP} is the far field radiation pattern for the P-waves, R is the epicentral distance of the source and $M_0(t)$ is the seismic moment. The seismic moment rate on a fix elementary surface dS can be written as:

$$d\dot{M}_0(t) = \mu \, d\Delta\dot{u}(t) \, dS \tag{6.9}$$

In order to express the slip velocity $\Delta\dot{u}(t)$ we assume a circular rupture, self-similar, i.e. with a constant slip velocity growth and a constant rupture velocity propagation with the form (which is consistent with a quasi-dynamic stress drop):

$$\Delta u(t) = \Delta\dot{u}_0 \; t \, H\left(t - \frac{r}{V_R}\right) \tag{6.10}$$

where $\Delta\dot{u}_0$ is a constant slip velocity, V_R is the rupture propagation velocity, r is the radius of the source and $H(t)$ is the Heaviside unit time function:

$$\begin{aligned} H(t) &= 0, \quad t < 0 \\ H(t) &= 1, \quad t > 0 \end{aligned} \tag{6.11}$$

Then, the derivative gives:

$$\Delta\dot{u}(t) = \Delta\dot{u}_0 \left[H\left(t - \frac{r}{V_R}\right) + t \, \delta\left(t - \frac{r}{V_R}\right) \right] \tag{6.12}$$

where δ is the Dirac function. We come back to the Equation 6.8 for the elementary radiation, which gives:

$$du_P(t) = \frac{1}{4\pi\rho\alpha^3} A^{FP} \frac{1}{R} \mu \, \Delta\dot{u}(t) \, dS \tag{6.13}$$

with $dS = 2\pi \, r \, dr$. Then, integrating the last equation, we have:

$$\begin{aligned} u_P(t) &= \frac{1}{2\rho\alpha^3} A^{FP} \frac{1}{R} \mu \int_0^{V_R t} \Delta\dot{u}(r,t) \, r \, dr \\ &= K \, \Delta\dot{u}_0 \left(\int_0^{V_R t} H\left(t - \frac{r}{V_R}\right) r \, dr + \int_0^{V_R t} t \, \delta\left(t - \frac{r}{V_R}\right) r \, dr \right) \\ &= K \, \Delta\dot{u}_0 \left(\left[\frac{r^2}{2} \right]_0^{V_R t} + t \, V_R \int_0^{V_R t} \delta(V_R t - r) \, r \, dr \right) \\ &= K \, \Delta\dot{u}_0 \left(\frac{V_R^2 \, t^2}{2} + t V_R V_R \, t \right) \\ &= \frac{3}{2} K \, \Delta\dot{u}_0 \, V_R^2 \, t^2 \end{aligned} \tag{6.14}$$

where K is a constant integrating the remaining variables (ρ, α, A^{FP}, R, μ).

Finally, the slip displacement $u_P(t)$ is proportional to t^2, thus the velocity $v_P(t) \propto t$ and the acceleration $a_P(t) \propto$ cste. We have analyzed B'_1, the slope of the average peak in velocity, which corresponds to an acceleration. Thus we have:

$$B'_1 \propto V_R^2 \, \Delta\dot{u}_0 \tag{6.15}$$

As we observe changes of several order of magnitude for the slope B'_1 and because the rupture velocity V_R can not physically change dramatically (usually $0.5V_S \leq V_R \leq 0.9V_S$ with sometimes super-shear velocity), we think that the rupture initiation is more controlled by the average slip rate $\Delta\dot{u}_0$. It means that large earthquakes start with high slip rate in average, whereas small events start slowly.

Moreover, the average slip rate is related to the dynamic stress drop $\Delta\sigma_d$, extracted from the quasi-dynamic model and based on the static expression [Ruff, 1999] by:

$$\Delta\dot{u}_0 = C\,\beta\,\frac{\Delta\sigma_d}{\mu} \tag{6.16}$$

where C is a geometric constant, and β is the source region shear velocity.

6.4.3 Different forcing

The multiplets $\mathscr{M}_1$ and $\mathscr{M}_3$ have been evidenced to be possibly forced by aseismic slow slip. The family $\mathscr{M}_1$ studied by Godano et al. [2014] is located at the border of the locked fault plane of the M_W6.3 1995 Aigion rupture [Bernard et al., 1997]. The authors suggested that this multiplet is surrounded by heterogeneous sub-fault with both locked and creeping areas given that the large cumulative coseismic slip found. The family $\mathscr{M}_3$ is a periodic repeater supposed to be driven by aseismic slip. Both families show similar relation between B'_1 and magnitudes.

On the contrary, the multiplet $\mathscr{M}_2$ is characterized by a clear migration of its events following a diffusion law and show the highest gradient in slope at the rupture initiation versus magnitude. However, taking into account the uncertainties on this trend, the gradient differences are probably not significant. The measured slopes are moreover of the same order of magnitude as the slopes of the others datasets.

Finally, the analyzed parameters do not enable here to detect differences in the rupture initiation as a function of triggering mechanisms. Nevertheless, we know that the fluid pore pressure affects the whole earthquake rupture process [Mulargia and Bizzarri, 2014], starting from the fault nucleation [Sibson, 1986], continues through mechanical lubrication [e.g. Brodsky and Kanamori, 2001] and often plays a role in triggering aftershocks [e.g. Nur and Booker, 1972; Yamashita, 1998]. The small magnitude events and noise level in the recorded waveforms may be a limitation in the reading of the rupture initiation characteristics. More works with dedicated approach are needed to hope to detect a signature of the triggering mechanism in the dynamic source parameters.

6.5 Conclusion

The relation highlighted between the slope in the first hundredth of seconds of the average peak velocity and the magnitude may have important consequences on the assessment of the earthquake final size. A large amount of works is still necessary before to be able to integrate these results to early warning system procedures. Indeed, the trend has been computed with an average amplitude over several stations and thus lots of records spanning different azimuths and distances,

whereas in real-time, the few data recording in a short-period arise from a specific source-station geometry which may influence the measures of the parameters.

Moreover, the few differences in rupture initiation parameters highlighted between the three multiplets are not conclusive in the sense that we are not able to distinguish specific properties as a function of forcing sources. It would be interesting to undertake a theoretical analysis with numerical modeling to find which parameters could be useful to associate a rupture behavior to a specific forcing. Here again, a substantial amount of work is needed to repeat the calculations over a larger number of multiplets and improve or discard these primary results.

6.6 Bilan

Les résultats de cette étude ont été obtenus grâce à une collaboration avec l'université de Naples, qui m'a accueillie pendant 1 semaine sur place. Cette semaine m'a permis de mieux comprendre et de prendre en main une méthode de calcul développée par Simona Colombelli et décrite dans Colombelli et al. [2014]. Le code permet de mesurer les amplitudes des formes d'ondes sur des fenêtres de temps glissantes, juste avant et au démarrage de l'onde P. Le code étant initialement écrit en lignes de commande bash et SAC, j'ai pris l'initiative de le réécrire en language Python afin d'utiliser les avantages et les optimisations de calculs de la librairie Obspy. Cette conversion a également facilité la prise en charge des fichiers de données du réseau CRL, grâce à quelques modules spécifiques que j'ai pu ajouter. Finalement, j'ai développé ces lignes de code en permettant le traitement en parallèle d'un certain nombre d'évènements et l'utilisation du cluster de calcul S-CAPAD pour un gros volume de formes d'onde. Cette opération optimise le traitement des données et diminue drastiquement les temps de calculs. Les discussions avec l'équipe napolitaine ont également permis mettre en évidence que les pointés manuels ne sont pas suffisamment précis pour ce genre d'analyse très fine sur quelques dizièmes de secondes. J'ai donc refait les pointés de l'onde P du premier jeu de données d'environ une centaine d'évènements enregistrés aux différentes stations, ainsi que les évènements de références pour les multiplets. Les délais obtenus par corrélation des formes d'ondes des autres évènements des multiplets permettent d'affiner et d'aligner leur pointé.

6.A Supplementary Figures

The attenuation equation 6.2 used in this study, which is a standard Ground Motion Prediction Equation (GMPE), has the same form as the generally adopted one in real-time applications. We compute the residuals "$\log(P_V)_{measured} - \log(P_V)_{theorical}$" (observations − predictions) to show that the attenuation relationship does not introduce any bias. The Supplementary Figure 6.16 shows that residuals are distributed around zero in the whole distance range and magnitude range and no evident bias appears except for the case of three $M_W \geq 4.5$. For these three events, the deviation from zero in the magnitude plot is likely related to the short P-wave time window used. The saturation effect of the initial amplitude is a well-known problem [e.g. Kanamori, 2005; Rydelek and Horiuchi, 2006]. The maximum of 0.5 s P-wave time window used may not capture a sufficient long period of the rupture process for these moderate earthquakes and results in lower initial peak values. It could be overcome by extended the time window to 1 s for instance for this magnitude range.

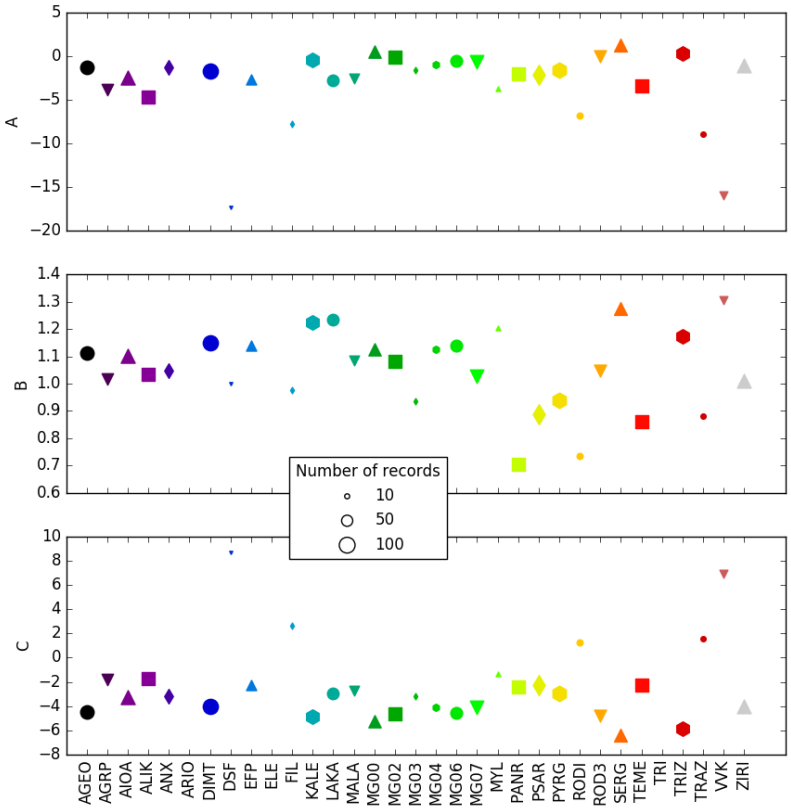

Figure 6.13 – Attenuation coefficients per station. Estimation of the coefficients A, B and C from the Equation 6.2 correcting for the attenuation, for each station separately.

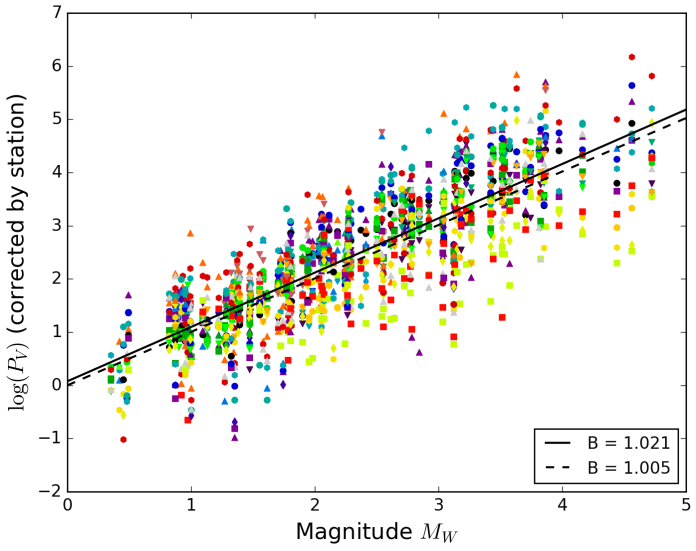

Figure 6.14 – Correction of the attenuation per station. The estimation of the coefficients A, B and C from the Equation 6.2 have been done for each station separately. The symbols and colors identify the stations (see Figure 6.13). We adjust a new linear regression through the distance corrected values $\log(P_V)$ per station to estimate a global slope B (black solid line). We compare it with the original B estimated for the whole stations together (black dashed line). It does not change much and the dispersion around is equivalent.

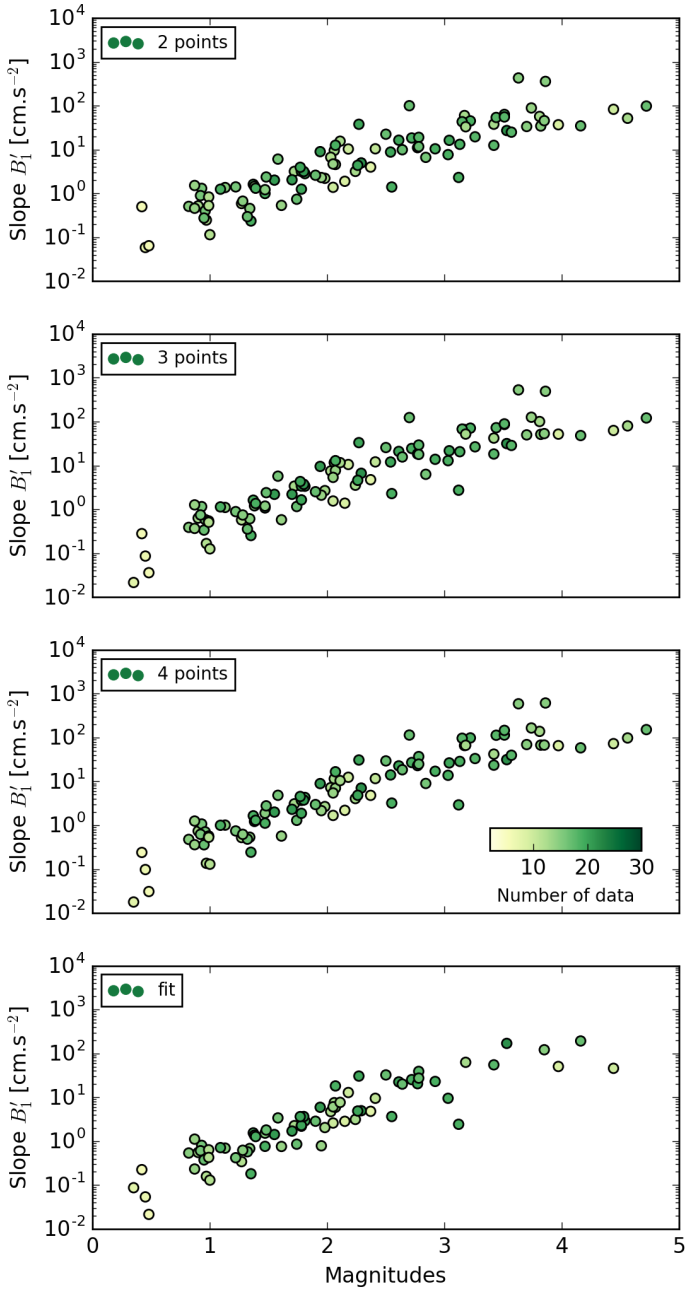

Figure 6.15 – Fitted parameter B_1'. Slope B_1' estimated with (a) the first 2 points, (b) the first 3 points, (c) the first 4 points, and (d) the piecewise linear fit model in the PTW–curves, as a function of the magnitude. The linear trend is conserved whatever the method used to estimate the slope at the very beginning of the rupture process.

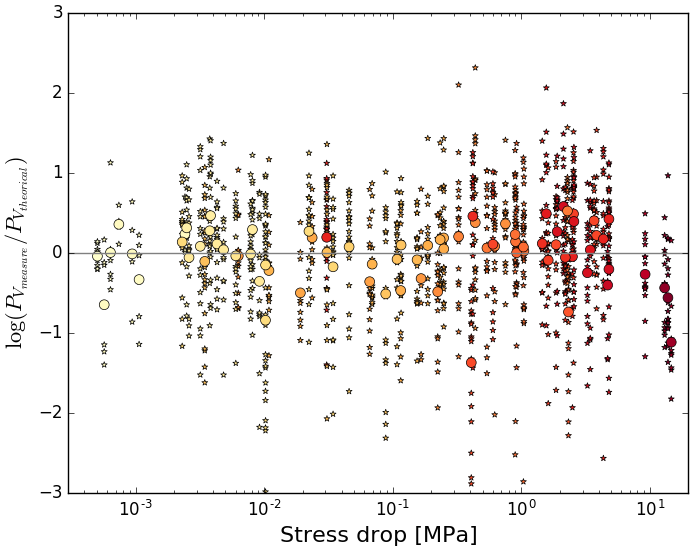

Figure 6.16 – Residual distribution of P_V. The residuals are the differences between the measured P_V and the predicted P_V by the Equation 6.2 as a function of distances (a) and magnitude (b). The circles represent the mean residual for events. The stars are the data at each station for all events.

6.B Significant differences in stress drop estimates according to the used model

We remind here that a quite large difference in stress drop estimation can be introduced depending on the model used. Indeed, assuming a circular crack model, the analytical solution for a uniform stress drop $\Delta\sigma$ is:

$$\Delta\sigma = \frac{7\,M_0}{16\,a^3} = \frac{7\,M_0}{2\,L^3} \tag{6.17}$$

[Eshelby, 1957] where M_0 is the seismic moment and a the source radius of the crack and L the source diameter or the source length. The source dimension can be related to the average of the corner frequencies f_c of body wave seismic spectra [e.g. Brune, 1970; Madariaga, 1976]:

$$a = \frac{k\,\beta}{f_{c_S}} \tag{6.18}$$

where β is the shear wave velocity near the source, f_{c_S} is the average corner frequency for the S-waves, and k is a constant depending on the considered fault rupture model.

The key issue is the choice of the parameter k. Many authors are using the Brune [1970]'s approximation, which assumed a kinematic model for a circular crack and obtained $k_S = 0.37$ for the S-waves. Hanks and Wyss [1972] assumed a similar relation for the P-waves as:

$$a = \frac{k\,\alpha}{f_{c_P}} \tag{6.19}$$

where α is the compresional wave velocity and f_{c_P} is the average corner frequency for the S-waves. However, they considered that $\frac{f_{c_S}}{f_{c_P}} = \frac{\beta}{\alpha}$, but this ratio is a little dependant on the rupture velocity [Sato and Hirasawa, 1973]. Thus implies a different k parameter for the P- and the S-waves.

Others are then using the analytical model of Sato and Hirasawa [1973] in which the rupture spreads radially from a starting point with a constant rupture velocity and stops abruptly at the source radius. In this model, which assumed that the solution of Eshelby [1957] holds at every instant of the rupture process, k depends on the rupture velocity V_R. For $V_R = 0.9\,\beta$, they obtained $k_P = 0.42$ for the P-waves and $k_S = 0.29$ for the S-waves. The most widely used model is probably the model of Madariaga [1976] in which dynamic calculations for a single crack spreading radially at a constant rupture velocity were performed. For $V_R = 0.9\,\beta$, Madariaga [1976] obtained $k_P = 0.32$ for P-waves and $k_S = 0.21$ for S-waves. Combining the equations 6.17 and 6.18 gives:

$$\Delta\sigma = \frac{7}{16}\left(\frac{f_{c_S}}{k_S\,\beta}\right)^3 M_0 \tag{6.20}$$

The difference between Brune's model ($k = 0.37$) and Madariaga's model ($k = 0.21$) lead to a factor of about 5.5 difference in stress drop with the Equation 6.20.

In our calculations, we used the methodology of Satriano et al. [2016] who implemented the Brune's stress drop using the Equation 6.17 and a shear wave velocity of 3 km.s^{-1}. This means that $k_S = 0.37$ or $q_S = 0.32$ for $V_R = 0.9\,\beta$ with $k = q\,\frac{V_R}{\beta}$. Godano et al. [2014] analyzed the events of the multiplet $\mathscr{M}_1$ assuming the model of Madariaga and for $V_R = 0.7\,\beta$ with $\beta = 3.4$ km.s^{-1}, and $q_P = 0.519$ and $q_S = 0.391$. Therefore, we have around two time smaller stress drop than them.

The Figure 6.17 shows the variation of stress drop estimates with the seismic moment of the multiplet $\mathscr{M}_1$, whereas Godano et al. [2014] estimated higher stress drops with less variability as a function of the magnitude. They proposed that the multiplet–866 $\in \mathscr{M}_1$ respects the self-similarity taking into account a possible minimum rupture length authorized by the numerical characteristics of the data.

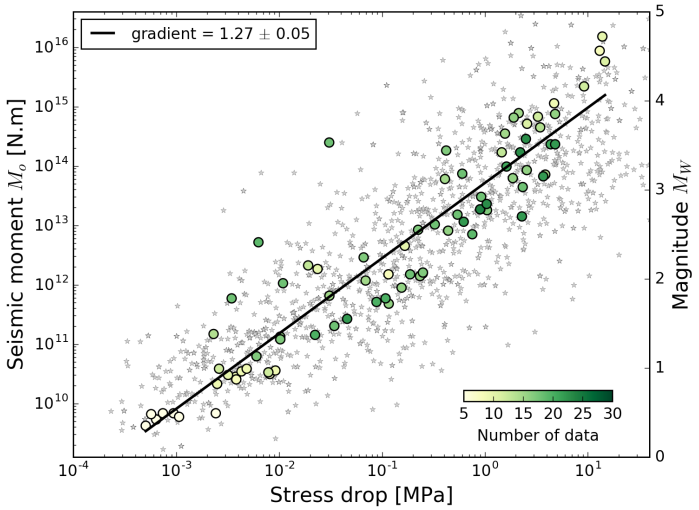

Figure 6.17 – Seismic moment as a function of the stress drop for the multiplet $\mathscr{M}_1$. (a) The circles represent the average seismic moment and average stress drop by event. The stars are the measurements for each event at each station. The black line is the best fit over the average data points. The gradient is estimated to ~ 0.85, giving a strange relation $M_0 \propto L^{-17}$, which means that L, the source length does not vary with the seismic moment, or decreases very slightly.

Conclusion générale et perspectives

Conclusions

Le rift de Corinthe présente une activité sismique très irrégulière avec des périodes de crises formant des essaims et des périodes de quiescence. L'origine de ces crises reste encore parfois obscure mais plusieurs éléments de réponses peuvent être apportés pour mieux comprendre leur formation et leur développement.

L'analyse détaillée de l'évolution spatio-temporelle des multiplets durant la crise sismique de 2003–2004 révèle un processus d'hydro-fracturation, dû à de la migration de pression de pore. Cette migration s'effectue dans un milieu très fracturé et perméable de 1–2 km d'épaisseur, aux structures complexes sur lesquelles se développent les essaims de microséismes. Elle est localisée à l'intersection des jeunes failles normales majeures de la côte sud et d'une couche géologique cassante faiblement perméable, héritée des nappes des Hellénides que nous supposons être la nappe des Phyllades. Les valeurs de diffusivités locales étant plus élevées au cœur de la couche de microsismicité, nous pensons qu'elles sont reliées à des plans de failles secondaires plus grands définis par les multiplets, qui permettent aux fluides de circuler plus facilement. Cette forte fracturation interne est interprétée comme provenant de la terminaison des failles dans la couche géologique, qui génèrent une zone plus intensément endommagée, orientée selon l'azimut des plans de failles. De plus, les images tomographiques indiquent la présence d'une région à fort rapport $\frac{\mathrm{V}p}{\mathrm{V}s}$ en profondeur, sous la couche de microsismicité, indiquant très possiblement la présence d'un réservoir de fluide sous pression. Ce réservoir, surplombé par une couche quasi-imperméable, serait connecté à la racine des failles de manière intermittente par des changements soudains de perméabilité le long des fractures.

La relocalisation globale par double-différence de la base de données des hypocentres du CRL entre 2000 et 2015 souligne avec détail l'organisation spatiale des essaims de microséismes. La corrélation spatiale entre les différentes structures majeures actives et cette dense activité microsismique a été améliorée par une nette clusterisation des évènements qui dessinent des petites structures fines mieux définies. Le prolongement en profondeur de la géométrie des plans de failles mesurée en surface est cohérent avec la distribution spatiale des essaims. Ces failles viennent se brancher dans une couche géologique épaisse à environ 6–7 km de profondeur et aux multiples fractures complexes. Dans cette couche, les vitesses de migration de la sismicité sont généralement lentes (de l'ordre de ~50 m/jour), mais des vitesses de migration bien plus rapides (de l'ordre du km/jour) sont également observées à plus petites échelles spatiales et temporelles.

La classification des microséismes en familles (multiplets et repeaters) par corrélation des formes d'ondes, couplée à l'analyse spatio-temporelle de leur activité, a permis de mettre en évidence de fortes variations latérales de comportement associées à des réponses mécaniques différentes au sein du rift. La partie ouest, au-delà de la zone de transition, alterne entre zones très fracturées avec des multiplets aux géométries très variées n'activant quasiment jamais les mêmes structures au milieu du golfe. Ces multiplets ne semblent vivre que quelques mois puis disparaissent, n'étant jamais réactivés dans la période d'observation. Les séismes de magnitude plus élevée et les multiplets de longue durée sont généralement localisés juste en-dessous ou dans la partie profonde

de l'épaisse couche microsismique, indiquant probablement un creep assez marginal ou se développant sur des structures de plus petite taille au sein de cette couche. L'étude des multiplets aux formes d'ondes fortement corrélées, couplée à l'analyse des temps inter-évènements a montré qu'il n'existait que très peu de vrais repeaters de longue durée dans le rift de Corinthe, contrairement à la région de Parkfield ou à la zone de subduction japonaise par exemple. Ceux identifiés sont généralement localisés plus au nord, alignés sur une structure plus fine et légèrement plus profonde. Ils montrent également une corrélation positive entre temps de récurrence et magnitude. La partie centrale du rift, au niveau des failles d'Eratini, semble justement gouvernée par du glissement lent asismique profond qui active quelques aspérités de manière relativement régulière à la racine d'un plan de faille bloqué. Ces aspérités s'alignent le long d'un plan très fin d'environ une centaine de mètres d'épaisseur qui semble continuer jusqu'à quasiment 15 km de profondeur, alors qu'il n'était visible que jusque 12–13 km auparavant. Cet aspect corrobore l'hypothèse d'un plan de détachement en formation [Lambotte et al., 2014] encore mal construit, mais atteignant possiblement la limite fragile–ductile à présent, et pouvant donc participer à l'ouverture du rift observée par GPS. Finalement, l'épaisse couche géologique pourrait être une zone tampon entre les plans de failles visibles en surface, qui viennent se brancher dedans, et ce plan de détachement plus profond sur lequel se développe du glissement lent.

La relocalisation comprenant les dernières années d'enregistrements sismiques a également révélé la présence de séismes plus superficiels autour de 3–4 km de profondeur, au niveau du système de failles de Kamarai, près de la ville d'Aigion et de la faille de Trizonia offshore. La faille d'Aigion a justement montré des phases de creep en surface révélées grâce aux données InSAR récentes [Elias, 2013] et reste donc à surveiller. Du creep a également été décelé du côté de Rio–Patras, plus à l'ouest, mais nous n'avons pas relocalisé de microsismicité superficielle dans cette région qui a été instrumentée plus récemment.

L'analyse de déclenchement dynamique a mis en évidence une assez faible sensibilité du rift de Corinthe au passage des ondes sismiques d'évènements lointains de forte magnitude $M \geq 7.5$ comme régionaux de magnitude modérée $M \geq 5$. Quelques cas d'augmentation de la sismicité locale du golfe ont été découverts notamment à la suite de l'évènement télésismique de Tohoku en 2011 et du doublet local d'Efpalio de 2010, tandis que de possibles ralentissements voire un arrêt temporaire de l'activité microsismique (Maule en 2010) sont également à considérer. Cet aspect nous incite à penser que les systèmes de failles ne sont pas dans un état instable généralisé, réduisant la possibilité d'une très grande rupture affectant plusieurs failles à la fois. D'autres fortes variations de l'activité sismique ont été enregistrées par le réseau CRL mais correspondent à des aspérités sur des systèmes de failles aux alentours du golfe, indépendants des failles normales majeures étudiées (séisme de Movri en 2008 et séismes de Lefkada en 2003 et 2014). La réponse aux passages des ondes sismiques semble accrue au milieu du golfe, le long du système de failles de Kamarai, là où les fluides ont un rôle prédominant dans le déclenchement de ruptures de petites aspérités. Cet aspect est cohérent avec l'idée que le passage des ondes peut entraîner de légères fluctuations du taux de contraintes et donc pressuriser des fluides interstitiels le long de plans de failles qui étaient déjà quasiment prêtes à casser. Les variations observées de taux de sismicité n'apparaissent quasiment jamais au moment même de l'arrivée du train d'ondes mais avec un certain délai s'étalant de plusieurs minutes à plusieurs heures. La présence de fluide peut là encore expliquer ce décalage temporel par diffusion des pressions de pore à des profondeurs crustales.

Finalement, l'initiation de la rupture des séismes de magnitude de moment de 1 à 5 du rift de Corinthe montre une relation entre les paramètres mesurés de nucléation des séismes et la magnitude complètement différente par rapport aux séismes plus grands du Japon, pour lesquels la même méthode d'analyse a été appliquée. Effectivement, nous avons mis en évidence une corrélation positive entre la pente calculée sur les premiers centièmes de seconde du pic moyen en vitesse (en $cm.m^{-1}$) des formes d'ondes à l'arrivée de P, et la magnitude. Cette loi déterminée à partir d'un jeu de données réduit pourrait avoir des conséquences importantes pour l'évaluation du risque sismique en permettant la "prédiction" de la taille finale d'un évènement en ne regardant

que son démarrage. Attention, le terme de prédiction ici signifie qu'il serait possible de connaître la magnitude finale d'un séisme avant que la rupture ne se termine, mais ne concerne en aucun cas l'occurrence du séisme. Une large quantité de travail est cependant toujours à fournir avant d'être capable d'intégrer ce genre de résultats dans des procédures d'alertes précoces. Notre premier essai d'identification du type de forçage à partir des paramètres extraits à l'initiation de la rupture s'est révélé infructueux. Cependant, nous savons que les fluides peuvent avoir une forte influence sur la rupture d'un séisme, depuis la phase de nucléation, pendant la phase de propagation, et jusqu'au déclenchement de séismes secondaires. Des études complémentaires sont donc à envisager.

Le rift de Corinthe reste assurément un site privilégié pour étudier les couplages sismique-asismiques liés à la contrainte tectonique long-terme et les interactions entre les différents type de forçages transitoires (Figure 6.18).

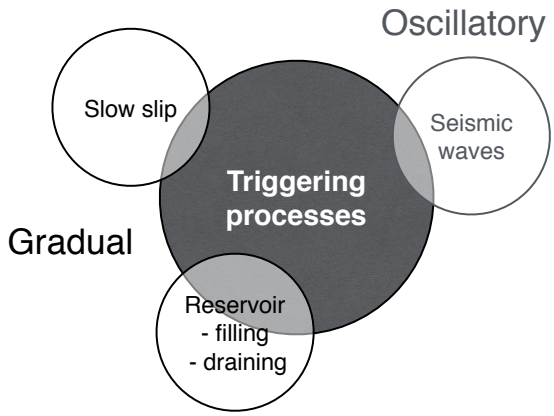

FIGURE 6.18 – Forçages externes transitoires. Les processus de déclenchement de la sismicité locale du rift de Corinthe, explorés à travers ce manuscrit, peuvent se résumer à des forçages progressifs (glissement lent et remplissage/drainage de réservoir) et oscillatoire (passage du train d'ondes sismiques).

Perspectives

L'étude des résultats présentés a permis à la fois d'identifier des pistes de recherche à privilégier pour améliorer et/ou vérifier notre compréhension des mécanismes du rift de Corinthe et de soulever de nouveaux questionnements à son égard.

Dans un premier temps, d'un point de vue méthodologique, plusieurs possibilités d'amélioration ou d'implémentation de nouvelles méthodes peuvent être proposées ici :

- Améliorer la détection automatique des évènements sismiques et affiner les pointés des ondes P et S pour une meilleure estimation de la localisation initiale. Cette perspective est actuellement déjà en cours de traitement avec des tests de la méthode Kurtosis développée par Baillard et al. [2014] et un changement des méthodes de détection pour l'utilisation des outils de *SeiSComp3*.
- Définir un modèle de vitesse 3D, à partir d'une étude tomographique, toujours pour améliorer la localisation initiale des séismes et faciliter l'utilisation de la méthode de relocalisation qui prend beaucoup de paramètres en entrée dépendants de cette première estimation.
- Uniformiser la technique de pointé sur l'ensemble de la base de données, qui devient conséquente, permettrait d'alléger les traitements au cas par cas en fonction du type de pointé (manuel, automatique). Moins d'options ou d'exceptions à gérer dans la compilation des codes serait un plus et accorderait davantage de souplesse et de facilité d'utilisation des données.
- Revoir et améliorer l'algorithme de classification des multiplets en établissant une limite minimale du nombre de stations qui corrèlent pour une même paire d'évènements, afin d'éviter la clusterisation de séismes qui ne sont enregistrés qu'à très peu de stations et qui

corrèlent facilement. Faire d'autres analyses statistiques sur les stations et leur décorrélation avec la distance ou d'autres paramètres.

- Rechercher les microséismes non détectés par les méthodes utilisées actuellement dans les données en continu, à l'aide notamment des techniques de *template matching* des formes d'ondes. Cette recherche pourrait débuter à partir de la base de données de multiplets définie dans cette thèse. Elle permettrait d'augmenter le nombre d'évènements par multiplet et donc d'affiner les études spatio-temporelles des essaims de séismes pour une meilleure quantification. Elle permettrait également d'entreprendre une analyse statistique globale de déclenchement dynamique sur un catalogue bien plus riche. Cette étape pourrait démarrer en tirant bénéfice de l'antenne sismique de Magoula.
- Reprendre la méthodologie développée par [Godano et al., 2014] consistant à estimer les paramètres de sources de manière bayésienne sur des multiplets. Maintenant qu'une base de donnée de multiplets est disponible, une adaptation du code pour un calcul systématique serait bénéfique et permettrait de définir le recouvrement des sources pour les multiplets les plus plats, donnant directement des indications mécaniques précieuses sur la dynamique des essaims.
- Une question importante reste cependant en suspens à la vue des estimations des chutes de contrainte par les méthodes classiques [Brune, 1970; Madariaga, 1976] qui semblent limitées par les caractéristiques numériques. Aucune solution viable n'est encore proposée pour améliorer le calcul de la chute de contrainte des multiplets non plats et des singlets de faible magnitude, pour le rift de Corinthe.
- Une recherche systématique de mécanismes au foyer pourrait également être développée en profitant des multiplets pour sommer les formes d'ondes et augmenter les basses fréquences. Ainsi l'inversion du tenseur de moment serait possible, en plus de l'analyse de la polarité des pointés.
- La mise en évidence des quelques séismes superficiels pourrait impliquer l'intégration des données de polarisation de l'onde P de ces séismes dans l'estimation de leur localisation afin de l'améliorer. En effet, cette localisation s'avère une donnée importante pour le domaine de l'aléa sismique.

D'un point de vue structural :

- Une étude magnéto-tellurique a été réalisée il y a maintenant plus de 15 ans [Pham et al., 2000] pour identifier la couche ductile et serait donc à croiser avec les informations sismologiques. Les nouveaux résultats de ces 3 dernières années soulèvent à nouveau la question de la profondeur de la limite fragile-ductile pour mieux comprendre la dynamique de l'ouverture du rift et cette problématique pourrait être mieux discutée grâce à de nouvelles campagnes électro-magnéto-telluriques plus précises ou une tomographie crustale de la région.
- Les variations spatiales et temporelles du rapport V_P/V_S à l'aide des temps de double-différences obtenus pourraient être analysées à la fois pour aider à la tomographie de la croûte, mais aussi pour déceler les erreurs de pointés dans la base de données sismologiques.
- Le degré de corrélation entre les différentes familles de séismes dans un volume donné pourrait servir de proxy afin d'estimer l'hétérogénéité des structures faillées et le taux de fractures en fonction des différentes zones du rift.

D'un point de vue mécanique :

- L'ajout de nouvelles stations sismiques près de Patras permettrait de mieux comprendre le fonctionnement de la faille de Rio-Patras qui présente du glissement lent mais sans détection de microsismicité superficielle pour le moment. Ces stations permettraient également de contraindre la profondeur du creep.

- Les aspérités pérennes des multiplets se concentrent principalement au nord du rift tandis que les multiplets du milieu du golfe ont une durée de vie courte, limitée à la durée des crises sismiques. Les causes de l'absence de réactivation tardive et de la disparition de ces multiplets restent à élucider, mais des pistes sont à analyser (abrasion, blocage, libération de l'énergie accumulée, modification du milieu).

D'un point de vue dynamique :

- La comparaison des données GPS et InSAR avec l'activité sismique permettrait de vérifier les géométries définies ainsi que les hypothèses mécaniques proposées. Ces études pourraient mieux définir les zones actives et estimer les glissements nécessaires pour rejoindre le chargement tectonique intersismique, ainsi que les glissements pulsatifs (essaims) locaux.
- Grâce à la relocalisation globale et à la base de données de multiplets créés, des études spatio-temporelles fines peuvent être réalisées en calculant systématiquement des vitesses de migration par exemple. Des statistiques spatiales pourraient être entreprises pour trouver des signatures de certaines zones, avec par exemple des multiplets migrant systématiquement à des vitesses identiques.
- Le calcul de l'énergie (ou de la contrainte apparente) des séismes de toute la base de données pourrait être envisagé afin de caractériser le coté impulsionnel des ruptures et permettre de nouveaux regroupements ou classements de familles en spatial et en temporel.

Au sujet des interactions et forçages transitoires :

- Analyser l'influence de la marée terrestre et océanique sur l'occurrence des microséismes du golfe. Cette étude n'a pas pu être entreprise durant ces travaux de thèse, mais semble extrêmement judicieuse à réaliser au vu des interactions observées entre ruptures sismiques et pressions de fluides.
- Essayer de quantifier les pressions de pore nécessaires au déclenchement de certains essaims, notamment la crise de 2003–2004, à l'aide de modèles hydromécaniques par exemple.
- Des modèles mécaniques globaux sont à envisager pour tester les hypothèses géométriques, dynamiques et les influences des différents forçages sur la sismicité du rift. Il serait judicieux de commencer avec un modèle cinématique simple utilisant les données GPS et la géométrie des failles, continuer avec un modèle mécanique élasto-visco-plastique solide intégrant la rhéologie et les lois de frottement, puis finir en ajoutant la composante hydraulique. Étudier la proportion de structures orientées parallèlement ou différemment dans l'espace à l'aide des multiplets pourrait être comparé à une augmentation du niveau de pression de pore activant l'ensemble des fractures environnantes ou à un cisaillement déclenchant des structures orientées selon un axe préférentiel.
- L'analyse de la sismicité profonde à 40–50 km enregistrée dans la base de données en continu, ainsi que l'établissement d'une tomographie profonde, pourraient aider à la définition de l'origine des fluides et à la connaissance du type de fluide mis en jeu (CO_2 supercritique, eau tellurique, fluide mantellique). Ces données pourraient également permettre de savoir si les fluides circulent en interne sous la forme de vases communicants ou s'ils proviennent d'une source externe.
- Des analyses statistiques par régions spatiales permettraient de définir des barrières de microsismicité au sein du rift, qui peuvent être de différents types : des barrières temporelles, c'est-à-dire que les séismes les franchissent après un certain temps, ou des barrières en probabilité, c'est-à-dire qu'un certain pourcentage de séismes passent au travers quelle que soit la durée.
- La corrélation des mesures extensométriques et inclinométriques, encore assez peu valorisées, avec l'activité sismique par zone, permettrait de trouver des anomalies temporelles et

de potentiellement mettre en lumière des transitoires de déformation encore non détectés. La crise sismique près de Trizonia, et celle près de Psathopyrgos en 2014, pourraient être de bons points de départ pour cibler une période temporelle à analyser dans les données extensométriques.

Finalement, nous pouvons souligner que les études menées au cours de ce travail, associant de nombreuses techniques de traitement et d'analyse de la sismicité, sont assez rarement menées de manière aussi intégrée, et pourraient s'appliquer à des contextes variés de microsismicité, naturelle ou induite.

Références

Bibliographie

Abercrombie, R. (1995). Earthquake source scaling relationships from -1 to 5 ml using seismograms recorded at 2.5-km depth. *Journal of Geophysical Research : Solid Earth*, 100(B12) :24015–24036. (page 143)

Aiken, C. and Peng, Z. (2014). Dynamic triggering of microearthquakes in three geothermal/volcanic regions of California. *Journal of Geophysical Research : Solid Earth*, 119(9) :6992–7009. (page 118)

Aki, K. and Richards, P. (2002). *Quantitative seismology*. (page 146)

Albini, P., Rovida, A., Scotti, O., and Lyon-Caen, H. (2017). Large eighteenth–nineteenth century earthquakes in western Gulf of Corinth with reappraised size and location. *Bulletin of the Seismological Society of America*, 107(4) :1663–1687. (page 33, 59)

Allam, A. and Ben-Zion, Y. (2012). Seismic velocity structures in the southern California plate-boundary environment from double-difference tomography. *Geophysical Journal International*, 190(2) :1181–1196. (page 44)

Allen, J. (2005). A multi-kilometer pseudotachylyte system as an exhumed record of earthquake rupture geometry at hypocentral depths (Colorado, USA). *Tectonophysics*, 402(1–4) :37–54. (page 44)

Allen, R. (1982). Automatic phase pickers : their present use and future prospects. *Bulletin of the Seismological Society of America*, 72(6B) :S225–S242. (page 39)

Ambraseys, N. and Jackson, J. (1990). Seismicity and associated strain of central Greece between 1890 and 1988. *Geophysical Journal International*, 101(3) :663–708. (page 32)

Ampuero, J.-P., Vilotte, J.-P., and Sanchez-Sesma, F. (2002). Nucleation of rupture under slip dependent friction law : simple models of fault zone. *Journal of Geophysical Research : Solid Earth*, 107(B12). (page 138)

Anderson, J., Brune, J., Louie, J., Zeng, Y., Savage, M., Yu, G., Chen, Q., et al. (1994). Seismicity in the western Great Basin apparently triggered by the Landers, California, earthquake, 28 June 1992. *Bulletin of the Seismological Society of America*, 84(3) :863–891. (page 20, 108)

Armijo, R., Meyer, B., King, G., Rigo, A., and Papanastassiou, D. (1996). Quaternary evolution of the Corinth Rift and its implications for the Late Cenozoic evolution of the Aegean. *Geophysical Journal International*, 126(1) :11–53. (page 26, 28, 30, 31, 45, 58, 90, 135)

Asanuma, H., Ishimoto, M., Jones, R., Phillips, W., and Niitsuma, H. (2001). A variation of the collapsing method to delineate structures inside a microseismic cloud. *Bulletin of the Seismological Society of America*, 91(1) :154–160. (page 47)

Aster, R. and Scott, J. (1993). Comprehensive characterization of waveform similarity in microearthquake data sets. *Bulletin of the Seismological Society of America*, 83(4) :1307–1314. (page 100)

Atkinson, C. (1965). The propagation of a brittle crack in anisotropic material. *International Journal of Engineering Science*, 3(1) :77–91. (page 19)

Avallone, A., Briole, P., Agatza-Balodimou, A., Billiris, H., Charade, O., Mitsakaki, C., Nercessian, A., Papazissi, K., Paradissis, D., and Veis, G. (2004). Analysis of eleven years of deformation measured by {GPS} in the Corinth Rift Laboratory area. *Comptes Rendus Geoscience*, 336(4–5) :301–311. (page 26, 31, 58, 59, 88, 89)

Baillard, C., Crawford, W., Ballu, V., Hibert, C., and Mangeney, A. (2014). An automatic kurtosis-based P- and S-phase picker designed for local seismic networks. *Bulletin of the Seismological Society of America*, 104(1) :394–409. (page 39, 157)

Baker, C., Hatzfeld, D., Lyon-Caen, H., Papadimitriou, E., and Rigo, A. (1997). Earthquake mechanisms of the Adriatic Sea and western Greece : implications for the oceanic subduction-continental collision transition. *Geophysical Journal International*, 131(3) :559–594. (page 33)

Beckers, A. (2015). *Late quaternary sedimentation in the western gulf of Corinth*. PhD thesis, Grenoble Alpes, Université de Liège, Université Savoie Mont Blanc. (page 68, 72, 92, 116, 136)

Beckers, A., Hubert-Ferrari, A., Beck, C., Bodeux, S., Tripsanas, E., Sakellariou, D., and De Batist, M. (2015). Active faulting at the western tip of the Gulf of Corinth, Greece, from high-resolution seismic data. *Marine Geology*, 360 :55–69. (page 31, 32, 58, 59, 89, 92, 94)

Bell, R., McNeill, L., Bull, J., and Henstock, T. (2008). Evolution of the offshore western Gulf of Corinth. *Geological Society of America Bulletin*, 120(1-2) :156–178. (page 30, 31, 44, 45, 58, 59, 135)

Bell, R., McNeill, L., Bull, J., Henstock, T., Collier, R., and Leeder, M. (2009). Fault architecture, basin structure and evolution of the Gulf of Corinth Rift, central Greece. *Basin Research*, 21(6) :824–855. (page 32, 59, 89)

Bernard, P., Boudin, F., Sacks, S., Linde, A., Blum, P.-A., Courteille, C., Esnoult, M.-F., Castarède, H., Felekis, S., and Billiris, H. (2004). Continuous strain and tilt monitoring on the Trizonia island, Rift of Corinth, Greece. *Comptes Rendus Geoscience*, 336(4) :313–323. (page 15)

Bernard, P., Briole, P., Meyer, B., Lyon-Caen, H., Gomez, J.-M., Tiberi, C., Berge, C., Cattin, R., Hatzfeld, D., Lachet, C., Lebrun, B., Deschamps, A., Courboulex, F., Larroque, C., Rigo, A., Massonnet, D., Papadimitriou, P., Kassaras, J., Diagourtas, D., Makropoulos, K., Veis, G., Papazisi, E., Mitsakaki, C., Karakostas, V., Papadimitriou, E., Papanastassiou, D., Chouliaras, M., and Stavrakakis, G. (1997). The Ms = 6.2, June 15, 1995 Aigion earthquake (Greece) : evidence for low angle normal faulting in the Corinth Rift. *Journal of Seismology*, 1(2) :131–150. (page 33, 34, 45, 59, 75, 94, 147, 208)

Bernard, P., Lyon-Caen, H., Briole, P., Deschamps, A., Boudin, F., Makropoulos, K., Papadimitriou, P., Lemeille, F., Patau, G., Billiris, H., Paradissis, D., Papazissi, K., Castarède, H., Charade, O., Nercessian, A., Avallone, A., Pacchiani, F., Zahradnik, J., Sacks, S., and Linde, A. (2006). Seismicity, deformation and seismic hazard in the western rift of Corinth : New insights from the Corinth Rift Laboratory (CRL). *Tectonophysics*, 426(1–2) :7–30. (page 32, 33, 58, 59, 94, 95)

Beroza, G. and Ellsworth, W. (1996). Properties of the seismic nucleation phase. *Tectonophysics*, 261(1) :209–227. (page 134, 145)

Beroza, G. and Ide, S. (2011). Slow earthquakes and nonvolcanic tremor. *Annual review of Earth and planetary sciences*, 39 :271–296. (page 16)

Boiselet, A. (2014). *Cycle sismique et aléa sismique d'un réseau de failles actives : le cas du rift de Corinthe (Grèce)*. PhD thesis, École Normale Supérieure de Paris, Institut de Radioprotection et de Sureté Nucléaire. (page 45, 94)

Bourouis, S. and Bernard, P. (2007). Evidence for coupled seismic and aseismic fault slip during water injection in the geothermal site of Soultz (France), and implications for seismogenic transients. *Geophysical Journal International*, 169(2) :723–732. (page 18, 44, 52)

Bourouis, S. and Cornet, F. (2009). Microseismic activity and fluid fault interactions : some results from the Corinth Rift Laboratory (CRL), Greece. *Geophysical Journal International*, 178(1) :561–580. (page 49, 52, 59, 60, 111, 135)

Briole, P., Rigo, A., Lyon-Caen, H., Ruegg, J., Papazissi, K., Mitsakaki, C., Balodimou, A., Veis, G., Hatzfeld, D., and Deschamps, A. (2000). Active deformation of the Corinth rift, Greece : Results from repeated Global Positioning System surveys between 1990 and 1995. *Journal of Geophysical Research : Solid Earth*, 105(B11) :25605–25625. (page 26, 31, 33, 34, 35, 58)

Brodsky, E. and Kanamori, H. (2001). Elastohydrodynamic lubrication of faults. *Journal of Geophysical Research : Solid Earth*, 106(B8) :16357–16374. (page 147)

Brodsky, E., Karakostas, V., and Kanamori, H. (2000). A new observation of dynamically triggered regional seismicity : Earthquakes in Greece following the August, 1999 Izmit, Turkey earthquake. *Geophysical Research Letters*, 27(17). (page 20, 108)

Brodsky, E., Roeloffs, E., Woodcock, D., Gall, I., and Manga, M. (2003). A mechanism for sustained groundwater pressure changes induced by distant earthquakes. *Journal of Geophysical Research : Solid Earth*, 108(B8). (page 108, 126, 128)

Brooks, M. and Ferentinos, G. (1984). Tectonics and sedimentation in the Gulf of Corinth and the Zakynthos and Kefallinia channels, western Greece. *Tectonophysics*, 101(1-2) :25–54. (page 28, 29)

Brown, K., Tryon, M., DeShon, H., Dorman, L., and Schwartz, S. (2005). Correlated transient fluid pulsing and seismic tremor in the Costa Rica subduction zone. *Earth and Planetary Science Letters*, 238(1) :189–203. (page 21)

Brune, J. (1970). Tectonic stress and the spectra of seismic shear waves from earthquakes. *Journal of Geophysical Research*, 75(26) :4997–5009. (page 136, 151, 158)

Brune, J. (1979). Implications of earthquake triggering and rupture propagation for earthquake prediction based on premonitory phenomena. *Journal of Geophysical Research : Solid Earth*, 84(B5) :2195–2198. (page 134)

Canitano, A., Bernard, P., and Allgeyer, S. (2017). Observation and modeling of the seismic seiches triggered in the Gulf of Corinth (Greece) by the 2011 Mw 9.0 Tohoku earthquake. *Journal of Geodynamics*, 109 :24–31. (page 127)

Canitano, A., Bernard, P., Linde, A., and Sacks, S. (2013). Analysis of signals of a borehole strainmeter in the western rift of Corinth, Greece. *Journal of Geodetic Science*, 3(1) :63–76. (page 38)

Canitano, A., Bernard, P., Linde, A., Sacks, S., and Boudin, F. (2014). Correcting high-resolution borehole strainmeter data from complex external influences and partial-solid coupling : the case of Trizonia, Rift of Corinth (Greece). *Pure and Applied Geophysics*, 171(8) :1759–1790. (page 38)

Cappa, F. (2009). Modelling fluid transfer and slip in a fault zone when integrating heterogeneous hydromechanical characteristics in its internal structure. *Geophysical Journal International*, 178(3) :1357–1362. (page 50)

Chamot-Rooke, N., Rangin, C., and Le Pichon, X. (2005). Dotmed—deep offshore tectonics of the mediterranean : A synthesis of deep marine data in eastern mediterranean. *Mem. Soc. Geol. Fr*, 177 :1–64. (page 27)

Chen, K., Nadeau, R., and Rau, R.-J. (2007). Towards a universal rule on the recurrence interval scaling of repeating earthquakes ? *Geophysical Research Letters*, 34(16). (page 17)

Chen, L., Chen, J., and Xu, Q. (2012a). Correlations between solid tides and worldwide earthquakes $M_S \geq 7.0$ since 1900. *Natural Hazards and Earth System Sciences*, 12(3) :587–590. (page 7)

Chen, X., Shearer, P., and Abercrombie, R. (2012b). Spatial migration of earthquakes within seismic clusters in Southern California : Evidence for fluid diffusion. *Journal of Geophysical Research : Solid Earth*, 117(B4). (page 21, 52, 88)

Chinnery, M. (1963). The stress changes that accompany strike-slip faulting. *Bulletin of the Seismological Society of America*, 53(5) :921–932. (page 19)

Chlieh, M., Avouac, J.-P., Hjorleifsdottir, V., Song, T.-R. A., Ji, C., Sieh, K., Sladen, A., Hebert, H., Prawirodirdjo, L., Bock, Y., et al. (2007). Coseismic slip and afterslip of the great Mw 9.15 Sumatra–Andaman earthquake of 2004. *Bulletin of the Seismological Society of America*, 97(1A) :S152–S173. (page 15)

Cochran, E., Vidale, J., and Tanaka, S. (2004). Earth tides can trigger shallow thrust fault earthquakes. *Science*, 306(5699) :1164–1166. (page 7)

Collier, R., Leeder, M., Rowe, P., and Atkinson, T. (1992). Rates of tectonic uplift in the Corinth and Megara Basins, central Greece. *Tectonics*, 11(6) :1159–1167. (page 31)

Colombelli, S., Caruso, A., Zollo, A., Festa, G., and Kanamori, H. (2015). A P-wave based, on-site method for Earthquake Early Warning. *Geophysical Research Letters*, 42 :1390–1398. (page 139)

Colombelli, S., Zollo, A., Festa, G., and Picozzi, M. (2014). Evidence for a difference in rupture initiation between small and large earthquakes. *Nature communications*, 5 :3958. (page 134, 135, 137, 138, 139, 140, 142, 145, 148)

Cornet, F., Doan, M., Moretti, I., and Borm, G. (2004). Drilling through the active Aigion Fault : the AIG10 well observatory. *Comptes Rendus Geoscience*, 336(4–5) :395–406. (page 32, 44, 49, 76)

Cornet, F., Helm, J., Poitrenaud, H., and Etchecopar, A. (1997). Seismic and aseismic slips induced by large-scale fluid injections. *Pure and applied geophysics*, 150(3-4) :563–583. (page 90)

Das, S. and Scholz, C. (1981). Theory of time-dependent rupture in the earth. *Journal of Geophysical Research : Solid Earth*, 86(B7) :6039–6051. (page 19)

Davidsen, J., Gu, C., and Baiesi, M. (2015). Generalized Omori–Utsu law for aftershock sequences in southern California. *Geophysical Journal International*, 201(2) :965–978. (page 199)

Davis, E., Wang, K., Thomson, R., Becker, K., and Cassidy, J. (2001). An episode of seafloor spreading and associated plate deformation inferred from crustal fluid pressure transients. *Journal of Geophysical Research : Solid Earth*, 106(B10) :21953–21963. (page 37)

Dercourt, J., Zonenshain, L., Ricou, L.-E., Kazmin, V., Pichon, X. L., Knipper, A., Grandjacquet, C., Sbortshikov, I., Geyssant, J., Lepvrier, C., Pechersky, D., Boulin, J., Sibuet, J.-C., Savostin, L., Sorokhtin, O., Westphal, M., Bazhenov, M., Lauer, J., and Biju-Duval, B. (1986). Geological evolution of the Tethys belt from the Atlantic to the Pamirs since the Lias. *Tectonophysics*, 123(1) :241–315. (page 26)

Douglas, A., Beavan, J., Wallace, L., and Townend, J. (2005). Slow slip on the northern Hikurangi subduction interface, New Zealand. *Geophysical Research Letters*, 32(16). (page 15)

Dragert, H., Wang, K., and James, T. (2001). A silent slip event on the deeper Cascadia subduction interface. *Science*, 292(5521) :1525–1528. (page 15)

Dublanchet, P., Godano, M., and Bernard, P. (2015). Inferring fault mechanical conditions from the source parameters of a complex microseismic multiplet in the Corinth rift, Greece. *Journal of Geophysical Research : Solid Earth*, 120(11) :7655–7682. (page 111, 135)

Durand, V., Bouchon, M., Floyd, M., Theodulidis, N., Marsan, D., Karabulut, H., and Schmittbuhl, J. (2014). Observation of the spread of slow deformation in Greece following the breakup of the slab. *Geophysical Research Letters*, 41(20) :7129–7134. (page 94, 120)

Duverger, C. (2014). Évolution spatio-temporelle de multiplets microsismiques à la base des failles du rift de Corinthe : des indices de migrations de fluides. Master's thesis, Institut de Physique du Globe de Paris, École Normale Supérieure de Paris. (page 49, 135, 136, 193)

Duverger, C., Godano, M., Bernard, P., Lyon-Caen, H., and Lambotte, S. (2015). The 2003–2004 seismic swarm in the western Corinth Rift : Evidence for a multiscale pore pressure diffusion process along a permeable fault system. *Geophysical Research Letters*, 42(18) :7374–7382. (page 44, 58, 59, 69, 76, 88, 111, 120, 127, 135)

El-Isa, Z. and Eaton, D. (2014). Spatiotemporal variations in the b-value of earthquake magnitude–frequency distributions : Classification and causes. *Tectonophysics*, 615 :1–11. (page 203)

Elias, Ηλίας, P. (2013). *Ground deformation observed in the western Corinth rift (Greece) by means of SAR interferometry*. PhD thesis, École Normale Supérieure de Paris. (page 88, 92, 156, 204)

Ellsworth, W. (2013). Injection-induced earthquakes. *Science*, 341(6142) :1225942. (page 18)

Ellsworth, W. and Beroza, G. (1995). Seismic evidence for an earthquake nucleation phase. *Science*, 268(5212) :851–855. (page 134)

Eshelby, J. (1957). The determination of the elastic field of an ellipsoidal inclusion, and related problems. *Proceedings of the Royal Society of London*, 241(1226) :376–396. (page 151)

Fischer, A., Sammis, C., Chen, Y., and Teng, T.-L. (2008). Dynamic triggering by strong-motion P and S waves : Evidence from the 1999 Chi-Chi, Taiwan, earthquake. *Bulletin of the Seismological Society of America*, 98(2) :580–592. (page 108)

Flotté, N., Sorel, D., Müller, C., and Tensi, J. (2005). Along strike changes in the structural evolution over a brittle detachment fault : Example of the Pleistocene Corinth–Patras rift (Greece). *Tectonophysics*, 403(1) :77–94. (page 30, 31, 32, 34, 59, 91, 92, 93)

Flotté, N. (2003). *Caractérisation structurale et cinématique d'un rift sur détachement : le rift de Corinthe-Patras, Grèce*. PhD thesis, Université Paris 11, Orsay. (page 88)

Ford, M., Hemelsdaël, R., Mancini, M., and Palyvos, N. (2016). Rift migration and lateral propagation : evolution of normal faults and sediment-routing systems of the western Corinth rift (Greece). *Geological Society, London, Special Publications*, 439 :SP439–15. (page 34, 93, 135, 141)

Ford, M., Rohais, S., Williams, E., Bourlange, S., Jousselin, D., Backert, N., and Malartre, F. (2013). Tectono-sedimentary evolution of the western Corinth rift (central Greece). *Basin Research*, 25(1) :3–25. (page 31, 59, 88, 93)

Ford, M., Williams, E., Malartre, F., Popescu, S.-M., Nichols, G., Williams, E., and Paola, C. (2009). Stratigraphic architecture, sedimentology and structure of the Vouraikos Gilbert-type fan delta, Gulf of Corinth, Greece. *Sedimentary processes, environments and basins*, pages 49–90. (page 59, 135)

Freed, A. (2005). Earthquake triggering by static, dynamic, and postseismic stress transfer. *Annual Reviews of Earth Planetary Sciences*, 33 :335–367. (page 21)

Ganas, A., Chousianitis, K., Batsi, E., Kolligri, M., Agalos, A., Chouliaras, G., and Makropoulos, K. (2013). The January 2010 Efpalion earthquakes (Gulf of Corinth, central Greece) : earthquake interactions and blind normal faulting. *Journal of seismology*, 17(2) :465–484. (page 74, 121)

Gautier, S., Latorre, D., Virieux, J., Deschamps, A., Skarpelos, C., Sotiriou, A., Serpetsidaki, A., and Tselentis, A. (2006). A new passive tomography of the Aigion area (Gulf of Corinth, Greece) from the 2002 data set. *Pure and applied geophysics*, 163(2-3) :431–453. (page 53, 59)

Gavrilenko, P., Melikadze, G., Chelidze, T., Gibert, D., and Kumsiashvili, G. (2000). Permanent water level drop associated with the Spitak earthquake : observations at Lisi borehole (Republic of Georgia) and modelling. *Geophysical Journal International*, 143(1) :83–98. (page 38)

Geller, R. and Mueller, C. (1980). Four similar earthquakes in central California. *Geophysical Research Letters*, 7(10) :821–824. (page 100)

Ghisetti, F. and Vezzani, L. (2004). Plio–Pleistocene sedimentation and fault segmentation in the Gulf of Corinth (Greece) controlled by inherited structural fabric. *Comptes Rendus Geoscience*, 336(4) :243–249. (page 30, 58)

Ghosh, A., Vidale, J., Peng, Z., Creager, K., and Houston, H. (2009). Complex nonvolcanic tremor near Parkfield, California, triggered by the great 2004 Sumatra earthquake. *Journal of Geophysical Research : Solid Earth*, 114(B12). (page 109)

Godano, M., Bernard, P., Marsan, D., and Dublanchet, P. (2015). Bayesian inversion of seismic spectral ratio for source scaling. application to a persistent multiplet in the western Corinth rift. *Journal of Geophysical Research*, 120(11) :7683–7712. (page 80, 88, 90, 193, 198)

Godano, M., Deschamps, A., Lambotte, S., Lyon-Caen, H., Bernard, P., and Pacchiani, F. (2014). Focal mechanisms of earthquake multiplets in the western part of the Corinth Rift (Greece) : influence of the velocity model and constraints on the geometry of the active faults. *Geophysical Journal International*, 197(3) :1660–1680. (page 33, 46, 48, 49, 76, 89, 135, 136, 145, 147, 151, 158)

Goldsworthy, M. and Jackson, J. (2001). Migration of activity within normal fault systems : examples from the Quaternary of mainland Greece. *Journal of Structural Geology*, 23(2) :489–506. (page 88, 93)

Gomberg, J., Blanpied, M., and Beeler, N. (1997). Transient triggering of near and distant earthquakes. *Bulletin of the Seismological Society of America*, 87(2) :294–309. (page 108)

Gomberg, J., Bodin, P., Larson, K., and Dragert, H. (2004). Earthquake nucleation by transient deformations caused by the M=7.9 Denali, Alaska, earthquake. *Nature*, 427(6975) :621–624. (page 127)

Gomberg, J. and Johnson, P. (2005). Seismology : Dynamic triggering of earthquakes. *Nature*, 437(7060) :830–830. (page 108)

Gomberg, J., Reasenberg, P., Bodin, P., and Harris, R. (2001). Earthquake triggering by seismic waves following the Landers and Hector Mine earthquakes. *Nature*, 411(6836) :462–466. (page 20, 21)

Gonzalez-Huizar, H., Velasco, A., Peng, Z., and Castro, R. (2012). Remote triggered seismicity caused by the 2011, M9.0 Tohoku-oki, Japan earthquake. *Geophysical Research Letters*, 39(10). (page 108, 109)

Got, J.-L., Fréchet, J., and Klein, F. (1994). Deep fault plane geometry inferred from multiplet relative relocation beneath the south flank of Kilauea. *Journal of Geophysical Research*, 99(B8) :15375–15386. (page 61, 64)

Gu, C., Schumann, A., Baiesi, M., and Davidsen, J. (2013). Triggering cascades and statistical properties of aftershocks. *Journal of Geophysical Research : Solid Earth*, 118(8) :4278–4295. (page 199)

Guéguen, Y., Gavrilenko, P., and Le Ravalec, M. (1996). Scales of rock permeability. *Surveys in Geophysics*, 17(3) :245–263. (page 52)

Hainzl, S. (2004). Seismicity patterns of earthquake swarms due to fluid intrusion and stress triggering. *Geophysical Journal International*, 159(3) :1090–1096. (page 21, 44)

Hainzl, S. and Fischer, T. (2002). Indications for a successively triggered rupture growth underlying the 2000 earthquake swarm in Vogtland/NW Bohemia. *Journal of Geophysical Research : Solid Earth*, 107(B12). (page 21)

Hainzl, S., Scherbaum, F., and Beauval, C. (2006). Estimating background activity based on interevent-time distribution. *Bulletin of the Seismological Society of America*, 96(1) :313–320. (page 83, 113)

Hanks, T. and Wyss, M. (1972). The use of body-wave spectra in the determination of seismic-source parameters. *Bulletin of the Seismological Society of America*, 62(2) :561–589. (page 151)

Harris, D. (1991). A waveform correlation method for identifying quarry explosions. *Bulletin of the Seismological Society of America*, 81(6) :2395–2418. (page 100)

Hasiotis, T., Papatheodorou, G., Kastanos, N., and Ferentinos, G. (1996). A pockmark field in the Patras Gulf (Greece) and its activation during the 14/7/93 seismic event. *Marine Geology*, 130(3-4) :333–344. (page 92)

Hatzfeld, D., Karakostas, V., Ziazia, M., Kassaras, I., Papadimitriou, E., Makropoulos, K., Voulgaris, N., and Papaioannou, C. (2000). Microseismicity and faulting geometry in the Gulf of Corinth (Greece). *Geophysical Journal International*, 141(2) :438–456. (page 59, 92)

Hauksson, E. and Shearer, P. (2005). Southern California hypocenter relocation with waveform cross-correlation, Part 1 : Results using the double-difference method. *Bulletin of the Seismological Society of America*, 95(3) :896–903. (page 64, 66)

Heezen, B., Ewing, M., and Johnson, G. (1966). The Gulf of Corinth floor. In *Deep Sea Research and Oceanographic Abstracts*, volume 13, pages 381–411. (page 75)

Heki, K., Miyazaki, S., and Tsuji, H. (1997). Silent fault slip following an interplate thrust earthquake at the Japan Trench. *Nature*, 386(6625) :595. (page 15)

Hess, H. (1962). History of the ocean basins. In of America, G. S., editor, *Petrologic Studies*, volume in honor of A.F. Buddington, pages 599–620. (page 10)

Hill, D. (2012). Dynamic stresses, Coulomb failure, and remote triggering – corrected. *Bulletin of the Seismological Society of America*, 102(6) :2313–2336. (page 21)

Hill, D. and Prejean, S. (2015). 4.09 - dynamic triggering. In *Treatise on Geophysics*. (page 19, 20, 21, 126, 128)

Hill, D., Reasenberg, P., Michael, A., Arabaz, W., Beroza, G., Brumbaugh, D., Brune, J., Castro, R., Davis, S., Ellsworth, W., et al. (1993). Seismicity remotely triggered by the magnitude 7.3 Landers, California, earthquake. *Science*, 260(5114) :1617–1624. (page 20, 21, 108)

Hirose, F., Miyaoka, K., Hayashimoto, N., Yamazaki, T., and Nakamura, M. (2011). Outline of the 2011 off the Pacific coast of Tohoku earthquake (Mw 9.0) – seismicity : foreshocks, mainshock, aftershocks, and induced activity. *Earth, Planets and Space*, 63(7) :513–518. (page 21)

Hirose, H., Hirahara, K., Kimata, F., Fujii, N., and Miyazaki, S. (1999). A slow thrust slip event following the two 1996 Hyuganada earthquakes beneath the Bungo Channel, southwest Japan. *Geophysical Research Letters*, 26(21) :3237–3240. (page 15)

Holmes, A. (1948). The oldest known minerals and rocks. *Transactions of the Edinburgh Geological Society*, 14 :176–194. (page 10)

Hough, S. and Kanamori, H. (2002). Source properties of earthquakes near the Salton Sea triggered by the 16 October 1999 M 7.1 Hector Mine, California, earthquake. *Bulletin of the Seismological Society of America*, 92(4) :1281–1289. (page 128)

Hsu, Y.-J., Simons, M., Avouac, J.-P., Galetzka, J., Sieh, K., Chlieh, M., Natawidjaja, D., Prawirodirdjo, L., and Bock, Y. (2006). Frictional afterslip following the 2005 Nias-Simeulue earthquake, Sumatra. *Science*, 312(5782) :1921–1926. (page 15)

Hubbert, M. and Rubey, W. (1959). Role of fluid pressure in mechanics of overthrust faulting I. Mechanics of fluid-filled porous solids and its application to overthrust faulting. *Geological Society of America Bulletin*, 70(2) :115–166. (page 21)

Hubert, A., King, G., Armijo, R., Meyer, B., and Papanastasiou, D. (1996). Fault re-activation, stress interaction and rupture propagation of the 1981 Corinth earthquake sequence. *Earth and Planetary Science Letters*, 142(3-4) :573–585. (page 32)

Husen, S., Wiemer, S., and Smith, R. (2004). Remotely triggered seismicity in the Yellowstone National Park region by the 2002 Mw 7.9 Denali Fault earthquake, Alaska. *Bulletin of the Seismological Society of America*, 94(6B) :S317–S331. (page 21)

Husker, A. and Brodsky, E. (2004). Seismicity in Idaho and Montana triggered by the Denali fault earthquake : A window into the geologic context for seismic triggering. *Bulletin of the Seismological Society of America*, 94(6B) :S310–S316. (page 127)

Hutchings, L. and Wu, F. (1990). Empirical Green's functions from small earthquakes : a waveform study of locally recorded aftershocks of the 1971 San Fernando earthquake. *Journal of Geophysical Research : Solid Earth*, 95(B2) :1187–1214. (page 100)

Ide, S. and Beroza, G. (2001). Does apparent stress vary with earthquake size ? *Geophysical Research Letters*, 28(17) :3349–3352. (page 145)

Ide, S., Beroza, G., Shelly, D., and Uchide, T. (2007). A scaling law for slow earthquakes. *Nature*, 447(7140) :76. (page 15)

Igarashi, T., Matsuzawa, T., and Hasegawa, A. (2003). Repeating earthquakes and interplate aseismic slip in the northeastern japan subduction zone. *Journal of Geophysical Research : Solid Earth*, 108(B5). (page 89)

Iio, Y. (1995). Observations of the slow initial phase generated by microearthquakes : implications for earthquake nucleation and propagation. *Journal of Geophysical Research : Solid Earth*, 100(B8) :15333–15349. (page 134)

Jackson, J., Gagnepain, J., Houseman, G., King, G., Papadimitriou, P., Soufleris, C., and Virieux, J. (1982). Seismicity, normal faulting, and the geomorphological development of the Gulf of Corinth (Greece) : the Corinth earthquakes of February and March 1981. *Earth and Planetary Science Letters*, 57(2) :377–397. (page 32)

Jackson, J. and White, N. (1989). Normal faulting in the upper continental crust : observations from regions of active extension. *Journal of Structural Geology*, 11(1-2) :15–36. (page 32)

Jacobshagen, V., Dürr, S., Kockel, F., Kopp, K., Kowalczyk, G., Berckhemer, H., and Büttner, D. (1978). Structure and geodynamic evolution of the Aegean region. *Alps, Apennines, Hellenides*, pages 537–564. (page 29)

Janssen, C., Wirth, R., Wenk, H.-R., Morales, L., Naumann, R., Kienast, M., Song, S.-R., and Dresen, G. (2014). Faulting processes in active faults – evidences from {TCDP} and {SAFOD} drill core samples. *Journal of Structural Geology*, 65 :100–116. (page 44)

Jolivet, L., Augier, R., Faccenna, C., Negro, F., Rimmele, G., Agard, P., Robin, C., Rossetti, F., and Crespo-Blanc, A. (2008). Subduction, convergence and the mode of backarc extension in the mediterranean region. *Bulletin de la Société Géologique de France*, 179(6) :525–550. (page 27)

Jolivet, L., Labrousse, L., Agard, P., Lacombe, O., Bailly, V., Lecomte, E., Mouthereau, F., and Mehl, C. (2010). Rifting and shallow-dipping detachments, clues from the Corinth Rift and the Aegean. *Tectonophysics*, 483(3-4) :287–304. (page 29, 30, 32, 45, 52, 59, 75)

Kanamori, H. (2005). Real-time seismology and earthquake damage mitigation. *Annual Review of Earth and Planetany Sciences*, 33 :195–214. (page 148)

Kanamori, H. and Kikuchi, M. (1993). The 1992 Nicaragua earthquake : a slow tsunami earthquake associated with subducted sediments. *Nature*, 361(6414) :714–716. (page 14)

Kapetanidis, V., Deschamps, A., Papadimitriou, P., Matrullo, E., Karakonstantis, A., Bozionelos, G., Kaviris, G., Serpetsidaki, A., Lyon-Caen, H., Voulgaris, N., et al. (2015). The 2013 earthquake swarm in Helike, Greece : seismic activity at the root of old normal faults. *Geophysical Journal International*, 202(3) :2044–2073. (page 88)

Keranen, K., Savage, H., Abers, G., and Cochran, E. (2013). Potentially induced earthquakes in Oklahoma, USA : Links between wastewater injection and the 2011 Mw 5.7 earthquake sequence. *Geology*, 41(6) :699–702. (page 18)

Kilb, D., Gomberg, J., and Bodin, P. (2000). Triggering of earthquake aftershocks by dynamic stresses. *Nature*, 408(6812) :570–574. (page 20)

Kim, Y.-S., Peacock, D., and Sanderson, D. (2004). Fault damage zones. *Journal of Structural Geology*, 26(3) :503–517. (page 49)

Kious, W. and Tilling, R. (1996). *This dynamic Earth : the story of plate tectonics*. DIANE Publishing. (page 9, 10)

Knopoff, L. (1964). The statistics of earthquakes in Southern California. *Bulletin of the Seismological Society of America*, 54(6A) :1871–1873. (page 19)

Kostoglodov, V., Singh, S., Santiago, J., Franco, S., Larson, K., Lowry, A., and Bilham, R. (2003). A large silent earthquake in the Guerrero seismic gap, Mexico. *Geophysical Research Letters*, 30(15). (page 15)

Koukouvelas, I. and Papoulis, D. (2009). Fluid involvement in the active Helike normal Fault, Gulf of Corinth, Greece. *Journal of Structural Geology*, 31(3) :237–250. (page 52)

Lambotte, S., Lyon-Caen, H., Bernard, P., Deschamps, A., Patau, G., Nercessian, A., Pacchiani, F., Bourouis, S., Drilleau, M., and Adamova, P. (2014). Reassessment of the rifting process in the western Corinth Rift from relocated seismicity. *Geophysical Journal International*, 197(3) :1822–1844. (page 18, 31, 32, 33, 34, 35, 36, 44, 45, 46, 49, 58, 59, 60, 61, 62, 63, 65, 66, 67, 75, 76, 88, 89, 95, 136, 156)

Latorre, D. (2004). *Imagerie sismique du milieu de propagation à partir des ondes directes et converties : application à la région d'Aigion (Golfe de Corinthe, Grèce)*. PhD thesis, Université Nice Sophia Antipolis. (page 29)

Latorre, D., Virieux, J., Monfret, T., Monteiller, V., Vanorio, T., Got, J.-L., and Lyon-Caen, H. (2004). A new seismic tomography of Aigion area (Gulf of Corinth, Greece) from the 1991 data set. *Geophysical Journal International*, 159(3) :1013–1031. (page 27, 44, 52, 58)

Le Pourhiet, L., Burov, E., and Moretti, I. (2004). Rifting through a stack of inhomogeneous thrusts (the dipping pie concept). *Tectonics*, 23(4). (page 28, 141)

Lee, W. and Lahr, J. (1972). A computer program for determining hypocenter, magnitude, and RST motion pattern of local earthquakes. Technical report, U.S. Geological Survey. (page 60)

Leeder, M., Mack, G., Brasier, A., Parrish, R., McIntosh, W., Andrews, J., and Duermeijer, C. (2008). Late-Pliocene timing of Corinth (Greece) rift-margin fault migration. *Earth and Planetary Science Letters*, 274(1) :132–141. (page 30)

Lengliné, O. and Marsan, D. (2009). Inferring the coseismic and postseismic stress changes caused by the 2004 mw= 6 parkfield earthquake from variations of recurrence times of microearthquakes. *Journal of Geophysical Research : Solid Earth*, 114(B10). (page 83, 84)

Linde, A., Gladwin, M., Johnston, M., Gwyther, R., and Bilham, R. (1996). A slow earthquake sequence on the San Andreas fault. *Nature*, 383(6595) :65. (page 15)

Lohman, R. and McGuire, J. (2007). Earthquake swarms driven by aseismic creep in the Salton Trough, California. *Journal of Geophysical Research : Solid Earth*, 112(B4). (page 44)

Long, J. and Imber, J. (2012). Strain compatibility and fault linkage in relay zones on normal faults. *Journal of Structural Geology*, 36 :16–26. (page 44)

Lyon-Caen, H., Papadimitriou, P., Deschamps, A., Bernard, P., Makropoulos, K., Pacchiani, F., and Patau, G. (2004). First results of the {CRLN} seismic network in the western Corinth Rift : evidence for old-fault reactivation. *Comptes Rendus Geoscience*, 336(4–5) :343–351. (page 33, 59)

Madariaga, R. (1976). Dynamics of an expanding circular fault. *Bulletin of the Seismological Society of America*, 66(3) :639–666. (page 151, 158)

Martini, P. D., Pantosti, D., Palyvos, N., Lemeille, F., McNeill, L., and Collier, R. (2004). Slip rates of the Aigion and Eliki faults from uplifted marine terraces, Corinth Gulf, Greece. *Comptes Rendus Geoscience*, 336(4–5) :325–334. (page 31)

Matthews, M. and Reasenberg, P. (1988). Statistical methods for investigating quiescence and other temporal seismicity patterns. *Pure and Applied Geophysics*, 126(2) :357–372. (page 20)

McGarr, A., Bekins, B., Burkardt, N., Dewey, J., Earle, P., Ellsworth, W., Ge, S., Hickman, S., Holland, A., Majer, E., et al. (2015). Coping with earthquakes induced by fluid injection. *Science*, 347(6224) :830–831. (page 18)

McKenzie, D. (1970). Plate tectonics of the mediterranean region. *Nature*, 226(5242) :239–243. (page 26)

McNeill, L., Collier, R., De Martini, P., Pantosti, D., and D'Addezio, G. (2005a). Recent history of the Eastern Eliki Fault, Gulf of Corinth : geomorphology, palaeoseismology and impact on palaeoenvironments. *Geophysical Journal International*, 161(1) :154–166. (page 30)

McNeill, L., Cotterill, C., Henstock, T., Bull, J., Stefatos, A., Collier, R., Papatheoderou, G., Ferentinos, G., and Hicks, S. (2005b). Active faulting within the offshore western Gulf of Corinth, Greece : implications for models of continental rift deformation. *Geology*, 33(4) :241–244. (page 30)

Melbourne, T., Webb, F., Stock, J., and Reigber, C. (2002). Rapid postseismic transients in subduction zones from continuous GPS. *Journal of Geophysical Research : Solid Earth*, 107(B10). (page 15)

Métivier, L., de Viron, O., Conrad, C., Renault, S., Diament, M., and Patau, G. (2009). Evidence of earthquake triggering by the solid earth tides. *Earth and Planetary Science Letters*, 278(3) :370–375. (page 7)

Miyazaki, S., Segall, P., Fukuda, J., and Kato, T. (2004). Space time distribution of afterslip following the 2003 Tokachi-oki earthquake : Implications for variations in fault zone frictional properties. *Geophysical Research Letters*, 31(6). (page 15)

Miyazawa, M. (2011). Propagation of an earthquake triggering front from the 2011 Tohoku-oki earthquake. *Geophysical Research Letters*, 38(23). (page 21)

Miyazawa, M. and Mori, J. (2006). Evidence suggesting fluid flow beneath Japan due to periodic seismic triggering from the 2004 Sumatra-Andaman earthquake. *Geophysical Research Letters*, 33(5). (page 109)

Moretti, I., Sakellariou, D., Lykousis, V., and Micarelli, L. (2003). The Gulf of Corinth : an active half graben ? *Journal of Geodynamics*, 36(1–2) :323–340. (page 31, 32, 34, 45, 58, 135)

Mulargia, F. and Bizzarri, A. (2014). Anthropogenic triggering of large earthquakes. *Scientific Reports*, 4. (page 147)

Nadeau, R. and Johnson, L. (1998). Seismological studies at parkfield vi : Moment release rates and estimates of source parameters for small repeating earthquakes. *Bulletin of the Seismological Society of America*, 88(3) :790–814. (page 86)

Nadeau, R. and McEvilly, T. (1999). Fault slip rates at depth from recurrence intervals of repeating microearthquakes. *Science*, 285(5428) :718–721. (page 17, 18)

Niu, F., Silver, P., Nadeau, R., and McEvilly, T. (2003). Migration of seismic scatterers associated with the 1993 Parkfield aseismic transient event. *Nature*, 426(6966) :544. (page 18)

Nocquet, J.-M. (2012). Present-day kinematics of the Mediterranean : A comprehensive overview of GPS results. *Tectonophysics*, 579 :220–242. (page 26)

Nomikou, P., Alexandri, M., Lykousis, V., Sakellariou, D., and Ballas, D. (2011). Swath bathymetry and morphological slope analysis of the Corinth Gulf. In *Earthquake Geology and Archaeology : Science, Society and Critical Facilities. 2nd INQUA-IGCP-567 International Workshop on Active Tectonics, Earthquake Geology, Archeology and Engineering*, pages 19–24. (page 29, 31)

Nur, A. and Booker, J. (1972). Aftershocks caused by pore fluid flow ? *Science*, 175(4024) :885–887. (page 21, 147)

Obara, K. (2002). Nonvolcanic deep tremor associated with subduction in southwest Japan. *Science*, 296(5573) :1679–1681. (page 15)

Ohta, Y., Freymueller, J., Hreinsdóttir, S., and Suito, H. (2006). A large slow slip event and the depth of the seismogenic zone in the south central Alaska subduction zone. *Earth and Planetary Science Letters*, 247(1) :108–116. (page 15)

Olson, E. and Allen, R. (2005). The deterministic nature of earthquake rupture. *Nature*, 438(7065) :212. (page 134)

Omori, F. (1894). On after-shocks. *Rep. Imp. Earthquake Inv. Corn.*, 2 :103–138. (page 16, 19, 84)

Ori, G. (1989). Geologic history of the extensional basin of the Gulf of Corinth (? miocene-pleistocene), Greece. *Geology*, 17(10) :918–921. (page 28, 32)

Ozawa, S., Murakami, M., and Tada, T. (2001). Time-dependent inversion study of the slow thrust event in the nankai trough subduction zone, southwestern Japan. *Journal of Geophysical Research : Solid Earth*, 106(B1) :787–802. (page 15)

Pacchiani, F. (2006). *Étude sismologique des failles normales actives du Rift de Corinthe*. PhD thesis, Université Paris 11, Orsay. (page 32, 33)

Pacchiani, F. and Lyon-Caen, H. (2010). Geometry and spatio-temporal evolution of the 2001 Agios Ioanis earthquake swarm (Corinth Rift, Greece). *Geophysical Journal International*, 180(1) :59–72. (page 44, 49, 58, 67, 76, 88, 111, 135)

Palyvos, N., Lemeille, F., Sorel, D., Pantosti, D., and Pavlopoulos, K. (2008). Geomorphic and biological indicators of paleoseismicity and Holocene uplift rate at a coastal normal fault footwall (western Corinth Gulf, Greece). *Geomorphology*, 96(1) :16–38. (page 59)

Palyvos, N., Pantosti, D., De Martini, P., Lemeille, F., Sorel, D., and Pavlopoulos, K. (2005). The Aigion–Neos Erineos coastal normal fault system (western Corinth Gulf Rift, Greece) : Geomorphological signature, recent earthquake history, and evolution. *Journal of Geophysical Research : Solid Earth*, 110(B9). (page 30, 31, 34, 45, 59, 88, 93, 135)

Pankow, K., Arabasz, W., Pechmann, J., and Nava, S. (2004). Triggered seismicity in Utah from the 3 November 2002 Denali fault earthquake. *Bulletin of the Seismological Society of America*, 94(6B) :S332–S347. (page 127)

Pantosti, D., De Martini, P., Koukouvelas, I., Stamatopoulos, L., Palyvos, N., Pucci, S., Lemeille, F., and Pavlides, S. (2004). Palaeoseismological investigations of the Aigion Fault (Gulf of Corinth, Greece). *Comptes Rendus Geoscience*, 336(4) :335–342. (page 32)

Papazachos, V., Papazachos, B., Papazachou, C., and Papazachou, K. (1997). *The earthquakes of Greece*. Editions Ziti. (page 26, 33, 34, 45, 92)

Parcharidis, I., Kourkouli, P., Karymbalis, E., Foumelis, M., and Karathanassi, V. (2011). Time series synthetic aperture radar interferometry for ground deformation monitoring over a small scale tectonically active deltaic environment (Mornos, Central Greece). *Journal of Coastal Research*, 29(2) :325–338. (page 92)

Parotidis, M., Rothert, E., and Shapiro, S. (2003). Pore-pressure diffusion : A possible triggering mechanism for the earthquake swarms 2000 in Vogtland/NW-Bohemia, central Europe. *Geophysical Research Letters*, 30(20). (page 52)

Parotidis, M., Shapiro, S., and Rothert, E. (2004). Back front of seismicity induced after termination of borehole fluid injection. *Geophysical Research Letters*, 31(2). (page 51)

Parsons, T. (2005). A hypothesis for delayed dynamic earthquake triggering. *Geophysical Research Letters*, 32(4). (page 108, 126)

Peng, Z., Gonzalez-Huizar, H., Chao, K., Aiken, C., Moreno, B., and Armstrong, G. (2013). Tectonic tremor beneath Cuba triggered by the Mw 8.8 maule and Mw 9.0 Tohoku-oki earthquakes. *Bulletin of the Seismological Society of America*, 103(1) :595–600. (page 109)

Peng, Z., Walter, J., Aster, R., Nyblade, A., Wiens, D., and Anandakrishnan, S. (2014). Antarctic icequakes triggered by the 2010 Maule earthquake in Chile. *Nature Geoscience*, 7(9) :677–681. (page 109)

Perfettini, H., Avouac, J.-P., Tavera, H., Kositsky, A., Nocquet, J.-M., Bondoux, F., Chlieh, M., Sladen, A., Audin, L., Farber, D., et al. (2010). Seismic and aseismic slip on the Central Peru megathrust. *Nature*, 465(7294) :78. (page 15)

Perissoratis, C., Mitropoulos, D., and Angelopoulos, I. (1986). Marine geological research at the eastern Corinthiakos Gulf. *Geological and Geophysical Research, Special Issue*, pages 381–401. (page 33)

Perouse, E., Chamot-Rooke, N., Rabaute, A., Briole, P., Jouanne, F., Georgiev, I., and Dimitrov, D. (2012). Bridging onshore and offshore present-day kinematics of central and eastern Mediterranean : implications for crustal dynamics and mantle flow. *Geochemistry, Geophysics, Geosystems*, 13(9). (page 27)

Pham, V., Bernard, P., Boyer, D., Chouliaras, G., Le Mouël, J., and Stavrakakis, G. (2000). Electrical conductivity and crustal structure beneath the central Hellenides around the Gulf of Corinth (Greece) and their relationship with the seismotectonics. *Geophysical Journal International*, 142(3) :948–969. (page 158)

Pirazzoli, P., Stiros, S., Fontugne, M., and Arnold, M. (2004). Holocene and Quaternary uplift in the central part of the southern coast of the Corinth Gulf (Greece). *Marine Geology*, 212(1–4) :35–44. (page 31)

Poupinet, G., Ellsworth, W., and Frechet, J. (1984). Monitoring velocity variations in the crust using earthquake doublets : An application to the Calaveras Fault, California. *Journal of Geophysical Research : Solid Earth*, 89(B7) :5719–5731. (page 17)

Prejean, S., Hill, D., Brodsky, E., Hough, S., Johnston, M., Malone, S., Oppenheimer, D., Pitt, A., and Richards-Dinger, K. (2004). Remotely triggered seismicity on the United States west coast following the Mw 7.9 Denali fault earthquake. *Bulletin of the Seismological Society of America*, 94(6B) :S348–S359. (page 21, 108, 128)

Protti, M., González, V., Kato, T., Iinuma, T., Miyazaki, S., Obana, K., Kaneda, Y., La Femina, P., Dixon, T., and Schwartrz, S. (2004). A creep event on the shallow interface of the Nicoya Peninsula, Costa Rica seismogenic zone. In *AGU Fall Meeting Abstracts*. (page 15)

Reverso, T., Marsan, D., and Helmstetter, A. (2015). Detection and characterization of transient forcing episodes affecting earthquake activity in the Aleutian Arc system. *Earth and Planetary Science Letters*, 412 :25–34. (page 199)

Rietbrock, A., Tiberi, C., Scherbaum, F., and Lyon-Caen, H. (1996). Seismic slip on a low angle normal fault in the Gulf of Corinth : Evidence from high-resolution cluster analysis of microearthquakes. *Geophysical Research Letters*, 23(14) :1871–1820. (page 33, 67)

Rigo, A., Lyon-Caen, H., Armijo, R., Deschamps, A., Hatzfeld, D., Makropoulos, K., Papadimitriou, P., and Kassaras, I. (1996). A microseismic study in the western part of the Gulf of Corinth (Greece) : implications for large-scale normal faulting mechanisms. *Geophysical Journal International*, 126(3) :663–688. (page 33, 34, 35, 46, 59, 60, 65, 92)

Ring, U., Glodny, J., Will, T., and Thomson, S. (2010). The Hellenic subduction system : high-pressure metamorphism, exhumation, normal faulting, and large-scale extension. *Annual Review of Earth and Planetary Sciences*, 38 :45–76. (page 26)

Rogers, G. and Dragert, H. (2003). Episodic tremor and slip on the Cascadia subduction zone : The chatter of silent slip. *Science*, 300(5627) :1942–1943. (page 15, 16)

Rohais, S. (2007). *Architecture stratigraphique et flux sédimentaires sur la marge sud du golfe de Corinthe (Grèce) : Analyse de terrain, modélisations expérimentales et numériques*. PhD thesis, Université Rennes 1. (page 30, 58)

Roland, E. and McGuire, J. (2009). Earthquake swarms on transform faults. *Geophysical Journal International*, 178(3) :1677–1690. (page 52, 96)

Ruff, L. (1999). Dynamic stress drop of recent earthquakes : Variations within subduction zones. *pure and applied geophysics*, 154(3-4) :409–431. (page 147)

Ruhl, C., Abercrombie, R., Smith, K., and Zaliapin, I. (2016). Complex spatiotemporal evolution of the 2008 Mw 4.9 Mogul earthquake swarm (Reno, Nevada) : Interplay of fluid and faulting. *Journal of Geophysical Research : Solid Earth*, 121(11) :8196–8216. (page 199, 200)

Rybicki, K. (1973). Analysis of aftershocks on the basis of dislocation theory. *Physics of the Earth and Planetary Interiors*, 7(4) :409–422. (page 19)

Rydelek, P. and Horiuchi, S. (2006). Is earthquake rupture deterministic ? *Nature*, 442(7100) :E5–E5. (page 148)

Sachpazi, M., Clément, C., Laigle, M., Hirn, A., and Roussos, N. (2003). Rift structure, evolution, and earthquakes in the Gulf of Corinth, from reflection seismic images. *Earth and Planetary Science Letters*, 216(3) :243–257. (page 31)

Sacks, I., Suyehiro, S., Linde, A., and Snoke, J. (1982). Stress redistribution and slow earthquakes. *Tectonophysics*, 81(3-4) :311–318. (page 14)

Sato, T. and Hirasawa, T. (1973). Body wave spectra from propagating shear cracks. *Journal of Physics of the Earth*, 21(4) :415–431. (page 151)

Satriano, C., Mejia Uquiche, A., and Saurel, J.-M. (2016). Spectral estimation of seismic moment, corner frequency and radiated energy for earthquakes in the lesser antilles. In *AGU Fall Meeting Abstracts*. (page 61, 136, 142, 151)

Schaff, D., Bokelmann, G., Ellsworth, W., Zanzerkia, E., Waldhauser, F., and Beroza, G. (2004). Optimizing correlation techniques for improved earthquake location. *Bulletin of the Seismological Society of America*, 94(2) :705–721. (page 63)

Schaff, D. and Waldhauser, F. (2005). Waveform cross-correlation-based differential travel-time measurements at the Northern California Seismic Network. *Bulletin of the Seismological Society of America*, 95(6) :2446–2461. (page 63, 100)

Schlagenhauf, A., Manighetti, I., Malavieille, J., and Dominguez, S. (2008). Incremental growth of normal faults : Insights from a laser-equipped analog experiment. *Earth and Planetary Science Letters*, 273(3) :299–311. (page 93)

Scholz, C. (2002). *The mechanics of earthquakes and faulting*. Cambridge University Press. (page 48, 52)

Segall, P. and Davis, J. (1997). GPS applications for geodynamics and earthquake studies. *Annual Review of Earth and Planetary Sciences*, 25(1) :301–336. (page 37)

Serpetsidaki, A., Elias, P., Ilieva, M., Bernard, P., Briole, P., Deschamps, A., Lambotte, S., Lyon-Caen, H., Sokos, E., and Tselentis, G.-A. (2014). New constraints from seismology and geodesy on the $M_W = 6.4$ 2008 movri (Greece) earthquake : Evidence for a growing strike-slip fault system. *Geophysical Journal International*, 198(3) :1373–1386. (page 110, 120, 121)

Shapiro, S., Huenges, E., and Borm, G. (1997). Estimating the crust permeability from fluid-injection-induced seismic emission at the KTB site. *Geophysical Journal International*, 131(2) :F15–F18. (page 44, 49, 50)

Shaw, B. (2009). Constant stress drop from small to great earthquakes in magnitude-area scaling. *Bulletin of the Seismological Society of America*, 99(2A) :871–875. (page 143)

Shimazaki, K. and Nakata, T. (1980). Time-predictable recurrence model for large earthquakes. *Geophysical Research Letters*, 7(4) :279–282. (page 13, 19)

Shimojo, K., Enescu, B., Yagi, Y., and Takeda, T. (2014). Fluid-driven seismicity activation in northern Nagano region after the 2011 M9.0 Tohoku-oki earthquake. *Geophysical Research Letters*, 41(21) :7524–7531. (page 21)

Sibson, R. (1982). Fault zone models, heat flow, and the depth distribution of earthquakes in the continental crust of the United States. *Bulletin of the Seismological Society of America*, 72(1) :151–163. (page 21)

Sibson, R. (1986). Brecciation processes in fault zones : inferences from earthquake rupturing. *Pure and Applied Geophysics*, 124(1-2) :159–175. (page 147)

Sibson, R. (1992). Implications of fault-valve behaviour for rupture nucleation and recurrence. *Tectonophysics*, 211(1–4) :283–293. (page 21, 22, 53)

Smith, S. and Van de Lindt, W. (1969). Strain adjustments associated with earthquakes in southern California. *Bulletin of the Seismological Society of America*, 59(4) :1569–1589. (page 19)

Sokal, R. (1958). A statistical method for evaluating systematic relationship. *University of Kansas science bulletin*, 28 :1409–1438. (page 69)

Sokos, E., Zahradník, J., Gallovič, F., Serpetsidaki, A., Plicka, V., and Kiratzi, A. (2016). Asperity break after 12 years : The Mw 6.4 2015 Lefkada (Greece) earthquake. *Geophysical Research Letters*, 43(12) :6137–6145. (page 110, 116)

Sokos, E., Zahradník, J., Kiratzi, A., Janskỳ, J., Gallovič, F., Novotny, O., Kostelecký, J., Serpetsidaki, A., and Tselentis, G.-A. (2012). The January 2010 Efpalio earthquake sequence in the western Corinth Gulf (Greece). *Tectonophysics*, 530 :299–309. (page 59, 74, 94, 111, 121, 127, 128)

Sorel, D. (2000). A Pleistocene and still-active detachment fault and the origin of the Corinth-Patras rift, Greece. *Geology*, 28(1) :83–86. (page 32, 34)

Stark, M. and Davis, S. (1996). Remotely triggered microearthquakes at the Geysers geothermal field, California. *Geophysical research letters*, 23(9) :945–948. (page 128)

Stefanos, A., Papatheodorou, G., Ferentinos, G., Leeder, M., and Collier, R. (2002). Seismic reflection imaging of active offshore faults in the Gulf of Corinth : their seismotectonic significance. *Basin Research*, 14(4) :487–502. (page 58, 135)

Stein, R., Barka, A., and Dieterich, J. (1997). Progressive failure on the North Anatolian fault since 1939 by earthquake stress triggering. *Geophysical Journal International*, 128(3) :594–604. (page 19)

Stein, R. and Lisowski, M. (1983). The 1979 Homestead Valley earthquake sequence, California : Control of aftershocks and postseismic deformation. *Journal of Geophysical Research : Solid Earth*, 88(B8) :6477–6490. (page 19)

Tanaka, S., Ohtake, M., and Sato, H. (2002). Evidence for tidal triggering of earthquakes as revealed from statistical analysis of global data. *Journal of Geophysical Research : Solid Earth*, 107(B10). (page 7)

Taylor, B., Weiss, J., Goodliffe, A., Sachpazi, M., Laigle, M., and Hirn, A. (2011). The structures, stratigraphy and evolution of the Gulf of Corinth rift, Greece. *Geophysical Journal International*, 185(3) :1189–1219. (page 34, 59, 89)

Taymaz, T., Jackson, J., and McKenzie, D. (1991). Active tectonics of the north and central Aegean Sea. *Geophysical Journal International*, 106(2) :433–490. (page 33)

Tsuruoka, H., Ohtake, M., and Sato, H. (1995). Statistical test of the tidal triggering of earthquakes : contribution of the ocean tide loading effect. *Geophysical Journal International*, 122(1) :183–194. (page 7)

Utsu, T., Ogata, Y., and Matsu'ura, R. (1995). The centenary of the omori formula for a decay law of aftershock activity. *Journal of Physics of the Earth*, 43(1) :1–33. (page 16)

Valoroso, L., Chiaraluce, L., and Collettini, C. (2014). Earthquakes and fault zone structure. *Geology*, 42(4) :343–346. (page 44)

Velasco, A., Hernandez, S., Parsons, T., and Pankow, K. (2008). Global ubiquity of dynamic earthquake triggering. *Nature Geoscience*, 1(6) :375–379. (page 21, 118)

Vidale, J., Ellsworth, W., Cole, A., Marone, C., et al. (1994). Variations in rupture process with recurrence interval in a repeated small earthquake. *Nature*, 368(6472) :624–626. (page 17)

Vidale, J. and Shearer, P. (2006). A survey of 71 earthquake bursts across southern California : Exploring the role of pore fluid pressure fluctuations and aseismic slip as drivers. *Journal of Geophysical Research : Solid Earth*, 111(B5). (page 16, 21)

Vita-Finzi, C. (1993). Evaluating late Quaternary uplift in Greece and Cyprus. *Geological Society, London, Special Publications*, 76(1) :417–424. (page 58)

Vorobieva, I., Narteau, C., Shebalin, P., Beauducel, F., Nercessian, A., Clouard, V., and Bouin, M.-P. (2013). Multiscale mapping of completeness magnitude of earthquake catalogs. *Bulletin of the Seismological Society of America*, 103(4) :2188–2202. (page 203, 204)

Vorobieva, I., Shebalin, P., and Narteau, C. (2016). Break of slope in earthquake size distribution and creep rate along the San Andreas Fault system. *Geophysical Research Letters*, 43(13) :6869–6875. (page 204, 208)

Waldhauser, F. and Ellsworth, W. (2000). A double-difference earthquake location algorithm : Method and application to the northern Hayward Fault, California. *Bulletin of the Seismological Society of America*, 90(6) :1353–1368. (page 61, 64)

Waldhauser, F., Ellsworth, W., Schaff, D., and Cole, A. (2004). Streaks, multiplets, and holes : High-resolution spatio-temporal behavior of Parkfield seismicity. *Geophysical Research Letters*, 31(18). (page 44)

Waldhauser, F. and Schaff, D. (2008). Large-scale relocation of two decades of northern California seismicity using cross-correlation and double-difference methods. *Journal of Geophysical Research : Solid Earth*, 113(B8). (page 61, 64)

Wells, D. and Coppersmith, K. (1994). New empirical relationships among magnitude, rupture length, rupture width, rupture area, and surface displacement. *Bulletin of the Seismological Society of America*, 84(4). (page 52)

Wesnousky, S. (2006). Predicting the endpoints of earthquake ruptures. *Nature*, 444(7117) :358–360. (page 134)

West, M., Sánchez, J., and McNutt, S. (2005). Periodically triggered seismicity at Mount Wrangell, Alaska, after the Sumatra earthquake. *Science*, 308(5725) :1144–1146. (page 109)

Wiemer, S. (2001). A software package to analyze seismicity : ZMAP. *Seismological Research Letters*, 72(3) :373–382. (page 20)

Wilcock, W. (2001). Tidal triggering of microearthquakes on the Juan de Fuca Ridge. *Geophysical Research Letters*, 28(20) :3999–4002. (page 7)

Yagi, Y., Kikuchi, M., and Nishimura, T. (2003). Co-seismic slip, post-seismic slip, and largest aftershock associated with the 1994 Sanriku-haruka-oki, Japan, earthquake. *Geophysical Research Letters*, 30(22). (page 15)

Yamashina, K. (1978). Induced earthquakes in the Izu Peninsula by the Izu-hanto-oki earthquake of 1974, Japan. *Tectonophysics*, 51(3-4) :139–154. (page 19)

Yamashita, T. (1998). Simulation of seismicity due to fluid migration in a fault zone. *Geophysical Journal International*, 132(3) :674–686. (page 147)

Zahradnik, J., Gallovic, F., Sokos, E., Serpetsidaki, A., and Tselentis, A. (2008). Quick fault-plane identification by a geometrical method : Application to the Mw 6.2 Leonidio earthquake, 6 January 2008, Greece. *Seismological Research Letters*, 79(5) :653–662. (page 121)

Zaliapin, I. and Ben-Zion, Y. (2013). Earthquake clusters in southern California I : Identification and stability. *Journal of Geophysical Research : Solid Earth*, 118(6) :2847–2864. (page 199, 200)

Zaliapin, I., Gabrielov, A., Keilis-Borok, V., and Wong, H. (2008). Clustering analysis of seismicity and aftershock identification. *Physical Review Letter*, 101 :018501. (page 199)

Zigone, D., Rivet, D., Radiguet, M., Campillo, M., Voisin, C., Cotte, N., Walpersdorf, A., Shapiro, N., Cougoulat, G., Roux, P., et al. (2012). Triggering of tremors and slow slip event in Guerrero, Mexico, by the 2010 Mw 8.8 Maule, Chile, earthquake. *Journal of Geophysical Research : Solid Earth*, 117(B9). (page 109)

Annexe A

The 2003–2004 seismic swarm in the western Corinth rift : evidence for a multiscale pore pressure diffusion process along a permeable fault system

A.1 Article and supplementary information

AGU PUBLICATIONS

Geophysical Research Letters

RESEARCH LETTER
10.1002/2015GL065298

Key Points:
- Multiplets reveal details on multiscale fault structure and permeability
- Microseismicity is triggered by pore pressure migration, with marginal creep
- Fault intersection with a brittle geological layer creates a permeable corridor

Supporting Information:
- Readme
- Movie S1
- Figure S1a
- Figure S1b
- Table S1

Correspondence to:
C. Duverger,
duverger@ipgp.fr

Citation:
Duverger, C., M. Godano, P. Bernard, H. Lyon-Caen, and S. Lambotte (2015), The 2003–2004 seismic swarm in the western Corinth rift: Evidence for a multiscale pore pressure diffusion process along a permeable fault system, *Geophys. Res. Lett.*, *42*, doi:10.1002/2015GL065298.

Received 9 JUL 2015
Accepted 11 AUG 2015
Accepted article online 14 AUG 2015

The 2003–2004 seismic swarm in the western Corinth rift: Evidence for a multiscale pore pressure diffusion process along a permeable fault system

Clara Duverger[1], Maxime Godano[1], Pascal Bernard[1], Hélène Lyon-Caen[2], and Sophie Lambotte[3]

[1]Institut de Physique du Globe de Paris, Sorbonne Paris Cité, Univ. Paris Diderot, UMR7154 CNRS, Paris, France, [2]Laboratoire de Géologie, École Normale Supérieure, Member of PSL Research University, UMR8538 CNRS, Paris, France, [3]Institut de Physique du Globe de Strasbourg, UMR7516 CNRS, EOST/Université de Strasbourg, France

Abstract Microseismic multiplets occurring in the western Corinth rift, Greece, during a large swarm are analyzed to retrieve their spatiotemporal characteristics. These multiplets activated small subfaults at depth (~7 km), up to 1 km long, at the root of two parallel active normal faults. The swarm migrates westward nearly horizontally over 10 km at an average velocity of 50 m/d with a diffusivity of 0.5 m^2 s^{-1}. It successively activates the Aigion fault, a relay zone in its hanging wall, and the Fassouleika fault. Within each multiplet, hypocenters also migrate with diffusivities ranging from 0.001 to 0.4 m^2 s^{-1}. The largest internal diffusivities appear at the core of the layer defined by the clusters. These results are interpreted as a hydroshear process caused by pore pressure migration within permeable corridors resulting from the intersection of the major faults with a brittle geological layer inherited from the Hellenic nappe stack.

1. Introduction

The characterization of the structure of active fault zones is essential for understanding earthquake nucleation, dynamic rupture, and fault evolution and can thus contribute to quantify the probability of major earthquake triggering. Our knowledge of fault zone structure and properties is mostly provided by geological and geomorphological studies based on direct observations of exhumed faults [e.g., *Allen*, 2005] and drilling projects that intersect active faults at depths [e.g., *Janssen et al.*, 2014; *Cornet et al.*, 2004]. Other inferences are obtained through indirect observations based on geophysical studies such as seismic reflection profiles [e.g., *Long and Imber*, 2012; *Bell et al.*, 2008] and tomographic investigations [e.g., *Allam and Ben-Zion*, 2012; *Latorre et al.*, 2004]. In particular, in the last decade, hypocentral locations of clustered events with double-difference techniques described the complex geometry of faults at depth, with a high-resolution [e.g., *Waldhauser et al.*, 2004; *Valoroso et al.*, 2014; *Lambotte et al.*, 2014]. Adding the temporal information to the spatial distribution allows studying the mechanical processes at work within fault systems during the migration of seismic swarms. In numerous cases, such migrations are associated with aseismic creep [e.g., *Lohman and McGuire*, 2007]. In other cases, fluid circulations at depth are invoked to explain spatiotemporal variations of the seismicity, as for induced earthquakes due to man-made pore pressure perturbations [*Shapiro et al.*, 1997; *Hainzl*, 2004]. Whether the controlling factor of a given seismic swarm is transient creep or pore pressure, their mutual cross-triggering and coupling with microseismicity is expected to produce complex mechanical processes [e.g., *Bourouis and Bernard*, 2007]. As these phenomena are controlled by the geometry, permeability, and frictional properties of the faults, often poorly known, a better understanding of the role of the fault zone structure on seismic and aseismic activities is a challenging issue.

These questions are addressed here with the detailed analysis of the 2003–2004 microseismic sequence that occurred in the western Corinth rift, Greece. We assume that the pore pressure mainly controls the observed swarm activity, as proposed by *Pacchiani and Lyon-Caen* [2010] for the nearby 2001 swarm. In this study, we first present the tectonic context and the data along with the tools used for characterizing the geometry of the multiplets and the seismicity diffusion process. We then present the global activated structures, in relationship with major faults, followed by our interpretation of the multiscale space-time evolution of the activity in terms of pore pressure migration. We finally discuss the inferred permeable channels and the pore pressure source.

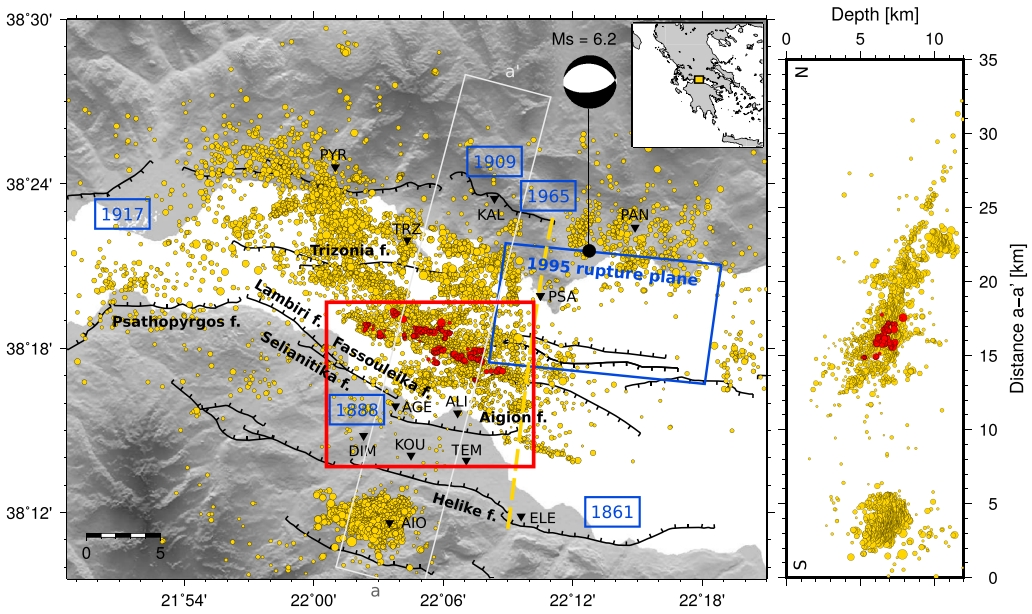

Figure 1. Map and vertical section of historical earthquakes and microseismicity between 2000 and 2007. Microseismicity (circles) was recorded by the network CRLNET (black triangles) and relocated by *Lambotte et al.* [2014]. Red circles represent the studied microearthquakes occurring in 2003–2004. The yellow dashed line locates the microseismicity transition between the highly seismic western zone and the quiescent eastern zone. Historical earthquakes (blue framed dates) are from *Papazachos et al.* [1997] and *Bernard et al.* [1997]. Focal mechanism is from *Bernard et al.* [1997]. Main active faults have been compiled by *Moretti et al.* [2003], *Palyvos et al.* [2005], *Bell et al.* [2008], and M. Ford (personal communication, 2014). The red box corresponds to the map of Figure 2.

2. Seismotectonics and Seismological Data

The Corinth rift is a highly active seismic region, with six earthquakes of magnitude $M_S > 6$ during the last century, all related to major normal faults developed by the back-arc extension of the Hellenic subduction and the dextral shear of the North Anatolian Fault [e.g., *Armijo et al.*, 1996; *Palyvos et al.*, 2005]. In the western rift, the last damaging earthquake occurred in 1995 ($M = 6.2$ [*Bernard et al.*, 1997]) and activated a low-angle, north dipping blind normal fault beneath the Gulf. On the southern coast, the last large earthquakes were felt in 1861 and 1888 [*Papazachos et al.*, 1997; *Boiselet*, 2014], respectively, activating the north dipping Helike and Aigion faults (Figure 1). Revisiting and integrating instrumental and historical earthquakes, *Boiselet* [2014] finds that there is around 50% chance to expect a $M_S > 6$ in the next 30 years in this region.

A permanent dense seismic network with 12 short-period three-component stations, the Corinth Rift Laboratory Network (CRLNET), has been installed since the years 2000–2001 in the western part of the rift. It has recorded about 10,000 earthquakes per year with $M_W > 1.0$ [*RESIF*, 2014], and the activity is strongly clustered in time and space (http://crlab.eu/). The swarms last days to months and extend from 1 to 10 km long, so that the daily seismicity rate ranges from 10 events per day in quiet periods to several hundreds during swarms. A clear drop in microseismicity rate is observed to the east, delimited by a NS discontinuity in the fault system (Figure 1). This discontinuity has the same strike as the Hellenic nappe stack [*Jolivet et al.*, 2010] inherited from the convergence tectonics, that constitutes the upper 5–10 km of the crust.

Recently, a detailed analysis of the microseismicity (multiplet identification, double-difference hypocenter relocation, and focal mechanism determination) between 2000 and 2007 in the western rift has revealed the complex internal structure of the main microseismic, 1–3 km thick brittle layer, that gently dips to the north between 5 and 9 km depth [*Lambotte et al.*, 2014; *Godano et al.*, 2014], questioning the original model of a major, crustal detachment proposed by *Rigo et al.* [1996]. This multiplet database, with highly correlated waveforms, provides the opportunity to better understand the fault zone structure and the seismic-aseismic coupling processes during swarms.

Here we focus on the largest swarm (October 2003 to June 2004) in which 24 multiplets were recorded, with more than seven events in each of them (Figure 2). They consist of 411 earthquakes, with magnitudes up to

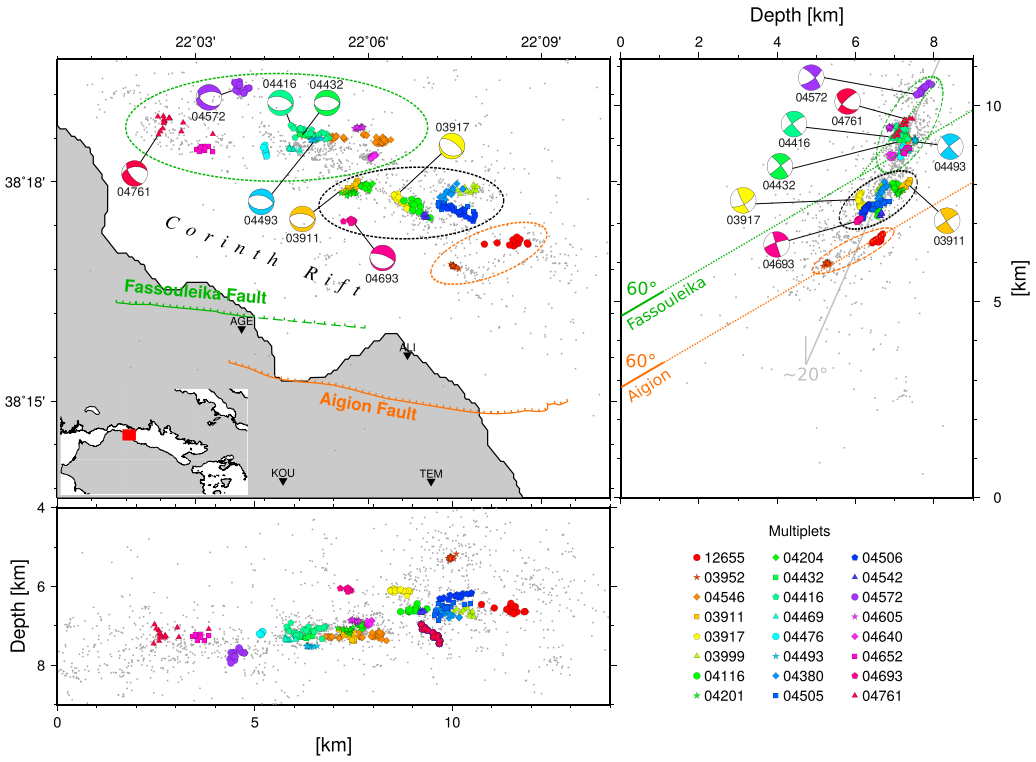

Figure 2. Map, EW, and NS vertical sections of the 2003–2004 swarm. The 24 main multiplets have specific colored symbols. The background microseismicity is represented as gray dots. The Aigion and Fassouleika faults dipping about 60° at surface are the two main structures illuminated at depth by, respectively, 2 (dashed orange ellipses) and 11 (dashed green ellipses) multiplets. A third structure (dashed black ellipses) between these faults is highlighted by the remaining multiplets and assimilated to a relay zone. Focal mechanisms are from *Godano et al.* [2014].

2.9 (b value $\simeq$ 1.2), located at a depth of about 7 km, within the main seismic layer (Figure 1). Their absolute location error is less than 1 km, and their relative one is about 10 m [*Lambotte et al.*, 2014]. Composite focal mechanisms for multiplets have been determined by jointly inverting the P polarities with the Sv/P, Sh/P, and Sv/Sh amplitude ratios of direct waves [*Godano et al.*, 2014].

3. Multiplet Geometry and Pore Pressure Changes

The geometry of the 24 multiplets (length, thickness, and orientation of the best fitting plane) was defined by calculating ellipsoids containing 95% of earthquakes. The methodology is described in the supporting information and Table S1 reports the results.

We calculated the internal diffusivity of each multiplet by assuming a pore pressure diffusion process and analyzing the spatiotemporal variations of seismicity. Based on Darcy's law and poroelasticity with a viscous fluid, the pore pressure perturbation p due to high-pressure fluid intrusion in the rock mass can be described by the diffusion's equation:

$$\frac{\partial p}{\partial t} = D\nabla^2 p \tag{1}$$

where D is the hydraulic diffusivity, typically ranging between 0.01 and 10 $m^2\ s^{-1}$ in the Earth's crust [*Scholz*, 2002] and proportional to the permeability. When applied to seismicity induced by a transient injection of fluid from a point-like source, and considering a homogeneous isotropic medium, the distance (radius) d to the diffusing pressure front triggering the seismicity can be approximated by

$$d = \sqrt{4\pi D t} \tag{2}$$

where t is the relative start time of the injection [*Shapiro et al.*, 1997].

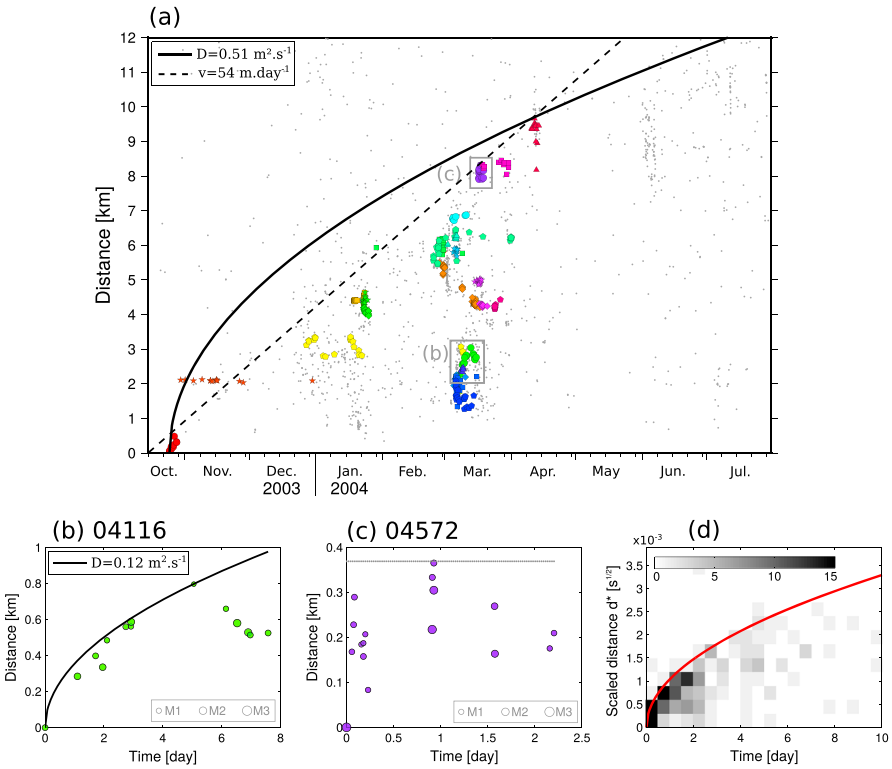

Figure 3. Microseismicity migration. (a) Distance-time graph considering the first event of the 2003–2004 crisis as the spatial origin. Colored symbols indicate the events of the 24 main multiplets. Gray dots show the background microseismicity. The black curve represents the theoretical diffusion law (equation (2)) with a diffusivity of 0.51 m^2 s^{-1}. The dotted line shows a constant migration velocity of 54 m/d. (b) Example of diffusion (04116 multiplet). (c) Example of fast activations (04572 multiplet). (d) Space-time event density for the 18 multiplets associated with a diffusion law, considering the first event of each multiplet as the origin. For each multiplet i with diffusivity D_i, the y axis is defined by $d^* = d/\sqrt{D_i} = \sqrt{4\pi t}$.

The application of this model to natural earthquakes is, however, not straightforward because (1) the location of fluid source and its geometry is unknown and (2) earthquakes must occur at an early stage of the pore pressure diffusion to resolve the time dependence of the radius as $\sqrt{t}$ [*Pacchiani and Lyon-Caen*, 2010]. The initial propagation of pore pressure could be seismically silent. Here diffusion coefficients are estimated considering the first event of the multiplet as an injection point and assuming an isotropic pore pressure diffusion. This starting point approximates the place of first fracturation, connecting the fluid reservoir to the activated faults.

4. Results

4.1. Fault and Multiplet Location

In the following we show, with the joint analysis of multiplet location, geometry, and focal mechanisms, that the swarm is mostly related to the activation of the two parallel north dipping normal faults of Aigion and Fassouleika, outcropping on the southern coast of the rift. First, the southern border of the large microseismically active zone (Figure 1) matches at depth the youngest Lambiri-Selianitica-Fassouleika-Aigion fault system [*Lambotte et al.*, 2014]. On a smaller scale (Figure 2), the first and easternmost two multiplets (12655 and 03952) are located in the downdip continuity of the Aigion fault, near its eastern edge, considering the reported dip angle of 50–60° inferred from the AIG10 borehole [*Cornet et al.*, 2004] and the 2000–2007 microseismicity [*Lambotte et al.*, 2014]. The westernmost multiplets (04761 and 04652) are coincident with the downdip continuity of the onland Fassouleika fault scarp assuming a similar dip angle. Eastward, the location of eight multiplets with similar normal focal mechanisms and depths shows a tight alignment with the two previous ones, potentially outlying an eastward, yet unmapped, off-shore extension of the Fassouleika fault. Eleven other multiplets appear to be located in between the above clusters, showing a complex geometry of the

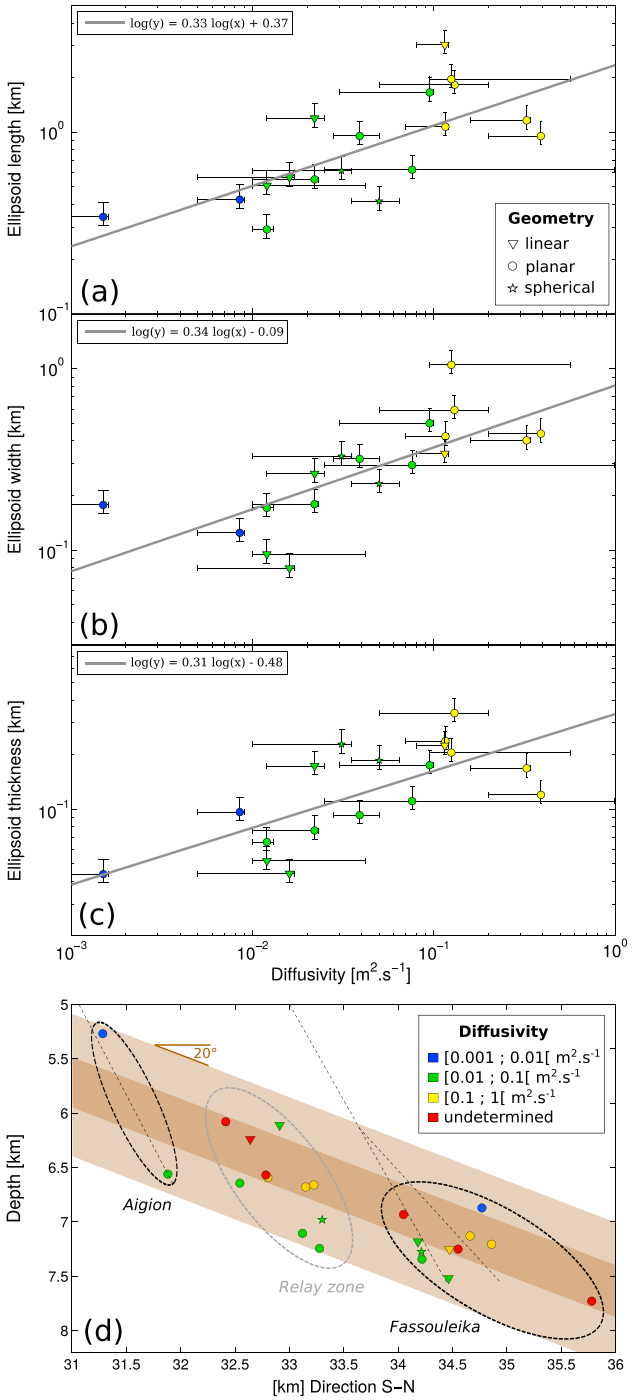

Figure 4. Relation between intradiffusivity, dimensions, and location of multiplets. (a) Ellipsoid length, (b) width, and (c) thickness of multiplets versus intradiffusivity of multiplets in log-log scale. (d) Multiplet mean location in depth along the SN section. Undetermined diffusivities (red) correspond to the six multiplets showing nearly simultaneous ruptures along large distances. They reflect fast phenomena assimilated to very high diffusivities. High diffusivities (red-yellow) are concentrated in a 400 m thick, ~20° dipping layer (dark brown) central to the microseismogenic zone (light brown).

Aigion-Fassouleika (AF) fault system at depth and suggesting the activation of a relay zone between these two en echelon faults. These events seem to draw a third fault zone, with similar dip and azimuth as the AF fault system.

The 2003–2004 multiplets are located within the large-scale microseismic layer identified by *Lambotte et al.* [2014] at the intersection with the AF fault system. Considering that (1) the planar 04572 multiplet about 1.5 km north of the main structure has a ~45° dipping plane, (2) the normal focal mechanisms of the Fassouleika multiplets show dip angles slightly lowering with depth, from 60° to 50° [*Godano et al.*, 2014], and (3) no microseismicity is reported beneath the seismogenic layer [*Lambotte et al.*, 2014], we propose that the AF fault system roots in this layer. The complexity and the thickness of the multiplet structures (Table S1) would then be consistent with the broadening of the fault damage zone at its root [*Kim et al.*, 2004].

4.2. Migration of the Microseismic Activity

4.2.1. Along and Across Fault Migration

The spatiotemporal analysis of microseismicity shows an overall migration from ESE to WNW at around 50 m/d, as already estimated by *Bourouis and Cornet* [2009]. This globally westward (over 10 km) and slightly downward (1 km) migration highlights the successive activation of the Aigion fault, of the relay zone, and of the Fassouleika fault. The swarm starts with the easternmost 12655 multiplet and first propagates upward along the Aigion fault to the 03952 multiplet. The latter, tightly clustered and breaking the same patch of 50 m diameter [*Duverger*, 2014], remains active during a whole month, suggesting repeater-like behavior, and thus some aseismic creep. The activity then jumped a few kilometers to the WNW, 500 m within the hanging wall. From then on, small migrations started from central to western multiplets within the relay zone, whereas the main migration continued northwestward, activating multiplets on the Fassouleika fault. The illumination of the central multiplets on the latter led to a backpropagation of activity to the eastern multiplets of the relay zone, whereas the main migration reached the western end of the Fassouleika fault (Movie S1). From equation (2) [*Shapiro et al.*, 1997] the global diffusivity is about 0.5 $m^2\ s^{-1}$ for the whole seismic crisis (Figure 3a), but one notes a better fit with simple constant migration velocity. The latter could be favored by an increased permeability of the fault zone resulting from its dilatancy during the creep [e.g., *Cappa*, 2009] induced near the pore pressure front.

4.2.2. Small-Scale Migration on Subfaults

At a smaller scale, we could estimate the internal diffusivity for 18 of the 24 multiplets (Figures 3b, 3d, and S1). The six remaining multiplets (04432, 04505, 04506, 04572, 04640, and 04693) show nearly simultaneous distant ruptures (Figures 3c and S1), so that no diffusion law could be adjusted to them. The estimated diffusivity values range between 0.001 and 0.4 $m^2\ s^{-1}$ (Table S1) and present a positive correlation (cubic root scaling trend) with the multiplet dimension, as shown in Figures 4a–4c. We also note that for the subfaults, the diffusivity pressure front triggers most of the activity during 2–3 days (Figure 3d), providing a possible evidence for a back front [*Parotidis et al.*, 2004].

Internal diffusivity was then jointly analyzed with the geometry and location of multiplets (Figure 4d). Using fitting ellipsoids and their aspect ratios, 18 multiplets are defined "planar," 5 "linear," and 2 "spherical" (see Text S1 for details). With this classification, the geometry does not seem to be correlated with the intradiffusivity or the multiplet epicentral position. However, on a SN vertical section, multiplets with high diffusivities ($\geq$ 0.1 $m^2\ s^{-1}$), or with nearly simultaneous activations, are concentrated within the core of the microseismic layer, along a thin band about 400 m thick, dipping 20°, whereas multiplets with lower diffusivities ($<$ 0.1 $m^2\ s^{-1}$) are above or below this band.

5. Discussion

5.1. Origin and Diffusion Mode of the Fluids

The global and intramultiplet diffusivities (0.5 $m^2\ s^{-1}$ and 0.001–0.4 $m^2\ s^{-1}$, respectively) are typical values of fluid diffusion found in fault zone contexts at crustal depth [*Scholz*, 2002]. In the geothermal Vogtlang/Bohemia region, *Parotidis et al.* [2003] report similar space-time swarm patterns, modeled with a diffusivity of 0.27 $m^2\ s^{-1}$. In Corinth rift, the migration velocity of 50 m/d (~2 m/h) compares with that of a pore pressure front diffusion [e.g., *Chen et al.*, 2012] but is significantly smaller than that estimated for creeping faults, on the order of 100–1000 m/h [e.g., *Roland and McGuire*, 2009]. However, the multiplets found with nearly simultaneous distant ruptures suggest stress transfer or creep propagation. There is thus some evidence for marginal local creep or earthquake triggering by stress transfer, but the global swarm activity appears to be dominantly fluid driven.

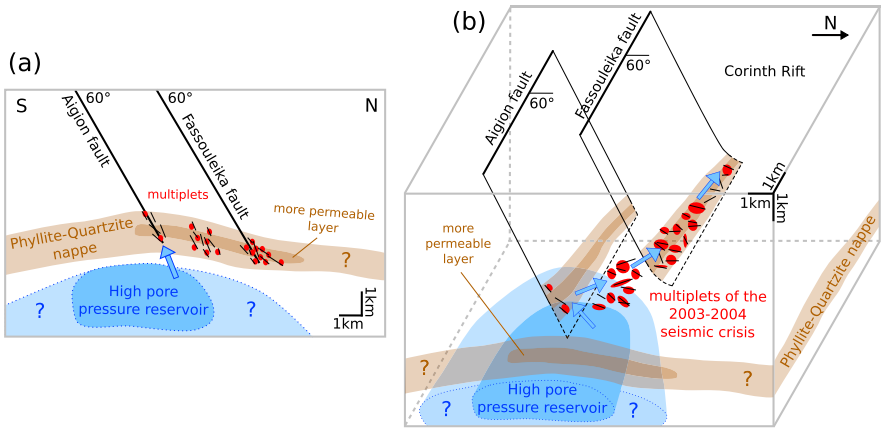

Figure 5. Sketch of proposed mechanisms for the 2003–2004 swarm. (a) SN section. (b) Three-dimensional view. The intersection of a Hellenic nappe with the AF system creates permeable corridors allowing the microseismicity diffusion forced by a deep capped high pore pressure reservoir. A fault-valve behavior [*Sibson*, 1992] may initiate the seismic crisis.

A few processes can lead to a slow build up of pore pressure at large crustal depths. A meteoric water overpressure effect is proposed by [*Bourouis and Cornet*, 2009] for the 2003–2004 swarm. However, our observation of an upward propagation of the seismicity in the early stage (from 12655 multiplet to 03952 multiplet) updip the Aigion fault contradicts this hypothesis. The overpressurized reservoir is thus probably at depth, fed either by upgoing mantellic fluids produced by the African subducting plate 50 km beneath the rift (as proposed by *Bourouis and Cornet* [2009] for the 2001 swarm) or by metamorphic processes within phyllosilicate-rich rocks in the seismogenic zone which may release structural water by dehydration reactions [*Latorre et al.*, 2004].

Whatever the process for a slow pore pressure increase near the root of the fault system, it has eventually led to large-scale hydroshear processes on preexisting faults, triggering the detected microseismicity. These processes were possibly accompanied by transient creep, as was reported for Soultz [*Bourouis and Bernard*, 2007]. This large-scale fracturation along several successive 0.1 to 1 km subfaults, is expected to have increased the local permeabilities within the fault system, which may explain the persistence of a large migration velocity.

5.2. Fault Zone Structure and the Geological Seismogenic Layer

The detailed multiplet geometries provide new insights on the AF fault system. Our proposed system, consisting of two main subparallel en echelon normal faults both dipping around 50–60°, provides the simplest explanation of the multiplet activity. The termination depth of both faults also fits standard values of aspect ratio (fault length-to-width ratio) [*Wells and Coppersmith*, 1994], with a 8–10 km length and 8–10 km width. Considering a Fassouleika fault restricted onland, a more complex fault model might also be proposed in which the northeastern multiplets mark the south dipping Trizonia fault at depth, consistent with the nodal planes of focal mechanisms (within 15° dip angle).

At subfault scale, the cubic root dependence of the multiplet size with its diffusion coefficient suggests that the larger the multiplet is, the higher the degree of fracturation is, increasing the permeability. This may arise from scale-dependent permeabilities [*Guéguen et al.*, 1996], as larger fractured rock volumes statistically sample more permeable paths. The reported highly fractured permeable layer, around 400 m thick, centered within the microseismically active layer, may be the core part of a thicker (1–2 km) brittle geological layer of the Hellenic nappe stack [*Jolivet et al.*, 2010]. Indeed, according to *Latorre et al.* [2004], the regional velocity change at 5–7 km depth seen from seismic tomography data could correspond to the tectonic contact between the karstic Gravrovo-Tripolitza limestone and the low-permeability Phyllite-Quartzite geological series. The latter, called Phyllade nappe, consists of phyllites, schists, and quartzites with local intercalation of metavolcanic rocks [*Koukouvelas and Papoulis*, 2009]. *Latorre et al.* [2004] emphasized that the specific characteristic of this geological unit, as well as its depth, may explain the seismicity concentration at about 6–8 km depth. Our study then strongly suggests that the intersection of the AF system with this layer produces a fractured zone building a long narrow permeable corridor in a low-permeability bulk, explaining the 1-D pore pressure migration. The presence of a higher diffusivity in the core of this layer might be enhanced by the fault terminations, as faults tips are generally associated with high damage zones.

5.3. High Pore Pressure Reservoir

The tomographic images by *Gautier et al.* [2006] also show a high $\frac{Vp}{Vs}$ anomalous zone at 8–9 km close to the bottom of the microseismic layer near the root of the Aigion fault, possibly revealing the top of a high pore pressure reservoir. This interpretation requires that the bulk of the geological layer sitting on top is impermeable and acts as a cap, except, temporarily along the channels created by the cross-cutting faults.

A schematic diagram (Figure 5) shows our interpretation of the mechanisms involved during the 2003–2004 swarm. We propose that slow changes of either strain or fluid pore pressure conditions near the deep fault system eventually reached a strength limit leading to a sudden permeability increase. This would create a hydraulic connection between a deeper reservoir, capped by the Phyllade nappe, and the bottom of the Aigion fault plane, following a process similar to the fault-valve model of *Sibson* [1992]. The pore pressure migration would then have continued along the most permeable paths, in the fractured corridor built within the geological layer and maintained by the seismic cycle of the AF fault system.

6. Conclusion

The detailed analysis of the multiplets activated around 7 km in depth during the 2003–2004 seismic swarm in the western Corinth rift reveals a hydromechanical process, involving the migration of a pore pressure transient over 10 km along a complex, permeable, and fractured structure. It reaches an average velocity of 50 m/d and a diffusivity of 0.5 $m^2\ s^{-1}$. This structure is defined by the intersection of two major normal faults with a deep low-permeability geological layer, possibly the Phyllade nappe. The highest local diffusivities, appearing in the core of the seismic layer, can be related to the largest subfault structures defined by the multiplets, and to the highest damage near the tip of the fault. The high $\frac{Vp}{Vs}$ region imaged by tomography below the main seismic layer is most likely a signal of high pore fluid pressure. This reservoir, capped by an impermeable layer, would be sporadically connected to the root of the faults above by sudden permeability changes of fractured channels. The pore pressure source, as well as the amount of aseismic creep in the area, still have to be investigated in more detail, in particular for quantifying their potential to trigger a large earthquake on the AF system. More refined tomographic images along with new studies of the most recent swarms in this area are still needed for a better characterization and quantification of the permeable paths and of the fluid pressure sources. Finally, this multiscale, high-resolution approach of natural microseismicity diffusion is also relevant for the study of microseismicity induced by man-made fluid injection, bringing valuable information on fault structure and permeabilities, useful for production and safety purpose.

Acknowledgments

Seismic data used in this study were collected by CRLNET (Corinth Rift Laboratory NETwork, http://crlab.eu), which has been supported by the INSU CNRS in France, by the European Community through REAKT project, and by the Agence Nationale de la Recherche with the SISCOR project. We thank two anonymous reviewers for their constructive suggestions and comments that improved this manuscript.

The Editor thanks two anonymous reviewers for their assistance in evaluating this paper.

References

Allam, A. A., and Y. Ben-Zion (2012), Seismic velocity structures in the Southern California plate-boundary environment from double-difference tomography, *Geophys. J. Int.*, *190*(2), 1181–1196, doi:10.1111/j.1365-246X.2012.05544.x.

Allen, J. L. (2005), A multi-kilometer pseudotachylyte system as an exhumed record of earthquake rupture geometry at hypocentral depths (Colorado, USA), *Tectonophysics*, *402*(1–4), 37–54, doi:10.1016/j.tecto.2004.10.017.

Armijo, R., B. Meyer, G. C. P. King, A. Rigo, and D. Papanastassiou (1996), Quaternary evolution of the Corinth Rift and its implications for the Late Cenozoic evolution of the Aegean, *Geophys. J. Int.*, *126*(1), 11–53, doi:10.1111/j.1365-246X.1996.tb05264.x.

Bell, R. E., L. C. McNeill, J. M. Bull, and T. J. Henstock (2008), Evolution of the offshore western Gulf of Corinth, *Geol. Soc. Am. Bull.*, *120*(1–2), 156–178, doi:10.1130/B26212.1.

Bernard, P., et al. (1997), The $M_s = 6.2$, June 15, 1995 Aigion earthquake (Greece): Evidence for low angle normal faulting in the Corinth rift, *J. Seismol.*, *1*(2), 131–150, doi:10.1023/A:1009795618839.

Boiselet, A. (2014), Cycle sismique et aléa sismique d'un réseau de failles actives: Le cas du rift de Corinthe (Grèce), PhD thesis, École Normale Supérieure de, Paris, Institut de Radioprotection et de Sureté Nucléaire.

Bourouis, S., and P. Bernard (2007), Evidence for coupled seismic and aseismic fault slip during water injection in the geothermal site of Soultz (France), and implications for seismogenic transients, *Geophys. J. Int.*, *169*(2), 723–732, doi:10.1111/j.1365-246X.2006.03325.x.

Bourouis, S., and F. H. Cornet (2009), Microseismic activity and fluid fault interactions: Some results from the Corinth Rift Laboratory (CRL), Greece, *Geophys. J. Int.*, *178*(1), 561–580, doi:10.1111/j.1365-246X.2009.04148.x.

Cappa, F. (2009), Modelling fluid transfer and slip in a fault zone when integrating heterogeneous hydromechanical characteristics in its internal structure, *Geophys. J. Int.*, *178*(3), 1357–1362, doi:10.1111/j.1365-246X.2009.04291.x.

Chen, X., P. M. Shearer, and R. E. Abercrombie (2012), Spatial migration of earthquakes within seismic clusters in southern California: Evidence for fluid diffusion, *J. Geophys. Res.*, *117*, B04301, doi:10.1029/2011JB008973.

Cornet, F. H., M. L. Doan, I. Moretti, and G. Borm (2004), Drilling through the active Aigion Fault: The AIG10 well observatory, *C. R. Geosci.*, *336*(4–5), 395–406, doi:10.1016/j.crte.2004.02.002.

Duverger, C. (2014), Évolution spatio-temporelle de multiplets microsismiques à la base des failles du rift de Corinthe: Des indices de migrations de fluides, Master's thesis, Institut de Physique du Globe de Paris, École Normale Supérieure de Paris.

Gautier, S., D. Latorre, J. Virieux, A. Deschamps, C. Skarpelos, A. Sotiriou, A. Serpetsidaki, and A. Tselentis (2006), A new passive tomography of the Aigion area (Gulf of Corinth, Greece) from the 2002 data set, *Pure Appl. Geophys.*, *163*(2-3), 431–453, doi:10.1007/s00024-005-0033-7.

Godano, M., A. Deschamps, S. Lambotte, H. Lyon-Caen, P. Bernard, and F. Pacchiani (2014), Focal mechanisms of earthquake multiplets in the western part of the Corinth Rift (Greece): Influence of the velocity model and constraints on the geometry of the active faults, *Geophys. J. Int.*, *197*(3), 1660–1680, doi:10.1093/gji/ggu059.

Guéguen, Y., P. Gavrilenko, and M. Le Ravalec (1996), Scales of rock permeability, *Surv. Geophys.*, *17*(3), 245–263, doi:10.1007/BF01904043.

Hainzl, S. (2004), Seismicity patterns of earthquake swarms due to fluid intrusion and stress triggering, *Geophys. J. Int.*, *159*(3), 1090–1096, doi:10.1111/j.1365-246X.2004.02463.x.

Janssen, C., R. Wirth, H.-R. Wenk, L. Morales, R. Naumann, M. Kienast, S.-R. Song, and G. Dresen (2014), Faulting processes in active faults—Evidences from TCDP and SAFOD drill core samples, *J. Struct. Geol.*, *65*(0), 100–116, doi:10.1016/j.jsg.2014.04.004.

Jolivet, L., L. Labrousse, P. Agard, O. Lacombe, V. Bailly, E. Lecomte, F. Mouthereau, and C. Mehl (2010), Rifting and shallow-dipping detachments, clues from the Corinth rift and the Aegean, *Tectonophysics*, *483*(3–4), 287–304, doi:10.1016/j.tecto.2009.11.001.

Kim, Y.-S., D. C. Peacock, and D. J. Sanderson (2004), Fault damage zones, *J. Struct. Geol.*, *26*(3), 503–517, doi:10.1016/j.jsg.2003.08.002.

Koukouvelas, I., and D. Papoulis (2009), Fluid involvement in the active Helike normal fault, Gulf of Corinth, Greece, *J. Struct. Geol.*, *31*(3), 237–250, doi:10.1016/j.jsg.2008.11.018.

Lambotte, S., H. Lyon-Caen, P. Bernard, A. Deschamps, G. Patau, A. Nercessian, F. Pacchiani, S. Bourouis, M. Drilleau, and P. Adamova (2014), Reassessment of the rifting process in the western Corinth rift from relocated seismicity, *Geophys. J. Int.*, *197*(3), 1822–1844, doi:10.1093/gji/ggu096.

Latorre, D., J. Virieux, T. Monfret, V. Monteiller, T. Vanorio, J.-L. Got, and H. Lyon-Caen (2004), A new seismic tomography of Aigion area (Gulf of Corinth, Greece) from the 1991 data set, *Geophys. J. Int.*, *159*(3), 1013–1031, doi:10.1111/j.1365-246X.2004.02412.x.

Lohman, R. B., and J. J. McGuire (2007), Earthquake swarms driven by aseismic creep in the Salton Trough, California, *J. Geophys. Res.*, *112*, B04405, doi:10.1029/2006JB004596.

Long, J. J., and J. Imber (2012), Strain compatibility and fault linkage in relay zones on normal faults, *J. Struct. Geol.*, *36*, 16–26, doi:10.1016/j.jsg.2011.12.013.

Moretti, I., D. Sakellariou, V. Lykousis, and L. Micarelli (2003), The Gulf of Corinth: An active half graben?, *J. Geodyn.*, *36*(1–2), 323–340, doi:10.1016/S0264-3707(03)00053-X.

Pacchiani, F., and H. Lyon-Caen (2010), Geometry and spatio-temporal evolution of the 2001 Agios Ioanis earthquake swarm (Corinth Rift, Greece), *Geophys. J. Int.*, *180*(1), 59–72, doi:10.1111/j.1365-246X.2009.04409.x.

Palyvos, N., D. Pantosti, P. M. De Martini, F. Lemeille, D. Sorel, and K. Pavlopoulos (2005), The Aigion-Neos Erineos coastal normal fault system (western Corinth Gulf Rift, Greece): Geomorphological signature, recent earthquake history, and evolution, *J. Geophys. Res. Solid Earth*, *110*, B09302, doi:10.1029/2004JB003165.

Papazachos, V., B. Papazachos, C. Papazachou, and K. Papazachou (1997), *The Earthquakes of Greece*, Editions Ziti, Thessaloniki, Greece.

Parotidis, M., E. Rothert, and S. A. Shapiro (2003), Pore-pressure diffusion: A possible triggering mechanism for the earthquake swarms 2000 in Vogtland/NW-Bohemia, central Europe, *Geophys. Res. Lett.*, *30*(20), 2075, doi:10.1029/2003GL018110.

Parotidis, M., S. A. Shapiro, and E. Rothert (2004), Back front of seismicity induced after termination of borehole fluid injection, *Geophys. Res. Lett.*, *31*, L02612, doi:10.1029/2003GL018987.

RESIF (2014), CL - Corinth Rift Laboratory Seismological Network; RESIF - Réseau Sismologique et géodésique Français, doi:10.15778/RESIF.CL.

Rigo, A., H. Lyon-Caen, R. Armijo, A. Deschamps, D. Hatzfeld, K. Makropoulos, P. Papadimitriou, and I. Kassaras (1996), A microseismic study in the western part of the Gulf of Corinth (Greece): Implications for large-scale normal faulting mechanisms, *Geophys. J. Int.*, *126*(3), 663–688, doi:10.1111/j.1365-246X.1996.tb04697.x.

Roland, E., and J. J. McGuire (2009), Earthquake swarms on transform faults, *Geophys. J. Int.*, *178*(3), 1677–1690, doi:10.1111/j.1365-246X.2009.04214.x.

Scholz, C. H. (2002), *The Mechanics of Earthquakes and Faulting*, Cambridge Univ. Press, Cambridge, U. K.

Shapiro, S. A., E. Huenges, and G. Borm (1997), Estimating the crust permeability from fluid-injection-induced seismic emission at the KTB site, *Geophys. J. Int.*, *131*(2), F15–F18, doi:10.1111/j.1365-246X.1997.tb01215.x.

Sibson, R. (1992), Implications of fault-valve behaviour for rupture nucleation and recurrence, *Tectonophysics*, *211*(1–4), 283–293, doi:10.1016/0040-1951(92)90065-E.

Valoroso, L., L. Chiaraluce, and C. Collettini (2014), Earthquakes and fault zone structure, *Geology*, *42*(4), 343–346, doi:10.1130/G35071.1.

Waldhauser, F., W. L. Ellsworth, D. P. Schaff, and A. Cole (2004), Streaks, multiplets, and holes: High-resolution spatio-temporal behavior of Parkfield seismicity, *Geophys. Res. Lett.*, *31*, L18608, doi:10.1029/2004GL020649.

Wells, D. L., and K. J. Coppersmith (1994), New empirical relationships among magnitude, rupture length, rupture width, rupture area, and surface displacement, *Bull. Seismol. Soc. Am.*, *84*(4), 974–1002.

Supporting Information for "The 2003–2004 seismic swarm in the western rift of Corinth: evidence for a multiscale pore pressure diffusion process along a permeable fault system"

Clara Duverger,[1] Maxime Godano,[1] Pascal Bernard,[1] Hélène Lyon-Caen,[2]

and Sophie Lambotte,[3]

Corresponding author: C. Duverger, Institut de Physique du Globe de Paris, 1 rue Jussieu, 75238 Paris Cedex 05, France. (duverger@ipgp.fr)

[1]Institut de Physique du Globe de Paris,

Sorbonne Paris Cité, Univ. Paris Diderot,

UMR7154 CNRS, Paris, France

[2]Laboratoire de Géologie, École Normale

Supérieure, Member of PSL Research

University, UMR8538 CNRS, Paris, France

[3]Institut de Physique du Globe de

Strasbourg, UMR7516 CNRS, EOST /

Univ. de Strasbourg, France

Contents of this file

1. Text S1.
2. Caption for large Table S1.
3. Caption for Movie S1.
4. Caption for large Figure S1.

Additional Supporting Information (Files uploaded separately)

1. Table S1.
2. Movie S1.
3. Figure S1.

Introduction

This supporting information includes a description of the method used to define the geometry of multiplets (Text S1), a figure presenting the spatio-temporal behaviour of the 24 earthquake multiplets (Figure S1), a large table summarizing all the characteristics of the multiplets (Table S1), and a movie showing the microseismic activity between October 2003 and July 2004 (Movie S1).

Text S1.

The geometry of the 24 multiplets was defined by calculating ellipsoids containing 95% of earthquakes. From the ratio between eigen axis lengths (λ_i) of the best-fitting ellipsoid, we classified the multiplets in three groups by setting thresholds L_{ij} [*Asanuma et al.*, 2001]:

1. Linear : $\lambda_2/\lambda_1 < L_{21}$ and $\lambda_3/\lambda_1 < L_{31}$
2. Planar : $\lambda_2/\lambda_1 > L_{21}$ and $\lambda_3/\lambda_1 < L_{31}$

3. Spherical : $\lambda_3/\lambda_1 > L_{31}$

where i and j are the ellipse axes. The critical values L_{ij} are all fixed to 1/4 after a visual pre-analysis of ellipsoid forms. Planar multiplets suggest ruptures along an unique fault plane or an en-echelon globally planar structure. Linear multiplets could be associated to the intersection of two fault planes, and spherical multiplets are assimilated to ruptures on non-coplanar en-echelon structures. The uncertainties on the length of the ellipsoid axes are estimated taking as minimal size (respectively maximal size) the size of the ellipsoid containing 90% (respectively 99%) of earthquakes.

From the eigen vectors of the major and intermediate ellipsoid axes, one can determine the dip and azimuth of the best-fitting plane of the multiplet. The uncertainties on the angles are estimated by randomly perturbing the location of multiplet events by at most 10 m and computing 1,000 new combinations of earthquake multiplets. We took the standard deviation of the resulting dip and azimuth solutions from the mean solutions, assuming a Gaussian distribution.

The results are summarized in the Table S1.

Table S1. CHARACTERISTICS OF THE 24 MULTIPLETS. Mulitplet identification number (ID), number of events, temporal information (starting time, duration [days]), mean location (longitude [°], latitude [°], depth [km]), spatial dimension (ellipsoid major a, intermediate b and minor c axis length [km]), angles of the best-fitting plane (azimuth ϕ [°], dip θ [°]), geometry type, and internal diffusivity D [$\mathrm{m}^2 \cdot \mathrm{s}^{-1}$]. The uncertainties for a parameter "p" are expressed as an acceptable range of values delimited by p_{min} and p_{max}.

Comments: We can see that most of the planar multiplets show small dip and azimuth uncertainties (around 5°) because of the well-constrained multiplet plane. Nearly all horizontal multiplets have a poor resolution in fault azimuth, but this is due to the parametrization which is not relevant in such a case. As expected, linear multiplets often have a poorly constrained dip or azimuth, and spherical multiplets show high uncertainties for dip and azimuth.

The best fitting-plane of multiplets 03911, 04416, 04432, 04572, 04693, and 04761, which are planar, are similar to the fault plane of the focal mechanisms computed by *Godano et al.* [2014] (misfits mean and max respectively of 8° and 20° for the strike, and 14° and 30° for the dip). The two other multiplets 03917 and 04493, which are linear, show a focal mechanism fault plane consistent with the Aigion or Fassouleika fault plane, but their best-fitting plane follows another orientation. This is certainly related to their linear character, for which the determination of a best-fitting plane is not a good feature. However, their major eigen-vector can be used to see if the mulitplet events follow the fault plane solution or define a different non-parallel direction. The 03917-multiplet is within its fault plane (only 3° of misfit), whereas the 04493-multiplet is 19° off the plane. It might indicate that the latter is at the intersection of two different structures.

Movie S1. MICROSEISMIC ACTIVITY. Spatio-temporal evolution of the October 2003 to July 2004 seismic swarm. Background microseismicity is represented as grey dots. Colored circles are multiplet earthquakes related to different fault zones (orange = the Aigion fault, black = the relay zone, green = the Fassouleika fault). The temporal resolution is 1 day.

Comments: We observe a propagation of the microseismicity mainly from ESE to WNW. At smaller scale, we see a back-propagation towards the E whithin the relay zone in March. In the hypothesis of a pore pressure migration, the back-activation of multiplets could be associated to the high pressure reaching a pre-existing high permeability channel within the relay zone. This back-propagation may also be assisted by creep increasing the local permeability. Assuming only stress transfer and no fluid effect implies that the back-propagation occurs on a shadow or destressed zone of the direct propagation towards the W, which appears quite unlikely.

Figure S1. INTERNAL MULTIPLET PORE PRESSURE DIFFUSION. Distance-time graphs considering the first event of the studied multiplet as the spatio-temporal origin and a source injection. Colored symbols are the multiplet events. Black curve is the theorical diffusion law $d = \sqrt{4\pi Dt}$ [*Shapiro et al.*, 1997] with a diffusivity D in $m^2.s^{-1}$ adjusted for each multiplet when possible. The uncertainties on D are estimated by manually adjusting diffusion laws as possible envelops (gray dashed curves) for the spatio-temporal multiplet pattern. The plots without diffusion curves correspond to the 6 multiplets (04432, 04505, 04506, 04572, 04640, 04693) showing fast activations.

References

Asanuma, H., M. Ishimoto, R. H. Jones, W. S. Phillips, and H. Niitsuma (2001), A variation of the collapsing method to delineate structures inside a microseismic cloud, *Bulletin of the Seismological Society of America*, *91*(1), 154–160, doi:10.1785/0120000063.

Godano, M., A. Deschamps, S. Lambotte, H. Lyon-Caen, P. Bernard, and F. Pacchiani (2014), Focal mechanisms of earthquake multiplets in the western part of the Corinth rift (Greece): influence of the velocity model and constraints on the geometry of the active faults, *Geophysical Journal International*, doi:10.1093/gji/ggu059.

Shapiro, S. A., E. Huenges, and G. Borm (1997), Estimating the crust permeability from fluid-injection-induced seismic emission at the ktb site, *Geophysical Journal International*, *131*(2), F15–F18, doi:10.1111/j.1365-246X.1997.tb01215.x.

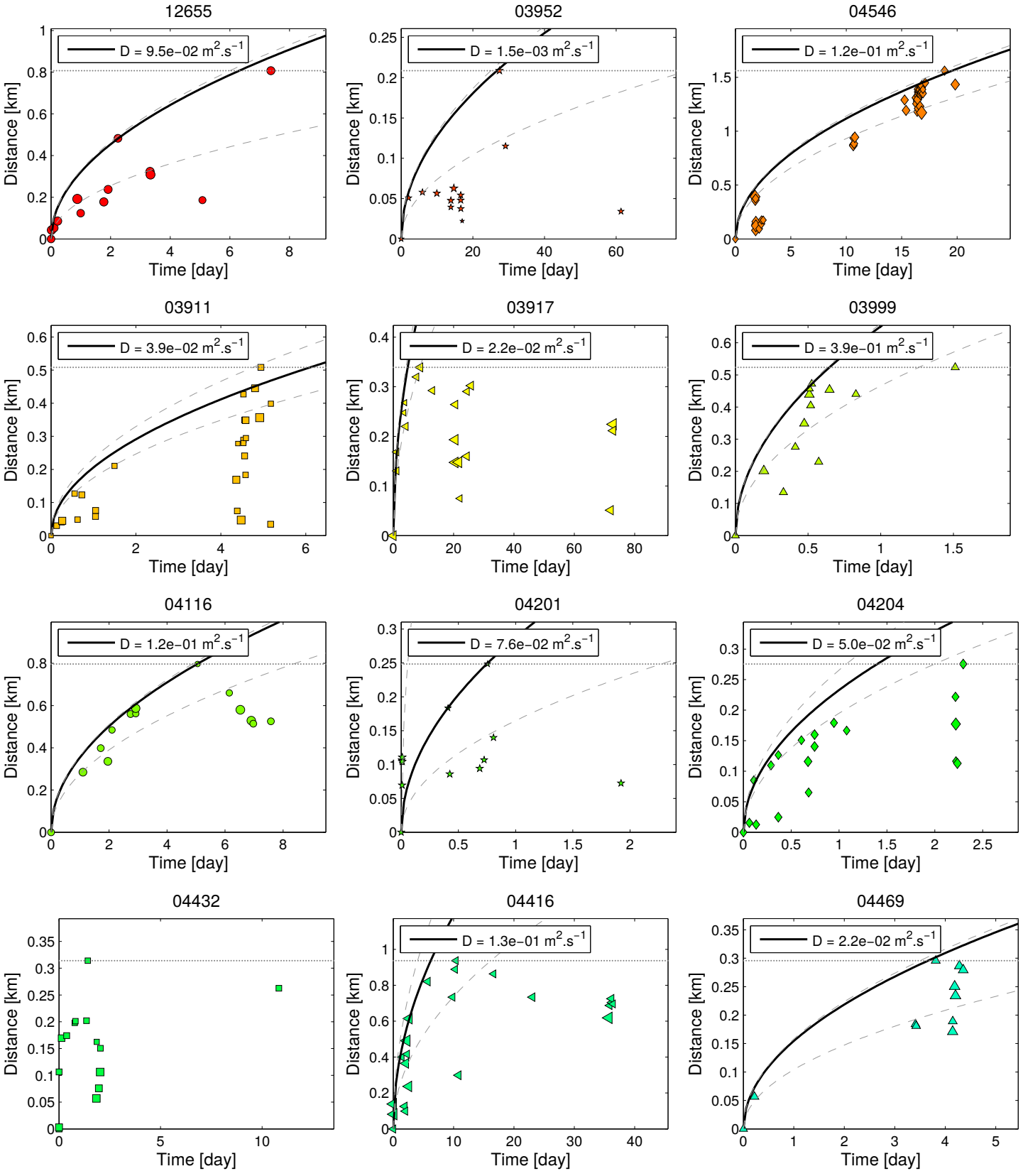
12655
D = 9.5e−02 m².s⁻¹
03952
D = 1.5e−03 m².s⁻¹
04546
D = 1.2e−01 m².s⁻¹
03911
D = 3.9e−02 m².s⁻¹
03917
D = 2.2e−02 m².s⁻¹
03999
D = 3.9e−01 m².s⁻¹
04116
D = 1.2e−01 m².s⁻¹
04201
D = 7.6e−02 m².s⁻¹
04204
D = 5.0e−02 m².s⁻¹
04432
04416
D = 1.3e−01 m².s⁻¹
04469
D = 2.2e−02 m².s⁻¹
Distance [km]
Time [day]

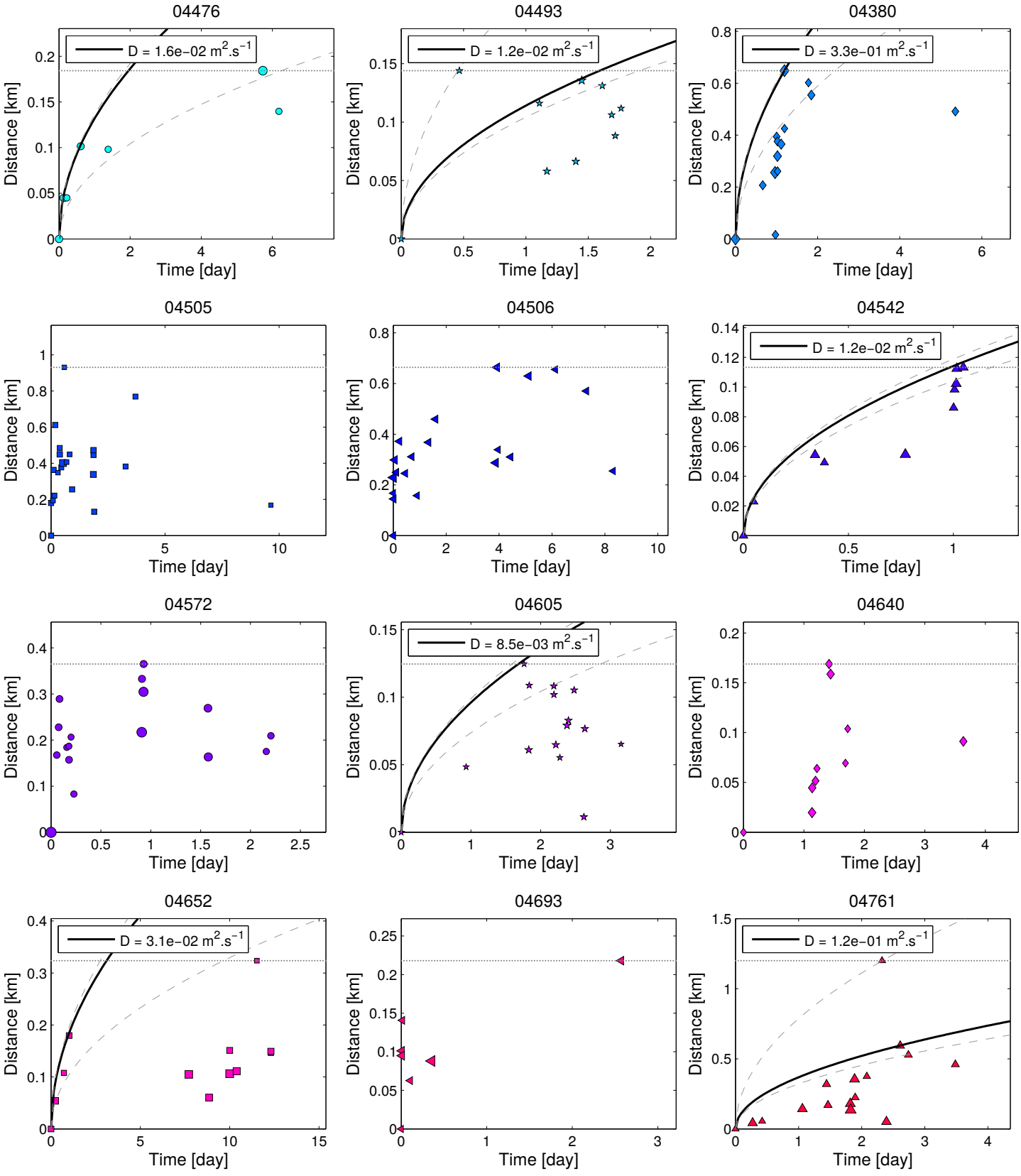
04476
D = 1.6e−02 m².s⁻¹
04493
D = 1.2e−02 m².s⁻¹
04380
D = 3.3e−01 m².s⁻¹
04505
04506
04542
D = 1.2e−02 m².s⁻¹
04572
04605
D = 8.5e−03 m².s⁻¹
04640
04652
D = 3.1e−02 m².s⁻¹
04693
04761
D = 1.2e−01 m².s⁻¹
Distance [km]
Time [day]

A.2 Source dimensions and spatio-temporel evolution of the 2003–2004 multiplets

FIGURE A.1 – Source dimensions of multiplet events projected on the best-fit rupture plane and evolution spatio-temporal. Each pannel is organized with (1) a graph representing the rupture plane of the multiplet with axes oriented along dip and strike. Estimated circular sources of events of the multiplet are projected on this plane. Stars represent the locations of multiplet events, black circles are the average dimensions of event sources, fully colored disks are the minimum dimensions and ligther colored disks represent the maximum dimensions. Two more panels represent the occurrence of events in time along (2) dip and along (3) strike. Box plots indicate the source dimensions along the projected axis with minimum and maximum estimations center on the event location. The errors take into account the dimension and the location uncertainties. For more details on the methodology used, please refer to Duverger [2014]; Godano et al. [2015].

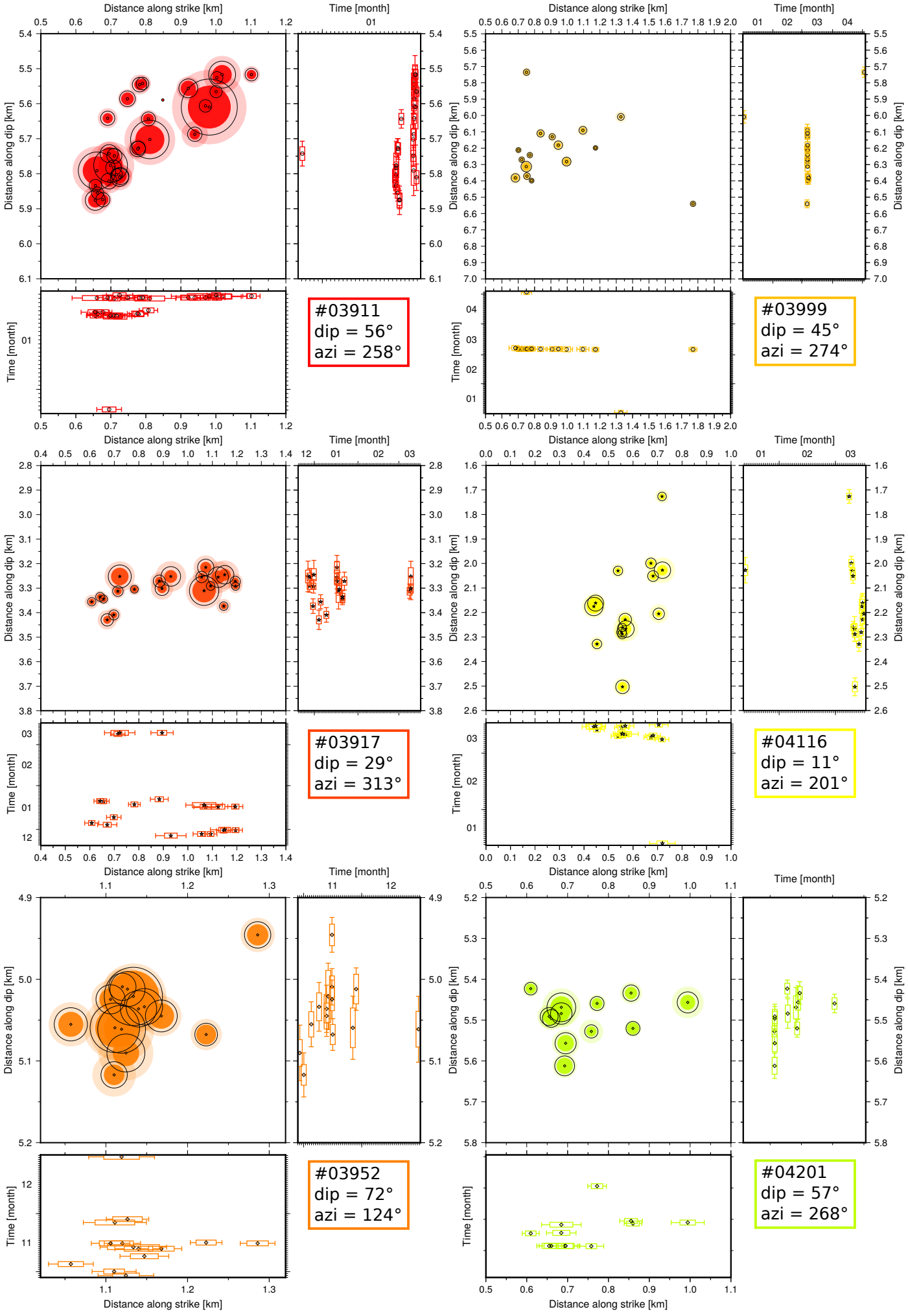
Distance along strike [km]
Time [month]
Distance along dip [km]
#03911
dip = 56°
azi = 258°
#03999
dip = 45°
azi = 274°
#03917
dip = 29°
azi = 313°
#04116
dip = 11°
azi = 201°
#03952
dip = 72°
azi = 124°
#04201
dip = 57°
azi = 268°

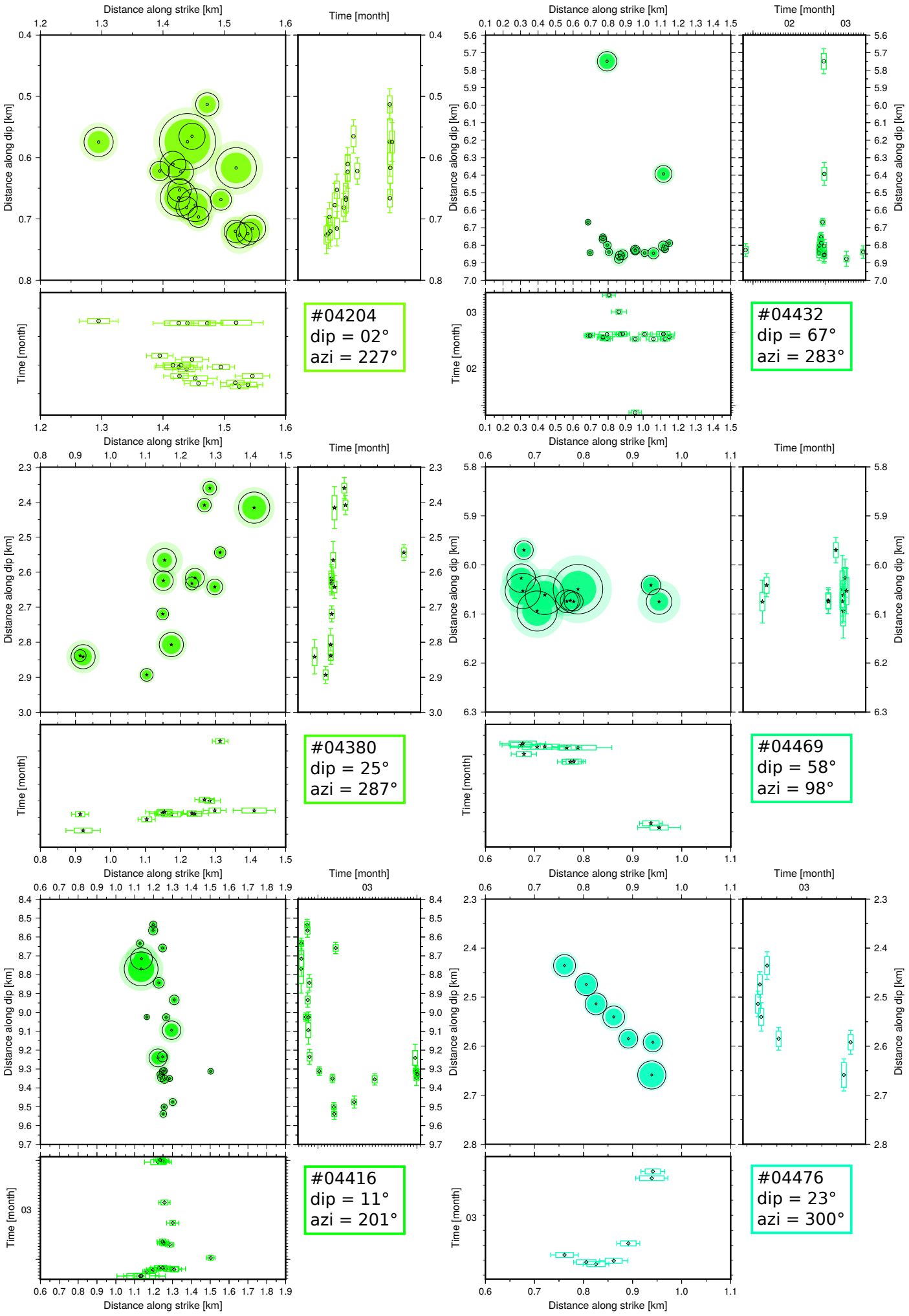
Distance along strike [km]
Time [month]
Distance along dip [km]
#04204
dip = 02°
azi = 227°
#04432
dip = 67°
azi = 283°
#04380
dip = 25°
azi = 287°
#04469
dip = 58°
azi = 98°
#04416
dip = 11°
azi = 201°
#04476
dip = 23°
azi = 300°

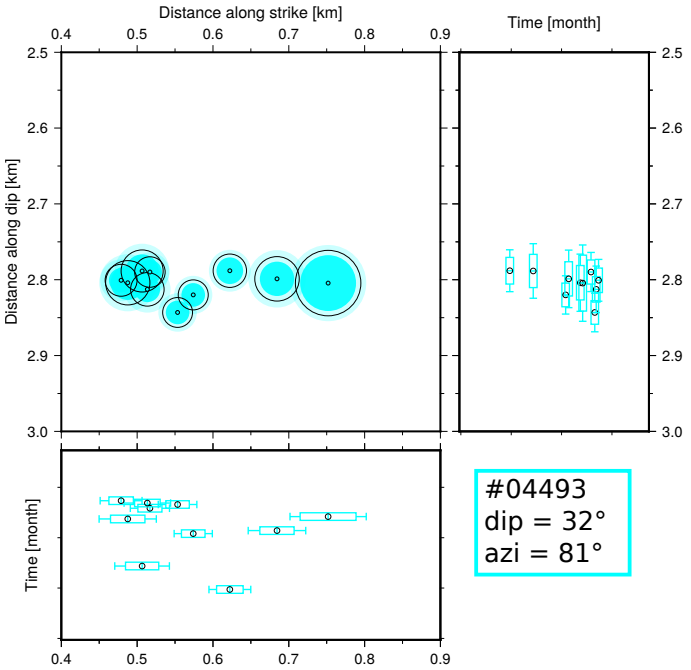
Distance along strike [km]
Time [month]
Distance along dip [km]
Time [month]
#04493
dip = 32°
azi = 81°

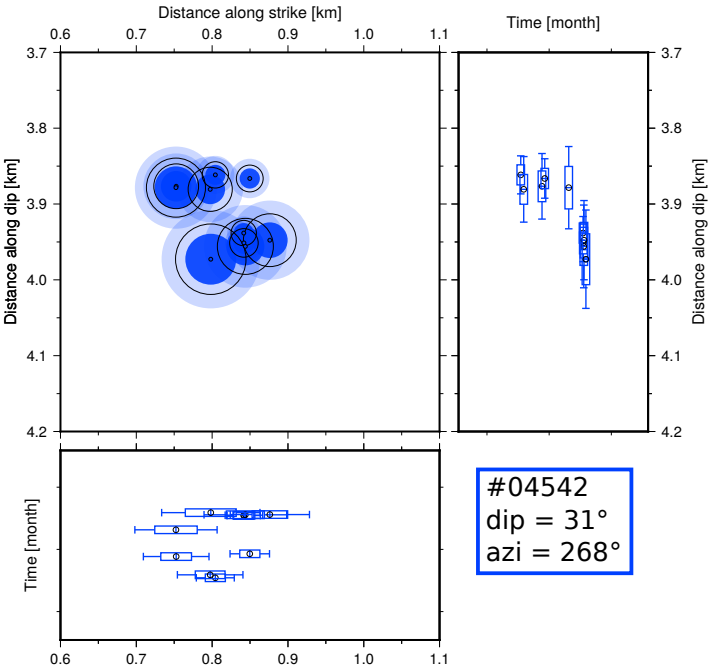
Distance along strike [km]
Time [month]
Distance along dip [km]
Time [month]
#04542
dip = 31°
azi = 268°

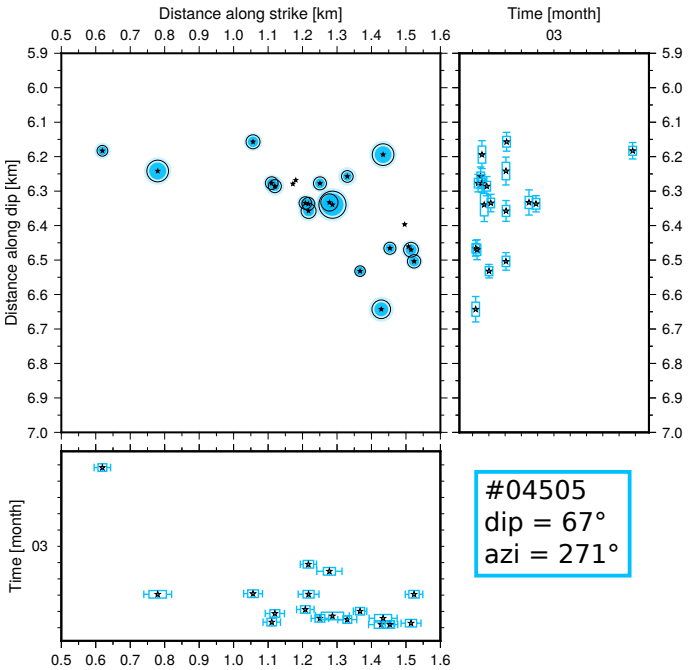
Distance along strike [km]
Time [month]
Distance along dip [km]
Time [month]
#04505
dip = 67°
azi = 271°

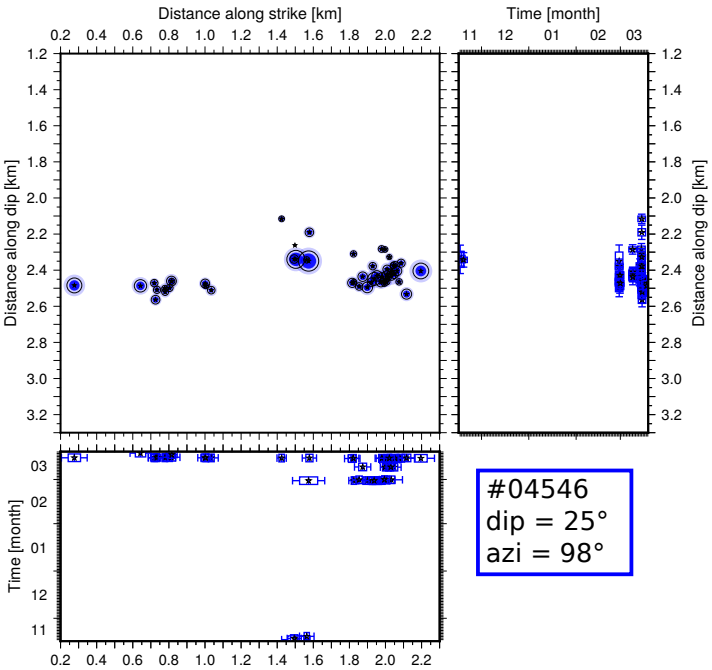
Distance along strike [km]
Time [month]
Distance along dip [km]
Time [month]
#04546
dip = 25°
azi = 98°

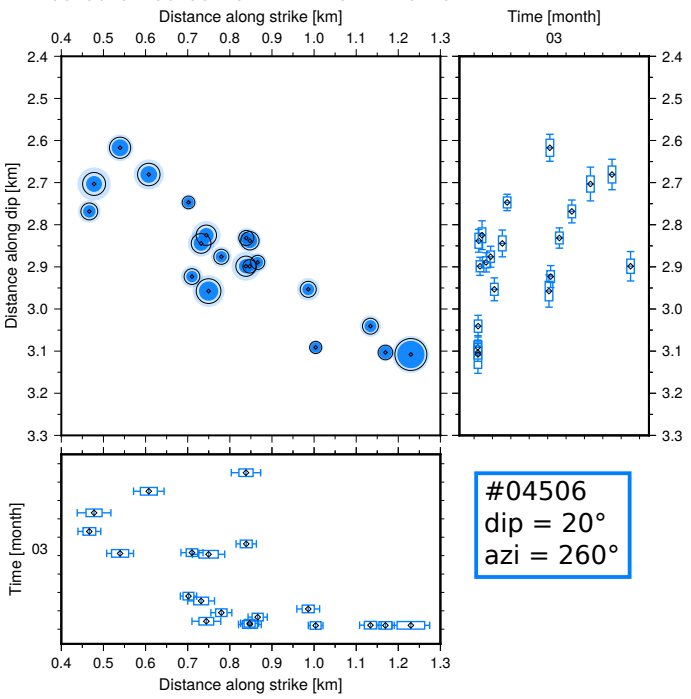
Distance along strike [km]
Time [month]
Distance along dip [km]
Time [month]
#04506
dip = 20°
azi = 260°

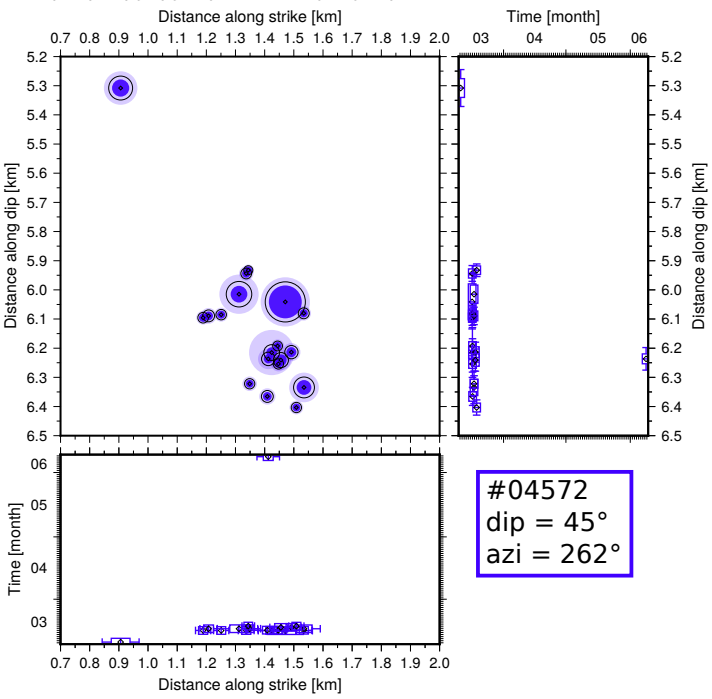
Distance along strike [km]
Time [month]
Distance along dip [km]
Time [month]
#04572
dip = 45°
azi = 262°

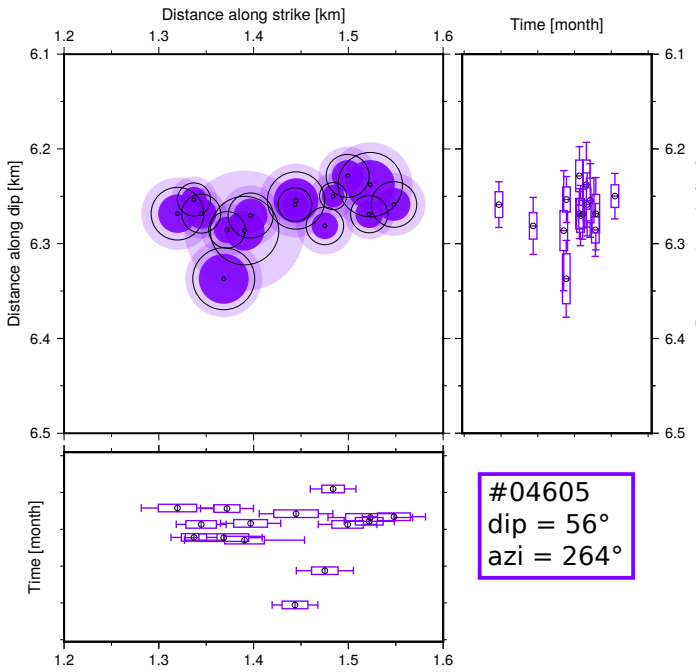
Distance along strike [km]
Time [month]
Distance along dip [km]
Time [month]
#04605
dip = 56°
azi = 264°

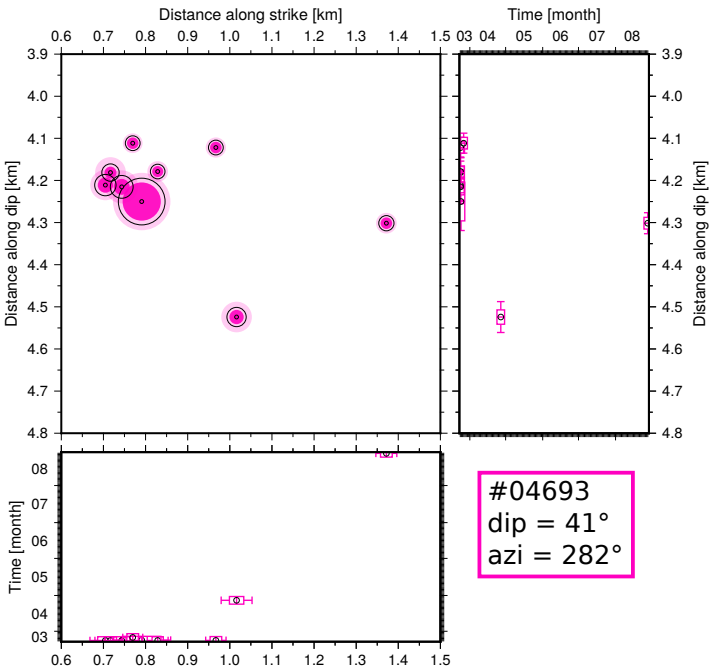
Distance along strike [km]
Time [month]
Distance along dip [km]
Time [month]
#04693
dip = 41°
azi = 282°

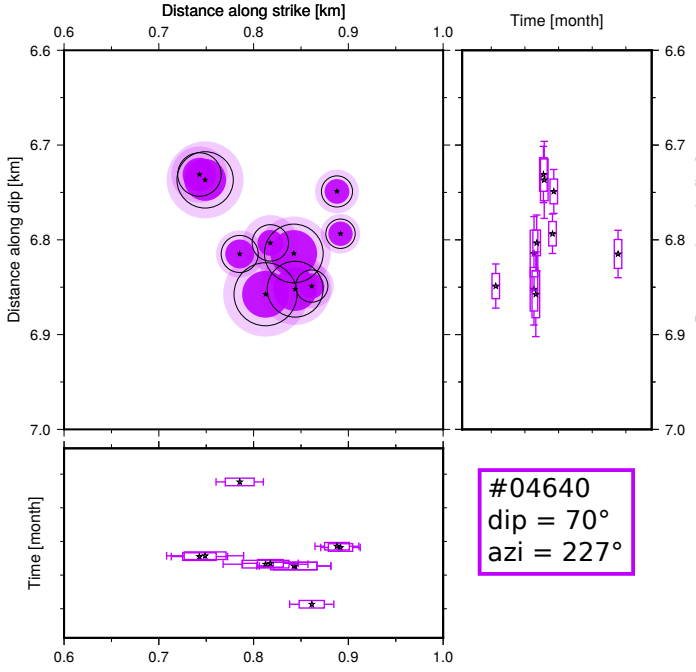
Distance along strike [km]
Time [month]
Distance along dip [km]
Time [month]
#04640
dip = 70°
azi = 227°

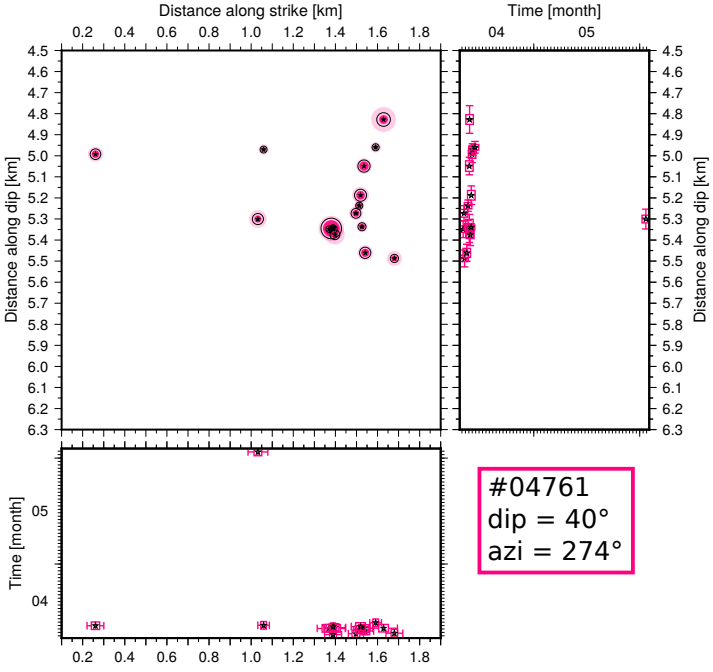
Distance along strike [km]
Time [month]
Distance along dip [km]
Time [month]
#04761
dip = 40°
azi = 274°

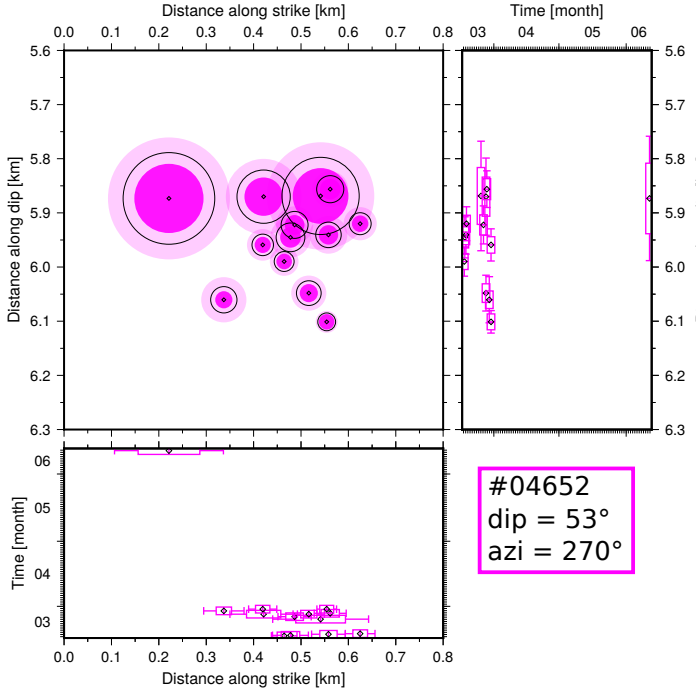
Distance along strike [km]
Time [month]
Distance along dip [km]
Time [month]
#04652
dip = 53°
azi = 270°

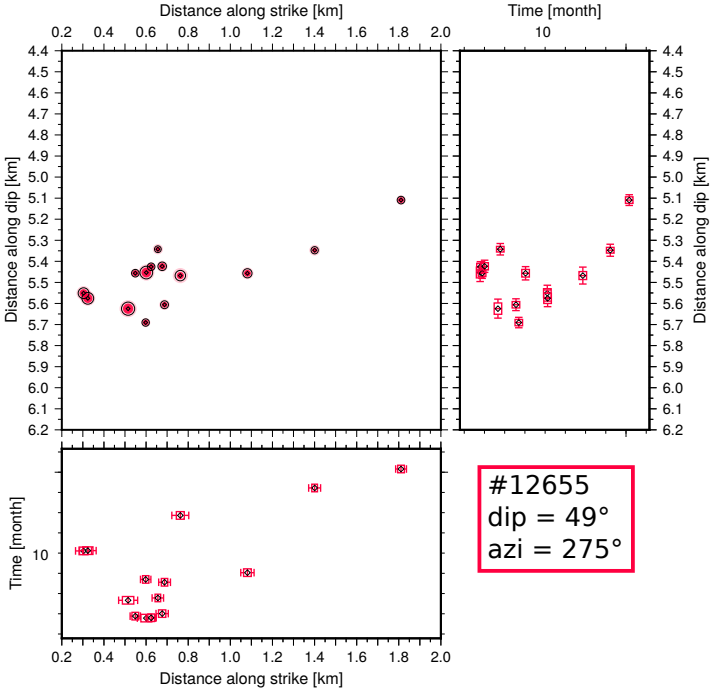
Distance along strike [km]
Time [month]
Distance along dip [km]
Time [month]
#12655
dip = 49°
azi = 275°

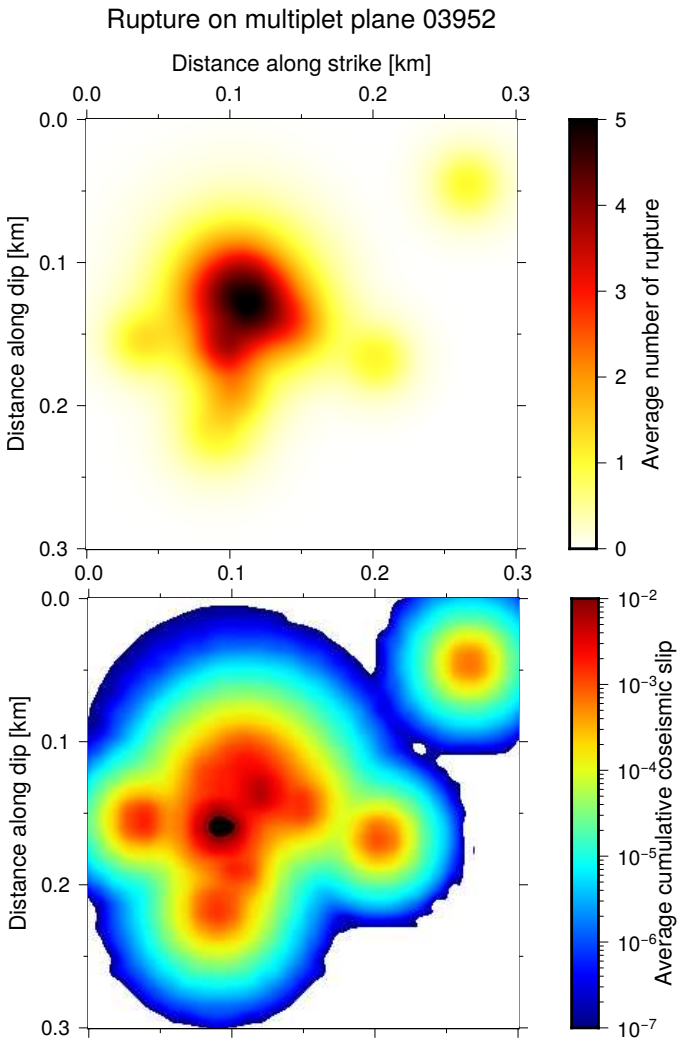

FIGURE A.2 – Bayesian inversion of source paramters of the 03952–multiplet events projected on its best-fit rupture plane. (a) Average cumulative number of ruptures estimated on the rupture plane of the multiplet, taking into account the location and source dimension uncertainties. (b) Average cumulative coseismic slip. The methodology is described in Godano et al. [2015].

Annexe B

Clusterization in space-time domain

The relocated catalog is highly clustered in space and time during swarm activity. Even if some active structures could be outlined manually, identifying the earthquakes associated with each ones is laborious and depends on the tectonic knownledges of the region. Therefore, to investigate spatial and temporal features of the microseismicity, we introduced an automatic method developped by Zaliapin et al. [2008] to identify dependent event clusters within seimsic crises.

B.1 Methodology

Following Zaliapin et al. [2008] and Zaliapin and Ben-Zion [2013], we computed the space-time-magnitude proximity between an earthquake j and an earlier earthquake i :

$$\eta_{ij} = t_{ij}\ (r_{ij})^{d_f}\ 10^{-bm_i} \tag{B.1}$$

where $t_{ij} = t_j - t_i$ is the interevent time (in years), r_{ij} is the hypocentral distance between the two earhquakes (in km), b is the Gutemberg-Richter frequency magnitude commonly known as the b-value, m_i is the magnitude of the parent event i, and d_f is the possible fractal dimension of hypocenter distribution. We computed the distance η_{ij} with parameters $b = 1.2$, $m_0 = 1.2$ and $d_f = 1.6$. In contrast to Zaliapin and Ben-Zion [2013], we used hypocentral than epicentral separation distance, because the vertical location uncertainties are quite small after the relocation process, and almost equivalent to the horizontal ones.

The nearest-neighbor distance n_j for a given event j is the minimal distance among η_{ij} where i goes over all earlier events. We called the event i having the minimal distance, the nearest-neighbor or the parent of event j.

For a convenient representation, we defined the rescaled space and time components of the nearest-neighbor distance, normalized by the magnitude as :

$$\mathrm{T}_{ij} = t_{ij}\ 10^{-qbm_i};\ \ \mathrm{R}_{ij} = (r_{ij})^{d_f}\ 10^{-(1-q)bm_i} \tag{B.2}$$

This definition ensures that $\eta_{ij} = \mathrm{T}_{ij}\ \mathrm{R}_{ij}$ or in logscale, $\log\eta_{ij} = \log\mathrm{T}_{ij} + \log\mathrm{R}_{ij}$, which is useful for the visualization of the data and to depict the bimodality of the nearest-neighbor distance. Indeed, the bimodal distribution of $(\log\mathrm{T}, \log\mathrm{R})$ has been documented in several catalogs of various regions presenting swarm activity [Davidsen et al., 2015; Gu et al., 2013; Reverso et al., 2015; Ruhl et al., 2016]. It corresponds to the existence of two different modes called the background mode and the clustered mode. The high-distance mode corresponds to the background seismicity governed by a stationary homogeneous Poisson process, while the low-distance mode consists of cluster

events that happen within a highly localized zones in both time and space. According to [Zaliapin and Ben-Zion, 2013], such groups are mainly foreshock-mainshock-aftershock sequences or swarms. In the next section, we will present the results of the (T, R) distribution for the western Corinth rift and used them to identify space-time clusters. These results will be compared to the multiplet classification.

B.2 Results

We first start by applying this nearest-neighbor method to the 2000–2015 relocated CRL catalog (see Chapter 4 and Figure 4.7) for comparison with others regions in the world. As expected, this large regional catalog of 94,000 micro-earthquakes ($1 \leq M \leq 5$) has a bimodal distribution of the nearest-neighbor distances (Figure B.1), similar to the background and clustered populations observed in Nevada [Ruhl et al., 2016] and in California [Zaliapin and Ben-Zion, 2013] for instance.

A clustering threshold c (solid white line in Figure B.1.a) can easily be chosen to separate the two modes of the distribution. In the examined catalog, the nearest-neighbor links (parent-child links) connect all earthquakes in a single-spanning network (Figure B.2.a). Removing the long links, those with nearest-neighbor distance above the threshold ($n_{ij} > c$), partitions this network into multiple sub-networks (Figure B.2.b). We obtain a collection of distinct trees, which correspond to short-links families of events or clusters, and isolated earthquakes or singles. We map separatly the events with strong and weak links in the Figure B.3 in order to identify areas with a particular behavior or being activated only by isolated events or clustered events. We observe that the strong links correspond to the main swarms occurred during the 16 years of the observational period. The two seismic swarms of 2002 and 2013 on the southern coast show a particular large amount of strong links, with almost no weaker links. We also observe a dense population of strongly linked events in the area of the 2003–2004 seismic crisis (see Chapter 3), and on the northern coast at the location of the Efpalio doublet and their aftershock sequence (see Figure 5.21). In the westernmost part, the strongly linked events mainly correspond to the 2014 swarm with migration patterns (see Chapter 4 and Figure 4.12). On the contrary, the north-eastern activity close to the 1995 Aigion fault rupture plane, as well as events in the Transition zone and the Trizona Island zone (see Figure 4.10) for the description of zone denominations) seem to show only weak linked events. However, we know that this region highlights several multiplets and is affected by slow aseismic slip (see Chapter 4). Even if most of these events belong to multiplets, they show long interevent times explaining their weak link.

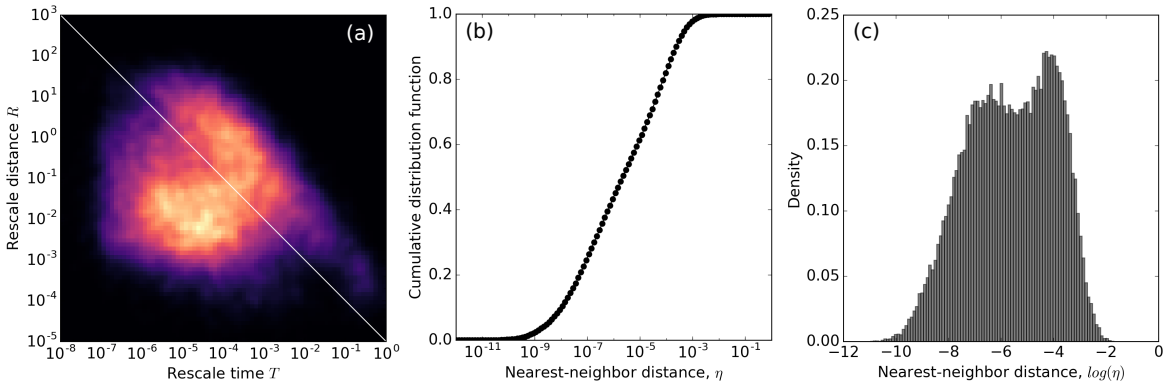

FIGURE B.1 – Distribution of the nearest-neighbor distances in the western Corinth rift using the relocated catalog. (a) The joint distribution of the rescaled time (T) and space (R) components, estimated using a Gaussian kernel smoothing. The color scale represents the number of data. (b) Cumulative distribution of the nearest-neighbor distance η in log-scale. (c) Histogram of the nearest-neighbor distance η normalized to sum up to unity. The bimodal distribution is clearly seen in the panels (a) and (c).

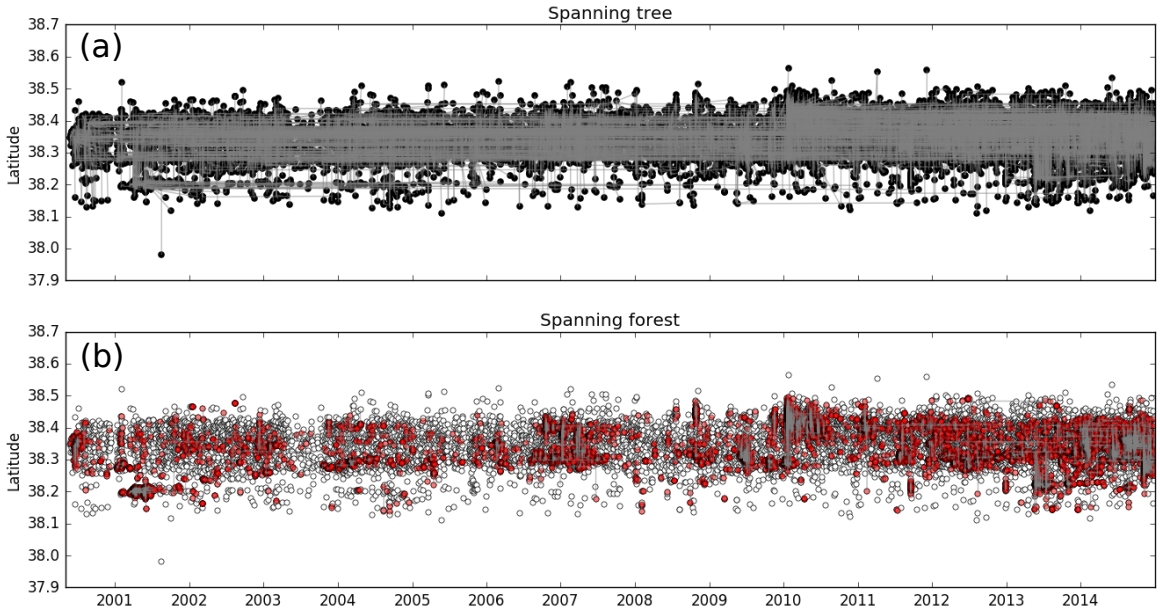

FIGURE B.2 – Spanning tree analysis of the nearest-neighbors for the relocated catalog. The nearest-neighbor links are shown in light grey lines. (a) Complete spanning tree of the nearest-neighbors. (b) Nearest-neighbor forest obtained in removing the long or weak links from the spanning tree. Open circles represent single events, filled circles represent families.

It would be interesting to compare the cluster families resulting from this methodology with the multiplet families extracted by cross-correlations and hierarchical clusterization, and to analyse the differences between the two methods. In any cases, the nearest-neighbor methodology, coupled with the classification in multiplets might be very useful to distinguish short-term multiplets occurring during seismic crises from long-term multiplets or repeaters with long recurrence time intervals possibly associated to slow slip. The association of both methods might reveal some new mechanical properties of the Corinth rift, and could help in the identification and understanding of different behaviors depending on the fault systems.

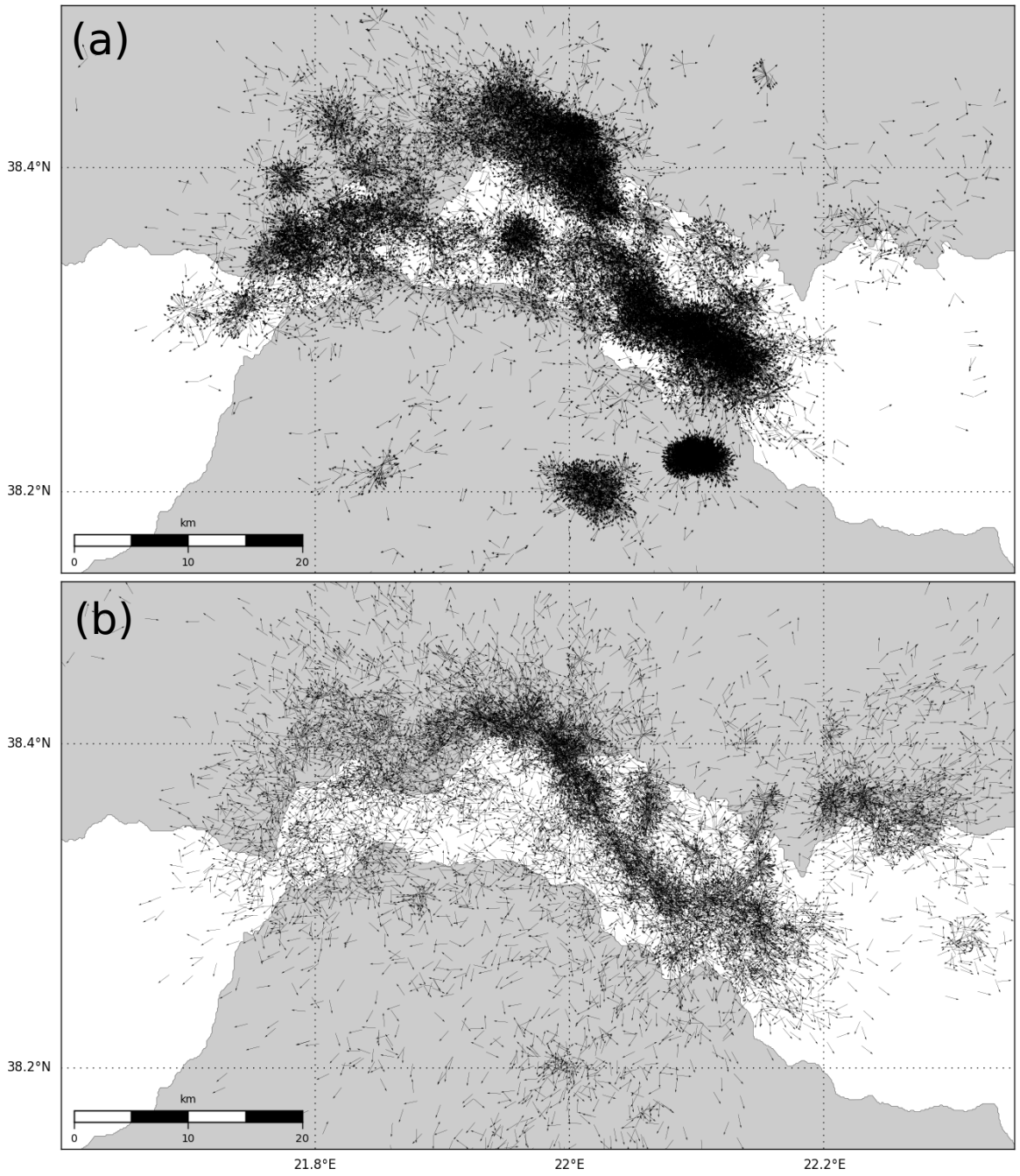

FIGURE B.3 – Map of the strong and weak nearest-neighbors for the relocated catalog. (a) Strong nearest-neighbor events. (b) Weak nearest-neighbor events. Each light black arrow represent a linked pair of events. The arrow edge points towards the parent event (not represented) whereas the arrow tail locates the child.

Annexe C

Estimation of the completeness magnitude

C.1 Methodology

We use the multiscale method described by Vorobieva et al. [2013] to estimate and map the completeness magnitude (M_c) of the CRL catalog of events. The method takes into account the spatial variation of the seismicity knowing that some areas may exhibit a specific type of seismicity not recover elsewhere in a same region. The idea of this multiscale mapping technic was at first develop for volcanological regions, where the seismicity is usually a mixture of different kinds of events and where the estimation of M_c is challenging because of the geographical contraints to implant local seismic networks. Given the geometry of the Gulf of Corinth, the reliefs of the coast which govern the CRL network configuration, and its seismicity organized in intense localized microseismic swarms with few $M > 6$ earthquakes every decades, the methodology seems totally appropriated for the region.

Basically, the method uses the Gutemberg-Richter law,

$$\log_{10}(N) = a - b\,M \tag{C.1}$$

so that N is the number of events having a magnitude $\geq$ M, and a and b are two constants. a is an indicator of the seismicity rate and b is well-known as the b-value representing the ratio between the large and small events. It is generally close to 1 in seismically active region, but values from 0.3 to 2.5 have been reported in different tectonical context worldwide [El-Isa and Eaton, 2014]. The multiscale method is also based on a relation between the magnitude range and the characteristic length scale of the domain for the data selection. It explores the whole ranges of magnitudes using an overlapping sliding window and each magnitude range $\mathscr{M}_i$ is associated to a radius R_i delineating a circle for data selection. This radius is defined as follow :

$$R_i = R_0\ 10^{pM_i} \tag{C.2}$$

for which p is a positive constant of the order of $b/2$ and R_0 is a characteristic length to set according to the required number of events within the magnitude ranges. For more details, we invit you to read the complete methodology developped and explained by Vorobieva et al. [2013], but here is a summary of the key steps.

In practise, they start from the smallest magnitude range $\mathscr{M}_i = [M_i, M_i + W_M]$, where W_M is the magnitude step, and they succesively test if M_i and M_c are according to the following conditions :

1. the number of events whithin the circle $\mathscr{C}_i$ of radius R_i in the magnitude range $\mathscr{M}_i$ is larger than a constant threshold number N_c.

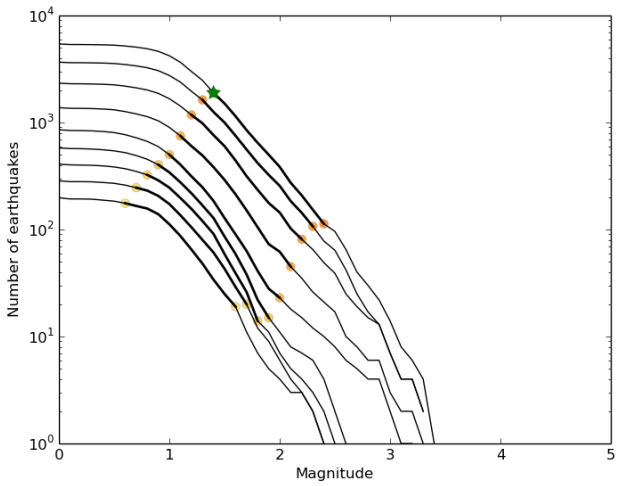

FIGURE C.1 – Multiscale estimation of the completeness magnitude M_c. For a given spatial grid node, we select events in different circles $\mathscr{C}_i$ associated to a magnitude range $\mathscr{M}_i$ and compute the FMD (black lines) for each set. These FMDs are highlighted within the magnitude range of constant width W_M (bold black curves) over which we test the consistency of the Gutemberg-Richter law. The warm colored circles are the limits $[M_i, M_i + W_M]$ with a color is proportional to M_i. The green star represents the estimated completeness magnitude M_c, which corresponds to the lower limit of the smallest $\mathscr{M}_i$ for which the GR law is satisfied.

2. the frequency-magnitude distribution (FMD) whithin the magnitude range $\mathscr{M}_i$ satifies the Gutemberg-Richter (GR) law.

To verify if the FMD follows the GR law, they developped an iterative procedure to estiamte the b-value on a given magnitude range $[M_{min}, M_{max}]$. When the procedure converges (Figure C.1), they compute the uncertainty δ of the b-value estimation and perform a last additional test to verify that this slope remains stable thoughout the smallest magnitudes.

With the description step by step of the method in Vorobieva et al. [2013], we implemented a homemade Python code to run it on the CRL catalog with a parallelization option.

C.2 Results

C.2.1 Mapping the completeness magnitude

The Figure C.2 presents the map of the spatial variation of the completeness magnitude M_C computed with the parameters R_0 = 10 km, p = 0.6 and N_c = 10 over the relocated earthquake catalog (see Chapter 4), and the uncertainty map of M_C. We also compute the map of the variation b-value obtained at the same time as the completeness magnitude (Figure C.3). We add the map of the parameters adjusted to compute the magnitude of completeness, including the number of events taking into account and the associated radius of the circle delineated the aera of selection of events (Figure C.4).

Globally, the results show a stable completeness magnitude about 1.2–1.3 with low uncertainties in the middle of the gulf where the seismicity is concentrated.

C.2.2 Break in Gutemberg-Richter law

We use the same approach as Vorobieva et al. [2016] in order to attempt to distinguish different type of deformation along the fault system of the western Corinth rift, by analysing the variations of the event size distributions at different locations. We only concentrate here on the Aigion fault as a first test and knowing that the fault was evidenced to partly creep thanks to InSAR measurements [Elias, 2013].

According to the completeness magnitude in the area of the Aigion faults $M_c \approx 1.3$, we select $M_W \geq 1.3$ relocated earthquakes from 2000 to 2015 in narrow bands of 2 km wide, or at a maximum distance of 1 km from the Aigion fault plane assuming a dip of 60° towards the north (Figure C.5.a). Then, we classify these events according to their position along the faults using an

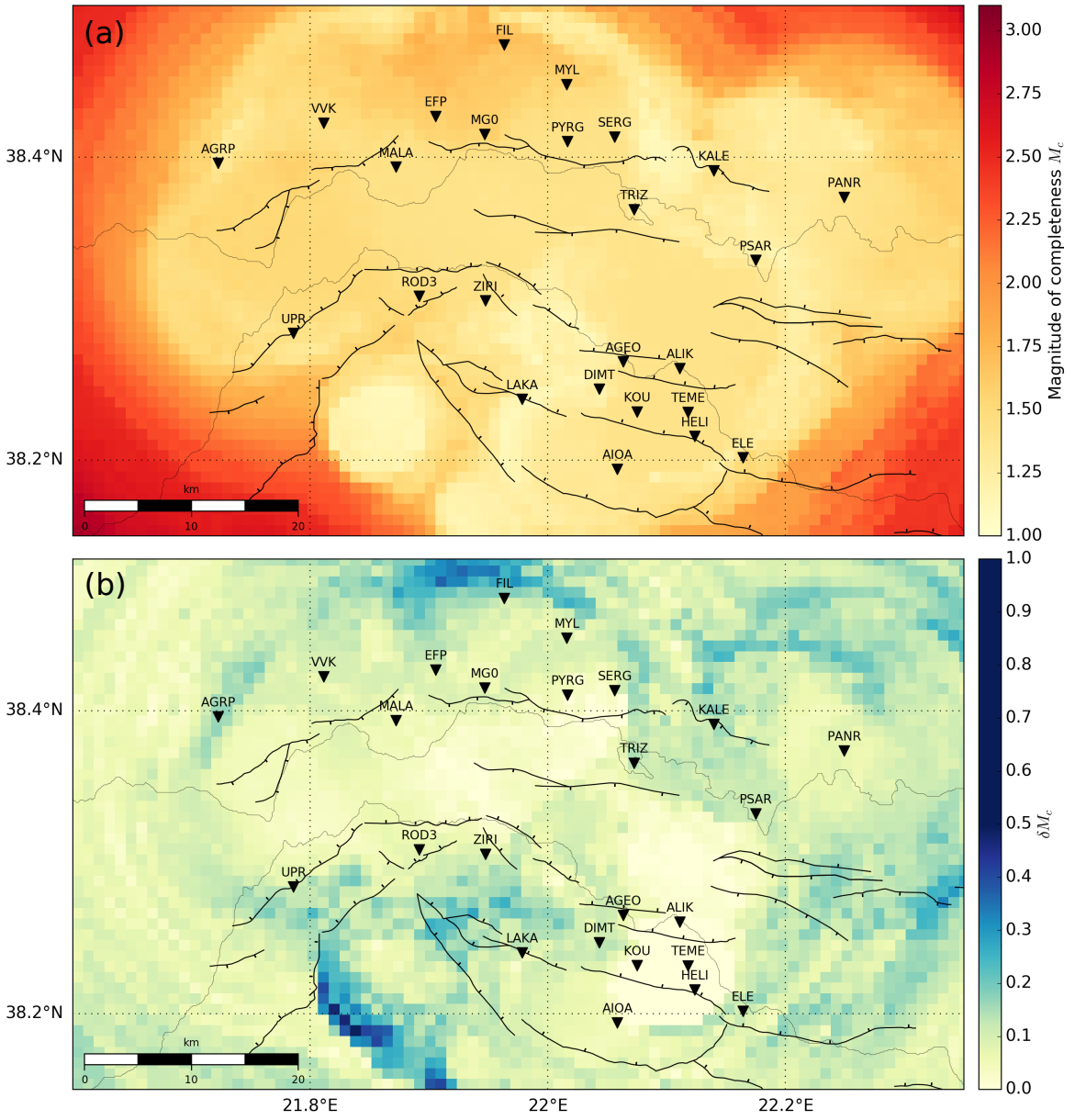

FIGURE C.2 – Spatiale variation of the completeness magnitude over the Corinth rift. (a) Map of completeness magnitude M_c. (b) Map of the uncertainty δM_c. The main normal faults are represented by black lines. Some stations are shown as visual marks with upside down black triangles.

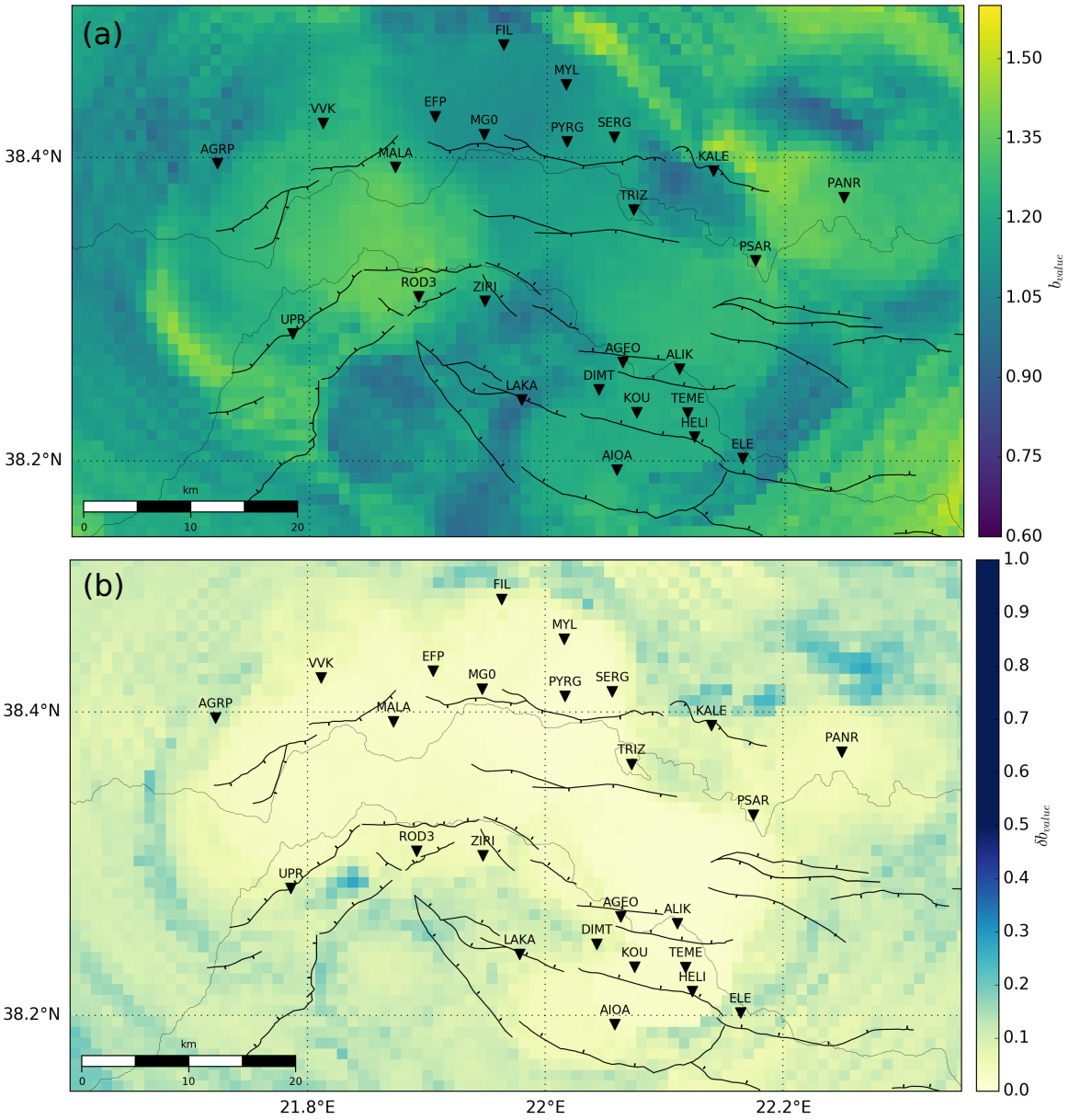

FIGURE C.3 – Spatiale variation of the *b*–value over the Corinth rift. (a) Map of the *b*–value. (b) Map of the uncertainty δb–value. Markers are the same as in the Figure C.2.

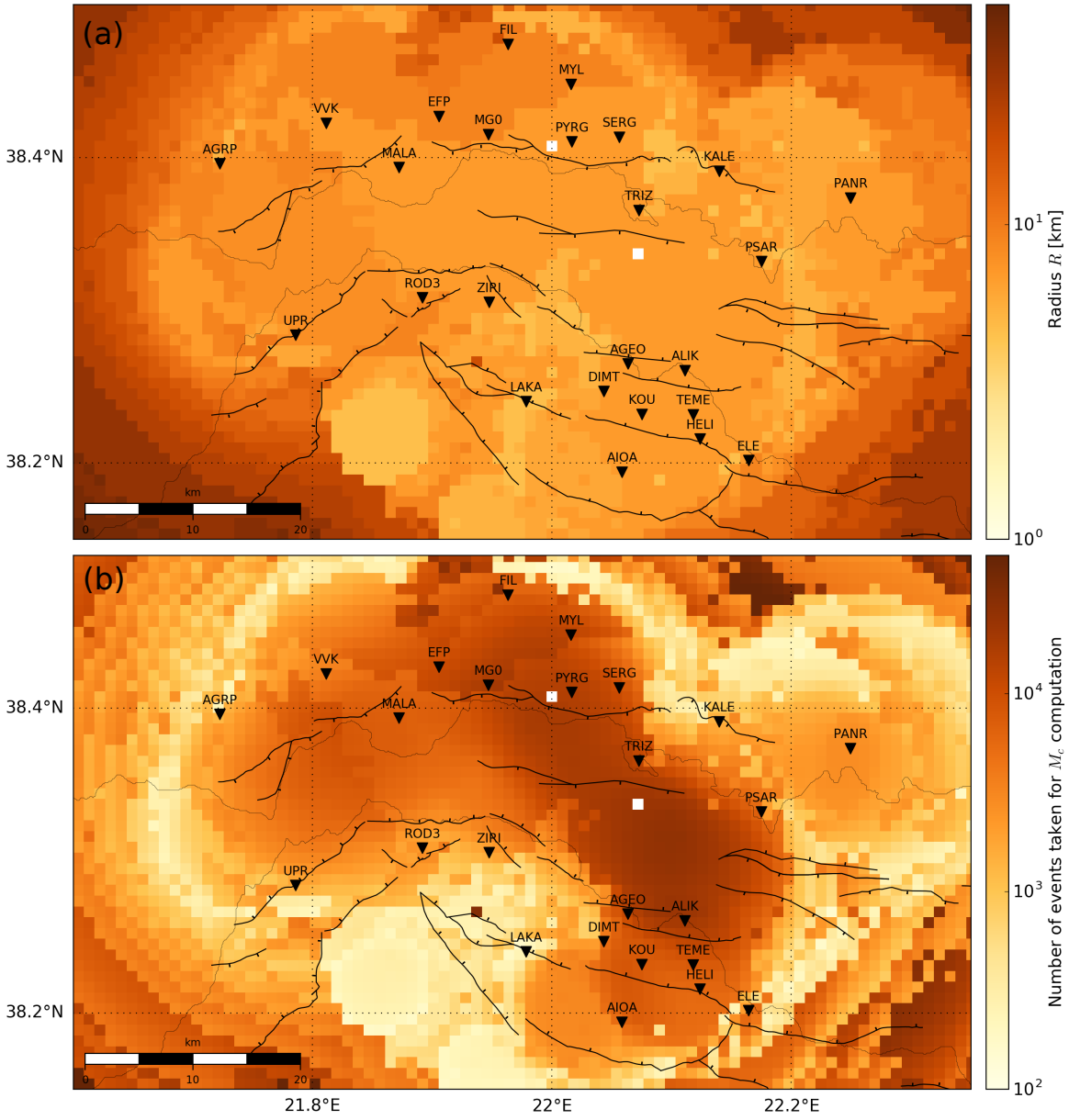

FIGURE C.4 – Spatial variation of the parameters to compute the completeness magnitude and the b–value. (a) Map of the circle radius R_i used for each cells. (b) Map of the number of events included in the calculations for each cells. Markers are the same as in the Figure C.2.

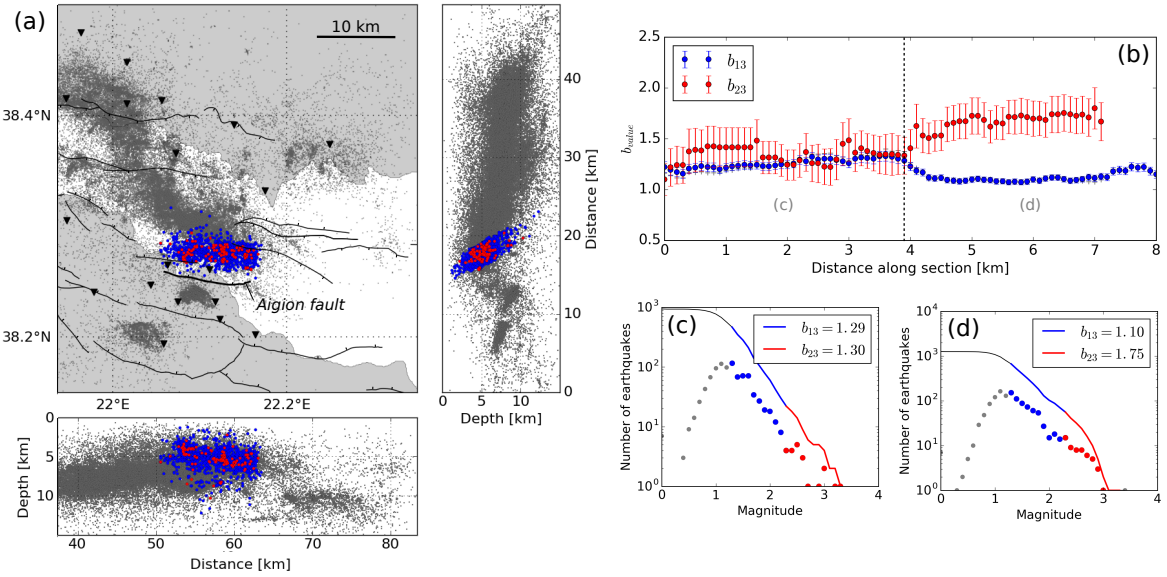

FIGURE C.5 – Break of slope in the Gutemberg-Richter law along the Aigion fault. (a) Map of the seismicity approximately along the Aigion fault plane dipping north 60°. We selected events at less than 1 km distance to the fault plane. The blue circles are events with magnitude $1.3 \geq M_W < 2.3$ and red circles are events with $2.3 \geq M_W < 3.3$. The main normal faults are represented by black lines and the stations by black upside down triangles. (b) $b_{M1.3}$–values (blue dots) and $b_{M2.3}$–values (red dots) estimated through slidding windows of 2 km long every 0.1 km along the fault trace. We notice a break in the slope at about 3.9 km (black dashed line). (c) and (d) represent respectively the magnitude distributions of events inside a 2 km long window at 2.8 km and 6.5 km distance from the west beginning of the fault trace. The colors distinguishes the two population of events taking into account, as before.

overlapping 2 km long sliding window with steps of 0.1 km. For each fault segment, we study the earthquake magnitude distribution in two non-intersecting magnitude ranges, [1.3, 2.3[and [2.3, 3.3[, using a truncated Gutemberg-Richter law [Vorobieva et al., 2016]. For the two populations of events, we estimate the $b_{M1.3}$–value and $b_{M2.3}$–value from the Gutemberg-Richter law using a maximum likelihood method, and assigned the found values to the center of the corresponding slidding window (Figure C.5). We fixed the minimum number of events to compute the b–value to 10, according to relatively small window length and number of total events taking into account. The uncertainties on the b–value are computed using a bootstrap technique.

Along the Aigion fault, which is about 8 km long, we success to estimate the $b_{M1.3}$–values everywhere but we do not have enough strong events in the 1 km easternend part of the fault trace for the estimation of the $b_{M2.3}$–values. Over the fault length, the $b_{M2.3}$–values range from 1.1 to 1.8 ±0.2 whereas the $b_{M1.3}$–values range stay relatively constant around 1.0–1.3 ±0.05.

The estimated b–values of the two populations superimposed in the first half length of the Aigion fault but differenciate on its eastern part (Figure C.5.b). This last zone is characterized by a deficit of large events, resulting in an increase of the $b_{M2.3}$–values. This lack and this difference in b–values may be interpretated as creep behavior [Vorobieva et al., 2016].

Therefore, it would be interesting to look into the InSAR data and the GPS data at thinner scale, in order to confirm or reject this hypothesis and quantify the possible aseismic slip difference between the western and eastern Aigion fault. We can notice that the Fassouleika fault overlap the Aigion fault trace on its western side, but this would theoretically not change the earthquake size distribution. However, they easternmost events are located at the Transition zone (TZ described in Chapter 4) which contains several multiplets and some repeaters at the border of the blind 1995 Aigion rupture plane [Bernard et al., 1997].

UNIVERSITÉ SORBONNE PARIS CITÉ

Sismicité, couplages sismique-asismiques et processus transitoires de déformation dans un système de failles actives : le rift de Corinthe, Grèce

par

Clara DUVERGER

La partie ouest du rift de Corinthe, en Grèce, s'ouvre à une vitesse d'environ 15 mm par an générant un taux de déformation parmi les plus élevés au monde, quelques séismes destructeurs de magnitude M > 6 par décennie, et une forte activité microsismique irrégulière spatialement et temporellement. Afin de mieux comprendre les mécanismes liés à cette déformation crustale et de préciser les structures majeures actives, ce travail de recherche exploite la base de données sismologiques du *Corinth Rift Laboratory* de 2000 à 2015 en analysant finement les microséismes et leur évolution spatio-temporelle. La relocalisation globale des sources sismiques ainsi que leur classification en multiplets ont permis de préciser la géométrie des failles et d'identifier des comportements mécaniques différents. La zone ouest, au milieu du golfe, est affectée par des variations de pressions de fluides dans une couche géologique, entraînant des migrations des essaims de microséismes à des vitesses d'environ 50 m par jour. Les multiplets profonds de la partie centrale, près de la côte nord, sont persistants et semblent déclenchés par des épisodes de glissements lents asismiques sur un détachement immature pouvant atteindre la croûte ductile. Le faible pourcentage de déclenchement dynamique par les ondes sismiques suggère que l'état global du système de failles n'est pas au seuil critique de rupture. La magnitude des séismes est corrélée à l'impulsivité initiale de la rupture. Ces résultats précisent la dynamique de déformation du rift, les interactions sismique-asismiques, et permettront d'améliorer les modèles d'aléas sismiques de la région.

Mots clés : failles actives, essaims sismiques, multiplet, déformation transitoire, pression de pore, glissement lent, migration sismique, déclenchement dynamique, initiation de la rupture, rift de Corinthe.

The western part of the Corinth Rift in Greece is opening at about 15 mm per year, generating one of the highest deformation rates in the world, some destructive earthquakes of magnitude M > 6 per decade, and high microseismic activity irregular in space and time. In order to better understand the mechanisms related to this crustal deformation and to specify the major active structures, this research work makes use of the seismological database of the *Corinth Rift Laboratory* from 2000 to 2015 by finely analyzing microearthquakes and their spatio-temporal evolution. The global relocation of the seismic sources and their classification into multiplets enable to refine the geometry of the faults and to identify different mechanical behaviors. The western zone, in the middle of the gulf, is affected by fluctuations of fluid pore pressures in a geological layer, resulting in microseismic swarm migrations at a velocity of about 50 m per day. The deep multiplets of the central part, near the northern coast, are persistent and appear to be triggered by episodes of slow aseismic slip along an immature detachment, which can reach the ductile crust. The low percentage of dynamic triggering by passing seismic waves suggests that the overall state of the fault system is not at the critical breaking point. The magnitude of earthquakes is correlated with the initial impulsiveness of the rupture. These results specify the dynamics of the rift deformation, the seismic-aseismic interactions, and will make possible the improvement of the seismic hazard models of the region.

Key words : active faults, seismic swarm, multiplet, transient deformation, pore pressure, slow slip, seismic migration, dynamic triggering, rupture initiation, Corinth rift.